



UNIVERSIDAD NACIONAL AUTÓNOMA DE MÉXICO
PROGRAMA DE POSGRADO EN ASTROFÍSICA

Instituto de Astronomía – Ciudad Universitaria

ESPECTROSCOPIA ESPACIALMENTE INTEGRADA
DE REGIONES HII GALÁCTICAS

TESIS

QUE PARA OPTAR POR EL GRADO DE
DOCTOR EN CIENCIAS (ASTRONOMÍA)

PRESENTA

VÍCTOR FRANCISCO ROBLEDO RELLA

TUTORA

DRA. MIRIAM DEL CARMEN PEÑA CÁRDENAS, INSTITUTO DE ASTRONOMÍA

MÉXICO, D. F. NOVIEMBRE 2014



Universidad Nacional
Autónoma de México

Dirección General de Bibliotecas de la UNAM

Biblioteca Central



UNAM – Dirección General de Bibliotecas
Tesis Digitales
Restricciones de uso

DERECHOS RESERVADOS ©
PROHIBIDA SU REPRODUCCIÓN TOTAL O PARCIAL

Todo el material contenido en esta tesis esta protegido por la Ley Federal del Derecho de Autor (LFDA) de los Estados Unidos Mexicanos (México).

El uso de imágenes, fragmentos de videos, y demás material que sea objeto de protección de los derechos de autor, será exclusivamente para fines educativos e informativos y deberá citar la fuente donde la obtuvo mencionando el autor o autores. Cualquier uso distinto como el lucro, reproducción, edición o modificación, será perseguido y sancionado por el respectivo titular de los Derechos de Autor.

Dedicatoria

Dedico esta tesis a todas las personas que alguna vez tuvieron un sueño y que lucharon incansablemente para conseguirlo. No te rindas, pues aunque el trabajo y el esfuerzo son grandes, mayor será la recompensa y sobre todo, la satisfacción de haberlo logrado.

Además, dedico esta tesis con todo mi amor a mi hijo *Sebastián Rigel Robledo Uribe* y a mi amada esposa *Ana Ruth Lozada Martínez*.

Dedico también esta tesis a mi madre Alma Virgen Rella Ceballos, a mi padre Humberto Robledo Prince, a mis hermanos Carlos Alberto, Alma Isabel y Ana Claudia. A Ma. Esther Uribe Duarte, a la Sra. Leticia Duarte Romero y a Don Miguel Uribe Rodríguez. También a la Sra. Bertha Martínez García, a Don David Lozada Templos, por su ejemplo de vida. A todos mis cuñados, pasados y presentes: Miguel Mario, Horacio, David, Oscar, Elías y Eliseo; Rubén y Víctor. A mis tíos de sangre y políticos: Gloria, Silo, Juan, Danilo, Meche y Tabaré; Miguel, Mario y Tere. A mis primos de sangre y políticos: Gloria, Víctor, Miguel, René, Lolis, Danilo, Marco, Giovanna, y Danila; Beatriz, Rodrigo, Liliana, Marito, Alejandro, Ofelia, Rocío y Fernando. A mis sobrinos de sangre y políticos: Iván, Lorena, Víctor, Adrián y Claudio; Luz Marián, Andrea Michel, Hanna, Miguelito y Marijose; Shirel, Sarahí, Hannia, Yamilet y Eliemerson.

A mis amigos Walter Schmidt Ballard, Laura López Fernández y Angélica Aragón Rodríguez, por su amistad y apoyo incondicional durante tantos años. A mis amigos Luis Neri Vitela, Julieta Noguez Monroy e Irma Salgado Escobar por su amistad en el Tecnológico de Monterrey.

Agradecimientos

Agradezco primeramente a ese Dios invisible(?) que nos dio la vida y que nos permite vivir esta vida mágica, material y espiritual en este precioso planeta Tierra, aquí y ahora. Esta vida llena de misterios, y fuerzas aún por descubrir, con sus átomos, sus estrellas y sus galaxias; con su gente, sus ideas, su corazón y su amor...

Agradezco el apoyo que me ha dado mi hijo Sebastián y mi esposa Ana Ruth.

Agradezco el apoyo, la guía y el consejo de mi querida directora de tesis, Dra. Miriam Peña durante todos estos años.

Agradezco al Dr. Peter S. Conti, del *Joint Institute for Laboratory Astrophysics*, en Boulder, Colorado, quien sugirió inicialmente el tema de tesis y por el apoyo económico que me brindó para realizar las observaciones astronómicas utilizadas en este trabajo.

Agradezco a los doctores Rafael Costero Gracia, Héctor Hernández Toledo, Héctor Castañeda Fernández y Roberto Vázquez Meza por revisar mi trabajo de tesis y aceptar formar parte del sínodo para mi examen de grado. Al Dr. Michael G. Richer, por su lectura cuidadosa y sus valiosos comentarios de versiones preliminares de algunos capítulos de este trabajo.

Agradezco a la Dra. Gloria Koeningsberger Horowitz, a la Dra. Silvia Torres-Peimbert y al Dr. Manuel Peimbert Sierra por la guía y el apoyo que recibí durante mis estudios de licenciatura y posgrado en el Instituto de Astronomía de la UNAM en Ciudad Universitaria.

Agradezco al CONACyT por el apoyo que recibí durante mis estudios de Maestría en la UNAM y a la Dirección General de Becas de la UNAM por el apoyo que recibí durante mi estancia en Boulder, Colorado, donde comencé con este proyecto.

Agradezco también a la Dra. Linda Medina Herrera y al Tecnológico de Monterrey, Campus Ciudad de México, loable institución, por el apoyo que recibí para poder concluir este proyecto.

Resumen

Cuando se obtiene un espectro de rendija larga de una región HII extragaláctica gigante (GEHR) no resuelta espacialmente o de una galaxia HII (HIIG) con resolución espacial moderada, toda la región emisora queda prácticamente dentro de la rendija, así que el espectro de líneas de emisión observado de la nebulosa está contaminado por el espectro de las estrellas excitadoras embebidas dentro del volumen en emisión. En investigación extragaláctica, esta contribución estelar se hace evidente debido al hecho de que la constante de enrojecimiento logarítmica en $H\beta$, $c(H\beta)$, presenta diferentes valores cuando se deriva a partir de distintos cocientes de flujos de líneas de Balmer: $F(H\alpha)/F(H\beta)$, $F(H\gamma)/F(H\beta)$, etc. (eg., Robledo-Rella & Firmani 1990). McCall, Rybski & Shields (1985; MRS85) también observaron que el cociente $F(H\gamma)/F(H\beta)$ corregido por enrojecimiento usando el cociente $F(H\alpha)/F(H\beta)$ observado, tiende a tomar valores por debajo de su valor teórico en GEHRs con anchos equivalentes en emisión de $H\beta$ pequeños ($W_\beta < 70 \text{ \AA}$). Esto es una muestra del efecto creciente de la absorción estelar subyacente en las líneas débiles de la serie de Balmer, y este pronunciamiento artificial del decremento de Balmer produce una sobreestimación del enrojecimiento que alterará las intensidades de las líneas desenrojadas y por lo tanto, los parámetros físicos y las abundancias de elementos derivadas. MRS85 asumieron que los anchos equivalentes intrínsecos de la serie de Balmer en absorción en estrellas calientes son los mismos para $H\alpha$, $H\beta$ and $H\gamma$, como lo sugieren los modelos de Kurucz (1979), y encontraron que el ancho equivalente en absorción estelar promedio para estas líneas de Balmer es $W_{\text{abs}} = 2.0 \pm 0.3 \text{ \AA}$. MRS85 señalan la importancia de corregir adecuadamente las líneas de emisión observadas debido a la absorción estelar subyacente, que de otro modo ocasiona que se sobreestime la extinción hasta en 0.9 mag, produciendo flujos de líneas sobreestimados hasta en 0.3 dex para líneas como [O II] $\lambda 3727$, por ejemplo.

El valor real de W_{abs} depende de varios parámetros de la población estelar subyacente, incluyendo su función inicial de masa (IMF), sus límites de masa superior e inferior, así como la historia de formación estelar. En espectros de alta resolución espectral, pueden verse las líneas de absorción estelares anchas alrededor de las líneas de emisión delgadas (eg. García-Rojas et al. 2006); sin embargo, en observaciones de baja resolución, las componentes estelares y nebulares están mezcladas y esto puede disminuir fuertemente las líneas de emisión débiles de H y de He. Kennicutt (1992) señaló la utilidad de los anchos equivalentes en emisión de $H\beta$ como indicadores de la tasa de formación estelar en galaxias de brote y estudió la distribución de los anchos equivalentes de $H\alpha$ y de $H\beta$ en una muestra local de galaxias espirales. Encontró evidencia de que el ancho equivalente estelar en absorción promedio es $W_{\text{abs}} = 5.0 \pm 2.0 \text{ \AA}$. Poco después, Izotov, Thuan & Lipovetsky (1994) estimaron W_{abs} para las líneas de hidrógeno usando un proceso iterativo para derivar simultáneamente $c(H\beta)$ y W_{abs} (ver el capítulo III), y encontraron que W_{abs} varía en el intervalo de 0 – 3.5 \AA para una

muestra de galaxias azules compactas. En un trabajos más recientes, Kennicutt et al. (2003), Bresolin et al. (2005, 2009) y Guseva et al. (2011) presentan observaciones de alta resolución espectral y alta señal a ruido para una muestra grande de GEHRs en galaxias espirales cercanas y en galaxias con líneas de emisión, y corrigen los espectros observados por absorción estelar subyacente en la serie de Balmer, determinando $c(H\beta)$, W_{abs} y la temperatura electrónica del gas T_e , mediante un método iterativo auto consistente que arroja valores de $c(H\beta)$ consistentes con diferentes cocientes de líneas de la serie de Balmer, principalmente de $H\alpha$ a $H\delta$. Estos autores reportan anchos equivalentes en absorción en el intervalo $W_{\text{abs}} = 0 - 6.0 \text{ \AA}$. Como referencia, Olofsson (1995) realizó cálculos de evolución espectral para un brote sencillo de formación estelar y encontró también que $W_{\text{abs}} = 1.0 - 6.5 \text{ \AA}$, dependiendo de los parámetros supuestos para la IMF del brote estelar.

Finalmente, Rosales-Ortega et al. (2010), Mármol-Queraltó et al. (2011) y Sánchez et al. (2011, 2012) presentan observaciones de Espectroscopia de Campo Integrada (IFS) para una muestra muy grande de regiones HII en galaxias cercanas. Estos autores desacoplan el continuo estelar subyacente de las líneas de emisión observadas modelando el continuo estelar mediante una malla para una o más poblaciones estelares simples, con una metalicidad, edad, e historia de formación estelar dadas, y corrigiendo el espectro con un corrimiento al rojo apropiado, ensanchándolo con la dispersión de velocidades apropiada y atenuado por una cierta extinción. Todos estos parámetros se varían simultáneamente para obtener el mejor ajuste al continuo observado, que luego se resta (incluyendo el correspondiente W_{abs} en absorción) al espectro observado para obtener así el espectro con la emisión pura del gas.

En resumen, es necesario un conocimiento preciso de la contribución de las estrellas en el espectro de emisión observado, en particular para las líneas de H y de He, por las siguientes razones: *a)* se necesitan los cocientes de líneas de Balmer verdaderos para derivar la cantidad correcta de extinción y el enrojecimiento necesario para obtener las intensidades de líneas desenrojadas; *b)* estas intensidades de líneas desenrojadas, en particular la línea [OII] $\lambda 3727$ en el extremo azul del espectro, son necesarias para derivar las condiciones físicas de densidad y temperatura (T_e , n_e), así como las abundancias iónicas a partir de líneas de excitación colisional (CEL) del gas en emisión; *c)* el conocimiento preciso de las abundancias iónicas es a su vez importante para derivar el parámetro de excitación (O^{++}/O) que se usa para calcular los factores de corrección por ionización (ICF) necesarios para derivar las abundancias totales de elementos; *d)* la contribución de luz estelar dispersada necesita tomarse en cuenta para corregir por absorción subyacente las débiles líneas de recombinación (RL) de OI y OII que se usan también para derivar las abundancias iónicas de O^+/H^+ and O^{++}/H^+ ; *e)* se necesita un conocimiento preciso de las intensidades de las líneas de He para derivar las abundancias correctas de He/H; *f)* Finalmente, los parámetros físicos como densidad, composición química, factor de llenado, además de la energía de entrada estelar total (Q_0) y su distribución espectral de energía (SED), se

necesitan como datos de entrada para modelos de fotoionización y modelos de síntesis de poblaciones para inferir las propiedades de la población estelar ionizante responsable de la emisión observada, estableciendo así restricciones sobre la IMF del brote estelar, la tasa de formación estelar y la historia de formación estelar necesarios para construir modelos de evolución química de galaxias HII.

Por lo anterior, uno de los objetivos principales de este trabajo es estimar cuantitativamente los efectos de la contribución estelar en el espectro integrado (gas más estrellas) de regiones HII galácticas, y estudiar el efecto del espectro de las estrellas embebidas en la derivación de parámetros físicos y abundancias de elementos de estas regiones.

Con esta finalidad, llevamos a cabo observaciones de espectroscopia espacialmente integrada con el telescopio de 1.5 m de Cerro Tololo, en Chile, cubriendo el intervalo de 3600 – 10200 Å mediante tres configuraciones distintas del espectrógrafo, obteniendo una resolución media. Se observaron 7 regiones HII galácticas: Carina, M8, M20, RCW6, RCW60, RCW107 y RCW110 (algunas de ellas divididas en subregiones) para las cuales conocemos a-priori los tipos espectrales y clases de luminosidad de sus estrellas excitadoras. Alineamos la rendija larga del telescopio en la dirección N–S y ajustamos la tasa de guiado del telescopio para “barrer” en un tiempo dado la región central de las regiones observadas, y de este modo conseguimos un espectro que contiene tanto la emisión del gas como la contribución de las estrellas que pasaron sobre la rendija durante el barrido. Trabajando con los espectros bidimensionales en el CCD, pudimos generar dos tipos de espectros: en el espectro *.all* dejamos la emisión mezclada tanto del gas como de las estrellas y en el espectro *.neb* “sustrajimos” del CCD el espectro de las estrellas antes de formar el espectro unidimensional. De esta manera somos capaces de estimar *cuantitativamente* el efecto de las estrellas embebidas en la derivación de condiciones físicas y abundancias de elementos. Los espectros *.all* serían comparables de alguna manera con observaciones de baja resolución espacial de regiones HII extra-galácticas donde las estrellas brillantes no pueden separarse de la pura emisión nebular.

Otro propósito de este trabajo es derivar los parámetros físicos y abundancias de elementos de la región extendida de Carina, para la cual las últimas determinaciones fueron reportadas por Peimbert et al. (1978) y Dennefeld & Stasińska (1983). Han habido muchos trabajos espectroscópicos y cinemáticos relacionados con el objeto η Car y el homúnculo a su alrededor (eg. Davidson et al. 1986, Nathan & Morse, 2004), pero no sobre las abundancias químicas de la región HII extendida.

Un tercer objetivo de este trabajo es medir y cuantificar el efecto de la luz dispersada por polvo en el espectro de regiones HII galácticas. Existe evidencia de la presencia de luz dispersada en regiones HII galácticas y en nebulosas planetarias (Sánchez & Peimbert, 1991; O’Dell & Harris, 2010; Simón-Díaz et al. 2011; O’Dell et al. 2013) pero nosotros realizamos un análisis sistemático usando nuestras

regiones con el fin de medir los efectos de la componente de luz dispersada en la derivación de parámetros físicos y abundancias totales.

En el capítulo II presentamos la técnica de barrido utilizada para las observaciones. Presentamos el proceso de reducción de datos y el proceso que seguimos para generar los espectros *.all* (gas + estrellas) y los espectros *.neb* (puro gas). Finalmente, presentamos los flujos observados junto con una estimación de sus errores, los cuales serán utilizados en los siguientes capítulos. En el apéndice I resumimos propiedades generales de nuestros objetos de estudio, incluyendo los parámetros principales de las estrellas excitadores identificadas.

En el capítulo III presentamos una comparación detallada de los espectros *.all* y *.neb* en términos de las líneas de Balmer, Paschen, líneas de HeI y líneas prohibidas. Presentamos también los flujos y anchos equivalentes utilizados para derivar simultáneamente $c(H\beta)$ y W_{abs} , usando los espectros *.all* y *.neb*. Encontramos que el efecto producido por las estrellas embebidas en el espectro integrado depende de los tipos espectrales y clases de luminosidad de las estrellas embebidas. Para estrellas típicas O tempranas, la absorción estelar subyacente reduce las líneas de Balmer hasta en un 10% en H δ . Por otro lado, si el volumen en emisión contiene estrellas peculiares tipo LBV o WR (como en nuestras subregiones CarSE y CarSW, respectivamente), entonces la *emisión* estelar subyacente puede incrementar las líneas de Balmer hasta un 15% en H δ . Los efectos de las estrellas son más pronunciados para las líneas más débiles de la serie de Balmer. Encontramos que las líneas de HeI no son afectadas dentro de los errores. Sin embargo, para la región CarSE (que contiene a la estrella η Car) y para el espectro completo integrado, Car Reg, las líneas de HeI $\lambda 6676$ y HeI $\lambda 5876$ aparecen sobreestimadas hasta en un 20% si no se eliminan las estrellas del espectro integrado. Las líneas prohibidas no se ven afectadas por el espectro estelar subyacente, excepto para los espectros CarSE y Car Reg, en los cuales los flujos de las líneas de [NII] $\lambda 6584$ and [NII] $\lambda 5755$ aparecen sobreestimados en un 20% en el espectro *.all* comparado con el espectro *.neb*, debido a que η Car es un objeto con líneas en emisión). En el apéndice II presentamos una comparación *.all* vs. *.neb* más extensa de las líneas prohibidas.

Encontramos también que las regiones que incluyen estrellas O tempranas, como CarNW, M8 y M20, sugieren un ancho equivalente en absorción subyacente $W_{\text{abs}} = 1 - 2 \pm 1.0 \text{ \AA}$. Por otro lado, para CarSE y CarSW (que incluye a la estrella HD93162, WN6ha), el espectro *.all* sugiere un ancho equivalente *negativo*, $W_{\text{abs}} = -2.0 \pm 1.0 \text{ \AA}$, indicando que aparece en emisión. Los valores de $c(H\beta)$ derivados simultáneamente con W_{abs} son 0.20 dex *menores* que los valores de $c(H\beta)$ derivados ignorando W_{abs} .

En el capítulo IV, analizamos las observaciones de 3 subregiones de $7' \times 7'$ en la región norte de Carina, incluyendo la estrella η Car. Derivamos una ley de extinción para Carina ajustando los

decrementos de Balmer y Paschen observados a sus valores teóricos y confirmamos que es una ley anómala, con $R_V = 4.4 \pm 0.4$, en acuerdo con estimaciones previas. Usando los espectros *.all* y *.neb*, derivamos las condiciones físicas y abundancias con respecto a H de O, N, S, Ne y Ar, sin fluctuaciones de temperatura, utilizando los ICF más recientes reportados por Delgado-Inglada et al. (2014; DI14) y comparamos nuestros resultados con determinaciones previas. Usamos el salto de Balmer observado, en emisión, para estimar la temperatura promedio de Balmer T_{Bal} , que nos permitió estimar el parámetro de fluctuaciones de temperatura de Peimbert (1967). Encontramos que $t^2 = 0.038 - 0.052$, con errores típicos de ± 0.024 y recalculamos las abundancias iónicas y totales incluyendo fluctuaciones de temperatura. Al considerar fluctuaciones de temperatura se incrementa la abundancia calculada de O/H en $0.20 - 0.30$ dex.

Nuestros espectros indican que Carina es una región HII con metalicidad relativamente baja (del orden de $0.1 - 0.2$ dex) comparada con otras regiones HII localizadas a distancias galactocéntricas similares. La región CarSE (que contiene a η Car) presenta cocientes de N/O y S/O mayores que las regiones CarNW y CarSW, poniendo en evidencia la fuerte contaminación de las eyecciones de η Car en su entorno. En el apéndice III derivamos la densidad *rms* y el factor de llenado de Carina usando observaciones del continuo de radio adaptadas de la literatura.

En el capítulo V presentamos y discutimos un estudio similar para las regiones de M8 y M20 (divididas en dos subregiones cada una), evaluando el efecto de los espectros *.all* y *.neb* en la derivación de condiciones físicas y abundancias de elementos. Considerando Carina, M8 y M20, encontramos que $c(\text{H}\beta)_{.all}$ derivada sólo a partir de la Serie de Balmer, es en promedio 0.07 dex *mayor* que $c(\text{H}\beta)_{.neb}$. Encontramos que las densidades $n_e(\text{SII})_{.all} \approx n_e(\text{SII})_{.neb}$ dentro de los errores. Respecto a la temperatura electrónica, encontramos que $T_e(\text{OIII})_{.all}$ es $200 - 500$ K *mayor* que $T_e(\text{OIII})_{.neb}$, aunque el error asignado a $T_e(\text{OIII})$ es de ± 600 K. Para la temperatura en la zona de baja ionización, nuestros resultados indican que $T_e(\text{NII})_{.all} \approx T_e(\text{NII})_{.neb}$ dentro de los errores. Excepto para la región CarSE, encontramos que $(\text{O}/\text{H})_{.all} \approx (\text{O}/\text{H})_{.neb}$ y $(\text{S}/\text{H})_{.all} \approx (\text{S}/\text{H})_{.neb}$, aunque $(\text{N}/\text{H})_{.all}$ y $(\text{Ar}/\text{H})_{.all}$ resultan ser 0.05 dex *menores* en promedio que los valores $(\text{N}/\text{H})_{.neb}$ y $(\text{Ar}/\text{H})_{.neb}$ correspondientes. Por otro lado, encontramos que $(\text{Ne}/\text{H})_{.all}$ es en promedio 0.07 dex *mayor* que $(\text{Ne}/\text{H})_{.neb}$. Sin embargo, dado que nuestra precisión en las abundancias derivadas no es mejor que $0.10 - 0.15$ dex, no podemos establecer una tendencia definitiva entre las abundancias *.all* y *.neb*. Se requieren más observaciones y mejor resolución espectral.

Encontramos que el uso de los nuevos ICF presentados por DI14 arroja las mismas abundancias totales de O/H y de S/H que aquellas derivadas usando los ICF clásicos recopilados por Kingsburgh & Barlow (1994). Sin embargo, encontramos que la abundancia “actualizada” de N/H es menor en -0.10 dex, la de Ar/H también es menor en -0.08 dex, pero la de Ne/H se incrementa bastante, en $+0.25$ dex.

Comparando el cociente Ne/O derivado para nuestros objetos con estudios similares encontrados en la literatura (García-Rojas, et al. 2006; 2007), con resultados de estrellas B en la región de formación estelar de Orión (Nieva & Simón-Díaz, 2011) y con el Sol (Asplund et al. 2009), encontramos que el uso de los nuevos ICF propuestos por D114 pueden estar sobreestimando la abundancia de Ne/H en 0.10 – 0.15 dex, excepto en nebulosas de baja excitación ($O^{++}/O < 0.20$), como es el caso de M20.

Finalmente, en el capítulo VI usamos los flujos observados de las líneas de Balmer y sus anchos equivalentes para derivar la fracción de luz dispersada presente en el continuo de nuestros objetos. Encontramos que $\sim 70\%$ del continuo observado en la serie de Balmer en Carina y M20 se debe a luz dispersada, mientras que en M8 esta contribución es $\sim 50\%$. Nuestros resultados para M8 y M20 coinciden con otros resultados reportados en la literatura y por primera vez se reporta la fracción de luz dispersada en la región de Carina. Comparamos el continuo dispersado con el continuo estelar, inferido a partir de nuestros espectros *.all* y encontramos que están correlacionados. Encontramos también que el continuo dispersado es más azul que el continuo *.neb*, lo cual indica que el producto del albedo y la sección transversal de extinción promedio de las partículas dispersoras aumenta hacia el azul, en acuerdo con predicciones teóricas (Mathis, 1983).

Presentamos y recopilamos evidencia que indica que la extinción interna es responsable de un 50 – 70% de la extinción total en regiones HII galácticas y en GEHRs, indicando la presencia de grandes cantidades de polvo dentro del volumen emisor. Encontramos una correlación marginal entre la constante de enrojecimiento $c(H\beta)$ y la fracción estimada de luz dispersada $\chi^d = i^d / (i^a + i^d)$.

Dado que los efectos de la luz dispersada son mayores hacia el azul, encontramos que la constante de enrojecimiento corregida por luz dispersada, $c(H\beta)_{corr}$, es 0.10 – 0.15 *mayor* que la constante derivada a partir del espectro observado, $c(H\beta)_{obs}$. Esto produce temperaturas electrónicas corregidas por luz dispersada, $T_e(corr)$ unos 120 – 150 K *mayores* que aquellas derivadas ignorando los efectos de la luz dispersada. Propagando estos efectos a las abundancias iónicas y totales, encontramos que las abundancias de O/H y Ne/H permanecen iguales, pero las abundancias de N/H, S/H y Ar/H corregidas por luz dispersada son ~ 0.06 dex *menores* que las abundancias no corregidas.

Si los efectos de la luz dispersada se aplican tanto a la constante de enrojecimiento como al espectro observado (*antes* de desenrojecerlo), encontramos que el hecho de usar una $c(H\beta)_{corr}$ mayor se compensa con el efecto de disminuir las líneas azules con respecto de las líneas rojas al corregir por luz dispersada, de modo que ambos efectos tienden a cancelarse, produciendo así las mismas temperaturas electrónicas y abundancias totales.

En el apéndice IV intentamos imponer restricciones sobre el tamaño y los tipos de granos de polvo presentes en nuestras nebulosas a partir de los *colores* derivados del continuo dispersado. En el apéndice V presentamos una revisión de modelos de nebulosas con polvo y presentamos evidencia de luz dispersada en observaciones de regiones GEHRs y HIIGs que deben tomarse en cuenta al estudiar las condiciones físicas de estos objetos.

Como trabajo futuro para este campo, planeamos extender el análisis a una muestra mayor de regiones HII galácticas para robustecer la determinación cuantitativa de los efectos de la contribución estelar en los espectros integrados de regiones HII galácticas y GEHRs. Resultados parciales de este trabajo han sido presentados por Robledo-Rella & Conti (1994), Robledo-Rella & Peña (1999), Robledo-Rella (2000) y Robledo-Rella (2002).

Index

Chapter I. Introduction	14
Chapter II. Observations and reductions: <i>.all</i> and <i>.neb</i> spectra	18
2.1 Introduction	18
2.2 Observations	18
2.2.1 Carina region	21
2.2.2 M8 and M20 regions	23
2.2.3 RCW objects	29
2.3. Images reduction and extraction of the spectra	34
2.3.1 Extraction of the <i>.all</i> and <i>.neb</i> spectra	36
2.4. Observed spectra	43
2.4.1 Line flux errors	50
2.5 Conclusions	51
Chapter III. Effects of the exciting stars	53
3.1 Introduction	53
3.2 Comparison of <i>.neb</i> and <i>.all</i> line fluxes	53
3.2.1 Balmer emission lines	53
3.2.2 HeI lines	55
3.2.3 Paschen lines	57
3.2.4 Forbidden lines	58
3.3 Effects of stellar spectra on reddening and underlying absorption equivalent widths	59
3.3.1 Observed line fluxes and equivalent widths	59
3.3.2 Determination of $c(H\beta)$ and W_{abs}	62
3.4 Conclusions	65
Chapter IV. Carina physical conditions and element abundances	67
4.1 Introduction	67
4.2 Extinction law and dereddened line fluxes	67
4.2.1 Comparison of extinction laws	74
4.3 Physical parameters: electron temperature and density	78
4.4 Ionic abundances	81
4.5 Total abundances without temperature fluctuations	83
4.6 Total abundances considering temperature fluctuations	90

4.7 Conclusions	98
Chapter V. M8 and M20 physical conditions and element abundances	101
5.1 Introduction	101
5.2 Reddening corrections	101
5.3 Physical parameters: electron temperature and density	105
5.4 Ionic abundances	107
5.5 Total abundances without temperature fluctuations	109
5.6 Total abundances including temperature fluctuations	115
5.7 Conclusions	121
Chapter VI. Scattered light in the spectra of HII regions	123
6.1 Introduction - Dust within HII regions	123
6.2 Evidence of scattered light within HII regions	124
6.3 Scattered continuum	127
6.4 Comparison between scattered continuum and stellar continuum	134
6.5 Scattered continua colors	136
6.6 Effects of scattered light on derived reddening, physical conditions and element abundances ..	142
6.6.1. Effects of scattering on derived reddening	143
6.6.2. Effects of scattering on derived temperatures	145
6.6.3. Effects of scattering on derived total abundances	147
6.7 Relation between reddening and scattering	153
6.8 Relation of the gas-to-dust ratio and the fraction of scattered light	155
6.9 Conclusions	157
General Conclusions	159
Appendix I. Additional information of our program nebulae and their exciting stars	163
Appendix II. Comparison of <i>.all</i> vs. <i>.neb</i> forbidden lines	167
Appendix III. Carina root mean square density and filling factor	169
III.1 Radio method	169
III.2 Optical method	172
Appendix IV. Dust extinction efficiency factors from scattered continuum	174
Appendix V. Review of models of dusty nebulae and implications for giant extragalactic HII regions	
V.1 Introduction	179
V.2 Review of models of dusty nebulae: internal extinction and reddening	179

V.2.1 Signatures of dust within HII regions	179
V.2.2 Internal extinction and reddening	181
V.3 Scattered light in GEHRs and HIIGs	187
V.4 Conclusions	192
Bibliography	193

Chapter I. Introduction

When one takes a long-slit spectra of an unresolved giant extragalactic HII region (GEHR) or HII galaxy (HIIG) with moderate spatial resolution, the emitting region is mostly encompassed by the slit, so the observed emission line spectra of the nebula is contaminated with the spectra of the exciting stars embedded within the emitting volume. In extragalactic research, this stellar contribution is evident by the fact that the logarithmic reddening constant at $H\beta$, $c(H\beta)$, presents different values as derived from different Balmer flux line ratios, $F(H\alpha)/F(H\beta)$, $F(H\gamma)/F(H\beta)$, etc. (eg., Robledo-Rella & Firmani, 1990). McCall, Rybski & Shields (1985; MRS85) also observed that the $F(H\gamma)/F(H\beta)$ ratio corrected for reddening using the observed $F(H\alpha)/F(H\beta)$ ratio tends to be below its theoretical value for GEHRs with low emission equivalent widths at $H\beta$ ($W_{\beta} < 70 \text{ \AA}$). This is an evidence of the increasing effect of the underlying stellar absorption in the weaker Balmer lines, and this artificial steepening of the Balmer decrement produces an overestimation of the reddening which alters the un-reddened line intensities and therefore the derived physical parameters and element abundances.

Balmer emission equivalent widths are in general underestimated in GEHRs and therefore, all other non-Balmer ratios relative to $H\beta$ tend to be overestimated regardless of the adopted extinction. Assuming that the Balmer equivalent width in absorption for hot stars is about the same for $H\alpha$, $H\beta$ and $H\gamma$, as supported by Kurucz (1979) models, MRS85 found that the average stellar absorption equivalent width for the Balmer lines is $W_{\text{abs}} = 2.0 \pm 0.3 \text{ \AA}$. These authors pointed out the relevance of properly correct the observed emission lines due to this underlying stellar absorption, which otherwise could yield derived extinctions overestimated by up to 0.9 mag, producing thus (eg.) [O II] $\lambda 3727$ line fluxes overestimated by up to 0.3 dex.

The actual value of W_{abs} depends on several parameters of the underlying stellar population including its initial mass function (IMF), its upper and lower mass limit values, as well as the star formation history (SFH). In high-resolution spectra, the broad stellar absorption lines can be seen surrounding the narrow emission lines (eg. García-Rojas et al. 2006), but in low resolution data, the stellar and nebular components are blended and may decrease severely the H and HeI weak emission lines. Kennicutt (1992) pointed out the usefulness of the $H\beta$ equivalent width in emission as an indicator of the star formation rate (SFR) in starburst galaxies, and studied the distribution of $H\alpha$ and $H\beta$ equivalent widths in a sample of local spiral galaxies. He finds evidence for a mean stellar absorption equivalent width, $W_{\text{abs}} = 5.0 \pm 2.0 \text{ \AA}$. Later, Izotov, Thuan & Lipovetsky (1994) estimated W_{abs} for the hydrogen lines using an iterative procedure, deriving simultaneously both the logarithmic reddening constant $c(H\beta)$ and W_{abs} (see Chapter III), and found values of $W_{\text{abs}} = 0 - 3.5 \text{ \AA}$ for a sample of blue compact galaxies. In more recent works, Kennicutt et al. (2003), Bresolin et al. (2005, 2009)

and Guseva et al. (2011) present high-spectral resolution and high S/N observations of a large sample of GEHRs in nearby spiral galaxies and emission-line galaxies and correct the observed spectra for the underlying Balmer stellar absorption by determining $c(\text{H}\beta)$, W_{abs} and the gas electron temperature T_e , by means of an iterative and self-consistent method, that yields $c(\text{H}\beta)$ values consistent with different Balmer line ratios, mainly from $\text{H}\alpha$ to $\text{H}\delta$. These authors report absorption equivalent widths in the range $W_{\text{abs}} = 0 - 6.0 \text{ \AA}$. For comparison, Olofsson (1995) carried out spectral evolutionary calculations for a single star-forming burst and found also that W_{abs} varies from 1.0 to 6.5 \AA depending on the assumed parameters of the cluster IMF.

Finally, Rosales-Ortega et al. (2010), Mármol-Queraltó et al. (2011), and Sánchez et al. (2011, 2012) present Integrated Field Spectroscopy (IFS) observations for a very large sample of HII regions in nearby galaxies (PINGS and CALIFA surveys). These authors decouple the underlying stellar continuum from the observed emission lines modeling the stellar continuum using a grid template for one or more simple stellar populations (SSP), with a given metallicity, age and SFH, correcting the spectra for the appropriate redshift, broadening it with the appropriate velocity dispersion and attenuated by a certain extinction. These parameters are varied simultaneously so to get the best fit to the observed continuum, which is then subtracted (including the corresponding stellar W_{abs}) to the observed spectra in order to get the pure-gas emission spectra.

In summary, an accurate knowledge of the contribution of the stellar features to the observed emission lines, specially for the H and He lines, is important for the following reasons: *a)* the true Balmer line ratios are needed to derive the real amount of extinction and the reddening extinction law needed to obtain the un-reddened line intensities; *b)* these un-reddened line intensities, in particular the [OII] $\lambda 3727$ line in the blue part of the spectrum, are needed to derive the physical conditions (T_e , n_e) and accurate ionic abundances from collisionally excited lines (CEL) of the emitting gas; *c)* the knowledge of accurate ionic abundances is important to derive the excitation parameter (O^{++}/O) used to estimate the Ionization Correction Factors (ICFs) needed to derive the total elemental abundances; *d)* the contribution of stellar scattered light has to be taken into account to correct for underlying absorption the faint OI and OII recombination lines (RL) used also to derive O^+/H^+ and O^{++}/H^+ ionic abundances; *e)* high-precision HeI lines intensities are needed in order to derive accurate He/H abundances. *f)* Finally, the derived density, chemical composition and filling factor for the plasma, along with the total stellar input (Q_0) and spectral energy distribution (SED), are used as input for photoionization models and population synthesis models to infer the properties of the stellar population responsible for the nebular emission, establishing thus restrictions upon the star cluster IMF, SFR and SFH, needed to build chemical evolution models of galaxies.

One of the goals of this thesis is to estimate quantitatively the effects of the stellar contribution in the integrated (nebular plus stellar) spectra of galactic HII regions, and to study the effect of these embedded exciting stars upon the derived physical parameters and elemental abundances. With this aim, we obtained *spatially integrated spectroscopy* of seven galactic HII regions for which we know a-priori the spectral type and luminosity class of the exciting stars. Having aligned a long slit in the N–S direction, we drifted the telescope over the face of the nebulae and obtained a spectra containing both the emission of the nebular gas and the contribution of the embedded stars that crossed the slit during the scan. Working with the 2-D CCD frames, we were able to “remove” the spectra of the exciting stars to get a *.neb* spectra (pure nebula) and a *.all* spectra (nebula + stars). In this way, we were able to quantitatively estimate the effect of the embedded stars’ spectra upon the derived reddening, physical conditions and elemental abundances.

Another goal of this work is to derive the physical parameters and elemental abundances of the extended Carina region, for which the latest determinations, as far as we can tell, are those of Peimbert et al. (1978) and Dennefeld & Stasińska (1983). There has been a many spectroscopic and kinematic works related to the η Car object and its surrounding homunculus (eg. Davidson et al. 1986, Nathan & Morse, 2004), but not about the chemical abundances of the HII region itself.

A third goal of this work is to measure and quantify the effect of dust-scattered light in the spectra of galactic HII regions. There is evidence of the presence of scattered light in galactic HII and PNs (Sánchez & Peimbert, 1991; O’Dell & Harris, 2010; Simón-Díaz et al. 2011; O’Dell et al. 2013) but we carried out a systematic analysis using our sample of galactic HII regions in order to measure the effects of the scattered light component upon the derived physical parameters and total abundances.

In Chapter II, we present the observing technique used to obtain the integrated mid-resolution spectra, from 3600 – 10200 Å, for our sample of 7 galactic HII regions (including Carina, M8 and M20). We present the data reduction procedure and the process followed to extract the data in order to obtain the *.all* spectra (including the ionizing stars) and the *.neb* spectra (excluding them). Finally, we present the observed line fluxes along with their estimated errors, which will be used in the following chapters to study each region in detail. In Appendix I we summarize general properties of our target nebula, including the main parameters of their identified exciting stars.

In Chapter III we present a detailed comparison of the *.all* and *.neb* spectra for the Balmer, Paschen, HeI and forbidden lines. We present the line fluxes and equivalent widths used to estimate simultaneously the logarithmic reddening constant $c(H\beta)$, and the underlying stellar absorption equivalent width W_{abs} , derived both with the *.all* and *.neb* spectra. In Appendix II we present a further comparison of the *.all* vs *.neb* forbidden lines.

In Chapter IV we analyze the observations for our 3 Carina $7' \times 7'$ subregions in the northern part of the nebula, which includes the η Car star. We derived an extinction law for Carina from the observed Balmer & Paschen line decrements, confirming that it has an anomalous $R_V = 4.4 \pm 0.4$. We derived the *.all* and *.neb* physical conditions and abundances with respect to H of O, N, S, Ne and Ar, without temperature fluctuations, using the latest ICFs from Delgado-Inglada et al. (2014), and compare our results with previous determinations. From the observed Balmer jump in emission, we estimated an average Balmer temperature T_{Bal} , that allowed us to estimate Peimbert's t^2 -temperature fluctuations parameter, and we recalculated the ionic and total abundances considering temperature fluctuations. We found that Carina is a relatively low metallicity HII as compared with other HII regions located at the same galactocentric distance. In Appendix III we derive the root mean square density and filling factor of the nebula using radio continuum observations adapted from the literature.

In Chapter V we present and discuss similar approaches for the galactic HII regions M8 and M20 (2 subregions each), evaluating the effects of the *.all* and *.neb* spectra on the derived physical conditions and elemental abundances.

Finally, in Chapter VI we use the observed Balmer line fluxes and equivalent widths to derive the fraction of dust-scattered light present in the continua of our program nebulae. We compare this scattered continua with the stellar continua inferred from our *.all* spectra and found that they are correlated. We also determine the wavelength dependence of this scattered continua confirming model predictions that it increases toward the blue (Mathis, 1983). We estimate the effects of the scattered light in the derived reddening, physical conditions and elemental abundances of our bright nebulae. In Appendix IV we attempt to impose some restrictions about the sizes and types of grains present in our nebula using the *colors* derived from the scattered continuum, and in Appendix V, we present a review of models for dusty nebula and comment evidence of scattered light in observations of GEHRs and HIIGs, that should be taken into account when analyzing their spectra.

In future work on this subject, we plan to extend this analysis for a larger sample of galactic HII regions in order to better assess *quantitatively* the effect of the stellar contribution on the integrated spectra of galactic and extragalactic H II regions. Partial results of this work have been presented by Robledo-Rella & Conti (1994), Robledo-Rella & Peña (1999), Robledo-Rella (2000) and Robledo-Rella (2002).

Chapter II. Observations and reductions: *.all* and *.neb* spectra

2.1 Introduction

In this chapter we present our observations and reduction procedure. In Sec. 2.2 we present the observations carried out for 7 Galactic HII regions studied in this project. In Sec. 2.3 we describe in detail the procedure followed to reduce the data so to obtain our working *.all* and *.neb* observed spectra. In Sec. 2.4 we present the observed line fluxes for our nebula along with an estimation of the errors assigned to the observational line fluxes. Our main results are summarized in Sec. 2.5.

2.2. Observations

We observed 7 galactic HII regions: Carina, M8, M20, RCW6, RCW60, RCW107 and RCW110. Due to its large extension in the sky, some nebulae were divided in 2 or 3 subregions. These HII regions were selected on the basis of knowing *a priori* the spectral types and luminosity classes of their exciting stars, and were chosen from the catalogues presented by Gum (1955), Sharpless (1959), Rodgers, Campbell & Whiteoak (1960; RCW) and Georgelin (1975).

The observations were carried out with a 348×576 pixels, thinned GEC CCD and the Cassegrain Spectrograph attached to the 1.5-m telescope at Cerro Tololo Inter-American Observatory from 1993 April 28 to May 2. The sky was clear all five nights with an estimated seeing of $1 - 2.5''$. The resulting plate scale was $1.89''/\text{pix}$. In order to cover the $3600 - 10200 \text{ \AA}$ spectral range, we used a 600 l/mm grating and several filter setups so to cover the following spectral ranges: Blue (B): $3600 - 5900 \text{ \AA}$; Yellow (Y): $5800 - 8000 \text{ \AA}$; and Red (R): $7900 - 10200 \text{ \AA}$, with an overall dispersion of approximately $4.12 \text{ \AA}/\text{pix}$. We used the largest available decenter, corresponding to a slit length equal to $7.60'$ on the sky with a slit-width of $5''$, giving a spectral resolution $\geq 12 \text{ \AA}$ FWHM (as measured on the comparison lamp). We aligned the slit N-S and *drifted* the telescope in RA from East to West over previously selected regions of the target nebulae, by adjusting its tracking rate. The formula used to compute the telescope's tracking rate X , in terms of the *swept length* in RA D_{RA} , the exposure time t_{exp} , and the target declination δ is:

$$X(\text{arcmin} / \text{min}) = 15 - \left[\frac{D_{RA}(\text{arcmin})}{t_{\text{exp}}(\text{min}) \times \cos \delta} \right] \quad (1)$$

For each region, we drifted the telescope such that $D_{RA} \approx 7.5'$ in RA, starting the drift at the same position within the nebulae for each spectral range. The slit's middle point declination remained fairly constant during each integration. At the telescope, we checked that the above expression worked well

for a few integrations. However, after we completed our observing run (5 nights), we compared the predicted scanned length D_{theo} given Eq. (1), with the actual scanned length as derived from the telescope’s starting and ending coordinates for several integrations, D_{teles} . We found that real scanned length was slightly shorter than the predicted one by about $0.4'$, as shown in Fig. 1.

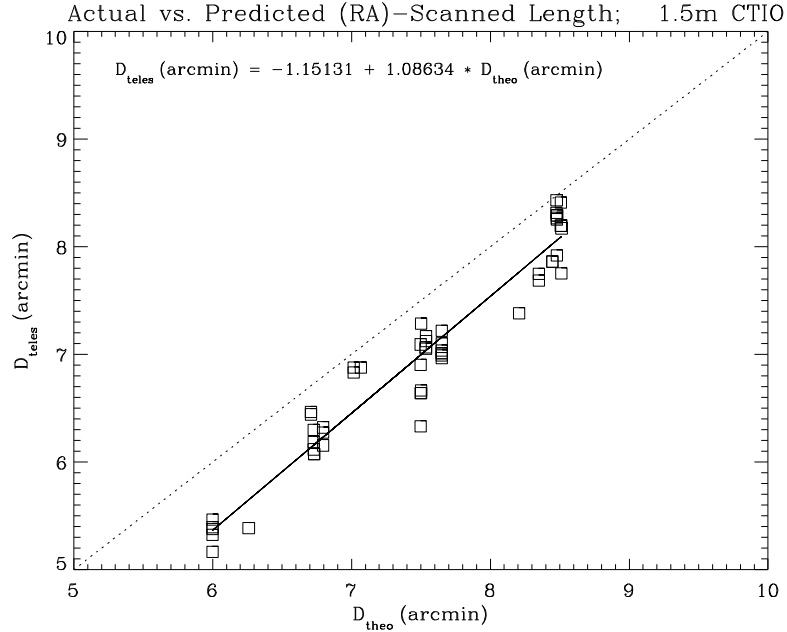


Fig. 1. Relation between the predicted scanned-length in RA D_{theo} , from Eq. (1) and the actual swept-length D_{teles} , derived from the telescope initial and final position coordinates for several integrations along our observing run.

We estimated our exposure times and scanned lengths so to avoid any saturation of the CCD, either due to the bright stars or to bright nebular lines, especially in the Y range. The integration times varied from 20 to 60 min for the B spectral range, from 15 to 30 min for the Y spectral range, and from 30 to 60 min for the R spectral ranges, depending on the brightness of the observed nebula and their exciting stars. For the brightest regions however, we also took shorter spectra of 5 min in the Y range to avoid saturation either of $H\alpha$ or the continuum from the brightest stars passing over the slit during the scan. All regions were observed at least twice in each of the B, Y, and R spectral ranges. For the wavelength calibration, we took each night exposures of a He–Ar comparison lamp with the telescope positioned at the targets. For the flux calibration we obtained at least two 4 to 10 min spectra with a wide slit for 3 standard stars taken from the list of Baldwin and Stone (1984).

Since the emitting region covers a larger area than our slit length, we obtained dark-sky frames to subtract the sky contamination in our program frames. We obtained each night at least two 10-min spectra for each spectral range pointing the telescope toward a previously identified region of the sky devoid of stars and nebulae as close as possible, but outside of our target nebulae. This step is very

important in order to subtract the sky contribution in our program frames, especially the strong H₂O and O₂ absorption bands in the 7000 – 10,000 Å range.

In Table 1 we summarize the log of our observations. For each nebula we give its FK5 2000 Equatorial and 1950 Galactic coordinates, total integration time in each spectral range, approximate optical angular size, and several common designations for each nebulae. The final scanned length in RA was $D_{RA} \approx 7.2'$ for the Carina regions, $7.1'$ for the M8 regions, and $6.5'$ for the M20 regions.

Table 1. Log of observations of the CTIO Run ^a

Nebula (1)	Equatorial (2000)		Galactic (1950)		$t_{\text{exp}} / \Delta\lambda$ -range (min)			Size ($'$) (9)	Other (10)
	α (2)	δ (3)	l (4)	b (5)	B	Y	R		
CarNW	10 44 24	-59 33 14	287.462	-0.5530	60	60	40	> 90	NGC 3372, RCW 53, G33, BBW 316A ^e , GRS 287.96 -00.82 ^e
CarSE	10 45 33	-59 40 56	287.651	-0.5987	60	15	60		
CarSW	10 44 32	-59 40 35	287.534	-0.6534	60	20	60		
M8-E	18 04 14	-24 22 58	6.030	-1.287	30	15	30	60 × 35	NGC 6523, RCW 146, S 25-(29), W29, GRS 006.00 -01.20, Lagoon
M8-W	18 03 48	-24 22 55	5.982	-1.201	30	30	30		
M20-S	18 02 39	-23 05 06	6.982	-0.333	30	20	30	30	NGC 6514, RCW 147, S30, Coll 360, Trifid
M20-N	18 02 39	-22 59 03	7.069	-0.284	30	20	30		
RCW 6	07 10 08	-18 29 31	231.351	-4.256	80	30	-	20 × 10	S301, G 5, BBW 7A ^e , GRS 231.60 -04.30 ^d , LPH 96 231.481-4.401 ^d
RCW 60-E	11 29 57	-62 37 13	293.603	-1.259	20	40	30	20 × 10	G 39, IC 2872, BBW 362C ^e
RCW 60-W	11 28 55	-62 37 13	293.812	-1.507	20	-	-		
RCW 107	16 34 09	-48 03 33	336.366	-0.281	60	40	-	8 × 4	NGC 6164-65, G52, GRS 336.4 -0.2 ^c , [W63]10 ^f
RCW 110 ^b	16 54 38	-45 13 47	340.793	-1.013	50	80	-	5 × 3	Part of G54, GRS 340.80 -1.00 ^c

^a Data adapted from Georgelin (1975), from ESO/SRC and POSS plates, and from *Simbad* Database. Columns give: (1) Nebula ID; (2) and (3) FK5 2000 Equatorial coordinates, α ($hr\ m\ s$) and δ ($^{\circ}\ ' \ ''$), respectively; (4) and (5) Corresponding (1950) Galactic coordinates l and b (both in $^{\circ}$); (6) – (8) Total integration time for each spectral range: B: 3400 – 5800 Å; Y: 5600 – 8000 Å, and R: 7800 – 10200 Å. (9) Approximate nebular optical angular size and (10) Other common names. ^b RCW110 is a faint object about 15' from RCW 111. ^c GRS = Galactic Radio Source. ^d From Lockman, Pisano & Howard (1996; LPH96). ^e From Brand, Blitz & Wouterloot (1986; BBW). ^f From Whiteoak (1963).

The three Carina regions will be analyzed in Chapter III, and the M8 and M20 regions will be studied in Chapter V. The RCW objects are fainter than Carina, M8 or M20, and our spectra did not allow us to measure line fluxes sensitive to the temperature, so we will not attempt a precise

determination of their physical conditions and elemental abundances. However, we will use the RCW objects to estimate the effect of the exciting stars upon the line intensities and upon the derived reddening. We also will use them to study the effects of the scattered light on the integrated spectra (see Chapter VI).

2.2.1 Carina Region

The Carina Nebula (NGC 3372, RCW 53, Gum 33) extends over an area on the sky greater than $180' \times 120'$ (Lang 1991). It is powered by many bright, hot O stars, which are members of the open clusters Tr 16 and Tr 14/Cr 232. We observed three subregions in the central part of the Carina Nebula, shown in Figs. 2a – 2d, referred hereafter as **CarNW**, **CarSE** and **CarSW**. The star η Car is in the middle of the CarSE region. In Figs. 2b – 2d, we have numbered the bright exciting stars that recorded a clear spectrum in the 2-D CCD frame during the scanning of each region (see Sec. 2.3 below). In Table 1a we list the initial equatorial and galactic coordinates of the slit’s middle point for the three Carina regions, which contain 5 of the 6 known O3 stars in the nebula, η Car and one WN6ha (Walborn, 1973a; Walborn, 1995; Crowther & Dessart, 1998; Nelan et al. 2004; Smith, 2006; Preibisch et al. 2011). Table 2a below presents the main parameters of the identified exciting stars.

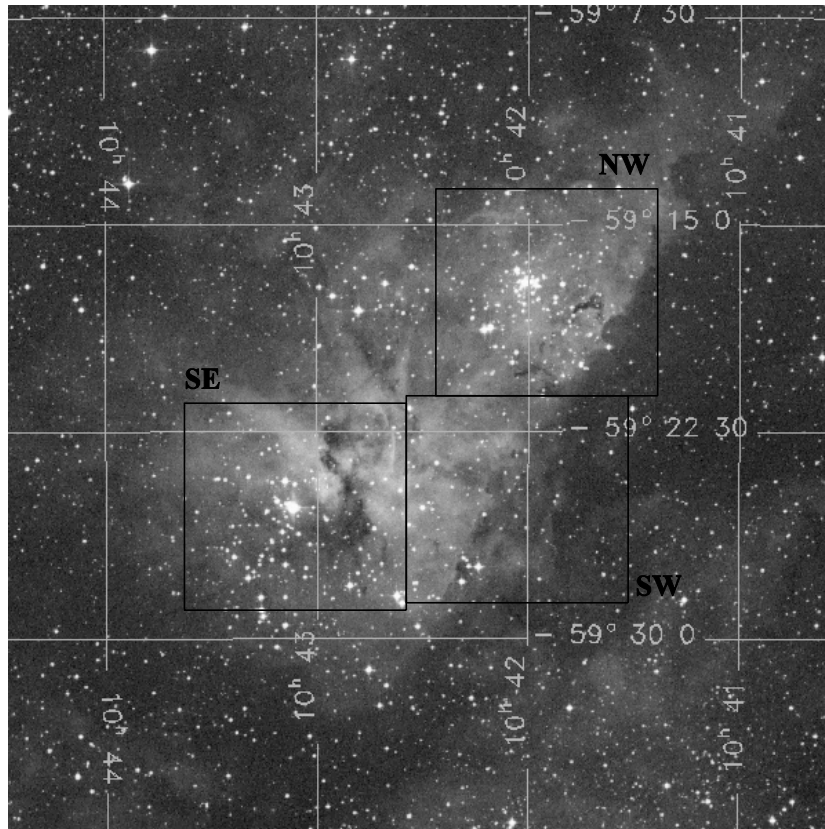


Fig. 2a. $30' \times 30'$ image of the northern Carina Nebula adapted from the *Digitized Sky Survey* showing the three scanned regions CarNW, CarSE and CarSW. The grid gives 1950 coordinates. North is up and east is left.

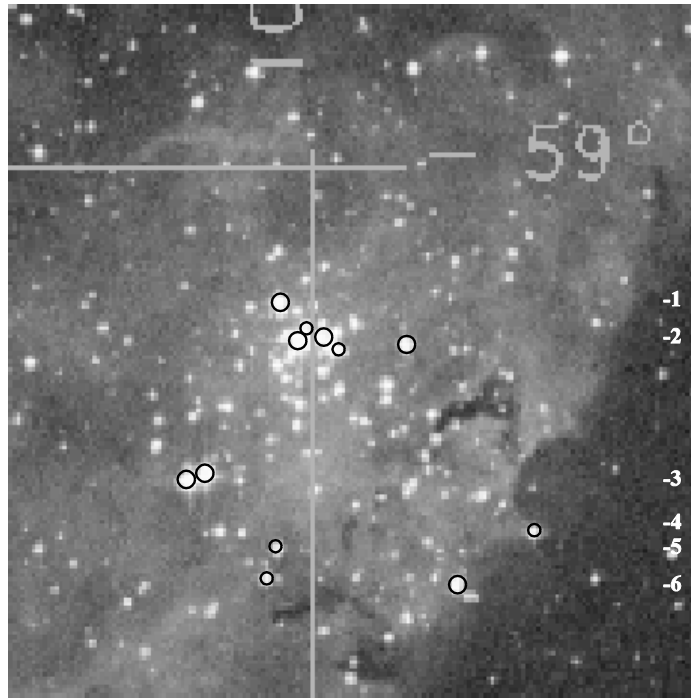


Fig. 2*b*. Detail of the CarNW region showing the brightest exciting stars which have been “removed” from the CCD before the extraction of the *.neb* spectra (see Sec. 2.3.1 below) and listed in Table 2*a*. The image is 1' larger on each side than our actual scanned area. The identification of individual stars was done using maps presented by Massey & Johnson (1993), Feinstein et al. (1973), and Thé, Bakker & Antalova (1980), who provide high spatial resolution maps for the stellar cluster.

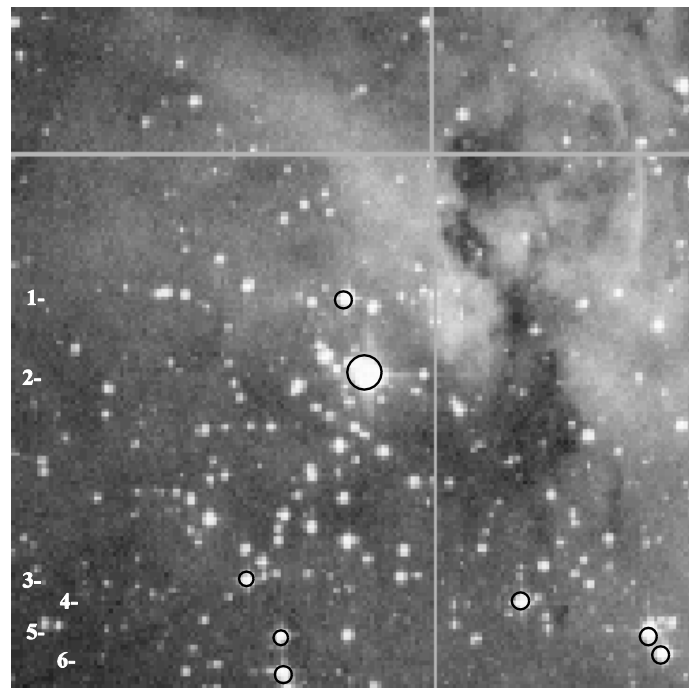


Fig. 2*c*. As Fig. 2*b* for the CarSE region. Note bright η Car at the center.

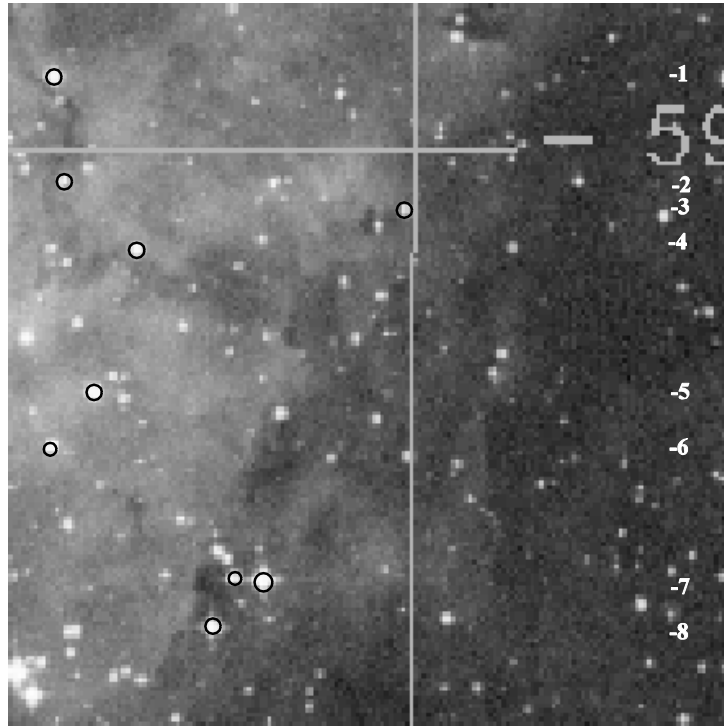


Fig. 2d. As Fig. 2b for the CarSW region.

2.2.2 M8 and M20 Regions

M8 (Lagoon Nebula, NGC 6523, S25, RCW 146, W9) covers about $90'$ on the sky and M20 (Trifid Nebula, NGC 6514, RCW 147, W29) covers about $30'$ on the sky, both in the visible. Both regions are located toward the galactic center and present an excellent opportunity to study HII regions dominated by massive stars. Each nebula was divided in two subregions, referred hereafter as **M8-E**, **M8-W**; and **M20-S** and **M20-N**. After matching the B, Y and R spectral ranges observed for each region, we ended up with final scanned areas on the sky of only $6.5'$ (N–S) \times $7.0'$ (W–E). In Table 1 of Appendix I we present additional information about M8 and M20 for future reference.

Fig. 3a shows a digitized wide-field image of M8 showing a huge dust lane running in front of the nebula, as well as dark patches of molecular gas. This molecular gas has been dissolved by the intense radiation and winds of the hot massive neighboring stars. The heart of the nebula contains the famous Hourglass, a $40''$ bipolar HII region powered by the star Herschel 36. *JHK* high-spatial resolution imaging of the Hourglass shows a wealth of young stars and evidence of a *Proplyd*, G5.97-1.17, about $3''$ N of Her 36, evidencing the ongoing star formation still taking place within the nebula (Stecklum et al. 1998, Mesa-Delgado & Esteban, 2010).

Table 2a. Identification of removed exciting stars in the Carina Regions ^a

Star number (1)	Star ID (2)	(3)	(4)	SpT (5)	V (mag) (6)	T_{eff} (10^3K) (7)	$\log(g)_{\text{spec}}$ (cm s^{-2}) (8)	$\log Q_0$ (s^{-1}) (9)	$\log Q_0$ (s^{-1}) (10)
CarNW (Tr14/ Cr232)									
NW1	192	14-8	CP-58 2620	O6.5 V((f))	9.45 ^B	42.28	3.90	49.23	49.18
NW2a (*)	177	--	HD93129A+B ^h	O3 If*	6.90 ^B	45.0 \pm 2.0 ^c	3.60 \pm 0.15 ^c	49.95	49.94
NW2b	165	14-9	--	O8 V	9.73 ^B	38.45	3.90	48.87	48.80
NW2c (*)	157	--	HD93128	O3 V((f))	8.81 ^B	48.0 \pm 3.0 ^c	3.85 \pm 0.15 ^c	49.66	49.62
NW2d	149	14-3	--	B0.5 IV-V	10.44 ^B	31.60	3.78	47.99	47.88
NW2e	115	14-20	CP-58 2611	O6 V((f))	9.65	43.56	3.90	49.34	49.29
NW3a (*)	238	--	HD93161A+B ^h	O6.5 V((f))	7.82	42.28	3.90	49.23	49.18
NW3b (*)	229	--	HD93160 ⁱ	O6 III(f)	7.88 ^B	42.64	3.67	49.58	49.55
NW4	71	14-30	--	B0 III-IV	10.10	31.54	3.57	48.45	48.14
NW5	195	14-126	--	B1 V	10.96	30.80 ^e	--	47.60 ^e	47.50 ^f
NW6a	200	14-127	--	O9 V	10.69	35.90	3.90	48.56	48.46
NW6b	91	--	--	(0.51)	10.44 ^B	--	--	--	--
CarSE (Tr16)									
SE1 (*)	480	16-7	HDE303308	O3 V((f))	8.19	45.5 \pm 3.0 ^c	3.90 \pm 0.15 ^c	49.48	49.42
SE2 ^b (*)	--	--	η Car	LBV	5.85 ^b	30.0 ^b	--	--	49.83 ^b
SE3 (*)	535	16-112	CP-59 2641	O6 V((f))	9.28	43.56	3.90	49.34	49.29
SE4 (*)	408	16-104	CP-59 2603	O7 V((f))	8.82	41.01 ^d	3.90	49.12	49.07
SE5a	517	16-110	CP-59 2636	O8 V	9.31	38.45	3.90	48.87	48.80
SE5b (*)	483	16-24	CP-59 2336	B2 V	11.50	28.0	3.89	47.00	47.00
SE5c (*)	342	--	HD93205A+B ^h	O3 V	7.76	51.23	3.91	49.87	49.85
(SE6a)	516	16-34	CP-59 2635	O8.5 V	9.27 ^B	37.17	3.90	48.72	48.67
SE6b	340	--	HD93204	O5 V((f))	8.48	46.12	3.90	49.53	49.50
CarSW (Tr16)									
SW1	327	16-10	--	B0 V	9.86	33.34	3.89	48.16	48.03
SW2	321	16-12	--	B1 V	11.52	30.80 ^e	3.89	47.60 ^e	47.50 ^f
SW3a	--	--	--	--	--	--	--	--	--
SW3b	--	--	--	--	--	--	--	--	--
SW4	289	16-11	--	B1.5 V	11.19	29.50 ^e	3.89	47.30 ^e	47.22 ^f
SW5 (*)	306	16-94	--	B1.5 V	9.88	29.50 ^e	3.89	47.30 ^e	47.22 ^f
SW6 (*)	329	16-17	--	B1 V	10.88	30.80 ^e	3.89	47.60 ^e	47.50 ^f
SW7a	257	16-244	--	O3-O4 If	10.78	49.20	3.70	50.07	50.06
SW7b (*)	245	16-177	HD93162 ^h	WN6ha ^g	8.11	39.00 ^e	--	--	49.96 ^g
SW8	265	16-36	CP-59 2567 ^h	1.34	9.44	(5.00)	--	--	--

^a Table entries adapted from Massey & Johnson (1993; MJ93) and references therein. Columns give: (1) Our ID number (see Figs. 1b – 1d). (2) MJ93 ID number. (3) Feinstein et al. (1973) ID number. (4) Other common designation (HD or CP). (5) and (6) Spectral Types [or $(B - V)_{\text{obs}}$] and V mag (or B mag as marked), adapted from MJ93 and references therein. (7), (8) and (9) Effective temperature, surface gravity and ionizing photon flux, derived from Vacca, Garmany & Shull (1996; VGS96). (10) Ionizing photon flux (for the given effective temperature), derived from Schaerer & de Koter (1997; SdK97). ^b Includes also stars Tr16-1, 16-2, 16-6, 16-64, 16-65, 16-66 and 16-77. V mag from Humphreys & Davidson (1994). T_{eff} and Q_0 from Davidson (1971), assuming $d_{\text{Car}} \approx 2.6$ kpc. ^c From Kudritzki & Hummer (1990) with $Y_{\text{stellar}} = 0.09$. ^d From Walborn et al. (1998). ^e Interpolated or extrapolated from VGS96. ^f Interpolated or extrapolated from SdK97. ^g From Crowther & Dessart (1998). ^h Notes on individual stars: NW2a = HD

93129A+B = CP -58 2618A+B; HD 93129B is an O3 V((f)), but it is 1.5 mag fainter than the primary star (Walborn 1973a, Simon et al. 1983) and was not included in the analysis; NW3a = HD 93161A+B = CP -58 2631A+B; NW3b = HD 93160 = CP -58 2631C; SE2 = η Car = HD 93308 = HR 4210; SE5c = HD 93205A+B = CP -59 2587, it is a double-line binary, the companion is an O8 V, about 3 times fainter than the primary (Conti & Walborn 1976); SW7a = HD 93162 = CP -59 2561 = WR25; SW8 = CP -59 2567 = UBV M40296. (*) With IUE Archive spectrum.

In Figs. 3b – 3d we show digitized images of the scanned subregions for M8-E and M8-W adapted from *Digitized Sky Survey* (McGlynn, Scollick & White, 1996 and McLean et al. 1996). As with the Carina regions, we have numbered in the expanded images the bright stars that produced noticeable spectra in the 2-D CCD frame. We marked with an asterisk those stars with a continuum at $\lambda 4861$ larger than 10% of the $H\beta$ nebular emission at both sides of the star as projected on the sky (see Sec. 2.3 below). We show in Figs. 4a – 4c the corresponding images for the M20 subregions.



Fig. 3a. Image of the whole M8 nebula, taken with the 3.5 m Calar Alto telescope (adapted from www.tls-tautenburg.de). The image is 32' on a side. North is up and East is left.

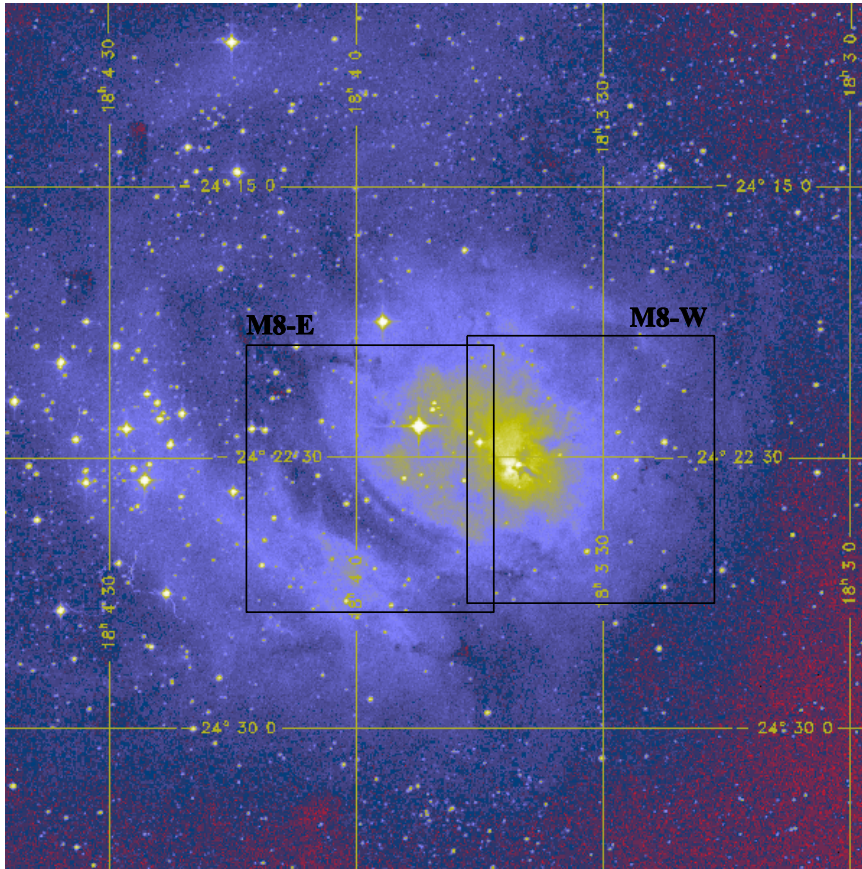
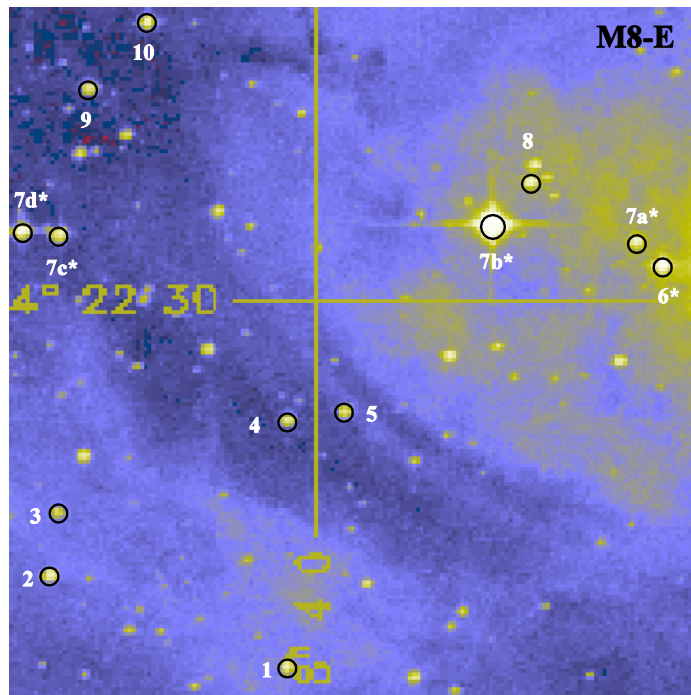
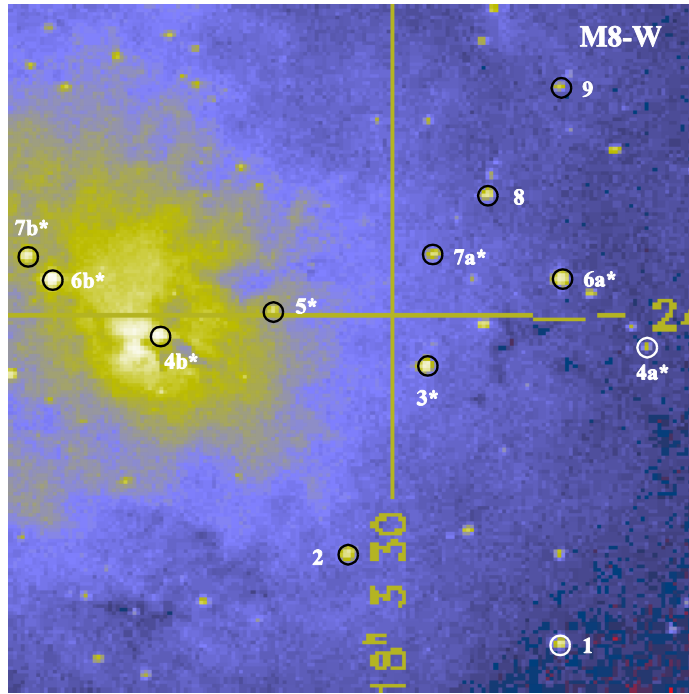


Fig. 3b. $24' \times 24'$ image of M8 adapted from the *Digitized Sky Survey* showing the two scanned regions, labeled M8-E and M8-W. The region M8-W contains the famous Hourglass nebula. The grid gives 2000 coordinates. North is up and East is left.





Figs. 3c – 3d. M8-E (upper) and M8-W (lower) regions showing the identified brightest stars (circles) and the “removed” stars (marked with an asterisk; see Sec. 2.3 below). The images are 7.0’ on a side. North is up and East is left.

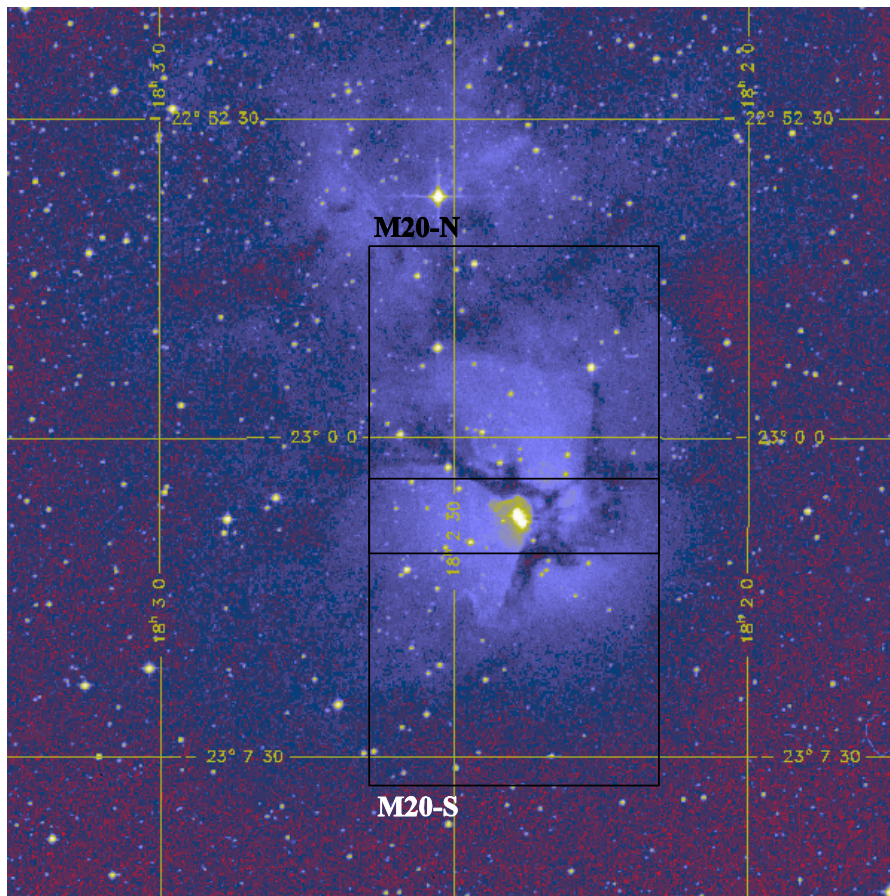
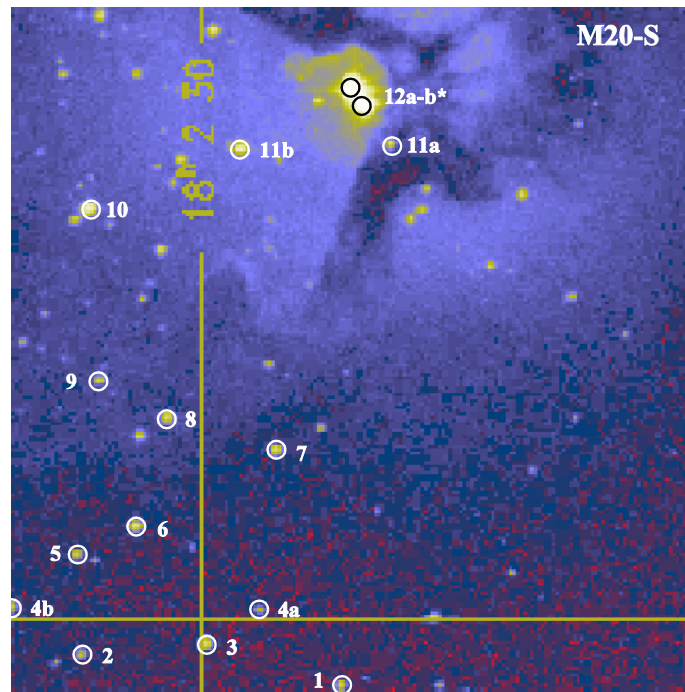
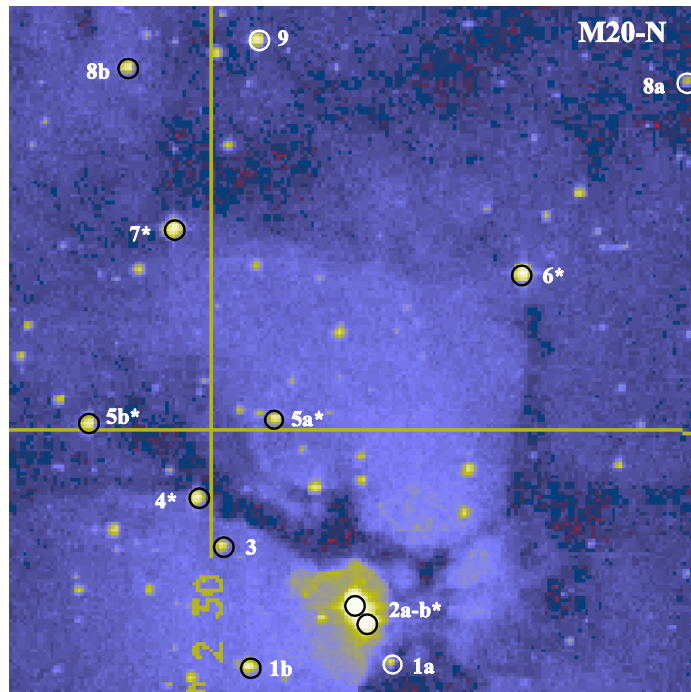


Fig. 4a. 21’ × 21’ image of M20 adapted from the *Digitized Sky Survey* showing the two scanned regions, labeled M20-N and M20-S. The grid gives 2000 coordinates. North is up and East is left.



Figs. 4b – 4c . M20–N (upper) and M20–S (lower) subregions showing the identified brightest stars (circles) and the “removed” stars (marked with an asterisk; see Sec. 2.3 below). The images are 6.3’ on a side. North is up and East is left.

M8 is powered by early O and B stars belonging to the open cluster NGC 6530. The more conspicuous members are HD 164794 (9 Sgr; O4 V((f)); Conti 1975), close to the center of our M8-E region (Fig. 3c), and HD 164740 (Her 36; O7 V; Woolf 1961), located a few arcsec W of the Hourglass within our M8-W region (Fig. 3d).

For M20, the star responsible for most of the ionization is HD 164492. It was classified as O7.5 III((f)) by Walborn (1973*b*), and as O7 V by Abt (1983). With the aid of HIPPARCOS satellite (ESA 1997), it was found that HD 164492 is actually composed of 7 components, 3 of which are now classified as: (B) A2 Ia, (C) B0 V and (E) F3 V. We focused our attention in the HII region and our scans did not include the star HD 164514 (F5 I, member of the Sgr OBI association), located outside the north boundary of our M20-N region. This star is responsible of the reflection nebula around it in the northern part of M20 (see Fig. 4*a*), and has been observed by Lynds & O’Neil (1986).

In Table 2*b*, we present a compilation of relevant stellar parameters for the ionizing stars in the M8 and M20 regions, indicating which stars were “removed” from the CCD to obtain the *.neb* spectra (see Sec. 2.3.1 below).

2.2.3 RCW Objects

We also observed 4 southern galactic HII regions from the RCW catalogue, using the same observational setup and *drift-scanning* technique mentioned above: RCW6, RCW60 (divided in 2 subregions), RCW107 and RCW110. These nebulae were selected on the basis of knowing *a priori* the spectral type of their exciting stars (however, see comment on RCW110 below). In Figs. 5*a* – 5*f* we show digitized images of each RCW nebulae, indicating the scanned areas and several identified stars in each field. In Tables 2*a* – 2*d* of Appendix I we give the available data for the stars identified in Figs. 5*a* – 5*f*, indicating with an asterisk which stars were “removed” from the CCD to obtain the *.neb* spectra (see Sec. 2.3.1 below).

In Table 2*c* we give the main parameters for the exciting stars of the RCW nebulae, including estimates of their spectral-photometric (d_*) and kinematical (d_{kin}) distances. Comparing d_* and d_{kin} , we identify LSS 207, O6 V, ($d_* = 5.6$ kpc) as the exciting star of RCW6 ($d_{\text{kin}} = 5.1$ kpc). Likewise, HD 99897 ($d_* = 2.4$ kpc) must be the exciting star of RCW60 ($d_{\text{kin}} = 3.0$ kpc). For RCW107 we found a discrepancy since HD 148937 is listed at $d_* \approx 1.3$ kpc, while kinematical measurements locate it at $d_{\text{kin}} \approx 5.6$ kpc (first solution) or 11.4 kpc (second solution). This points to a miss-identification of RCW107 with the radio source quoted by Caswell & Haynes (1987). Part of this discrepancy may be due to deviations from circular galactic motion since H α Fabry-Perot observations of Georgelin & Georgelin (1970*b*) also place it at a much higher distance (4.2 kpc). This issue deserves further investigation.

Table 2*b*. Physical parameters of identified stars in M8 and M20. ^a

Name	VJ	SpT	V (mag)	E_{B-V} (mag)	T_{eff} (10^3 K) VGS96	T_{eff} (10^3 K) C97	$\log(g)_{\text{spec}}$ (cm s^{-2})	$\log Q_0$ (s^{-1}) VGS96	$\log Q_0$ (s^{-1}) C97
(1)	(2)	(3)	(4)	(5)	(6)	(7)	(8)	(9)	(10)
M8-E									
1	132	B5.5 V	11.49	0.35	–	15.0	3.89	–	–
2	155	–	11.75	0.22/–0.29	–	–	–	–	–
3	151	–	13.19	0.81/0.12	–	–	–	–	–
4	133	–	11.59	0.17/–0.36	–	–	–	–	–
5	127	–	11.93	0.60/0.03	–	–	–	–	–
6*	107	B2.5 V	10.03	0.35	~27	19.0	3.893	~46	–
7a*	108	–	11.52	–	–	–	–	–	–
7b*	HD 164794	O4 V((f)) ^b	5.96	0.35	48.7	44.0	3.905	49.70	49.32
7c*	152	B3 Ve	10.38	0.34	~26	17.5	3.892	45.5	–
7d*	156	K0 III	9.84	–	–	–	–	–	–
8	114	–	11.79	0.35	–	–	–	–	–
9	147	–	11.66	0.22/–0.26	–	–	–	–	–
M8-W									
1	85	–	11.76	0.35	–	–	–	–	–
2	101	–	11.45	–	–	–	–	–	–
3*	97	K4 III ?	10.67	0.35	–	–	–	–	–
4a*	–	–	–	–	–	–	–	–	–
4b*	HD 164740	O7.5 V(n) ^c	10.20	0.89	39.6	37.6	3.899	48.90	48.70 Her36
5*	6842_01148	–	–	–	–	–	–	–	–
6a*	88	–	12.68	–	–	–	–	–	–
(6b*)	(107)	–	–	–	–	–	–	–	–
7a*	95	–	12.75	0.35	–	–	–	–	–
(7b*)	(HD 164794)	–	–	–	–	–	–	–	–
8	90	–	12.03	0.35	–	–	–	–	–
9	–	–	–	–	–	–	–	–	–
M20-S									
12a*	HD 164492(A)	O7V ^d	9.4 ^f	–	37.5 ^e	–	–	–	–
M20-N									
5b*	HDE 313596	B8	10.2	–	–	–	–	–	–

^a Columns give: (1) Our star designation (see Figs. 3*c* – 3*d* for M8–E and M8–W, and Figs. 4*b* – 4*c* for M20–S and M20–N); (2) VJ, HD or GSC number; (3) Spectral Type; (4) V mag.; (5) Color excess, and $(B - V)/(U - B)$ if more than one value is given. Columns 3, 4 and 5 are adapted from van Altena & Jones (1972), McCall, Richer & Visvanathan (1990; MRV90), and the CGO compiled by Garmany, Conti & Chiosi (1982, and references therein); (6) and (7) Effective temperature, adapted from the SpT – T_{eff} calibration of Vacca, Garmany & Shull (1996; VGS96) and by Crowther (1997; C97), respectively; (8) Spectroscopic gravity, adapted from VGS96; (9) and (10) H–Ionizing photon flux from Schaerer & de Koter (1997; SdK97) using VGS96 and C97 T_{eff} scales, respectively. ^b 9 Sagit. From Conti (1975), although it was also classified as an O9 If by Hoffleit & Jascheck (1982). ^c From Woolf (1961). ^d From Abt (1983). ^e From Lynds & O’Neil (1985). ^f Blaauw (1963) gives an absolute magnitude, $M_V = -5.2$ mag. As asterisk means that the star was “removed” from the CCD to obtain the .*neb* spectra (Sec. 2.3.1 below).

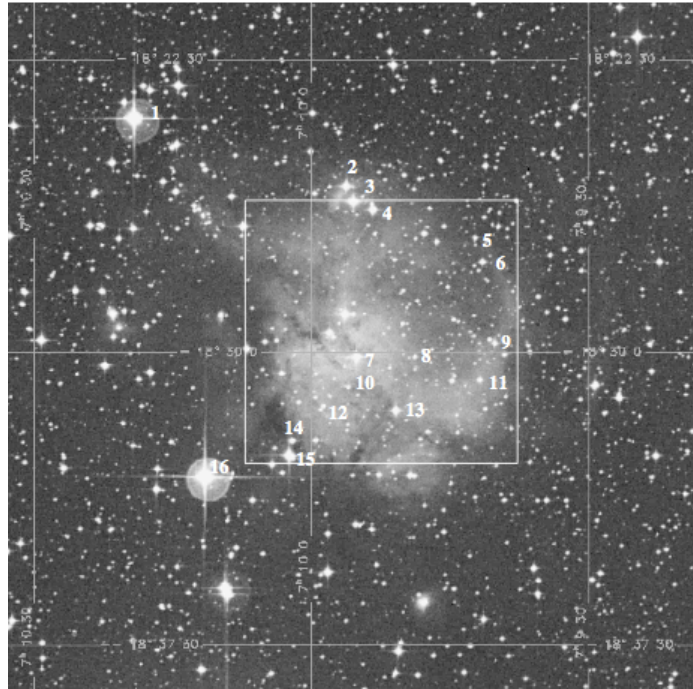


Fig. 5a. $18' \times 18'$ image of RCW6 adapted from the *Digitized Sky Survey* showing the scanned region and several identified stars (see Table 2b of Appendix I). Grid gives 2000 coordinates with image center at $(\alpha, \delta) = (7\ 09\ 55, -18\ 30\ 00)$. North is up and East is left.

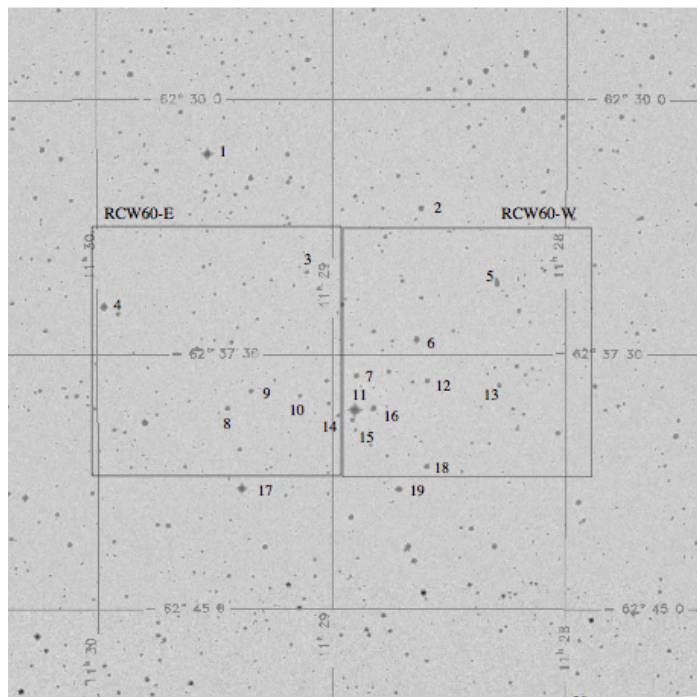


Fig. 5b. $21' \times 21'$ image of RCW60 adapted from the *Digitized Sky Survey* showing the scanned regions (RCW60-E and RCW60-W) and several identified stars (see Table 2c of Appendix I). Grid gives 2000 coordinates with image center at $(\alpha, \delta) = (11\ 29\ 00, -62\ 37\ 30)$. North is up and East is left. The nebula does not appear in this Digitized Survey image, but we show a POSS red picture of the same region in Fig. 5c.

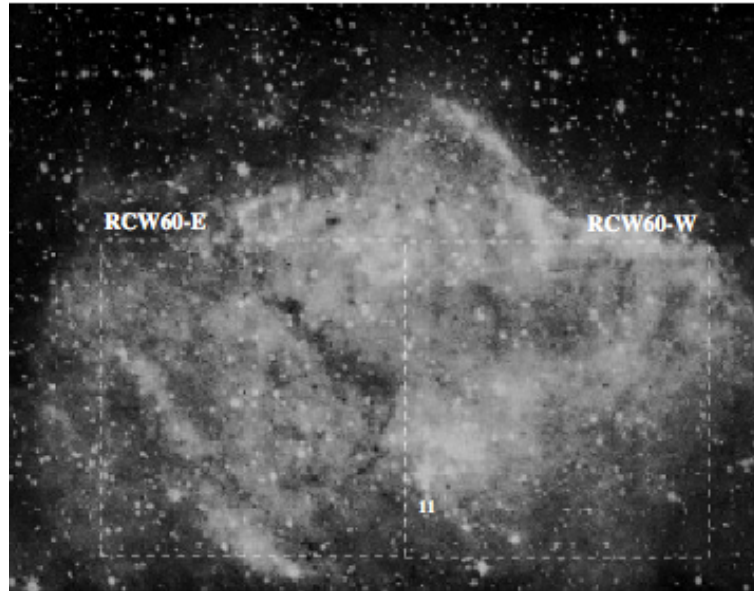


Fig. 5c. RCW60 scanned image adapted from a POSS red plate showing the same scanned regions and star No. 11 as in Fig. 5b as a reference. North is up and East is left.

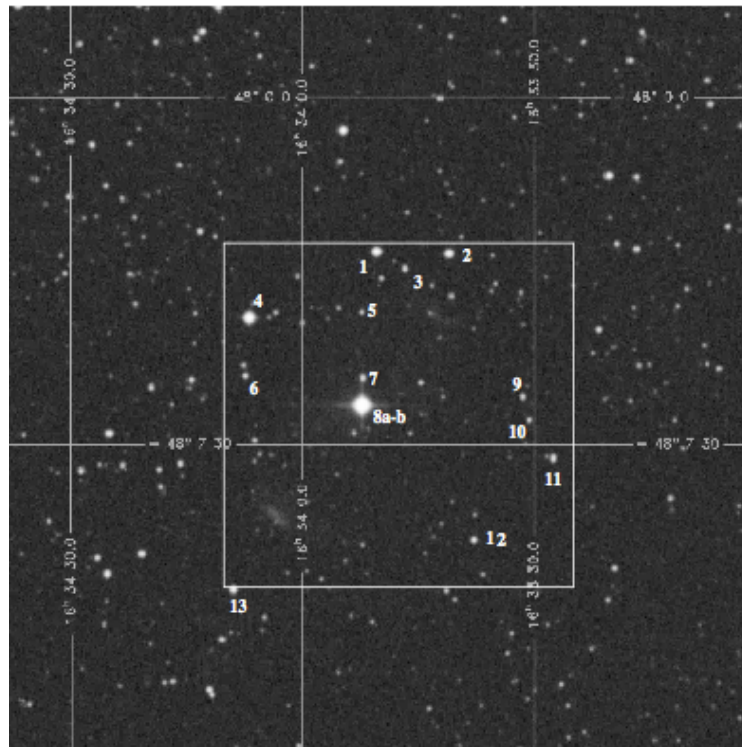


Fig. 5d. $16' \times 16'$ image of RCW107 adapted from the *Digitized Sky Survey* showing the scanned region and several identified stars (see Table 2d of Appendix I). Grid gives 2000 coordinates, image center at $(\alpha, \delta) = (16\ 33\ 52, -48\ 06\ 40)$, with North up and East left. The nebula is barely seen on this image, but we show an $H\alpha$ image of it in Fig. 5e.

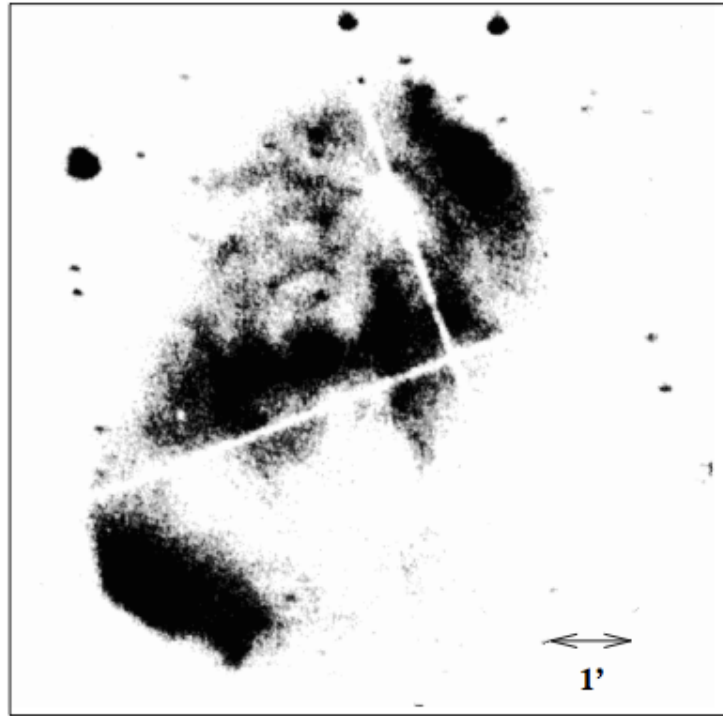


Fig. 5e. $H\alpha$ interference filter image of RCW107 adapted from Pişmiş (1974). North is up and East left. NGC 6164 is located NW from the central star, while NGC 6165 is located SE from the central star. The square box corresponds approximately with the scanned region (compare with Fig. 5d).



Fig. 5f. $12' \times 12'$ image of RCW110 adapted from the *Digitized Sky Survey* showing the scanned region and several identified stars (see Table 2e of Appendix I). Grid gives 2000 coordinates, image center at $(\alpha, \delta) = (16\ 54\ 15, -45\ 12\ 47)$, with North up and East left. (RCW111 is $12'$ N and $9'$ E of RCW110, out of this field.)

For RCW110 it is not clear which is its exciting star: HD 152386 (LSS 3825), is an O5 Ia, with $d_* = 2.8$ kpc, and although it is hot enough, is lies $\sim 16'$ N from the main nebula (about 11 pc, at $d = 2.3$ kpc), and it is more likely associated with RCW111 (Georgelin et al. 1996). There are also two hot stars identified in our RCW110 field (Fig. 5f): star No. 14 = HD 329100A+B (LSS 3815), an O8.5 V, and star No. 18 = CD -45 11034 (LSS 3799), an O8.5 III, which however are *not* surrounded by any apparent nebulosity. Instead, RCW110 surrounds our star No. 11 (the second brightest star within our scanned region, after star No. 15), but it is missing spectral classification! Given the estimated distances to these two stars (Table 2d of Appendix I) we will consider HD 329100A+B (~ 2.2 kpc) as the exciting star of RCW110 (2.3 kpc).

In Table 3 of Appendix I we present a compilation of radio continuum observations, electronic temperatures and estimated distances for the RCW nebulae.

Table 2c. Physical parameters of the RCW nebulae exciting stars. ^a

Nebula	Star-ID	SpT	V (mag)	T_{eff} (kK)	$\log Q_0$ (s^{-1})	d (kpc)	d_{kin} (kpc)
(1)	(2)	(3)	(4)	(5)	(6)	(7)	(8)
RCW6	LSS 207 *	O6 V	10.87	43.7 ^{b,c}	49.30 ^{b,c}	5.6 ± 0.5	1.5–5.1
RCW60–E	HD 99897 *	O6 V	8.23	43.7 ^b	49.30 ^b	2.4 ± 0.2	2.2–4
RCW60–W	LSS 2355 *						
RCW107	HD 148937/ LSS 3646 *	O6 I	7.19	41.8 ^d	49.80 ^e	1.4 ± 0.3	4.2–6.9
RCW110	HD 329100 A+B/ LSS 3815 *	O8.5 V	10.99	37.2	48.63	2.3 ± 0.2	2.2–2.5

^a Columns give: (1) Nebula ID; (2) Exciting star ID; (3) Spectral type and Luminosity Class; (4) Visual magnitude; (5) Effective temperature, derived from VGS96’s SpT – T_{eff} calibration; (6) H^0 -ionizing photon flux for the given T_{eff} and LC, derived from SdK97 calibration; (7) Adopted (spectro-photometric) distance; (8) Kinematical distance (from several estimations, see Table 3 of Appendix I). ^b Georgelin, Lortet-Zuckerman & Monnet (1975) estimated (T_{eff} (kK), $\log Q_0$ (s^{-1}), u (pc cm^{-2})) = (39.4, 49.43, 86) for LSS 207, and (< 39.4, 49.43, 86) for HD 99897, using their SpT – T_{eff} calibration, respectively. ^c Vílchez & Esteban (1996) estimated (T_{eff} (kK), $\log Q_0$ (s^{-1})) = (40.0, 49.05) for LSS 207. T_{eff} was estimated from Q_0 using Panagia (1973) calibrations, and Q_0 was estimated from radio continuum data by FS91. ^d Leitherer & Chavarria-K. (1987) assumed 37.8 kK. ^e Assuming an O6 III, yields $Q_0 = 49.55 \text{ s}^{-1}$; while Panagia (1973) calibration yields $Q_0 = 49.15 \text{ s}^{-1}$. * These stars were “removed” from the CCD to obtain the .neb spectra (Sec. 2.3.1 below).

2.3. Images reduction and extraction of the spectra

We reduced the data using the standard procedures within IRAF following the “CSCCD Reduction with IRAF” Cookbook by Hamuy and Wells (1992).

1) We start by subtracting the electronic bias determined from the over-scan columns at the far edge of the CCD for each working frame. 2) We trimmed all our 2-D working frames, cutting-off all unwanted lines and columns and keeping only the CCD area that was actually exposed. 3) We subtracted a zero-level image from all working frames. The zero-level image is a nightly average of 20 overscan-subtracted bias exposures. 4) For this long-slit program, it is very important to have an accurate flat fielding and illumination-correction. Each night we obtained 5 – 10 *sky-flats* taken at dusk and dawn with integration times from 30 sec to 5 min, and 20 *projector-flats* using an internal quartz lamp with appropriate cut-off filters. As with the bias frames, we combined these flat fields to get an average projector-flat and an average sky-flat for each night. After inspection of the illumination decline *outside* the edges of the slit for the projector-flats, we applied a correction for scattered light *inside* the spectrograph. Even with this correction, the illumination profiles along the slit for the projector-flats and sky-flats were different for each of the B, Y and R spectral ranges. To solve this problem, we applied to the projector-flat an illumination correction in several wavelength bands, and we ran the IRAF task *response* on this “even illuminated” projector-flat to obtain a final projector-flat field that corrects for the pixel-to-pixel variations on the CCD as function of wavelength. Finally, we ran a second illumination correction on this final projector-flat field thereby obtaining a final flat field that was flat both in the spectral and spatial directions. Thus, we ended up with evenly illuminated profiles along the slit (at a given λ) both for the “dark sky” and “flat-sky” frames. Finally, we applied this final flat field to all our program frames. With this correction, we were left with an effective slit length of 240 pixels, corresponding to $\sim 7.6'$ on the sky.

5) We removed by hand the cosmic rays from the CCD by comparing two different exposures per object. 6) We did not make any correction for dark current generated during our integrations. Likewise, we did not correct for bad pixels since we found this merged some important features on the CCD. 7) We extracted the *.all* and *.neb* spectra as discussed in Sec. 2.3.1 below. 8) We carried the wavelength calibration for our extracted program spectra using a He-Ar comparison lamp. We obtained for each spectral range a dispersion solution with an uncertainty of about 3 – 4 Å for $\lambda < 10,000$ Å, and 5 – 10 Å for $\lambda > 10,000$ Å. Our adopted dispersion-solution gave us λ -calibrated program frames with a precision better than 8 Å for lines in the λ -overlapping regions of our B, Y, and R spectra. 9) We obtained spectra for three standard stars from the list of Baldwin and Stone (1984): LTT 4364 and LTT 7379 were observed in all three spectra ranges and EG 274 was observed only in the R range. The flux calibration and the correction for atmospheric extinction was done using IRAF *onedstdsctio newcal* package for standard stars. We derived a sensitivity function for each spectral-range, verifying that this function correctly calibrated the flux of the standard stars. We applied this sensitivity function to our program and dark-sky spectra. For all observed nebulae, we obtained a reasonable match (within 5 – 8%) for the continuum level in the overlapping regions of the B – Y, and Y – R spectra, confirming the

stability of the observing conditions during the observing run. Considering the errors involved in the calibration procedure, we estimate that our fluxes are accurate within 7 – 10% (see Sec. 2.5.1 below).

10) We subtracted from our program spectra the corresponding dark-sky spectra, linearly scaling the latter to the appropriate exposure time. This operation removed most of the sky-features in the B and Y frames. However, we could only measure upper limits for the [O I] $\lambda 5577$ and He I $\lambda 5876$ lines due to an over-subtraction on these lines. The sky subtraction in the R frames is uncertain due to the presence of many strong atmospheric OH, O₂ and H₂O absorption bands far in the red (starting at $\lambda \geq 7000$ Å), and their intensity variation on rather short time-scales (Stevenson, 1994). Comparison of the final sky-subtracted and dark-sky spectra shows that the prominent absorption features present in the final *.neb* and *.all* spectra as discussed below, arise from inadequate sky subtraction. We estimate that this introduces an error in the line fluxes of at least 10% for lines with $\lambda > 7000$ Å and equivalent widths less than 10 Å.

11) Finally, we got for each observed region our final working spectra averaging the two available exposures that we had for each spectral range. These two exposures were very similar to each other, showing the stability of the observing conditions throughout the night.

2.3.1 Extraction of the *.neb* and *.all* spectra

In order to assess quantitatively the effects of the stellar spectra in the integrated spectrum of our HII regions, we proceeded as follows. Before extracting any spectra, we made sure there were no saturation zones on our CCD program frames. We define the bright exciting stars in each region as those stars having a continuum flux at $\lambda 4861$ Å greater than 10% of the H β nebular emission at both sides of the star, as projected on the sky. These exciting stars are marked with an * in the set of figures presented in Figs. 2 to Figs. 5, and are indicated with an asterisk in Tables 2a – 2c, where we include some of their physical parameters, such as spectral type, luminosity class, and visual magnitude. Since we aligned the slit N-S and drifted the telescope from E to W, all stars within a given region having similar declinations produced a single *combined* spectra on the CCD. This multiplicity of stars with similar declinations occurred mostly in the Carina regions, and is represented in Tables 2a – 2c with letters in decreasing RA (e.g. Star 2a, 2b, 2c, etc.).

In order to have a spectrum covering from 3600 – 10,200 Å arising from the same emitting region, we extracted equal number of pixels (along the spatial direction) corresponding to the *same* region on the sky for each of our B, Y and R spectral ranges. Due to small differences in the initial declination of the slit's middle point at the beginning of each integration, the overlapping of the three

spectral ranges yielded working areas of only 206 pix in the spatial direction, which correspond to 6.6' in the N-S direction. Thus, our scans covered actually about 6.4' \times 7.1' for each region.

We extracted the spectra in two different ways:

- *.all case*: We extracted the spectra along the whole spatial dimension on the CCD, including both the nebular emission *and* the recorded spectra of the exciting stars passing through the slit during the drift. We will call these the *.all* spectra.
- *.neb case*: For a given region, we “removed” from the 2D CCD spectra the bright stars (identified in Tables 2a – 2c with an *), before extracting the spectra so to obtain as best as possible a spectra composed only from the nebular emission. A bright star’s spectrum covers typically a width of about 10 pixels along the slit, and if we discard from the CCD those pixels containing the stellar spectra, we would also be removing a fraction of the nebular emission arising from points having the same declination as the removed star. Considering the number of stars to be removed for a given region (especially for the Carina regions), this adds up to about 30% of the nebular emission for a region emitting uniformly along the slit, yielding thus underestimated nebular fluxes. To avoid this problem, we “removed” from the CCD only the stellar component *above* a certain flux value determined by the nebular emission arising from two points adjacent to the star in the N–S direction as projected on the sky. At each wavelength, we made a linear interpolation of the nebular emission arising from these adjacent points so to cover the CCD pixels that were occupied by the star spectra. This approach is approximate since: *i*) the rows of the CCD were not perfectly aligned along the dispersion, giving a tilt of the spectra of about 3 pixels from side to side along the dispersion (576 pixels) and, *ii*) due to the combined effect of the wavelength-dependence of both the CCD’s quantum efficiency and the focus of the grating, the width of a bright star’s spectra on the CCD varied along the dispersion, particularly for the R and B frames, changing by as much as 5 pixels in width along the whole spectral range. We estimate from these considerations that the total underestimation of the whole nebular spectrum in the *.neb* spectra is less than 2%. We will refer to these extracted spectra as the *.neb* spectra. Note that the *.all* and *.neb* spectra refer to exactly the *same* rectangular areas on the sky.

For the Carina regions, we identified 31 bright, hot stars earlier than B2 V within the total scanned area of ~ 150 arcmin², including the star η Car, 16 O stars, and one WR star, with *V* magnitudes ranging from 6 to 11.5 mag. The following stars, though hot and bright, were not included in our Carina scans: HD 93343 (O8 V + O7-8.5 V); BD -59° 2600 (O6 V); HD 93250 (O4 III(fc));

HDE 303311 (O5 V); and HD 93130, (O6 III), which should be considered when estimating the total energy input for the nebula.

We followed the same procedure to “remove” the bright stars in our M8 and M20 subregions, which are marked with an asterisk in Figs. 2c – 3d, Figs. 4b – 4c and in Table 2b. For the 4 RCW objects, the removed stars are marked with an asterisk in Tables 2a – 2d of Appendix I.

As an example, in Figs. 6a – 6b we show views of the 2D CCD B spectra for the M8 regions, where we have labeled the spectra corresponding to the stars numbered in Figs. 3c – 3d, according to their declination. Note how the nebular flux has been interpolated, at any given λ , in the pixel spaces where a bright star was removed.

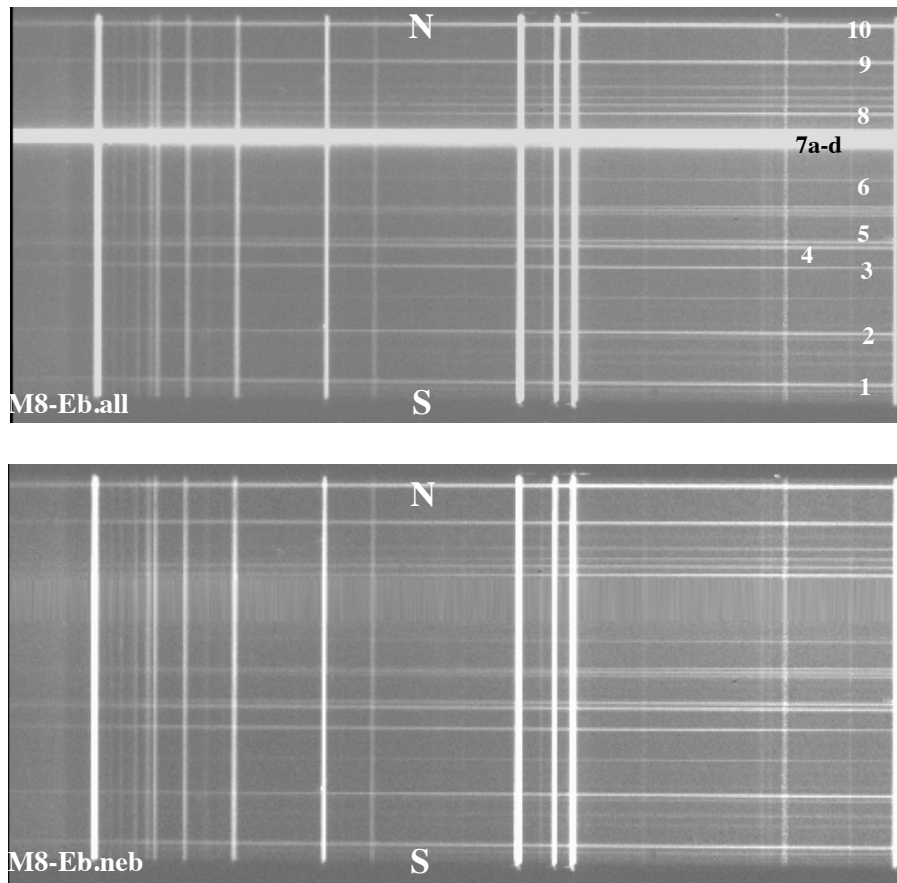


Fig. 6a. Views of the bias-, flat field-, illumination-, and cosmic ray-corrected 2D CCD frames of M8-E’s Blue spectrum including (*upper*) and excluding (*lower*) the exciting stars. We have labeled the spectra of those stars identified in Fig. 3c.

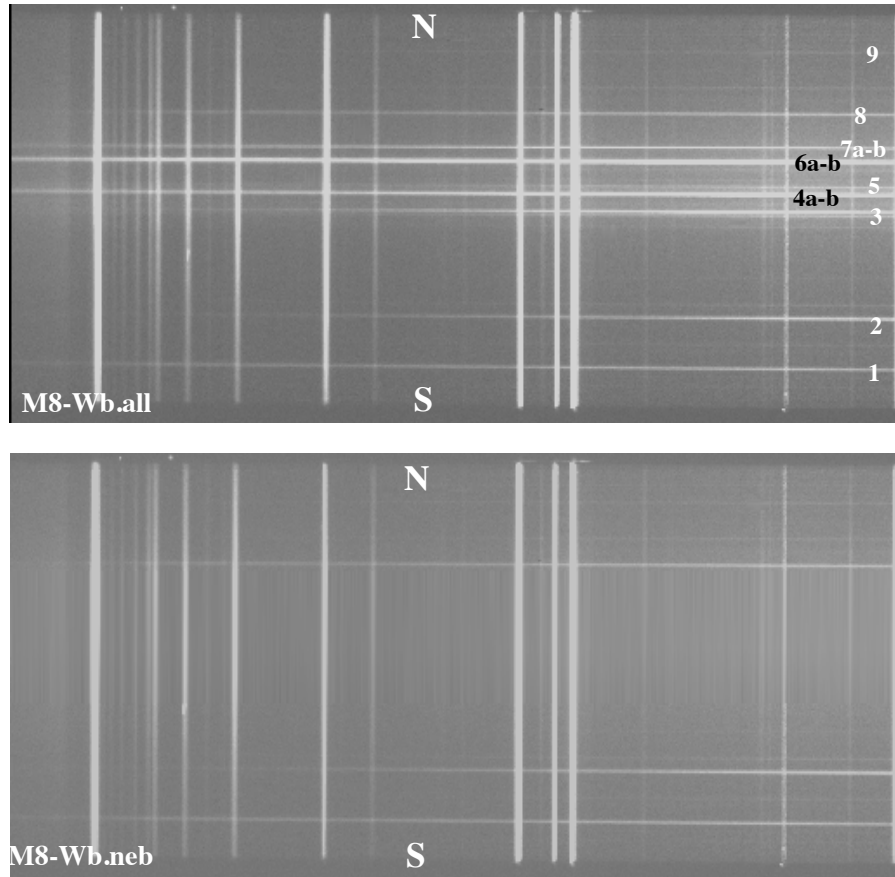


Fig. 6b. As Fig. 6a but for the M8-W region.

As an example, in Fig. 7a we present our final λ -, flux-calibrated and sky-subtracted observed *.neb* spectrum for the CarSE region: CarSE.*neb*. In Figs. 7b and 7c we present details of the B and Y spectra for this CarSE region, including and excluding the stars. It is apparent the effect of η Car in the *.all* spectra as compared with the *.neb* spectra. Figs 8a – 8c show similar plots for the M8-E region.

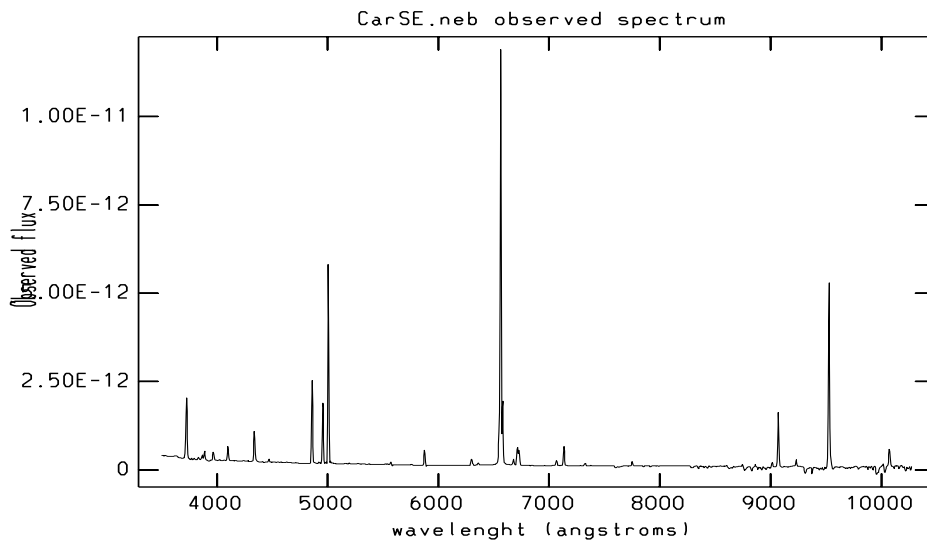


Fig. 7a. CarSE.*neb* flux-calibrated and sky-subtracted observed spectrum F_{λ}^{obs} ($\text{erg cm}^{-2} \text{s}^{-1} \text{\AA}^{-1}$) vs. λ (\AA).

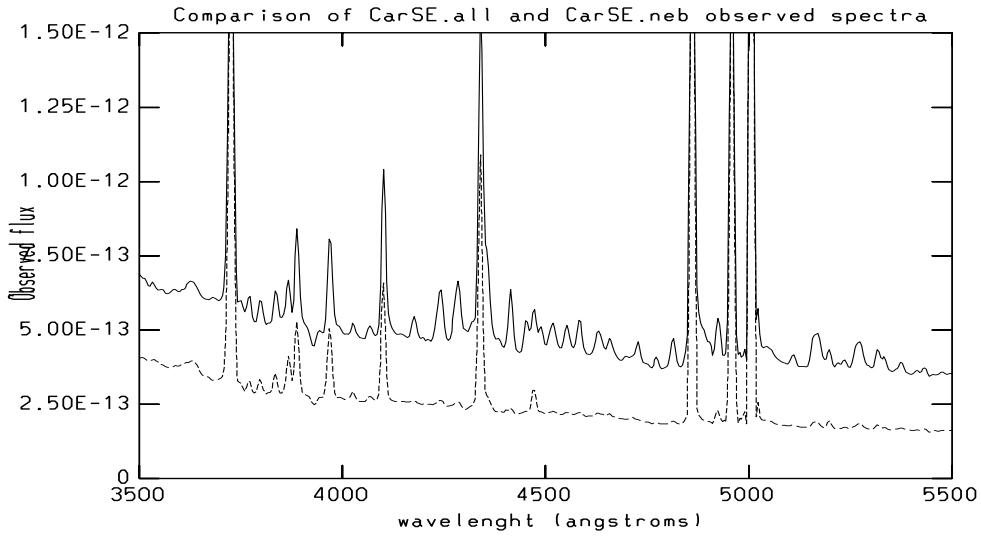


Fig. 7b. Detail of the CarSE.all (solid line) and CarSE.neb (dashed line) Blue observed spectra.

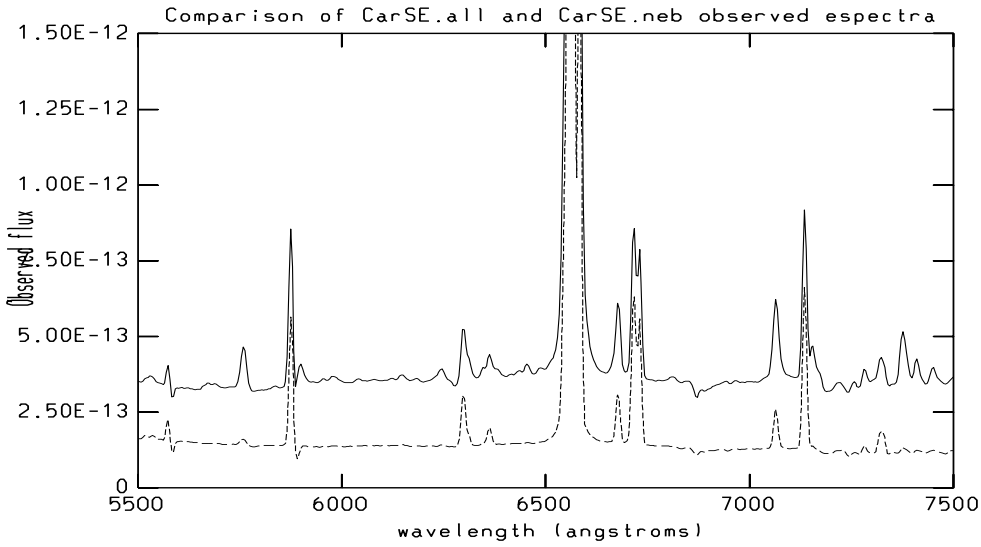


Fig. 7c. Detail of the CarSE.all (solid line) and CarSE.neb (dashed line) Yellow observed spectra.

We checked the consistency of our absolute fluxes derived for each of the three spectral ranges by comparing the overlapping wavelengths between the B and Y spectra and between the Y and R spectra. We found that the continuum fluxes in the overlapping wavelength range agree within 3–13% for the B and Y spectra, and within 13–20% for the Y and R spectra. We show this graphically for the M8 regions in Figs. 9a–9b.

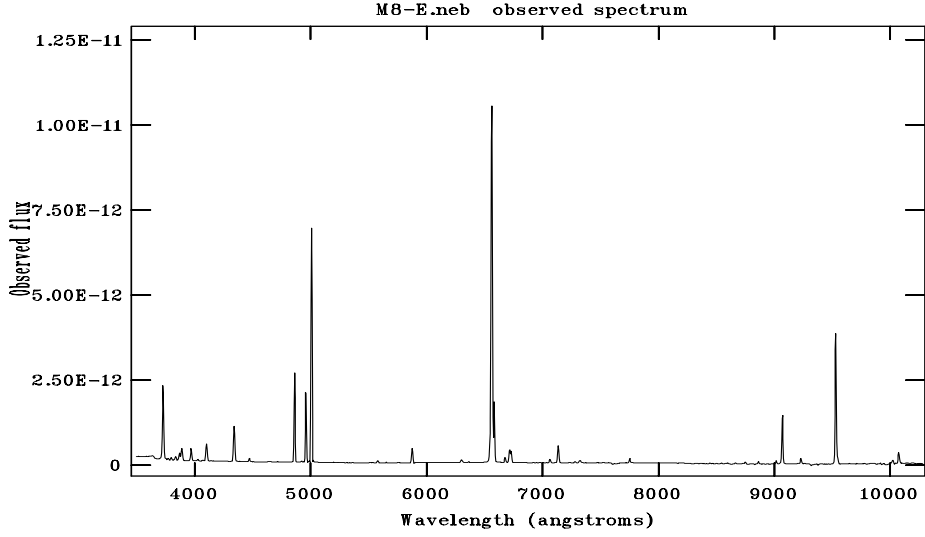


Fig. 8a. M8-E.neb flux-calibrated and sky-subtracted observed spectra $F(\lambda)_{\text{obs}}$ ($\text{erg cm}^{-2} \text{s}^{-1} \text{\AA}^{-1}$) vs. λ (\AA).

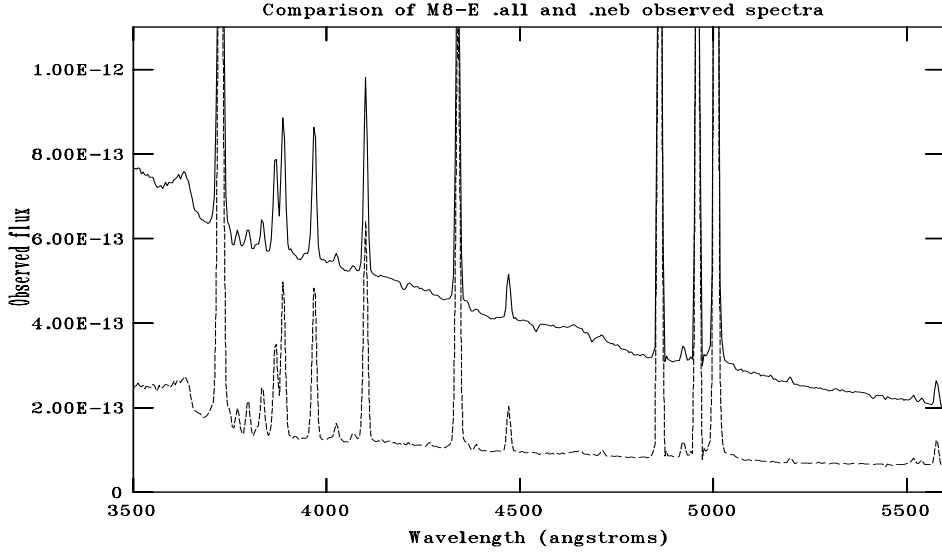


Fig. 8b. Detail of the .all (solid line) and .neb (dashed line) Blue observed spectra for region M8-E.

For each spectra, we measured individually each of the identified lines using the IRAF task *splot*, defining visually the best continuum level and line centers, and computing the total flux above this continuum level. Special care was taken in measuring $\text{H}\alpha$ emission. We fitted two Gaussians to the centers of the $([\text{NII}] \lambda 6548 + \text{H}\alpha) + [\text{NII}] \lambda 6584$ feature, fixing the relative spacing of the line centers. We assumed an intrinsic line ratio $[\text{NII}] \lambda 6584 / \lambda 6548 = 2.9$ (Pradhan & Peng 1995) to find the $[\text{NII}] \lambda 6548$ contribution to be subtracted from $\text{H}\alpha$. Our spectral resolution did not allow us to resolve the Pa8 $\lambda 9546$ line from $[\text{SIII}] \lambda 9531$. We estimated the Pa8 line flux by comparing the line fluxes of Pa7 and Pa9 and subtracted it to the observed $[\text{SIII}] \lambda 9531$ line flux. The correction applied was about 7% of the original uncorrected $[\text{SIII}] \lambda 9531$ observed line flux.

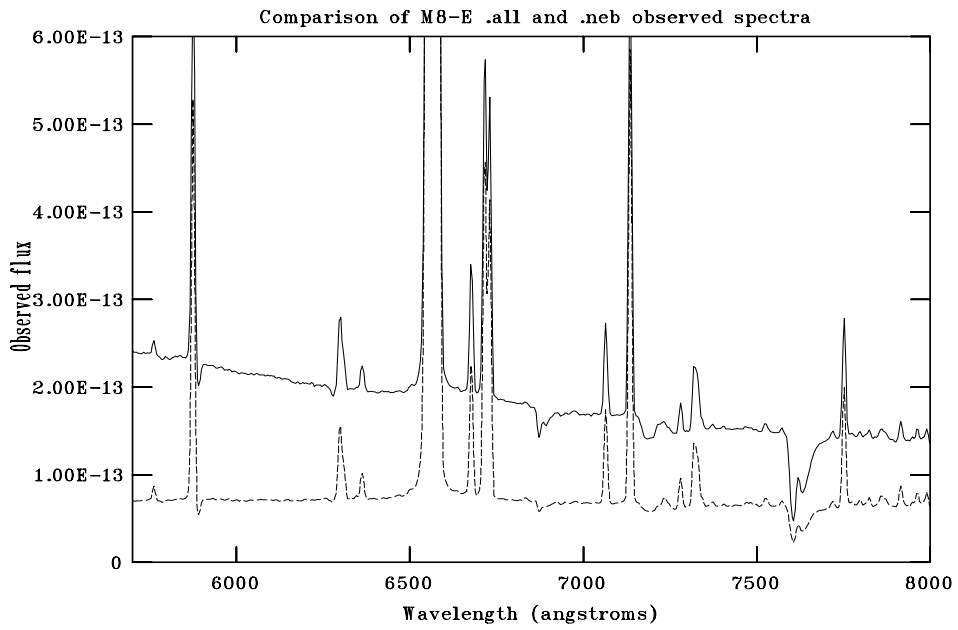


Fig. 8c. Detail of the *.all* (solid line) and *.neb* (dashed line) Yellow observed spectra for region M8-E.

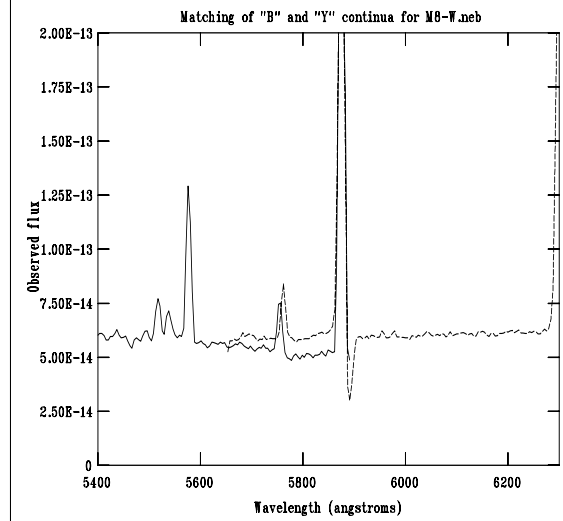
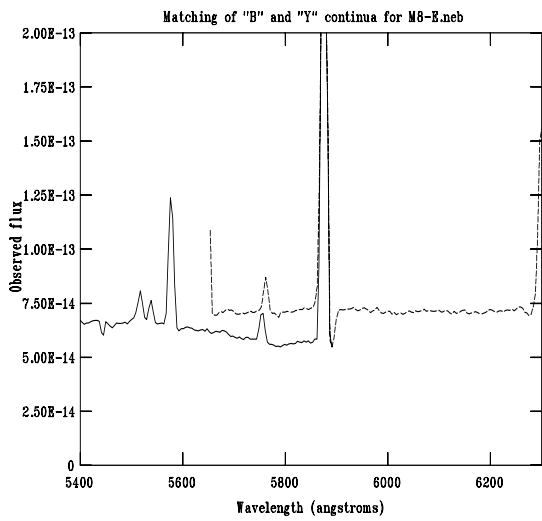


Fig. 9a. Overlapping continua between the B and Y spectral ranges for the M8 regions.

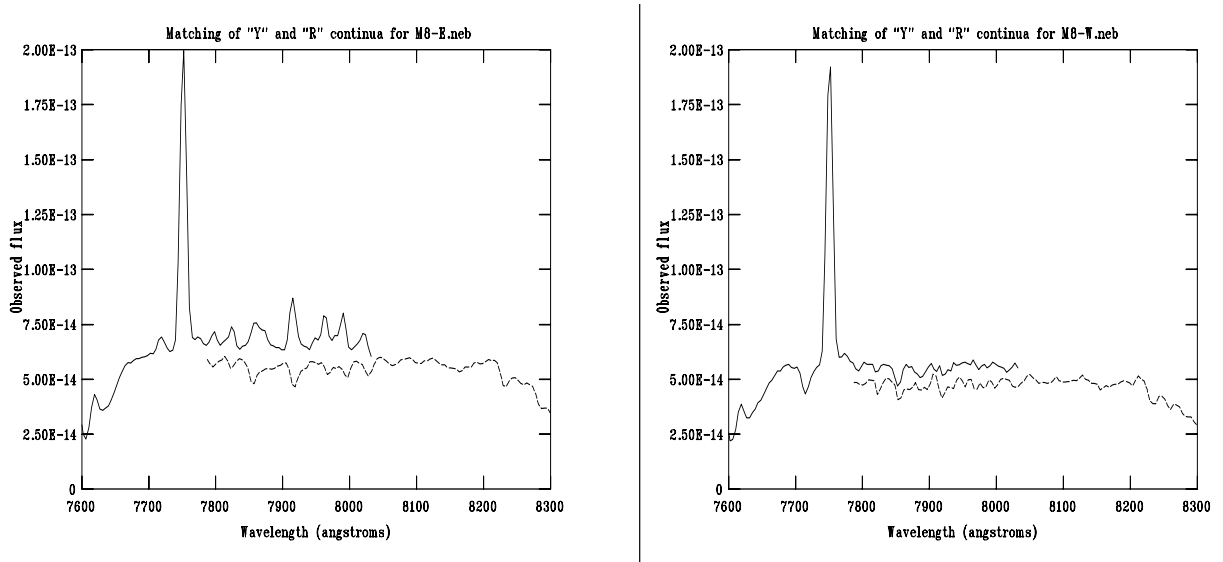


Fig. 9b. Overlapping continua between the Y and R spectral ranges for the M8 regions.

2.4. Observed spectra

In Table 3a, we present the final $(F_{\lambda}/F_{\text{H}\beta}).all$ and $(F_{\lambda}/F_{\text{H}\beta}).neb$ observed line fluxes for the Carina regions arising from our $6.6' \times 5''$ entrance slit. The quoted errors were estimated from several measurements on our two individual spectra for each region and arise from the uncertainty in defining the continuum-level and line centers, especially for those lines which had to be de-convolved. We present a more careful analysis of the line flux errors in Sec. 2.4.1 below. The fluxes of the weaker Paschen lines are uncertain because the continuum is strongly affected by the process of sky-subtraction in this wavelength range. Note the many [FeII] and [FeIII] lines present in the CarSE.all and CarSE.neb spectra (Damineli, et al. 1998). For each region, we also list in Table 3a the parameter $r = F_{\lambda}.neb / F_{\lambda}.all$, that will be discussed in Chapter II. We present in Tables 3b and 3c the observed .neb and .all line fluxes for the M8 and M20 regions, respectively, and in Tables 3d – 3h we present the corresponding observed line fluxes for the 4 RCW nebulae.

Table 3a. Observed *.all* and *.neb* line fluxes for the Carina regions. ^a

λ	Ion-ID	NW. <i>all</i>	NW. <i>neb</i>	NW	SE. <i>all</i>	SE. <i>neb</i>	SE	SW. <i>all</i>	SW. <i>neb</i>	SW
		F_{λ}/F_{β}	F_{λ}/F_{β}	r^d	F_{λ}/F_{β}	F_{λ}/F_{β}	r^d	F_{λ}/F_{β}	F_{λ}/F_{β}	r^d
3624	He I	--	--	--	0.041	0.047	0.88	--	--	--
3727	[O II]	0.956	0.952	1.01	0.661	0.876	1.00	0.859	0.849	1.00
3771	H11	0.011	0.015	1.40	0.024	0.015	0.48	0.013	0.015	1.18
3798	H10	0.009	0.016	1.88	0.027	0.020	0.56	0.021	0.024	1.17
3820	He I	--	--	--	--	0.005	--	0.004	0.004	1.05
3835	H9	0.014	0.022	1.95	0.038	0.026	0.52	0.041	0.044	1.07
3869	[Ne III]	0.103	0.100	0.98	0.054	0.060	0.85	0.093	0.093	1.00
3889	H8+HeI	0.104	0.121	1.17	0.111	0.112	0.76	0.126	0.128	1.02
3970	He+ [NeIII]	0.092	0.113	1.25	0.122	0.108	0.68	0.129	0.137	1.07
4026	He I	0.007	0.012	1.70	0.015	0.013	0.66	0.011	0.011	1.02
4069	[S II]	0.005	0.006	1.25	0.013	0.007	0.43	0.007	0.010	1.36
4102	H δ	0.164	0.178	1.10	0.222	0.190	0.65	0.192	0.195	1.01
4144	He I	--	--	--	0.004	--	--	--	--	--
4169	He I	--	--	--	0.027	0.007	0.21	--	--	--
4244	[Fe II]	--	--	--	0.087	0.012	0.10	--	--	--
4287	[Fe II]	--	--	--	0.109	0.014	0.10	--	--	--
4340	H γ	0.385	0.403	1.06	0.420	0.395	0.71	0.404	0.405	1.00
4363	[O III]	0.014	0.012	0.90	0.107	0.012	0.09	0.010	0.010	1.04
4387	He I	--	--	--	--	--	--	0.004	0.004	0.92
4415	O II	--	--	--	0.073	0.014	0.15	0.004	0.003	0.77
4452	O II	--	--	--	--	0.010	--	--	--	--
4471	He I	0.035	0.036	1.06	0.047	0.035	0.57	0.037	0.037	0.99
4815	[Fe II]	--	--	--	0.036	0.007	0.15	--	--	--
4861	H β	1.000	1.000	1.01	1.000	1.000	0.76	1.000	1.000	1.00
4922	He I	0.014	0.015	1.10	0.047	0.018	0.29	0.015	0.015	0.97
4959	[O III]	0.982	0.974	1.01	0.574	0.752	0.99	0.914	0.918	1.00
5007	[O III]	3.069	3.019	1.00	1.825	2.346	0.98	2.847	2.838	1.00
5112	[Fe II]	--	--	--	0.013	--	--	--	--	--
5159	[Fe II]	--	--	--	0.081	0.016	0.15	0.007	0.009	1.26
5200	[N I]	0.016	0.017	1.07	0.017	0.011	0.48	0.008	0.010	1.15
5270	[Fe III]	--	--	--	0.062	0.013	0.16	0.008	0.007	0.88
5334	[Fe II]	--	--	--	0.013	0.004	0.25	--	--	--
5412	[Fe III]	--	--	--	0.005	--	--	--	--	--
5433	[Fe II]	--	--	--	0.012	0.006	0.40	--	--	--
5518	[Cl III]	0.007	0.007	1.19	0.003	0.006	1.54	0.005	0.005	1.00
5539	[Cl III]	0.004	0.006	1.27	0.004	0.005	1.06	0.005	0.004	0.87
5577	[O I]	0.029 ^c	0.027 ^c	0.93	0.015 ^c	--	--	0.076 ^c	0.076 ^c	1.00
5755	[N II]	0.007	0.007	0.97	0.032	0.013	0.31	0.008	0.007	0.94
5876	He I	0.187 ^c	0.192 ^c	1.04	0.192 ^c	0.190 ^c	0.69	0.204 ^c	0.203 ^c	1.00
6300	[O I]	0.108 ^c	0.104 ^c	0.97	0.048 ^c	0.078 ^c	1.22	0.051 ^c	0.051 ^c	0.99
6312	[S III]	0.016	0.019	1.17	0.042	0.019	0.34	0.013	0.011	0.85
6364	[O I]	0.034 ^c	0.033 ^c	0.99	0.029 ^c	0.022 ^c	0.59	0.016 ^c	0.014 ^c	0.85
6563	H α	5.681	5.648	1.01	4.644	5.634	0.920	5.616	5.594	1.00
6584	[N II]	0.749	0.734	0.99	0.919	0.797	0.66	0.610	0.600	0.98
6678	He I	0.070	0.071	1.02	0.099	0.072	0.55	0.070	0.071	1.01
6716	[S II]	0.242	0.238	0.99	0.168	0.223	1.01	0.220	0.218	0.99
6731	[S II]	0.180	0.176	0.99	0.141	0.179	0.97	0.158	0.160	1.02
7065	He I	0.055	0.054	1.00	0.135	0.057	0.32	0.053	0.057	1.08
7136	[Ar III]	0.261	0.257	1.00	0.198	0.228	0.87	0.237	0.240	1.01
7155	[Fe II]	--	--	--	0.063	--	--	--	--	--
7281	He I	0.009	0.007	0.86	0.020	0.011	0.41	0.015	0.013	0.87
7325	[O II]	0.049	0.048	1.00	0.042	0.047	0.86	0.036	0.037	1.02
7378	[Ni II]	--	--	--	0.107	--	--	--	--	--
7412	[Ni II]	--	--	--	0.038	--	--	--	--	--
7453	[Fe II]	--	--	--	0.027	--	--	--	--	--
7751	[Ar III]	0.053	0.055	1.04	0.042	0.054	0.97	0.055	0.052	0.95

7890	[Ni III]	--	--	--	0.012	0.012	0.76	--	--	--
8438	Pa18	0.021	0.021	0.99	0.021	0.019	0.68	0.014	0.022	1.56
8467	Pa17	0.010	0.012	1.15	--	--	--	--	--	--
8503	Pa16	0.007	0.007	0.93	--	--	--	--	--	--
8545	Pa15	0.010	0.010	1.00	0.013	0.008	0.44	--	0.013	--
8598	Pa14	0.015	0.015	1.00	0.024	0.015	0.48	0.013	0.025	1.92
8750	Pa12	0.021	0.024	1.18	0.024	0.022	0.69	0.018	0.028	1.51
8863	Pa11	0.035	0.035	1.00	0.037	0.032	0.65	0.035	0.045	1.27
9015	Pa10	0.057	0.060	1.06	0.065	0.070	0.81	0.073	0.092	1.26
9069	[S III]	0.580	0.575	1.01	0.578	0.746	0.98	0.744	0.728	0.98
9124	[Cl II]	--	--	--	0.039	0.013	0.24	--	--	--
9229	Pa9	0.081	0.085	1.06	0.120	0.084	0.53	0.081	0.098	1.22
9531	[S III]	2.592 ^e	2.534 ^e	0.99	2.077 ^e	2.579 ^e	0.94	2.674 ^e	2.643 ^e	0.99
9850	[C I]	0.011	0.011	1.01	--	--	--	--	--	--
10028	He I	0.024	0.029	1.21	--	--	--	--	0.041	--
10049	Pa7	0.250	0.253	1.02	0.489	0.261	0.41	0.284	0.319	1.12
10287	[S II]	0.016	0.017	1.06	--	--	--	--	--	--
$F(\text{H}\beta)$ ^b		2.28 ±	2.31 ±		3.62 ±	2.74 ±		1.79 ±	1.78 ±	
		0.11	0.11		0.18	0.14		0.09	0.09	

^a Line fluxes normalized to $F(\text{H}\beta) = 1.000$. The estimated line flux errors are as follow: if $(F_\lambda/F_\beta) \geq 1.00$, error = 4%; if $1.00 > (F_\lambda/F_\beta) \geq 0.50$, error = 7%; if $0.50 > (F_\lambda/F_\beta) \geq 0.10$, error = 10%; if $0.10 > (F_\lambda/F_\beta) \geq 0.02$, error = 15%; if $0.02 > (F_\lambda/F_\beta)$, error = 20%; ^b $F(\text{H}\beta)$ fluxes in units of $10^{-11} \text{ erg cm}^{-2} \text{ s}^{-1}$, arising from our $6.6' \times 5''$ entrance slit. ^c Upper limit due to inaccurate sky-subtraction. ^d $r = F_{\lambda}^{.neb} / F_{\lambda}^{.all}$. ^e The line flux was decreased by 7% to take into account the P8 $\lambda 9546$ contribution.

Table 3b. Observed *.all* and *.neb* line fluxes for M8 regions. ^a

λ	Ion ID	M8-E		M8-W	
		$(F_\lambda / F_{\text{H}\beta})_{.neb}$	r^b	$(F_\lambda / F_{\text{H}\beta})_{.neb}$	r^b
3727	[O II]	1.061	1.01	1.388	0.94
3771	H11	0.018	1.50	0.017	0.95
3798	H10	0.031	1.71	0.034	1.05
3835	H9	0.050	1.74	0.053	0.96
3869	[Ne III]	0.100	1.01	0.076	0.95
3889	H8+He I	0.152	1.14	0.143	0.98
3970	He I+[Ne III]	0.166	1.19	0.170	1.00
4026	He I	0.014	1.27	0.014	0.93
4069	[S II]	0.008	1.00	0.012	0.75
4102	H δ	0.216	1.16	0.220	0.97
4267	C II	0.0040	0.88	-	-
4340	H γ	0.432	1.06	0.426	0.93
4363	[O III]	0.0043	1.17	0.0048	1.28
4388	He I	-	-	0.0043	1.12
4471	He I	0.043	1.01	0.041	1.00
4658	[Fe III]	-	-	0.0044	0.79
4713	He I	-	-	0.0046	0.79
4861	H β	1.000*	1.02*	1.000*	0.94*
4922	He I	0.014	1.06	0.014	1.06
4959	[O III]	0.863	1.02	0.680	0.91
5007	[O III]	2.610	1.01	2.110	0.95
5200	[N I]	0.0063	1.11	0.0073	0.86
5270	[Fe III]	-	-	0.0031	1.36

5518	[Cl III]	0.0053	1.01	0.0061	1.14
5539	[Cl III]	0.0034	0.74	0.0041	0.96
5577	[O I]	0.024 ^c	0.92	0.021 ^c	0.94
5755	[N II]	0.0053	1.15	0.0067	1.00
5876	He I	0.176 ^c	1.05	0.147 ^c	0.93
6300	[O I]	0.034	1.05	0.064	0.99
6312	[S III]	0.0057	0.46:	0.011	1.06
6364	[O I]	0.012	1.01	0.023	0.93
6563	H α	4.501	1.01	4.370	0.99
6584	[N II]	0.695	1.00	0.954	0.98
6678	He I	0.058	1.04	0.050	0.91
6716	[S II]	0.153	0.99	0.194	1.00
6731	[S II]	0.131	1.01	0.178	0.99
7065	He I	0.041	0.98	0.038	0.95
7136	[Ar III]	0.193	1.00	0.175	0.99
7231	C II	-	-	0.0042	1.06
7281	He I	0.014	1.00	0.0079	0.97
7325	[O II]	0.052	0.95	0.060	0.93
7751	[Ar III]	0.054	1.02	0.042	0.99
8392	Pa 20	-	-	0.0035	1.34
8413	Pa 19	0.0059	0.89	0.0050	1.10
8446	O I	0.011	1.10	0.012	0.91
8467	Pa 17	0.0037	1.16	0.0043	0.83
8503	Pa 16	0.0056	0.96	0.0072	1.08
8545	Pa 15	0.0088	1.20	0.0089	1.04
8598	Pa 14	0.012	1.18	0.0084	0.85
8665	Pa 13	0.011	1.03	0.011	0.94
8750	Pa 12	0.019	1.09	0.018	0.93
8863	Pa 11	0.030	1.03	0.026	0.98
9015	Pa 10	0.039	1.09	0.034	0.91
9069	[S III]	0.621	1.00	0.560	0.88
9229	Pa 9	0.064	1.01	0.056	0.89
9531	[S III]	1.567 ^d	1.00	1.397 ^d	0.89
9850	[C I]	-	-	0.0064	0.91
10028	He I	0.036	1.05	0.027	0.93
10049	Pa 7	0.151	1.01	0.136	0.89
* $F(H\beta)$		3.053 \pm 0.150	1.018	3.817 \pm 0.190	0.938

^a Line fluxes normalized to $F(H\beta) = 1.000$. $F(H\beta)$ flux in units of 10^{-11} erg cm^{-2} s^{-1} , from an entrance slit of $6.6' \times 5''$. The estimated line flux errors are as in Table 3a. The *.all* line fluxes are given by $(F\lambda/F\beta).all = (F\lambda/F\beta).neb \times r\beta / r\lambda$. ^b $r = F\lambda.^{neb} / F\lambda.^{all}$. ^c Upper limit due to inaccurate sky-subtraction. ^d The line flux was decreased by 7% to take into account the P8 $\lambda 9546$ contribution.

Table 3c. Observed *.all* and *.neb* line fluxes for M20 regions. ^a

λ	Ion ID	M20-S		M20-N	
		$(F\lambda/FH\beta).neb$	r^b	$(F\lambda/FH\beta).neb$	r^b
3530?	He I	0.0079	1.32	-	-
3704?	He I	0.0015	0.51	-	-
3727	[O II]	2.296	1.02	2.329	1.01
3771	H 11	0.022	1.59	0.010	0.88
3798	H 10	0.029	2.61	0.019	1.59
3835	H 9	0.048	2.01	0.025	2.21
3869	[Ne III]	0.014	0.79	0.017	0.78
3889	H8+He I	0.127	1.29	0.105	1.20
3970	He ϵ + [Ne III]	0.111	1.34	0.088	1.50
4069	[S II]	0.019	1.39	0.017	0.95

4102	H δ	0.201	1.19	0.190	1.23
4340	H γ	0.421	1.06	0.423	1.07
4363	[O III]	0.0059	0.88	0.0052	1.06
4471	He I	0.029	1.27	0.038	1.55
4861	H β	1.000 *	1.04	1.000 *	1.04
4922	He I	0.010	1.28	-	-
4959	[O III]	0.211	1.00	0.205	0.95
5007	[O III]	0.656	1.00	0.619	1.01
5200	[N I]	0.015	0.96	0.024	1.04
5518	[Cl III]	0.0056	0.92	-	-
5539	[Cl III]	0.0046	1.47	-	-
5577	[O I]	0.143 ^c	0.99	0.259 ^c	1.00
5755	[N II]	0.012	1.05	0.013	0.95
5876	He I	0.122 ^c	1.06	0.142 ^c	0.98
6300	[O I]	0.114	0.92	0.048	0.95
6312	[S III]	0.0090	-	0.025	-
6364	[O I]	0.036	1.01	0.012	1.00
6563	H α	4.237	1.00	5.210	1.01
6584	[N II]	1.440	1.00	1.700	1.01
6678	He I	0.041	1.06	0.050	1.04
6716	[S II]	0.396	1.00	0.510	1.00
6731	[S II]	0.296	1.00	0.371	1.01
7065	He I	0.028	1.20	0.030	1.07
7136	[Ar III]	0.129	1.00	0.154	1.00
7325	[O II]	0.047	1.02	0.065	1.03
7379	[Ni II]	0.0085	0.96	0.013	1.05
7751	[Ar III]	0.021	1.03	0.027	0.90
7816	He I	0.0066	1.23	-	-
8242?	N I	0.0056	1.25	-	-
8346	Pa 23	0.013	1.06	0.0097	1.31
8392	Pa 20	0.0059	1.05	0.0063	0.92
8438?	Pa 18	-	-	0.0082	0.77
8446	O I	0.0043	0.77	-	-
8467	Pa 17	0.0073	1.43	0.0030	0.47
8503	Pa 16	0.011	1.48	-	-
8545	Pa 15	0.0043	0.47	-	-
8579	[Cl II]	-	-	0.0074	1.15
8598	Pa 14	0.010	1.08	0.0067	0.78
8665	Pa 13	0.0092	1.02	-	-
8733?	He I	-	-	0.0048	0.61
8750	Pa 12	0.028	1.05	0.015	0.83
8863	Pa 11	0.025	1.08	0.028	0.81
8915	He I	0.0080	0.91	-	-
9015	Pa 10	0.024	0.99	0.032	1.25
9069	[S III]	0.505	0.97	0.564	0.94
9229	Pa 9	0.055	1.00	0.054	0.85
9464	He I	0.013	0.92	-	-
9531	[S III]	1.352 ^d	0.99	1.508 ^d	0.96
9850	[C I]	0.022	1.02	0.023	0.87
10028	He I	0.0716	1.09	-	-
10049	Pa 7	0.150	1.04	0.153	0.97
10287?	[S II]	0.021	0.73	0.054	1.44
* $F(\text{H}\beta)$		1.039 \pm 0.050	1.044	0.694 \pm 0.035	1.035

^a Line fluxes normalized to $F(\text{H}\beta) = 1.000$. The $F(\text{H}\beta)$ flux in units of $10^{-11} \text{ erg cm}^{-2} \text{ s}^{-1}$, from an entrance slit of $6.6' \times 5''$. The estimated line flux errors are as in Table 3a. The .all line fluxes are given by $(F\lambda/F\beta).all = (F\lambda/F\beta).neb \times r\beta / r\lambda$. ^b $r = F\lambda^{.neb} / F\lambda^{.all}$. ^c Upper limit due to inaccurate sky-subtraction. ^d The line flux was decreased by 7% to take into account the P8 $\lambda 9546$ contribution.

Table 3d. Observed and de-reddened *.all* and *.neb* line fluxes for RCW6 ^a

ID	λ	$f(\lambda)$	$F(\lambda)^{\text{all}}$	$F(\lambda)^{\text{neb}}$	r_{obs}	$I(\lambda)^{\text{all}}$	$I(\lambda)^{\text{neb}}$	r_0
(1)	(2)	(3)	(4)	(5)	(6)	(7)	(8)	(9)
[O II]	3727	0.322	1.573	1.547	0.993	3.636	3.496	0.907
H δ	4102	0.229	0.207:	0.282:	1.377:	0.375:	0.504:	1.266:
H γ	4340	0.157	0.521:	0.519:	0.996:	0.784:	0.757:	0.909:
H β	4861	0.000	1.000	1.000	1.010	1.000	1.000	0.942
[O III]	4959	-0.026	0.431	0.427	1.000	0.403	0.400	0.935
[O III]	5007	-0.038	1.166	1.153	0.998	1.057	1.047	0.934
[N II]	5755	-0.185	0.016	0.020	1.276	0.010	0.012	1.204
He I	5876	-0.203	0.469:	0.476:	1.025	0.277:	0.285:	0.970
[N II]	6548	-0.296	0.342	0.336	0.994	0.158	0.159	0.946
H α	6563	-0.298	6.159	6.081	0.997	2.836	2.859	0.950
[N II]	6583	-0.300	1.026	1.009	0.994	0.470	0.472	0.946
[S II]	6716	-0.318	0.554	0.561	1.023	0.242	0.251	0.976
[S II]	6731	-0.320	0.219	0.215	0.992	0.095	0.095	0.946
[Ar III]	7136	-0.374	0.202	0.203	1.013	0.076	0.079	0.970
[O II]	7325	-0.399	0.170	0.164	0.972	0.060	0.060	0.933
$F(\text{H}\beta)^{\text{b}}$			1.80	1.82	1.010	24.34	22.94	0.942
$c(\text{H}\beta)_{\text{H}\alpha}$			1.13	1.10				

^a Columns give: (1) Ion ID; (2) Line wavelength (\AA); (3) CCM89 extinction law for $R = 3.1$; (4) Observed $F(\lambda)$ and (7) de-reddened $I(\lambda)$ *.all* line fluxes with respect to $F(\text{H}\beta)$; (5) Observed $F(\lambda)$ and (8) de-reddened $I(\lambda)$ *.neb* line fluxes with respect to $F(\text{H}\beta)$; (6) observed and (9) de-reddened parameter $r = F(\lambda)^{\text{neb}} / F(\lambda)^{\text{all}}$. ^b Observed and de-reddened H β flux from our entrance slit $\Omega_{\text{slit}} = 5'' \times 6.5''$ in units of $10^{-12} \text{ erg s}^{-1} \text{ cm}^{-2}$. Line flux errors as in Table 3a.

Table 3e. Observed and de-reddened *.all* and *.neb* line fluxes for RCW60-E ^a

ID	λ	$f(\lambda)$	$F(\lambda)^{\text{all}}$	$F(\lambda)^{\text{neb}}$	r_{obs}	$I(\lambda)^{\text{all}}$	$I(\lambda)^{\text{neb}}$	r_0
(1)	(2)	(3)	(4)	(5)	(6)	(7)	(8)	(9)
[O II]	3727	0.322	1.742	1.719	0.998	4.026	3.944	0.968
H δ	4102	0.229	0.131	0.168	1.299	0.237	0.303	1.262
H γ	4340	0.157	0.494:	0.464:	0.941:	0.701:	0.754:	1.062:
H β	4861	0.000	1.000	1.000	1.011	1.000	1.000	0.988
[O III]	4959	-0.026	0.239	0.240	1.015	0.223	0.224	0.992
[O III]	5007	-0.038	0.624	0.623	1.009	0.565	0.564	0.987
[N II]	5755	-0.185	0.023	0.023	0.979	0.014	0.014	0.962
He I	5876	-0.203	0.431:	0.440:	1.031	0.254:	0.260:	1.012
[N II]	6548	-0.296	0.413	0.410	1.003	0.191	0.191	0.987
H α	6563	-0.298	6.181	6.129	1.002	2.846	2.842	0.986
[N II]	6583	-0.300	1.239	1.229	1.003	0.568	0.567	0.987
[S II]	6716	-0.318	0.608	0.607	1.009	0.266	0.267	0.994
[S II]	6731	-0.320	0.249	0.244	0.991	0.108	0.107	0.976
[Ar III]	7136	-0.374	0.146	0.143	0.985	0.055	0.054	0.971
[O II]	7325	-0.399	0.110	0.106	0.972	0.039	0.038	0.959
Pa 10	9015	-0.590	0.035	0.035	1.00	0.008	0.008	1.005
[S III]	9069	-0.594	0.377	0.376	1.01	0.080	0.081	1.013
Pa 9	9229	-0.605	0.045	0.043	0.96	0.009	0.009	0.968
[S III]	9532	-0.625	1.136	1.120	1.00	0.223	0.224	1.001
Pa 7	10049	-0.656	0.118	0.112	0.96	0.021	0.021	0.967
$F(\text{H}\beta)^{\text{b}}$			2.79	2.82	1.011	37.65	37.19	0.988
$c(\text{H}\beta)_{\text{H}\alpha}$			1.13	1.12				

^a Same columns as in Table 3d. ^b Observed and de-reddened H β flux from our entrance slit $\Omega_{\text{slit}} = 5'' \times 6.5''$ in units of $10^{-12} \text{ erg s}^{-1} \text{ cm}^{-2}$. Line flux errors as in Table 3a.

Table 3f. Observed and de-reddened *.all* and *.neb* line fluxes for RCW60-W ^a

ID	λ	$f(\lambda)$	$F(\lambda)^{\text{all}}$	$F(\lambda)^{\text{neb}}$	r_{obs}	$I(\lambda)^{\text{all}}$	$I(\lambda)^{\text{neb}}$	r_0
(1)	(2)	(3)	(4)	(5)	(6)	(7)	(8)	(9)
[O II]	3727	0.322	1.640	1.605	1.005	3.791	3.682	0.975
H δ	4102	0.229	0.138	0.152	1.131	0.251	0.275	1.100
H γ	4340	0.157	0.455:	0.435	0.956:	0.685:	0.652	0.956:
H β	4861	0.000	1.000	1.000	1.027	1.000	1.000	1.004
[O III]	4959	-0.026	0.272	0.264	1.000	0.254	0.247	0.978
[O III]	5007	-0.038	0.729	0.723	1.018	0.661	0.655	0.996
[N II]	5755	-0.185	0.009	0.011	1.298	0.006	0.007	1.272
$F(\text{H}\beta)^{\text{b}}$			3.25	3.34	1.027	43.84	44.00	1.004
$c(\text{H}\beta)_{\text{H}\alpha}$			1.13	1.12				

^a Same columns as in Table 3d. ^b Observed and de-reddened H β flux from our entrance slit $\Omega_{\text{slit}} = 5'' \times 6.5''$ in units of $10^{-12} \text{ erg s}^{-1} \text{ cm}^{-2}$. Line flux errors as in Table 3a.

Table 3g. Observed and de-reddened *.all* and *.neb* line fluxes for RCW107 ^a

ID	λ	$f(\lambda)$	$F(\lambda)^{\text{all}}$	$F(\lambda)^{\text{neb}}$	r_{obs}	$I(\lambda)^{\text{all}}$	$I(\lambda)^{\text{neb}}$	r_0
(1)	(2)	(3)	(4)	(5)	(6)	(7)	(8)	(9)
[O II]	3727	0.322	0.463	0.370	0.835	1.161	0.869	0.635
[Ne III]	3869	0.291	-	0.026:	-	-	0.057:	-
H δ	4102	0.229	0.026:	0.180:	7.213:	0.050:	0.330:	5.585:
H γ	4340	0.157	0.329	0.367	1.164	0.515	0.556	0.916
[O III]	4363	0.149	0.033:	0.002:	0.063:	0.050:	0.003:	0.051:
[Fe III]	4735	0.036	-	0.009	-	-	0.009	-
H β	4861	0.000	1.000	1.000	1.044	1.000	1.000	0.849
[O III]	4959	-0.026	0.385	0.353	0.985	0.357	0.330	0.782
[O III]	5007	-0.038	1.130	1.066	0.985	1.014	0.964	0.807
[N II]	5755	-0.185	0.056	0.028	0.522	0.033	0.017	0.441
He I	5876	-0.203	0.293:	0.421:	1.501	0.165:	0.246:	1.271
[N II]	6548	-0.296	1.089	0.747	0.723	0.468	0.342	0.626
H α	6563	-0.298	6.660	6.281	0.985	2.844	2.853	0.851
[N II]	6583	-0.300	2.129	1.859	0.912	0.905	0.839	0.787
He I	6678	-0.313	0.104	0.103	1.034	0.043	0.045	0.897
[S II]	6716	-0.318	0.123	0.115	0.979	0.049	0.050	0.850
[S II]	6731	-0.320	0.100	0.105	1.095	0.040	0.045	0.951
[Ar III]	7136	-0.374	-	0.185	-	-	0.069	-
$F(\text{H}\beta)^{\text{b}}$			1.56	1.63	1.044	27.16	23.05	0.849
$c(\text{H}\beta)_{\text{H}\alpha}$			1.24	1.15				

^a Same columns as in Table 3d. ^b Observed and de-reddened H β flux from our entrance slit $\Omega_{\text{slit}} = 5'' \times 6.5''$ in units of $10^{-12} \text{ erg s}^{-1} \text{ cm}^{-2}$. Line flux errors as in Table 3a.

Table 3*h*. Observed and de-reddened *.all* and *.neb* line fluxes for RCW110 ^a

ID	λ	$f(\lambda)$	$F(\lambda)^{\text{all}}$	$F(\lambda)^{\text{neb}}$	r_{obs}	$I(\lambda)^{\text{all}}$	$I(\lambda)^{\text{neb}}$	r_0
(1)	(2)	(3)	(4)	(5)	(6)	(7)	(8)	(9)
[O II]	3727	0.322	0.741	0.671	0.968	3.462	2.955	0.759
H δ	4102	0.229	0.026:	0.047:	1.895:	0.079:	0.134:	1.509:
H γ	4340	0.157	0.216	0.227	1.051	0.459	0.468	0.908
H β	4861	0.000	1.000	1.000	1.069	1.000	1.000	0.889
[O III]	4959	-0.026	0.065	0.057	0.936	0.057	0.050	0.780
[O III]	5007	-0.038	0.176	0.187	1.064	0.147	0.157	0.953
[N II]	5755	-0.083	0.102	0.093	0.978	0.068	0.063	0.824
He I	5876	-0.203	0.594:	0.563:	1.015	0.224:	0.221:	0.877
[N II]	6548	-0.296	1.359	1.264	0.995	0.329	0.323	0.873
H α	6563	-0.298	11.89	11.22	1.009	2.854	2.844	0.886
[N II]	6583	-0.300	4.076	3.792	0.995	0.969	0.952	0.874
[S II]	6716	-0.318	1.719	1.618	1.006	0.375	0.374	0.887
[S II]	6731	-0.320	1.034	0.997	1.031	0.223	0.228	0.909
[O II]	7325	-0.399	0.595	0.569	1.023	0.089	0.092	0.919
$F(\text{H}\beta)^{\text{b}}$			0.371	0.397	1.069	44.63	39.69	0.889
$c(\text{H}\beta)_{\text{H}\alpha}$			2.08	2.00				

^a Same columns as in Table 3*d*. ^b Observed and de-reddened H β flux from our entrance slit $\Omega_{\text{slit}} = 5'' \times 6.5''$ in units of $10^{-12} \text{ erg s}^{-1} \text{ cm}^{-2}$. Line flux errors as in Table 3*a*.

2.4.1 Line flux errors

The reported line flux errors from spectroscopic observations have several possible contributions, including *a*) internal CCD readout noise, *b*) line identification, *c*) flux calibration errors during the data-reduction process, *d*) flux line profile fitting (Gaussian or not) and *d*) line continuum adoption (Visual or background). We estimate that factors *a*) and *b*) contribute only with a small fraction of a percent. From our data-reduction procedure, we consider that our flux calibration is accurate within 3 – 5%. Regarding the line flux measurement, we have found that measuring the line flux under the line above a given continuum or measuring the line flux by fitting a Gaussian to the line profile, may produce differences of about 1 – 2% for bright lines (eg. H α or H β) and up to 10 – 15% for weaker lines, such as Balmer H9, H10 and H11. We found that these differences are more pronounced in the *.all* spectra than in the *.neb* ones. The line fluxes considered in this work were calculated by measuring the line flux under the line above a visually adopted background continuum.

Besides these systematic errors, we should also estimate the statistical errors by measuring the same line flux on at least two different spectra of the same object, observed with the same telescope and reduced using the same procedure. A more rigorous line flux error estimation would be to observe the same region, with similar slits, but using different telescopes and different data-reduction procedures (eg. Esteban et al. 1999, and García-Rojas et al. 2006). As mentioned before, we observed our Carina, M8 and M20 regions at least two times for a given spectral range (B, Y and R) during the same night. In order to estimate this error, we measured a number of lines in *two* different spectra of the same object. We did this exercise for the Balmer lines and some bright and weak forbidden lines in

the Carina regions and our results are presented in Fig. 10. We show the absolute value of the line flux error (in %), but note that some lines were overestimated and some were underestimated when comparing one spectrum with the other.

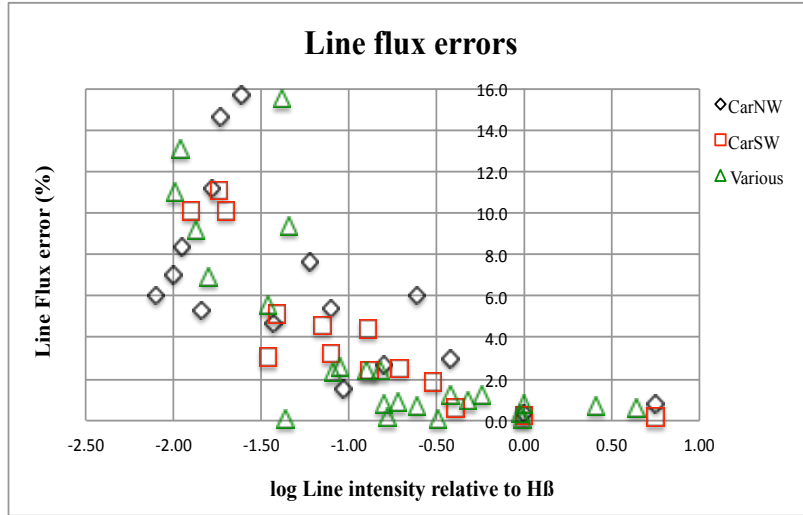


Fig. 10. Absolute line flux errors as function of line flux intensity (relative to $H\beta$) for several measurements of the same line in two different spectra of the same object obtained during the same night.

As expected, the weaker lines have larger errors. From these results we conclude that the statistical errors are as follow: if $F_{\lambda}/F_{\beta} \sim 1-5$, then error = 1%; if $F_{\lambda}/F_{\beta} \sim 0.5$, then error = 3%; $F_{\lambda}/F_{\beta} \sim 0.1$, then error = 6%; if $F_{\lambda}/F_{\beta} \sim 0.05$, then error = 10%; and if $F_{\lambda}/F_{\beta} \sim 0.01$, then error = 15%. (See Tables 3a – 3h.)

However, the largest source of error for a line flux measurement in relatively low S/N spectra comes from the adoption of the background continuum level. We performed a set of measurements for strong and weak lines using both background fitting and without it. For strong lines such as $H\alpha$, $H\beta$ or $[OIII] \lambda 5007$, the line flux differences were less than 1%, however for weaker lines such as $[NII] \lambda 5755$ or $[OIII] \lambda 4363$ we found differences as large as 30%, especially for $[OIII] \lambda 4363$, which was de-blended from $H\gamma \lambda 4340$ (See Chapter IV).

In the next chapter we analyze these data and discuss the effects of the stellar spectra in the integrated nebular spectrum in our observed nebulae.

2.5. Conclusions

In this chapter we present mid-resolution spectroscopy from 3600 – 10200 Å of 7 Galactic HII regions: Carina, M8, M20, RCW6, RCW60, RCW107 and RCW110, obtained with the 1.5-m telescope at CTIO. We aligned the slit N–S and drifted the telescope over the bright central part of each nebula during a given integration time. For each nebula, we identified the bright exciting stars and compiled

their main physical parameters from the literature. Working with the 2D CCD frames we were able to reduce the data so to obtain a *.all* and a *.neb* spectra. The *.all* spectra correspond to the emission arising both from the nebular gas and the stars that crossed the slit during the scans, while in the *.neb* spectra, the bright stars were “removed” from the CCD before obtaining the 1D spectra. The *.all* spectra would be comparable to low-spatial resolution observations of giant extragalactic HII regions where the bright stars cannot be disentangled from the pure nebular emission. The procedure used to measure the line fluxes (Gaussian fitting or not, and Background fitting or not) introduced an error in the line fluxes of about 1 – 2% for bright lines and up to 10 – 15% for weak lines.

Chapter III. Effects of the exciting stars

3.1. Introduction

In this chapter we analyze in more detail the effect of the embedded stars in the line fluxes. In Sec. 3.2 we compare the *.all* and *.neb* observed line fluxes for the Balmer series, for the HeI lines, for the Paschen lines and for the forbidden lines. In Sec. 3.3 we present the observed fluxes and equivalent of our brightest nebulae used to derive simultaneously the logarithmic reddening correction constant and the underlying stellar absorption equivalent, both for the *.all* and *.neb* spectra. Our conclusions are presented in Sec. 3.4.

3.2 Comparison of *.neb* and *.all* line fluxes

3.2.1 Balmer lines

In this section we compare the *.all* vs. *.neb* line fluxes for the Balmer series. In Fig 1*a* – 1*d* we show the behavior of the parameter $r = F_{\lambda}^{.neb} / F_{\lambda}^{.all}$, as function of wavelength for the Balmer series for all our studied objects. In Fig. 1*a* (for the Carina regions), we see that the inclusion of the stellar spectra produces different effects on the r parameter depending upon the spectral type and luminosity class of the embedded exciting stars. If the region is mostly dominated by O stars, as in the CarNW region (O3 If*, O3 V, O6 III), the observed *.neb* Balmer lines are *larger* than the *.all* ones, evidencing the underlying stellar absorption present in the *.all* spectra. This effect is stronger for the weaker Balmer lines (H9, H10, H11), although our uncertainty increases for these lines. On the other hand, if the region is dominated by a mixture of LBV emission stars and early O stars, as in the CarSE region (which includes η Car and some O3 V stars), then the *.neb* Balmer lines are *smaller* than the *.all* ones, evidencing thus the effect of the Balmer *emission* present in the LBV star. For the CarSW region, which contains both an O3–O4 If star ($V = 10.8$ mag) and a WN6ha ($V = 8.1$ mag), the effects tend to cancel out giving a parameter $r \approx 1$ for most of the Balmer series. We also include the results for the “Car Reg” spectra, composed from the addition (λ to λ) of the CarNW, CarSE and CarSW spectra, which would be similar to what may be observed in extragalactic HII regions. As we can see, even that there are 16 early O stars present in the three Carina regions, the effect of the bright η Car is still apparent in the Car Reg spectrum. According to the flux error estimated in Chapter II, and given that the parameter r is a *ratio* of observed fluxes, we have assigned uncertainties of *a*) $\pm 30\%$ to lines about $0.01 F_{\beta}$ (as H9, H10 and H11); *b*) $\pm 20\%$ to lines about $0.1 F_{\beta}$ (as H ϵ and H8); *c*) $\pm 10\%$ to lines about $0.5 F_{\beta}$ (as H γ and H δ) and *d*) $\pm 5\%$ to lines about 1 – $5 F_{\beta}$ (as H β and H α). In Fig. 2*a*, we show only the 4 brightest Balmer lines which are the less uncertain. As we see, the underlying stellar effect is still important for the Car Reg spectrum, giving H γ and H δ overestimated by about 10% if the stars are not

removed from the integrated spectra. For the sake of clarity, we show only the error bars for the Car Reg spectrum.

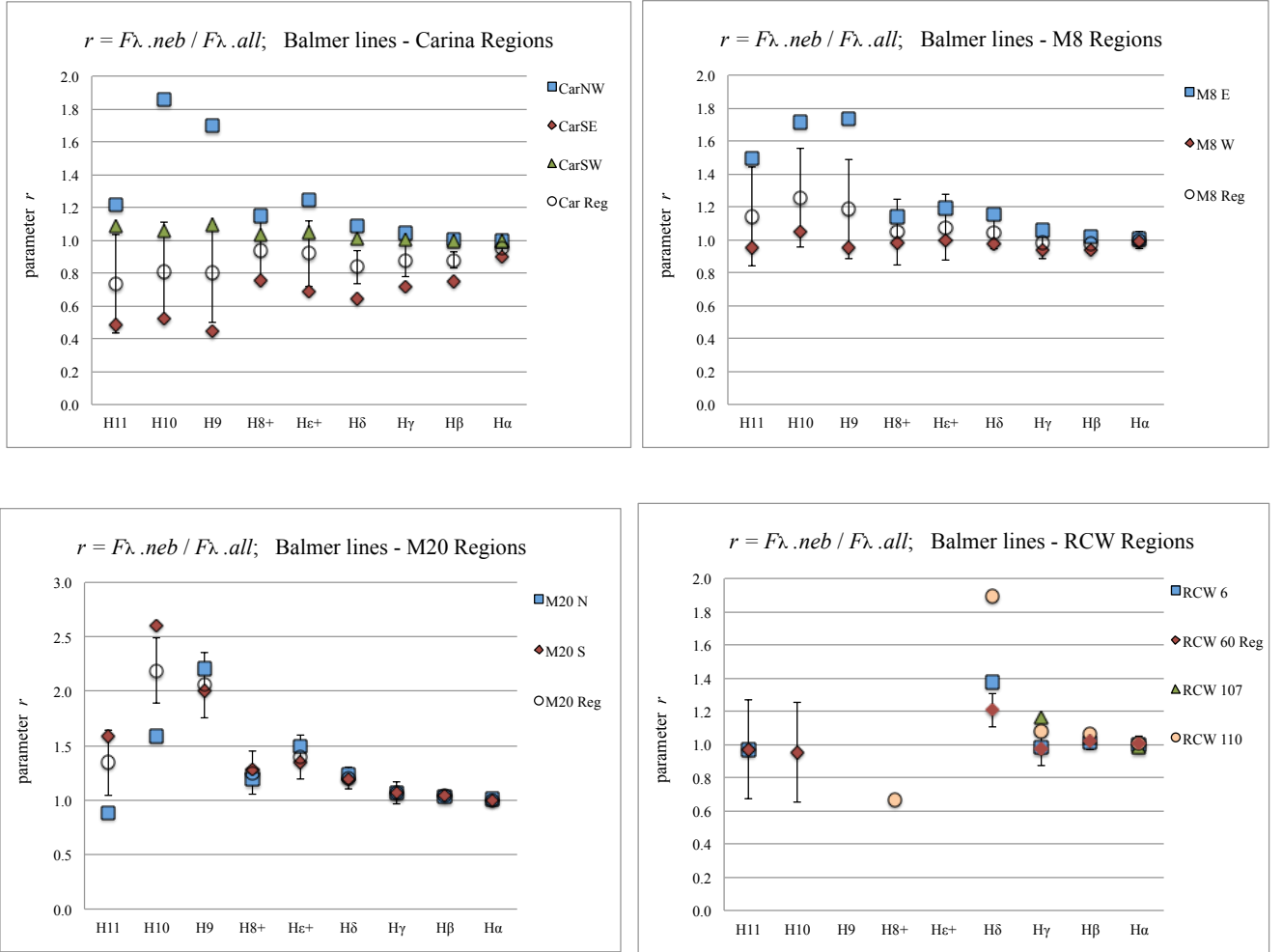


Fig. 1a – 1d. Observed parameter $r = F\lambda_{.neb} / F\lambda_{.all}$ for the Balmer lines for our sample objects: a) Carina regions, b) M8 regions, c) M20 regions and d) RCW objects.

In Figs. 1b – 1c, and Figs. 2b – 2c, we present similar plots for the M8 and M20 regions. M8 is powered by an O4 V and an O7.5 V; while M20 is excited by an O7 V. For both objects, the *.neb* Balmer lines are stronger than the *.all* ones, an effect that increases for weaker lines, evidencing the presence of underlying stellar absorption in these regions. As with the Carina region, we include the combined spectra M8 Reg = M8-E + M8-W and M20 Reg = M20-N + M20-S, obtained by adding the corresponding fluxes λ to λ . For M8 Reg, the results are consistent with $r \approx 1$ within the uncertainties, however for M20 Reg we obtain that $r \approx 1.2$ for Hδ (see Fig. 2c). For clarity, we include only the errors of M8 Reg and M20 Reg. Finally, Figs. 1d and 2d show the corresponding plots for our 4 RCW objects for those Balmer lines that could be measured. Their corresponding exciting stars are: O6 V (RCW6), O6 V (RCW60), O6 I (RCW107), and O8.5 V (RCW110). For the sake of clarity, we show only the

error bars for RCW60 Reg. As can be seen from Fig. 2d, for RCW6 and RCW60 Reg, $r > 1$ for H δ above our assigned uncertainty of $\pm 10\%$.

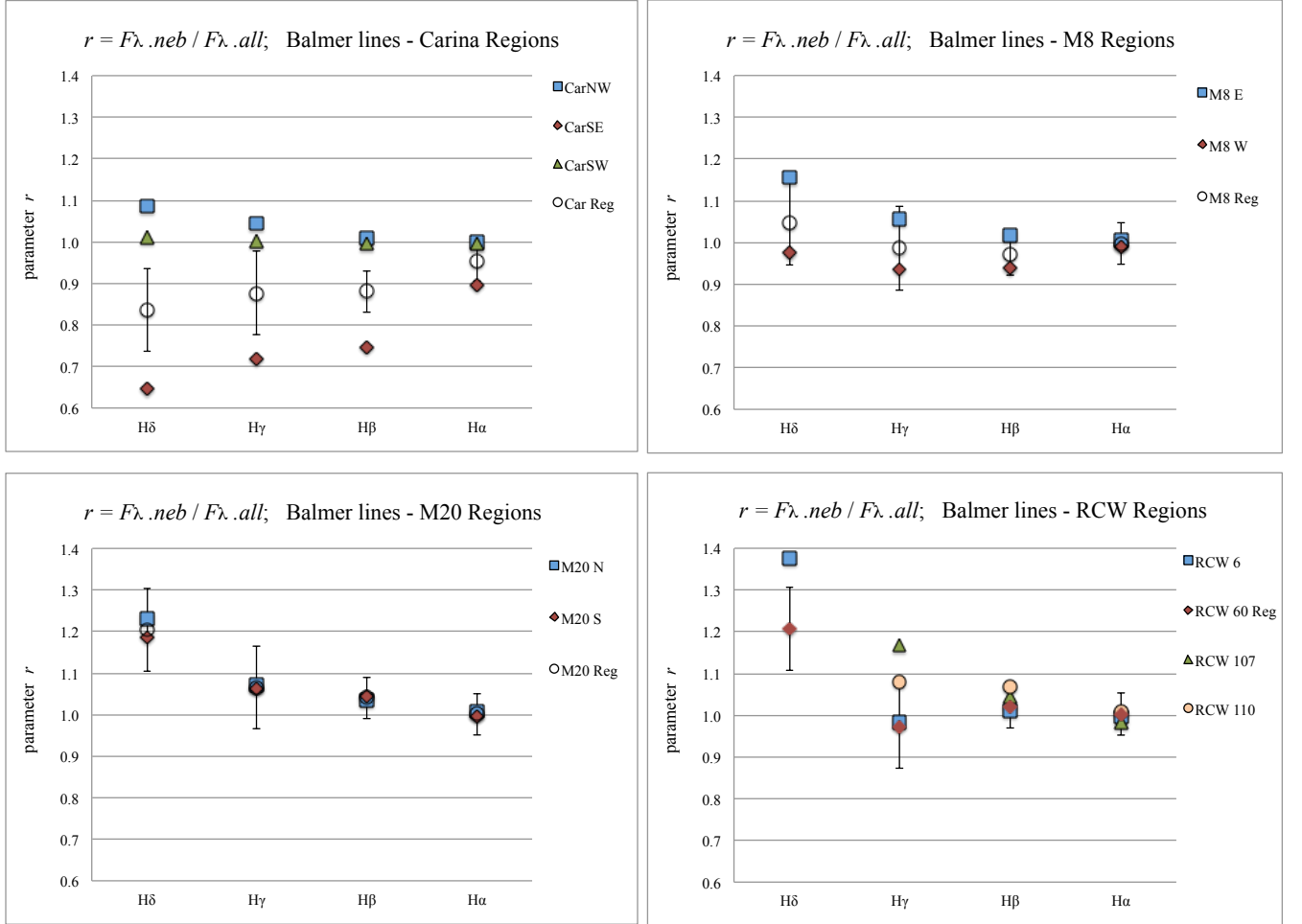


Fig. 2a – 2d. Observed parameter $r = F_{\lambda}^{.neb} / F_{\lambda}^{.all}$ for the bright Balmer lines for our sample objects: a) Carina regions, b) M8 regions, c) M20 regions and d) RCW objects.

3.2.2 He I lines

Following the same approach as before, in Figs. 3a – 3d we present the behavior of the brightest well-identified HeI lines measured in our sample objects. We ordered the lines from faintest to strongest, from left to right, and have assigned errors bars with the same criteria as defined for the Balmer lines above. For simplicity, we show only the error bars for the integrated spectra (Car Reg, M8 Reg, M20 Reg, and RCW60). For most of the regions, except for the CarSE region (and consequently, Car Reg), our parameter r is consistent with $r \approx 1$ for most of the Helium lines, except for $r_{\lambda 4026} \approx 1.6 \pm 0.5$ in CarNW, which may be due to observational errors being this a faint line. The contribution of η Car at these HeI wavelengths is due in part to some HeI lines and to several FeII and [FeII] lines present in its spectrum. Thus, η Car's contribution may increase the brightest HeI lines ($\lambda 7065$, $\lambda 6678$ and $\lambda 5876$) by up to 40% if its contribution is not extracted from the integrated spectrum. Using the high-resolution

spectra of η Car presented by Damineli et al. (1998), we found that several lines of the CarSE.*all* spectrum are contaminated by emission arising in η Car: HeI λ 4922 is contaminated by a permitted FeII line; HeI λ 6678 is the result of a HeI narrow line plus a broad stellar component; HeI λ 7281 is affected by errors due to sky subtraction; HeI λ 4026 has no emission reported in the η Car spectrum!; HeI λ 4471 is blended with a [FeII] line at this wavelength; HeI λ 5876 is affected by a narrow and a broad stellar emission feature and finally, HeI λ 7065 is also affected by a narrow and a broad stellar emission feature from η Car. In conclusion, the *.all* spectra of an extragalactic HII region should be examined carefully to take into account the possible HeI contribution due to possible embedded LBV stars to avoid an overestimation of the derived nebular He abundances. For M8 most of the HeI lines are consistent with $r \approx 1$, however for M20, the HeI λ 4471 seems to be overestimated in the *.neb* spectra with respect to the *.all* spectra.

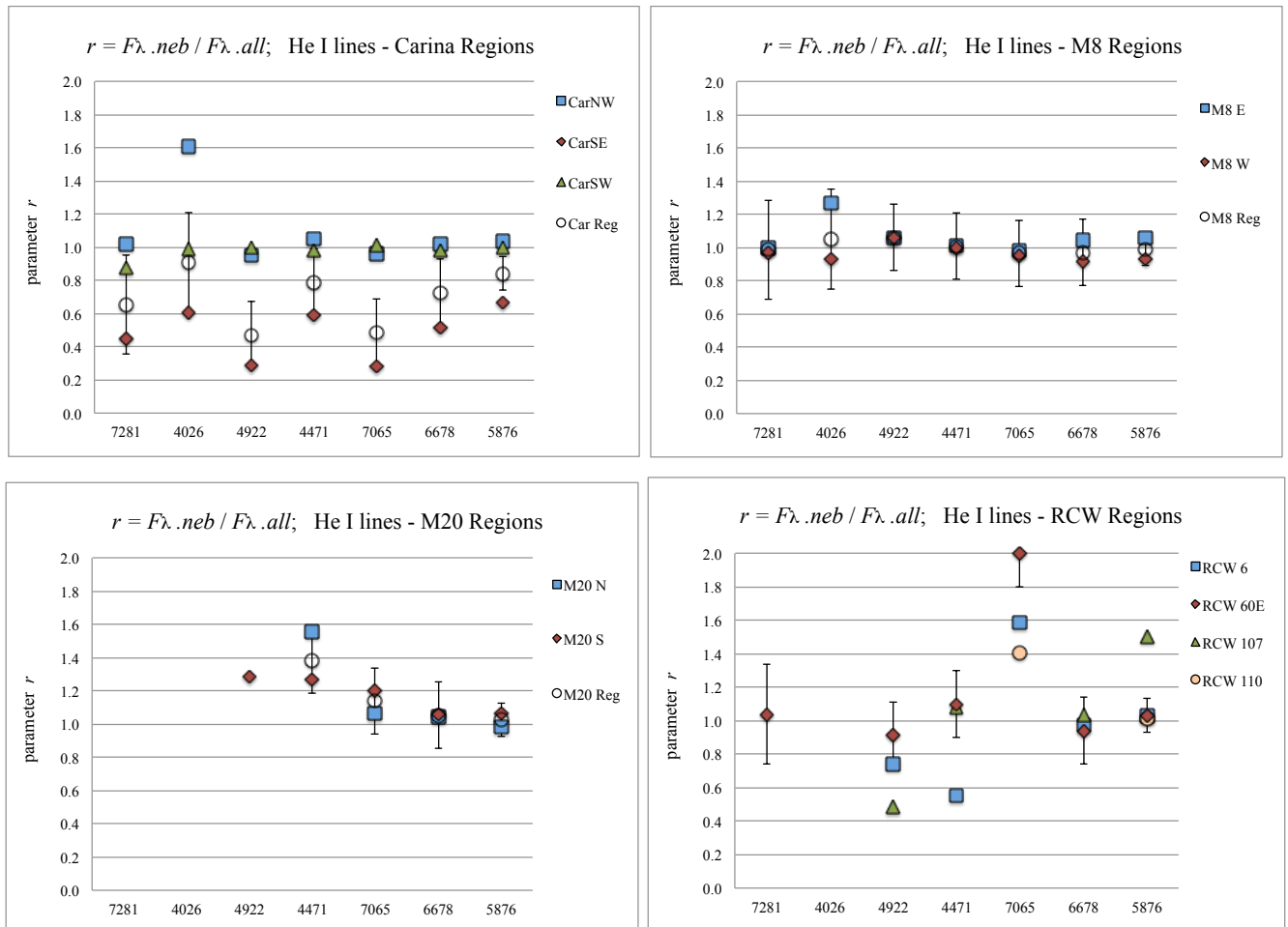


Fig. 3a – 3d. Observed parameter $r = F_{\lambda}^{neb} / F_{\lambda}^{all}$ for HeI lines for our sample objects: a) Carina regions, b) M8 regions, c) M20 regions and d) RCW objects.

3.2.3 Paschen lines

Figs. 4a – 4d show similar plots for the well-identified Paschen lines in the Carina, M8 and M20 regions. As with the Balmer lines, we have assigned an error to the r parameter according to the corresponding line intensities. For simplicity, we indicate the error bars only in the integrated spectra. These lines have a larger uncertainty because many of them fall in a part that is severely affected by the process of sky-subtraction. The spectrum of η Car is evident in the CarSE spectra and therefore in the Car Reg spectrum, with an average r value around $\langle r \rangle \approx 0.8$. For the CarSW region, the effect is in the opposite direction, with r values larger than 1, suggesting the presence of the Pa lines in absorption in the embedded B stars encompassed in this region. For CarNW, there is not an important stellar absorption effect on the Paschen lines, neither for M8 nor M20, except for the Pa17 $\lambda 8467$ and Pa15 $\lambda 8545$ lines, which have a large uncertainty.

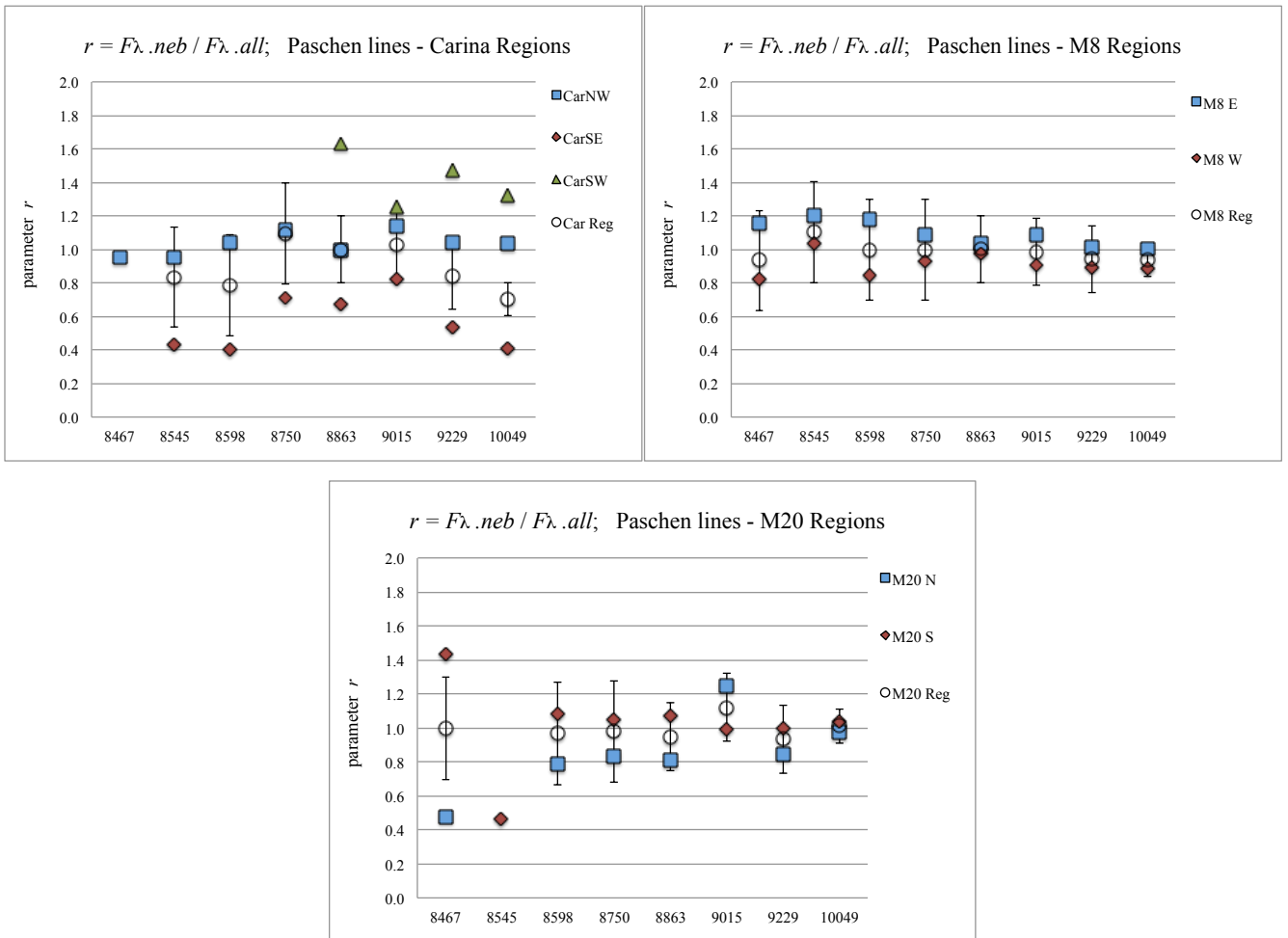


Fig. 4a – 4c. Observed parameter $r = F\lambda_{.neb} / F\lambda_{.all}$ for the Paschen lines for our bright objects: a) Carina regions, b) M8 regions, and c) M20 regions.

3.2.4 Forbidden lines

As before, Figs. 5a – 5d show our r plots for a set of well-identified forbidden lines. We have ordered the lines from faint to strong, from left to right, and have grouped them by ion, and show the corresponding error only for the further integrated spectra. As expected, the average parameter r for this set of lines for each of our objects is $\langle r \rangle \approx 1$. Only the CarSE (and Car Reg) spectrum presents some deviations beyond the assigned errors. A comparison of the selected forbidden lines with the spectra of η Car reported by Damineli et al. (1998) give the following results:

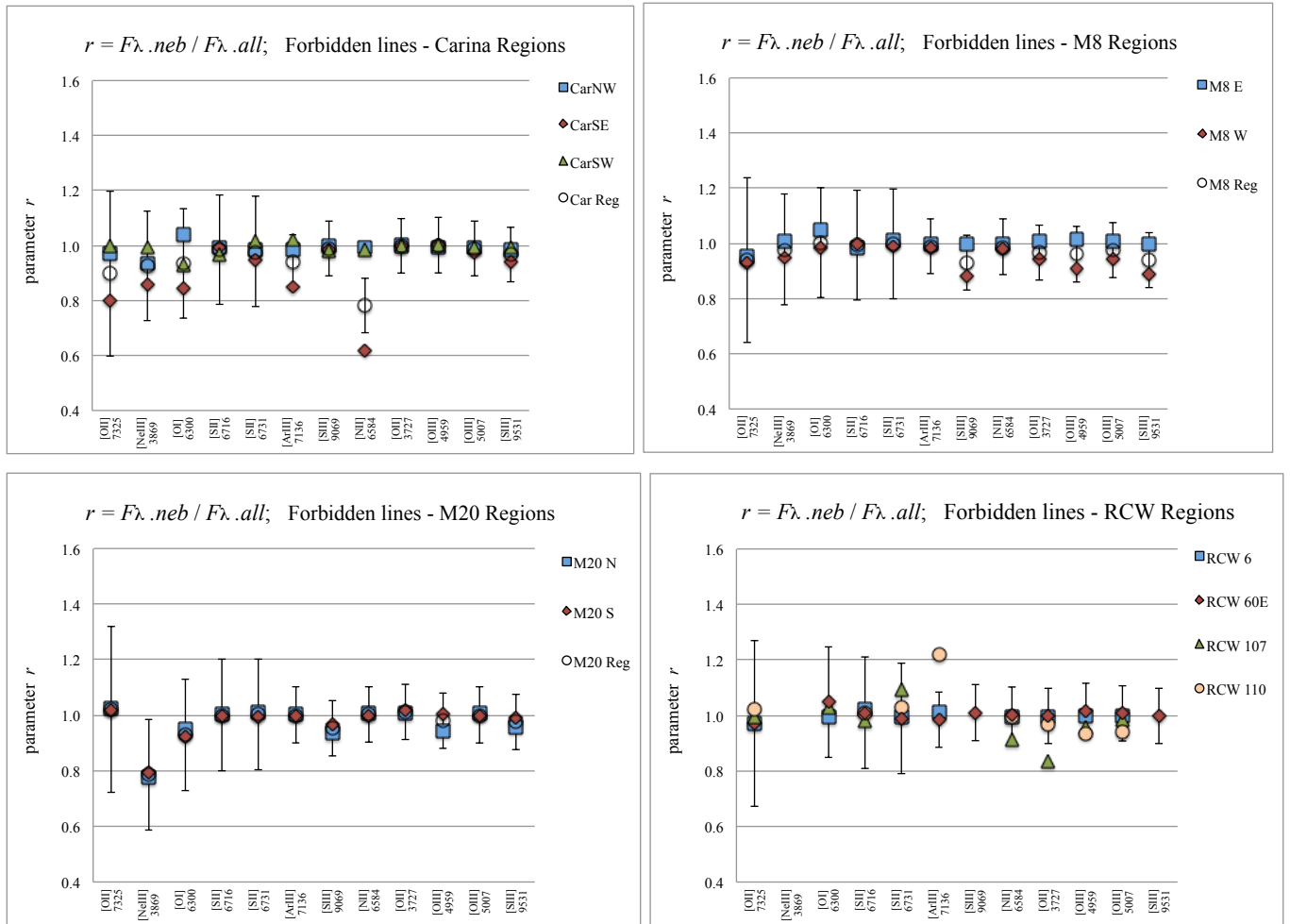


Fig. 5a – 5d. Observed parameter $r = F_{\lambda.\text{neb}} / F_{\lambda.\text{all}}$ for forbidden lines for our sample objects: a) Carina regions, b) M8 regions, c) M20 regions and d) RCW objects.

[OI] $\lambda 6300$ is weakly present in the η Car spectrum, and is uncertain due to the process of sky-subtraction; [OII] $\lambda 3727$ is not present; [OII] $\lambda 7325$ is not covered by Damineli et al. and it is also uncertain due to sky-subtraction; [OIII] $\lambda 4959$ and [OIII] $\lambda 5007$ are *not* present but there are faint [FeII] and [FeIII] lines at these wavelengths, respectively; [NII] $\lambda 6584$ is strong and broad, and is highly blended with very strong and broad H α ; [NII] $\lambda 5755$ is strong and narrow; [NI] $\lambda 5200$ is not

present but it coincides with a narrow permitted FeII line; [SII] $\lambda 6716$ and $\lambda 6731$ are weakly present; [SIII] $\lambda 9069$ and [SIII] $\lambda 9531$ are not reported and are uncertain due to the process of sky-subtraction; [ArIII] $\lambda 7136$ is weakly present; and [NeIII] $\lambda 3869$ is present and narrow. In summary, most forbidden lines remain unaffected in the integrated spectra within the uncertainties. However, for the CarSE and Car Reg spectrum, the nitrogen lines are overestimated by as much as 30% if the stars are not taken into account. As with the HeI lines, this stellar contribution should be taken into account when estimating the N abundance of unresolved giant HII regions. In Fig. 1 of Appendix II we present similar plots of our r parameter for a wider set of forbidden lines.

3.3. Effects of the stellar spectra on reddening and underlying absorption equivalent widths

3.3.1 Observed lines fluxes and equivalent widths

One of the main motivations for this work is to study the effect that the stellar spectra has on the integrated spectra of gaseous nebulae. This is particularly important in the case of unresolved giant extra-galactic HII regions (GEHRs), starburst galaxies (SB), HII galaxies (HIIGs) and blue compact galaxies (BCGs), where individual stars cannot be spatially resolved in most cases. Since the last four decades there have been several works aimed to derive the physical parameters that characterize the stellar population in GEHRs and HIIGs, including, the initial mass function, its upper and lower mass limits, the age and duration of the star formation bursts, the total cluster stellar mass, the proportion of different stellar populations, e.g. the WR/O ratio, etc. In order to constrain these parameters, it is necessary to have an accurate knowledge of the physical conditions of the emitting gas including the reddening, the electron temperature and electron density, the ionization parameter and the chemical composition. These nebular parameters are derived from the analysis of the integrated nebular spectra, usually affected by underlying stellar continuum, stellar absorption lines, and by stellar emission features in the case of young bursts ($\sim 3 - 5$ Myr) containing an appreciable fraction of young massive stars with strong winds, as WR stars or LBV stars. Other observational evidence useful to constrain the stellar population includes: *i*) the observed UV-NIR continuum (specially in the nuclear region of HIIGs); *ii*) the detection of stellar features, either in emission, as the so called WR optical bumps (around $\lambda 4640$ and $\lambda 5810$) observed in WR galaxies and “WR regions” (Conti, 1991); *iii*) stellar features in absorption, as the Calcium II Triplet lines ($\lambda 8498$, $\lambda 8542$ and $\lambda 8662$, referred as CaT lines), which indicate the presence of an older stellar population, and *iv*) the profile of HeI lines and high Balmer lines, which are the most affected by the underlying stellar absorption. The presence of faint [FeII] and [FeIII] emission lines in the integrated spectrum may be also an indication of “ η Car”-like stars embedded within the emitting volume.

As we saw in the previous section, the underlying stellar spectra in our observed nebulae have a noticeable effect in the observed spectra, especially for the high-Balmer lines and in some HeI lines. The effect of η Car on the CarSE or Car Reg spectra is probably *too* large as compared to the actual proportion of gas and stars in normal GEHRs and HIIGs. That is, for the CarSE region, the contribution of η Car (and the other O stars) at $\lambda 4861 \text{ \AA}$ with respect to the nebular emission at H β is probably too large as compared with regular GEHRs (eg. R136/30 Dor in the LMC, Conti, 2000). The emitting volumes are also very different: for the whole Carina region we estimated a lower limit of 60 – 90 pc (Chapter IV), considerable smaller than the estimated size of GEHRs or SBs nucleus, e.g. ~ 250 pc for the GEHR NGC 2363 (González-Delgado et al. 1994), ~ 500 pc for region A in the SB NGC 7714, or ~ 1 kpc for the nuclear region of NGC 7714 (González-Delgado et al. 1995). An additional consideration that must be taken into account when comparing the observed equivalent width at H β (W_β) of GEHRs with theoretical predictions is presence of a considerable λ -dependent component of scattered light in the observed continuum as discussed later in Chapter VI and Appendix IV.

In Tables 1a – 1b we present the *.all* and *.neb* Balmer line intensities F_λ and equivalent widths W_λ for Carina, M8 and M20 regions. We will use these parameters to derive simultaneously the logarithmic reddening constant $c(\text{H}\beta)$ and the underlying stellar absorption equivalent width W_{abs} .

Table 1a. Carina *.neb* and *.all* observed H I line fluxes F_λ and equivalent widths W_λ ^a

λ	ID	F_λ <i>.neb</i>	W_λ <i>.neb</i>	F_λ <i>.all</i>	W_λ <i>.all</i>	F_λ <i>.neb</i>	W_λ <i>.neb</i>	F_λ <i>.all</i>	W_λ <i>.all</i>
CarNW					CarSE				
3771	H11	0.0321	0.96	0.0264	0.56	0.0413	1.33	0.0850	1.61
3798	H10	0.0351	1.18	0.0189	1.20	0.0551	1.63	0.105	1.60
3835	H9	0.0506	2.06	0.0298	0.70	0.0612	2.72	0.137	2.80
3889	H8+	0.281	9.11	0.244	4.15	0.300	9.72	0.398	7.24
3970	H ϵ +	0.260	9.21	0.209	3.70	0.290	10.3	0.422	8.69
4102	H δ	0.404	14.3	0.372	6.93	0.515	17.8	0.799	15.4
4340	H γ	0.925	38.0	0.885	19.0	1.08	44.3	1.51	33.5
4861	H β	2.30	123	2.28	61.0	2.74	134	3.67	85.9
6563	H α	13.0	856	13.0	477	15.4	779	17.2	374
CarSW					Car Reg				
3771	H11	0.0267	1.80	0.0245	1.31	0.100	1.31	0.136	0.93
3798	H10	0.0414	--	0.0390	1.89	0.132	1.59	0.163	1.01
3835	H9	0.0791	5.74	0.0723	3.94	0.191	2.93	0.239	1.91
3889	H8+	0.228	15.8	0.220	11.7	0.808	10.5	0.862	6.21
3970	H ϵ +	0.238	17.9	0.226	12.4	0.787	10.9	0.857	6.99
4102	H δ	0.343	27.0	0.340	19.2	1.26	18.2	1.51	12.0
4340	H γ	0.719	63.7	0.718	47.0	2.73	45.9	3.11	37.8
4861	H β	1.78	183	1.78	138	6.81	141	7.73	82.0
6563	H α	9.94	832	9.99	671	38.4	816	40.2	464

^a Line fluxes in $10^{-11} \text{ erg s}^{-1} \text{ cm}^{-2}$, obtained measuring the total flux under the line above a given continuum defined visually. Entrance slit $\Omega_{\text{slit}} = 6.5' \times 5''$. Equivalent widths in \AA . H8+ includes He I, and H ϵ + includes [Ne III].

As mentioned in the previous chapter, the measured line fluxes have an intrinsic uncertainty depending on how they are measured. We explored this by measuring the line fluxes with two different methods. First, we used the IRAF routine *splot* to measure the line flux below the line profile and above a continuum level by eye inspecting the adjacent continuum at both sides of the line. We will call these the $F\lambda^{\text{total}}$ fluxes. The second method was to measure the line flux by fitting a Gaussian to the line profile, defining the continuum level as before; we will call these $F\lambda^{\text{gauss}}$ fluxes. We measured the Balmer line fluxes and we found that $F\lambda^{\text{total}}$ and $F\lambda^{\text{gauss}}$ agree within the uncertainties for lines brighter than, say H δ . However, for fainter lines, e.g. H9, H10 and H11, we found differences up to 20% between $F\lambda^{\text{total}}$ and $F\lambda^{\text{gauss}}$, with no systematic trend among our observed regions. In the case of the *.all* spectra, these differences became larger, especially for the CarSE region, due to the wide wings present in the Balmer lines of the η Car spectrum, yielding $(F\lambda^{\text{total}}/F\lambda^{\text{gauss}}) = 1.3$ at H γ , and $(F\lambda^{\text{total}}/F\lambda^{\text{gauss}}) = 1.1$ for the whole Balmer Car Reg spectrum. The *.neb* $W\lambda^{\text{total}}$ and $W\lambda^{\text{gauss}}$ also agree within a few percent, except for the fainter Balmer lines, for which $(W\lambda^{\text{total}}/W\lambda^{\text{gauss}}) \approx 1.1$. Note that Zaritsky, Kennicutt & Huchra (1994) also reported differences in the 3 – 5% range between their $F\lambda^{\text{total}}$ and $F\lambda^{\text{gauss}}$ line fluxes for a set of HII regions in a sample of spiral galaxies. In the present work we have adopted the line fluxes measured using the first method.

Table 1b. M8 and M20 *.neb* and *.all* observed Balmer line fluxes $F\lambda$ and equivalent widths $W\lambda$.^a

λ	ID	$F\lambda$ <i>.neb</i>	$W\lambda$ <i>.neb</i>	$F\lambda$ <i>.all</i>	$W\lambda$ <i>.all</i>	$F\lambda$ <i>.neb</i>	$W\lambda$ <i>.neb</i>	$F\lambda$ <i>.all</i>	$W\lambda$ <i>.all</i>	$F\lambda$ <i>.neb</i>	$W\lambda$ <i>.neb</i>	$F\lambda$ <i>.all</i>	$W\lambda$ <i>.all</i>
M8-E				M8-W				M8 Reg					
3771	H11	0.0562	3.87	0.0375	0.64	0.0661	8.43	0.0695	5.54	0.122	4.67	0.107	1.46
3798	H10	0.0942	6.81	0.0550	0.95	0.129	13.0	0.123	8.93	0.223	8.68	0.178	2.41
3835	H9	0.154	11.4	0.0884	1.55	0.203	18.7	0.213	14.2	0.357	13.9	0.301	4.05
3889	H8+	0.464	34.9	0.407	7.17	0.545	53.4	0.557	41.6	1.01	43.2	0.964	13.8
3970	H ϵ +	0.506	40.3	0.424	7.64	0.650	66.5	0.651	52.0	1.16	55.4	1.07	16.3
4102	H δ	0.660	53.5	0.572	11.0	0.839	100	0.862	71.7	1.50	75.5	1.43	23.0
4340	H γ	1.32	126	1.25	28.2	1.62	203	1.74	159	2.94	161	2.99	53.8
4861	H β	3.05	368	3.00	95.6	3.82	536	4.07	417	6.87	450	7.07	174
6563	H α	13.7	1640	13.7	680	16.7	2114	16.8	1800	30.4	1990	30.5	1080
M20-S				M20-N				M20 Reg					
3771	H11	0.0233	2.90	0.0146	0.74	0.0069	0.78	0.0078	0.60	0.0302	2.11	0.0225	0.89
3798	H10	0.0305	3.78	0.0117	0.58	0.0129	1.34	0.0081	0.44	0.0434	3.05	0.0198	1.31
3835	H9	0.0500	6.15	0.0249	1.24	0.0176	1.86	0.0080	0.43	0.0676	4.89	0.0329	2.27
3889	H8+	0.132	16.5	0.103	5.10	0.0729	7.54	0.0610	3.21	0.205	13.1	0.164	5.30
3970	H ϵ +	0.115	14.1	0.0856	4.28	0.0609	6.27	0.0406	2.13	0.176	11.5	0.126	3.71
4102	H δ	0.209	27.1	0.176	9.48	0.132	14.4	0.107	6.01	0.341	21.4	0.283	7.90
4340	H γ	0.437	65.9	0.411	25.7	0.293	38.0	0.274	17.7	0.730	50.4	0.685	21.2
4861	H β	1.03	200	0.995	82.7	0.694	110	0.670	54.6	1.73	150	1.66	68.7
6563	H α	4.40	1040	4.42	557	3.62	726	3.58	361	8.02	799	8.01	452

^a Line fluxes in 10^{-11} erg s^{-1} cm^{-2} , obtained measuring the total flux under the line above a given continuum defined visually. Entrance slit $\Omega_{\text{slit}} = 6.5'' \times 5''$. Equivalent widths in \AA . H8+ includes He I, and H ϵ + includes [Ne III].

3.3.2 Determination of $c(\text{H}\beta)$ and W_{abs}

As commented in the previous section, the presence of an underlying stellar population in the integrated spectra of giant HII regions may affect the observed Balmer decrement, and therefore, may affect the derived reddening, which also has consequences in the derived physical conditions of the emitting gas. Following the formalism proposed by McCall, Rybski & Shields (1985; MRS85), as presented by Izotov, Thuan & Lipovetsky (1994), we estimated iteratively the logarithmic reddening constant $c(\text{H}\beta)$, and the equivalent width in absorption due to the underlying stellar population W_{abs} , for our Carina, M8 and M20 regions. The relation between the de-reddened flux ratios (I_{λ}/I_{β}), the observed flux ratios (F_{λ}/F_{β}), the logarithm reddening correction constant $c(\text{H}\beta)$, the extinction law $f(\lambda)$, and the stellar equivalent width in absorption W_{abs} , is:

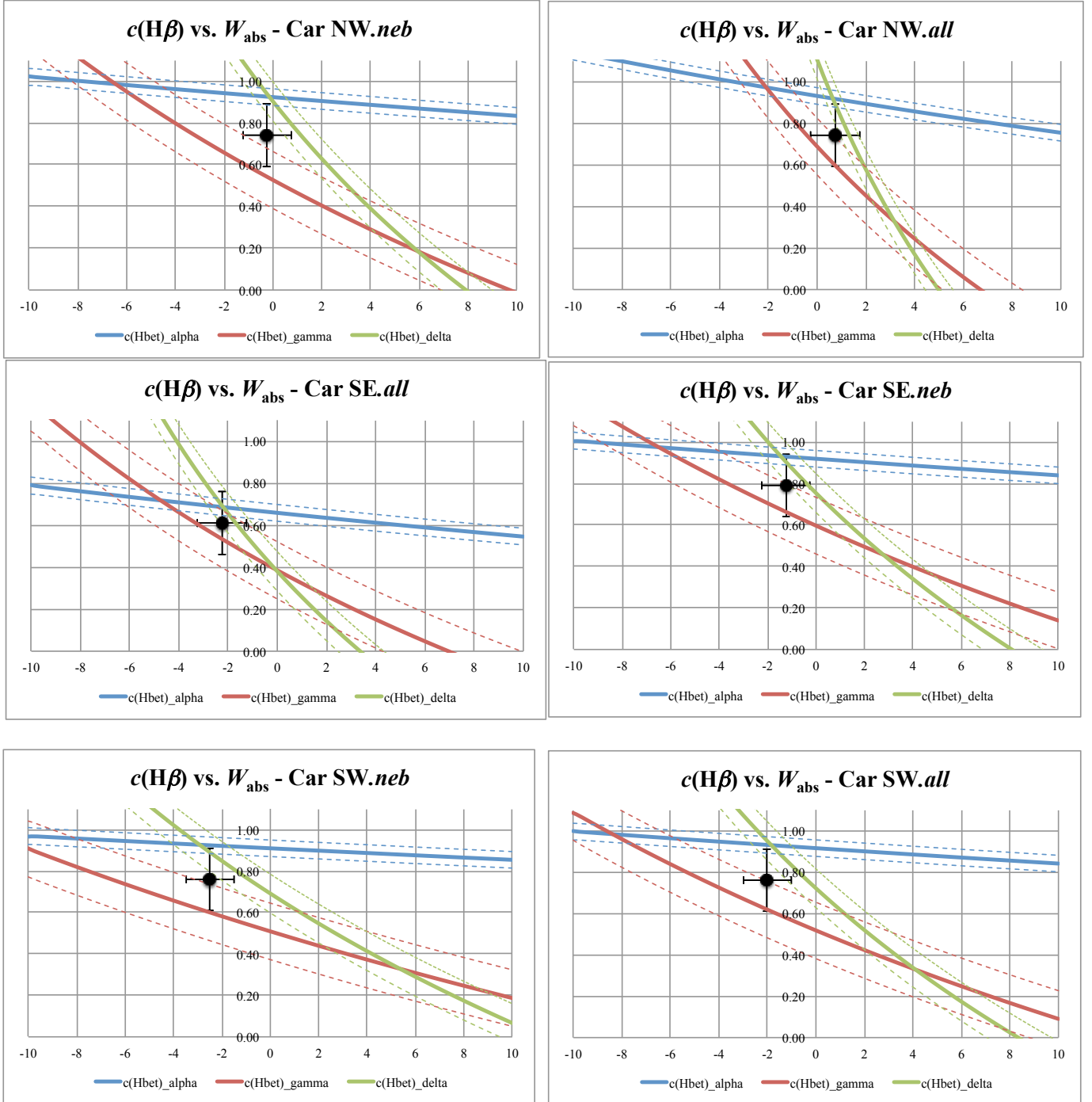
$$\left(\frac{I_{\lambda}}{I_{\beta}}\right) = \left(\frac{F_{\lambda}}{F_{\beta}}\right) \times 10^{f(\lambda)c(\text{H}\beta)} \frac{(1 + W_{\text{abs}}/W_{\lambda})}{(1 + W_{\text{abs}}/W_{\beta})} \quad (1)$$

where W_{λ} and W_{β} are the nebular emission equivalent widths at λ and at $\text{H}\beta$, respectively. The above equation, assumes that the underlying stellar absorption equivalent width W_{abs} , is the same for the first members of the Balmer series, as supported by stellar models (Olofsson, 1995). In the case that $W_{\text{abs}} = 0$, we obtain the classical expression for de-reddening nebular spectra ignoring the underlying stellar absorption.

We used the observed fluxes F_{λ} and observed equivalent widths W_{λ} given in Tables 1a – 1b above. We assumed Storey & Hummer (1995; SH95) case B recombination ratios at 10 kK, and Seaton (1979; S79) extinction law. From Eq. (1) above, we can solve for $c(\text{H}\beta)$ as function of W_{abs} for different line ratios ($\text{H}\alpha/\text{H}\beta$, $\text{H}\gamma/\text{H}\beta$ and $\text{H}\delta/\text{H}\beta$). We decided to use only these four lines (and not the higher members of the series) since they have the smaller line flux errors and are not blended.

In Fig. 6a we present our solutions for CarNW, CarSE, CarSW and Car Reg. We present both the *.neb* and *.all* results. In Figs. 6b and 6c, we present similar plots for the integrated M8 Reg and M20 Reg regions only. For an ideal HII region, the three curves should yield the same solution. We verified this using the spectra of several HII regions in the galaxy NGC318 (courtesy of M. Peña). However, as we can see from our plots, for these *integrated spectra*, covering a wide range of lines of sight, we have a wide spread revealing *a)* the uncertainties in the measured line ratios and *b)* possible variations of extinction across the face of the scanned nebulae, like dust lanes crossing the slit during the scan, or cloud condensations, like the Hourglass in the center of M8, know to have a higher extinction than its surroundings (Esteban et al. 1999). From these plots we derived values for $c(\text{H}\beta)$ and W_{abs} that best fit all the curves simultaneously and show our result as a black dot. The curve's uncertainties shown were

estimated considering the line flux assigned errors. It is worth mention that the line equivalent widths in emission are *extremely* sensitive to the adopted continuum, which was assigned visually, with uncertainties of about 10 – 20%. The position of the black dot in Fig. 1a corresponds to the best compromise for all three lines. From these plots, we assigned uncertainties of ± 0.15 for $c(H\beta)$ and ± 1.0 Å for W_{abs} . We summarize our results in Table 2 below.



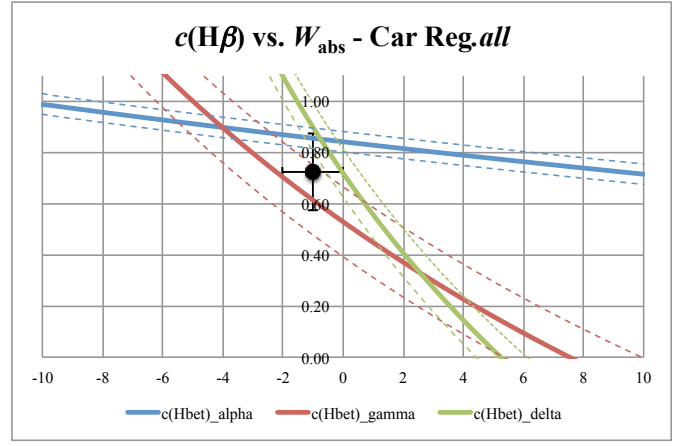
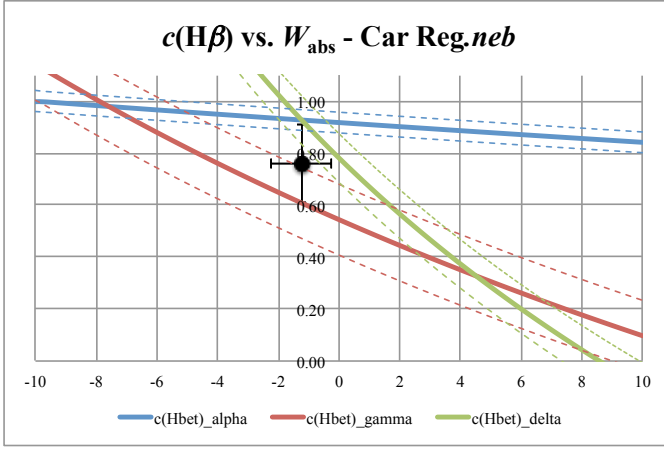


Figure 6a. $c(H\beta)$ vs. W_{abs} solutions for our CarNW, CarSE, CarSW and Car Reg regions, for the *.neb* spectra (left column) and *.all* spectra (right column), using Eq. (1). The solid lines are derived from the values reported in Table 1a. The dashed lines consider uncertainties of 4% for the F_{α}/F_{β} ratio and 7% for the F_{γ}/F_{β} and F_{δ}/F_{β} ratios.

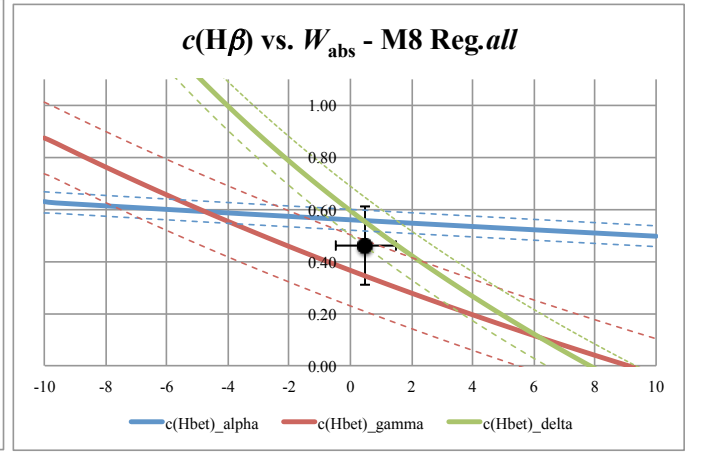
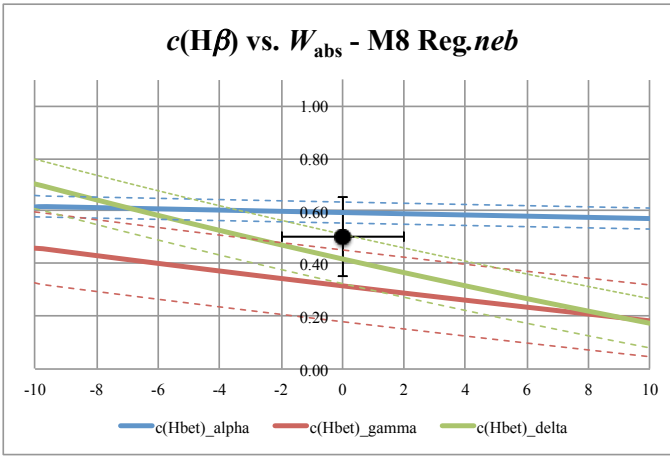


Figure 6b. As Fig. 6a for the M8 Reg.

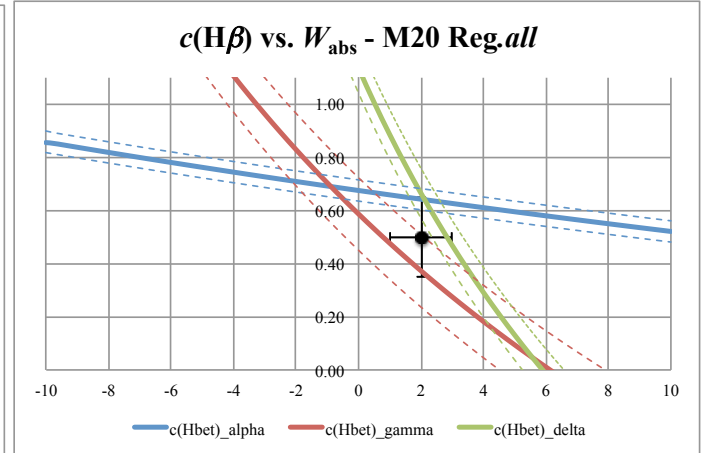
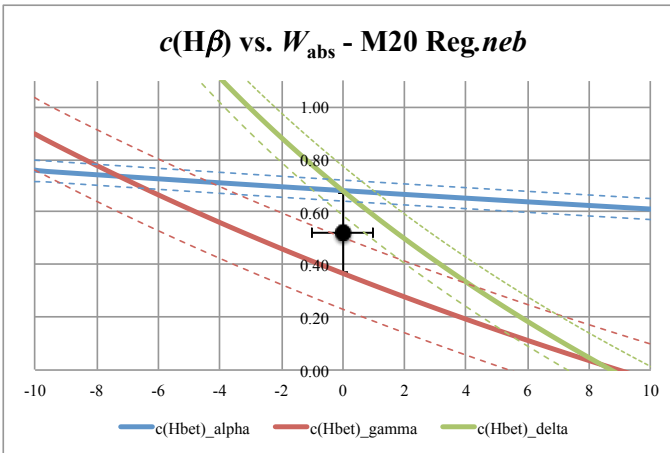


Figure 6c. As Fig. 6a for M20 Reg.

Table 2. Derived values of $c(H\beta)$ and W_{abs} from Eq. (1)

	$c(H\beta) \pm 0.15$		$W_{\text{abs}} \pm 1.0 \text{ \AA}$	
	<i>.neb</i>	<i>.all</i>	<i>.neb</i>	<i>.all</i>
CarNW	0.74	0.74	-0.25	0.75
Car SE	0.79	0.61	-1.2	-2.2
Car SW	0.76	0.76	-2.5	-2.0
Car Reg	0.76	0.72	-1.2	-1.0
M8 - E	0.50	0.50	--	1.0
M8 - W	0.51	0.41	--	0.0
M8 Reg	0.50	0.46	--	0.50
M20 - S	0.42	0.41	1.0	2.8
M20 - N	0.60	0.57	0.0	1.5
M20 Reg	0.52	0.50	0.0	2.0

As we can see from Table 2, the $c(H\beta)_{.all}$ and $c(H\beta)_{.neb}$ agree within the uncertainties, although the *.all* value tends to be somewhat smaller than the *.neb* value. For CarNW.*all* we derived an underlying absorption equivalent width of $0.75 \pm 1.0 \text{ \AA}$ ($W_{\text{abs}} > 0$), which is expected, since this regions is dominated by early O stars. For CarNW.*neb* we derive an underlying stellar equivalent width consistent with $W_{\text{abs}} = 0$. For CarSE.*all*, CarSW.*all* and Car Reg.*all* we derived $W_{\text{abs}} < 0$, evidencing the emission of η Car (in CarSE) and HD93162 (WN6ha in CarSW). The corresponding *.neb* values are also negative probably due to scattered light in their spectra. The M8-E.*all* and M8-W.*all* are consistent with $W_{\text{abs}} = 0.1 - 1.0 \pm 1.0 \text{ \AA}$. On the other hand, the M8-E.*neb* and M8-W.*neb* spectra did not converged to a reasonable value of W_{abs} and their spectra needs to be reviewed. For M20, there are variations of reddening between M20-S and M20-N, in agreement with previous determinations found in the literature (eg. Lynds & O'Neil 1982). Their spectra indicate $W_{\text{abs}} = 2.0 \pm 1.0 \text{ \AA}$ in absorption ($W_{\text{abs}} > 0$), what is consistent with what has been derived (or assumed!) for GEHRs. The classical correction used in many works is $W_{\text{abs}} = 2 \text{ \AA}$, as estimated by McCall, Rybski & Shields (1985), More recently, Kobulnicky et al. (1999) studied a sample of spiral galaxies and found that $W_{\text{abs}}(H\beta) = 1 - 6 \text{ \AA}$, with a mean of $3 \pm 2 \text{ \AA}$, while Moustakas & Kennicutt (2006) found $W_{\text{abs}}(H\beta) = 4.4 \pm 0.6$ and $W_{\text{abs}}(H\alpha) = 2.8 \pm 0.4$ for a large sample of nearby galaxies.

3.5 Conclusions

In this chapter we present results showing the effects produced by the spectra of the exciting stars on the integrated nebular spectra. These effects depend on the spectral types and luminosities of the embedded stars. We found that for typical early O stars, the underlying stellar absorption may decrease the Balmer lines by as much as 10% at $H\delta$. At the other hand, if the emitting volume contains WR stars or peculiar LBVs, then the underlying stellar *emission* may increase the Balmer lines by as much as 15% at $H\delta$.

These results may have consequences in the derived reddening and derived chemical composition of the emitting regions (see Chapters IV and V).

The helium lines are not affected for most of the regions within the uncertainties. However, for the CarSE region (which contains η Car), and therefore, for the further integrated Car Reg spectrum, the brightest HeI $\lambda 6678$ and HeI $\lambda 5876$ are overestimated by as much as 20% if the stars are not removed from the integrated spectra. The forbidden lines are not affected by the underlying stellar spectra, except for the CarSE and Car Reg spectra, in which the [NII] $\lambda 6584$ and [NII] $\lambda 5755$ line fluxes appear overestimated by about 20% in the *.all* spectra with respect to the *.neb* spectra.

We used a procedure to derive simultaneously the logarithmic reddening correction constant $c(\text{H}\beta)$, and the underlying stellar absorption equivalent width W_{abs} from our *.neb* and *.all* spectra. We found that $c(\text{H}\beta)_{\text{neb}}$ and $c(\text{H}\beta)_{\text{all}}$ agree within the uncertainties, although the *.all* values tend to be somewhat smaller (0.04 dex) than the *.neb* ones. The regions that include early O stars, as CarNW, M8 and M20, suggest an underlying equivalent width in absorption, $W_{\text{abs}} = 1 - 2 \pm 1.0 \text{ \AA}$. However, for CarSE (which hosts η Car) and CarSW (which includes the star HD93162, WN6ha), our *.all* spectra suggest a *negative* underlying equivalent width, $W_{\text{abs}} = -2.0 \pm 1.0 \text{ \AA}$ indicating that it appears in emission.

Chapter IV. Carina physical conditions and element abundances

4.1. Introduction

In this chapter we present the procedure used to obtain the intrinsic line fluxes of our 3 Carina regions, needed to derive their physical conditions and ionic and total abundances. We calculate these parameters both with the *.all* and *.neb* spectra, in order to study the effect of the stellar spectra. In Sec. 4.2 we derive the extinction law for the Carina region and compare it with previous determinations. In Sec. 4.3 we calculate the physical conditions (n_e and T_e) for the plasma. In Sec. 4.4 we derive Carina ionic abundances ignoring temperature fluctuations and in Sec. 4.5 we estimate the total abundances (O, N, S, Ne and Ar) using the latest ionization correction factors. In Sec. 4.6 we calculate the Balmer electron temperature and use it along with the electron temperatures from forbidden lines, to derive the ionic and total abundances considering temperature fluctuations. Finally, in Sec. 4.7 we summarize our main results.

4.2 Extinction law and de-reddened fluxes

The interstellar extinction toward the Carina Nebula has been studied since the early 70's and it is now accepted that the Carina region has an anomalous and variable extinction law (e.g. Pagel 1969, Herbst 1976, Smith 1987, Tapia et al. 1988, Thé & Graafland 1995, Tapia et al. 2003, Povich et al. 2011). The average ratio of total to selective extinction $R_V = A_V/E_{B-V} \approx 4$, but it varies from 2.6 to 5.9 for different stars/zones in the region. Besides the effects of the total interstellar and internal extinction, the observed Balmer decrements may also be affected by shocks within the region, especially for our CarSE region which contains η Car. The reported expansion velocities from *HST* observations with high spatial and spectral resolution for the “ η Car object”, including the homunculus, are in the range ~ 40 – 50 km/s (Davidson et al. 1997). There are also structures closer to the central object with much higher velocities, ~ 700 km/s, (Hester et al. 1991). However, our observed regions cover ~ 7 arcmin² each, so any shocked gas near the hot stars will be diluted in our wide-angle integrated spectra.

An accurate knowledge of the extinction law and the value of the R_V parameter is needed to calculate the distance and luminosity of the cluster stars, and in order to obtain the intrinsic emission lines fluxes needed to derive the physical conditions and element abundances of the corresponding HII region. We started de-reddening our Carina observed spectra using the standard extinction law given by Cardelli, Clayton, & Mathis (1989; CCM89) but obtained Balmer and Paschen “corrected” decrements quite deviant from the theoretical ones, especially for the high Balmer and low Paschen lines. Therefore, we decided to derive our own extinction law by fitting the observed Balmer and Paschen line decrements, which allows us to de-redden the whole spectra. Finally, we derive the usual

extinction law $f(\lambda)$ for our Carina regions normalizing our extinction law at $H\alpha$ to that of CCM89. We estimate then the logarithmic reddening constant $c(H\beta)$, the $B - V$ color excess E_{B-V} and the R_V parameter, and compare our results with other determinations.

For simplicity, in what follows we will adopt the notation $F_\lambda/F_\beta = F(\lambda)/F(H\beta)$. Using the observed Balmer and Paschen line decrements, we constructed the function $g(\lambda)$, defined as

$$g(\lambda) = -\log \left[\frac{\left(F_\lambda / F_\beta \right)_{\text{obs}}}{\left(F_\lambda / F_\beta \right)_{\text{theo}}} \right] \quad (1)$$

where $(F_\lambda/F_\beta)_{\text{theo}}$ are the theoretical line ratios and $(F_\lambda/F_\beta)_{\text{obs}}$ are the observed line ratios corrected for atmospheric extinction. The theoretical values were taken from Storey & Hummer (1995; SH95), assuming case B recombination, with $T_e = 10^4$ K and $n_e = 10^2$ cm⁻³. Note that SH95 emissivities give the same HI line ratios (within 0.2%) as those given by Hummer and Storey (1987). We then interpolated this *observable* $g(\lambda)$ function to obtain the de-redden line fluxes with respect to $H\beta$ for any λ , $(F_\lambda/F_\beta)_0$, without the need of evaluating the reddening constant:

$$\log \left(F_\lambda / F_\beta \right)_0 = \log \left(F_\lambda / F_\beta \right)_{\text{obs}} + g(\lambda) \quad (2)$$

What is the relation between this $g(\lambda)$ function and the common extinction law $f(\lambda)$? By definition, the relation between the intrinsic flux at a given wavelength F_λ^0 , and the observed flux F_λ^{obs} , affected by an amount of total absorption of A_λ magnitudes is: $2.5 \log F_\lambda^0 = 2.5 \log F_\lambda^{\text{obs}} + A_\lambda$, which implies:

$$\log \left(F_\lambda / F_\beta \right)_0 = \log \left(F_\lambda / F_\beta \right)_{\text{obs}} + 0.4(A_\lambda - A_{H\beta}). \quad (3)$$

Assuming that the extinction is interstellar, the common extinction law is given by (Costero & Peimbert 1970; CP70):

$$f(\lambda) = \left(A_\lambda / A_{H\beta} \right) - 1, \quad (4)$$

which can be used to derive the intrinsic line ratios,

$$\log \left(F_\lambda / F_\beta \right)_0 = \log \left(F_\lambda / F_\beta \right)_{\text{obs}} + c(H\beta) f(\lambda), \quad (5)$$

where $c(H\beta)$ is the common logarithmic reddening constant at $H\beta$. We see that:

$$g(\lambda) = 0.4(A_\lambda - A_{H\beta}) = c(H\beta)f(\lambda), \quad (6)$$

where $f(H\beta) = 0$ and $f(\lambda \rightarrow \infty) = -1$. From the above equations, it is clear that,

$$c(H\beta) = 0.4A_{H\beta}, \quad (7)$$

$$R = \frac{f(V)+1}{f(B)-f(V)}, \text{ and} \quad (8)$$

$$E_{B,V} = \frac{2.5c(H\beta)}{R}[f(V)+1]. \quad (9)$$

$$\text{In general, we have that } E_{\lambda_1, \lambda_2} = 2.5c(H\beta)[f(\lambda_1) - f(\lambda_2)]. \quad (10)$$

To derive the amount of extinction at $H\beta$, A_β , we would need in principle a radio-continuum measurement (e.g. CP70). However, given that the extinction law for Carina between $H\alpha$ and $H\beta$ is not very different from the standard extinction law (Tapia et al. 1988), we normalized our $g(\lambda)$ function at $H\alpha$ to the value obtained from CCM89, that is, we assumed, $g(H\alpha) = c(H\beta) \times f(H\alpha)_{\text{CCM}}$, so that,

$$A_{H\beta} = g(H\alpha)/[0.4f(H\alpha)_{\text{CCM}}]. \quad (11)$$

With this A_β and our *observed* $g(\lambda)$ function, we derived an $f(\lambda)$ extinction law for each of the Carina regions, both with the *.neb* and *.all* spectra, using Eq. (6). The $f(\lambda)$ function was derived using IDL routines fitting our observed Balmer and Paschen decrements with a 5th-order polynomial in the variable $(1/\lambda)$, in μm^{-1} :

$$f(\lambda) = a_0 + a_1(1/\lambda) + a_2(1/\lambda)^2 + a_3(1/\lambda)^3 + a_4(1/\lambda)^4 + a_5(1/\lambda)^5. \quad (12)$$

In Table 1, we present the a_i coefficients used to compute $f(\lambda)$, as well as the total-to-selective extinction ratio $R_V = A_V/E_{B-V}$, obtained for each region.

In Tables 2a – 2c below, we present the *.all* and *.neb* derived extinction law for each Carina region, along with the de-reddened line fluxes relative to $H\beta$ derived using Eq. (5). We list also the derived $c(H\beta)$, and the total de-reddened $H\beta$ flux from our 5'' \times 6.6' slit. The uncertainty in our $f(\lambda)$ depends on the wavelength range, being larger toward both ends of the spectrum. For comparison, in Table 2a (CarNW) we also list the standard extinction law derived from CCM89, $f(\lambda)_{\text{CCM}}$, considering $R = 4.2$. The estimated line flux errors are (see Chapter III): $\sigma_F = 4\%$ if $(F_\lambda/F_\beta)_0 \geq 1.00$; $\sigma_F = 7\%$ if 1.00

$> (F_\lambda/F_\beta)_0 \geq 0.50$; $\sigma_F = 10\%$ if $0.50 > (F_\lambda/F_\beta)_0 \geq 0.10$; $\sigma_F = 15\%$ if $0.10 > (F_\lambda/F_\beta)_0 \geq 0.02$, and $\sigma_F = 20\%$ if $0.02 > (F_\lambda/F_\beta)_0$.

Table 1. Derived $f(\lambda)$ extinction law coefficients for the Carina regions.

	CarNW. <i>all</i>	CarNW. <i>neb</i>	CarSE. <i>all</i>	CarSE. <i>neb</i>	CarSW. <i>all</i>	CarSW. <i>neb</i>
a_0	-1.000	-1.000	-1.000	-1.000	-1.000	-1.000
a_1	+1.933	+0.9960	-0.9813	+0.4688	+0.0418	-0.1930
a_2	-3.978	-1.865	+1.268	-0.6322	+0.0393	+0.0007
a_3	+3.803	+2.005	+0.3028	+0.9364	+0.5756	+1.002
a_4	-1.540	-0.8583	-0.5003	-0.4516	-0.3779	-0.6493
a_5	+0.2261	+0.1291	+0.1079	+0.0717	+0.0679	+0.1165
$f(B)$	0.126	0.107	0.0767	0.101	0.0995	0.0768
$f(V)$	-0.111	-0.114	-0.0926	-0.116	-0.112	-0.104
R_V	4.0 ± 0.1	4.1 ± 0.1	5.4 ± 0.2	4.2 ± 0.1	4.3 ± 0.1	5.0 ± 0.2

Table 2a. Extinction law and *.all* and *.neb* de-reddened line fluxes for CarNW ^a

λ	Ion-ID	$f(\lambda)^b$	$f(\lambda)$	$f(\lambda)$	$(F_\lambda/F_\beta)_0$	$(F_\lambda/F_\beta)_0$
		CCM	<i>.all</i>	<i>.neb</i>	<i>.all</i>	<i>.neb</i>
3727	[O II]	0.235	0.635	0.444	4.267	2.689
3727	[O II]	0.235	0.635	0.444	1.669 ^e	1.653 ^e
3771	H11	0.229	0.565	0.401	0.040	0.037
3798	H10	0.225	0.527	0.377	0.023	0.040
3835	H9	0.219	0.479	0.347	0.044	0.050
3869	[Ne III]	0.213	0.439	0.322	0.291	0.212
3869	[Ne III]	0.213	0.439	0.322	0.170 ^e	0.164 ^e
3889	H8+HeI	0.210	0.417	0.308	0.279	0.248
3970	Heε+[Ne III]	0.195	0.340	0.258	0.205	0.207
4026	He I	0.184	0.296	0.229	0.012	0.021
4069	[S II]	0.175	0.266	0.208	0.009	0.010
4102	Hδ	0.168	0.245	0.194	0.292	0.281
4340	Hγ	0.115	0.133	0.113	0.527	0.525
4363	[O III]	0.110	0.125	0.106	0.019	0.016
4471	He I	0.085	0.091	0.078	0.043	0.044
4861	Hβ	0.000	0.000	0.000	1.000	1.000
4922	He I	-0.012	-0.012	-0.015	0.013	0.014
4959	[O III]	-0.020	-0.019	-0.022	0.939	0.925
5007	[O III]	-0.029	-0.028	-0.031	2.872	2.808
5200	[N I]	-0.064	-0.063	-0.066	0.014	0.015
5539	[Cl III]	-0.115	-0.121	-0.124	0.003	0.004
5577	[O I]	-0.118	-0.128	-0.131	0.022	0.019
5755	[N II]	-0.124	-0.157	-0.161	0.005	0.005
5876	He I	-0.149	-0.177	-0.181	0.123	0.126
6300	[O I]	-0.220	-0.243	-0.247	0.061	0.058
6312	[S III]	-0.221	-0.245	-0.249	0.009	0.010
6364	[O I]	-0.228	-0.252	-0.257	0.019	0.018
6563	Hα	-0.252	-0.281	-0.286	2.929	2.895
6584	[N II]	-0.255	-0.284	-0.289	0.384	0.374
6678	He I	-0.266	-0.297	-0.302	0.035	0.035
6716	[S II]	-0.271	-0.302	-0.307	0.119	0.116
6731	[S II]	-0.273	-0.304	-0.309	0.088	0.086
7065	He I	-0.314	-0.346	-0.353	0.024	0.024

7136	[Ar III]	-0.323	-0.354	-0.361	0.113	0.110
7281	He I	-0.340	-0.371	-0.379	0.004	0.003
7325	[O II]	-0.346	-0.376	-0.384	0.020	0.020
7751	[Ar III]	-0.397	-0.419	-0.430	0.020	0.020
8438	Pa18	-0.474	-0.475	-0.493	0.007	0.007
8467	Pa17	-0.477	-0.478	-0.495	0.003	0.004
8503	Pa16	-0.481	-0.480	-0.498	0.002	0.002
8545	Pa15	-0.485	-0.483	-0.502	0.003	0.003
8598	Pa14	-0.491	-0.486	-0.506	0.005	0.005
8750	Pa12	-0.505	-0.496	-0.517	0.006	0.007
8863	Pa11	-0.516	-0.503	-0.525	0.011	0.010
9015	Pa10	-0.529	-0.512	-0.536	0.017	0.017
9069	[S III]	-0.533	-0.515	-0.540	0.172	0.163
9229	Pa9	-0.546	-0.523	-0.550	0.024	0.023
9531	[S III] ^c	-0.569	-0.537	-0.568	0.692	0.633
9850	[C I]	-0.592	-0.550	-0.586	0.003	0.003
10028	He I	-0.603	-0.557	-0.595	0.006	0.007
10049	Pa7	-0.605	-0.558	-0.596	0.067	0.063
10287	[S II]	-0.619	-0.565	-0.607	0.004	0.004
<hr/>						
<i>c</i> (H β)					1.03 \pm 0.08	1.02 \pm 0.08
<i>F</i> (H β) ₀ ^d					24.12 \pm 2.40	23.98 \pm 2.40

^a Line fluxes normalized to H β = 1.000. ^b Derived from the CCM89 for $R = 4.2$. ^c Corrected with an estimated 6% contribution from unresolved Pa8. ^d $F(\text{H}\beta)_0$ fluxes in units of 10^{-11} erg s⁻¹ cm⁻² arising from our 5'' \times 6.6' entrance slit. ^e Dereddened with CCM89 extinction law for $R = 4.2$

Table 2b. Extinction law and *.all* and *.neb* de-reddened line fluxes for CarSE. ^a

λ	Ion-ID	$f(\lambda)$ <i>.all</i>	$f(\lambda)$ <i>.neb</i>	$(F_\lambda/F_\beta)_0$ <i>.all</i>	$(F_\lambda/F_\beta)_0$ <i>.neb</i>
3624	He I	0.565	0.443	0.104	0.132
3727	[O II]	0.420	0.359	1.332	2.024
3727	[O II]	0.420	0.359	0.981 ^e	1.513 ^e
3771	H11	0.370	0.330	0.044	0.032
3798	H10	0.343	0.313	0.047	0.041
3820	He I	0.323	0.300	–	0.010
3835	H9	0.309	0.291	0.064	0.051
3869	[Ne III]	0.281	0.273	0.086	0.114
3869	[Ne III]	0.281	0.273	0.077 ^e	0.098 ^e
3889	H8+HeI	0.266	0.263	0.173	0.206
3970	He+[Ne III]	0.214	0.226	0.174	0.183
4026	He I	0.184	0.203	0.020	0.021
4069	[S II]	0.164	0.187	0.016	0.011
4102	H δ	0.151	0.176	0.285	0.286
4144*	He I	0.135	0.162	0.005	–
4169*	He I	0.127	0.154	0.033	0.011
4244*	[Fe II]	0.104	0.132	0.103	0.016
4287*	[Fe II]	0.093	0.120	0.127	0.019
4340	H γ	0.081	0.106	0.481	0.506
4363	[O III]	0.076	0.101	0.115	0.014
4415*	O II	0.066	0.088	0.081	0.018
4452*	O II	0.059	0.079	–	0.011
4471	He I	0.056	0.075	0.051	0.041
4815*	[Fe II]	0.005	0.004	0.036	0.007
4861	H β	0.000	0.000	1.000	1.000
4922	He I	-0.009	-0.017	0.047	0.018
4959	[O III]	-0.015	-0.024	0.560	0.712
5007	[O III]	-0.021	-0.032	1.761	2.175

5159*	[Fe II]	-0.043	-0.060	0.075	0.014
5200	[N I]	-0.049	-0.067	0.016	0.009
5270*	[Fe III]	-0.059	-0.080	0.056	0.011
5334*	[Fe II]	-0.069	-0.091	0.012	0.003
5412*	[Fe III]	-0.082	-0.105	0.005	-
5518	[Cl III]	-0.099	-0.123	0.003	0.004
5539	[Cl III]	-0.102	-0.126	0.003	0.004
5577	[O I]	-0.109	-0.133	0.013	-
5755	[N II]	-0.140	-0.163	0.027	0.009
5876	He I	-0.161	-0.182	0.160	0.124
6300	[O I]	-0.241	-0.248	0.032	0.044
6312	[S III]	-0.243	-0.250	0.028	0.011
6364	[O I]	-0.253	-0.258	0.019	0.012
6563	H α	-0.291	-0.286	2.859	2.892
6584	[N II]	-0.295	-0.289	0.562	0.406
6678	He I	-0.313	-0.302	0.059	0.036
6716	[S II]	-0.320	-0.307	0.098	0.109
6731	[S II]	-0.323	-0.309	0.082	0.087
7065	He I	-0.385	-0.353	0.071	0.025
7136	[Ar III]	-0.398	-0.362	0.102	0.098
7155*	[Fe II]	-0.402	-0.364	0.032	-
7281	He I	-0.424	-0.379	0.010	0.005
7325	[O II]	-0.432	-0.384	0.020	0.019
7378*	[Ni II]	-0.442	-0.391	0.051	-
7412*	[Ni II]	-0.448	-0.394	0.018	-
7453*	[Fe II]	-0.455	-0.399	0.013	-
7751	[Ar III]	-0.506	-0.431	0.018	0.020
7890*	[Ni III]	-0.528	-0.446	0.005	0.004
8438	Pa18	-0.613	-0.497	0.008	0.006
8545	Pa15	-0.628	-0.506	0.005	0.002
8598	Pa14	-0.636	-0.510	0.008	0.005
8750	Pa12	-0.656	-0.523	0.008	0.007
8863	Pa11	-0.672	-0.532	0.012	0.009
9015	Pa10	-0.691	-0.543	0.021	0.020
9069	[S III]	-0.698	-0.547	0.180	0.209
9124	[Cl II]	-0.705	-0.551	0.012	0.004
9229	Pa9	-0.718	-0.558	0.036	0.023
9531	[S III] ^c	-0.753	-0.579	0.554	0.633
10049	Pa7	-0.808	-0.610	0.127	0.063
<hr/>					
$c(H\beta)$				0.73 \pm 0.14	1.01 \pm 0.08
$F(H\beta)_0^b$				19.21 \pm 1.90	28.20 \pm 2.80

^a Line fluxes normalized to $H\beta = 1.000$. ^b $F(H\beta)_0$ fluxes in units of 10^{-11} erg s⁻¹ cm⁻² arising from our 5'' \times 6.6' entrance slit. ^c Corrected with an estimated 7% and 6% contribution from unresolved Pa8 for *.all* and *.neb* respectively. ^e Dereddened with CCM89 extinction law for $R = 4.2$. * Only detected in the CarSE spectra (although $\lambda 4415$, $\lambda 5159$ and $\lambda 5270$ were also measured in the CarSW spectra).

Table 2c. Extinction law and *.all* and *.neb* de-reddened line fluxes for CarSW. ^a

λ	Ion-ID	$f(\lambda)$ <i>.all</i>	$f(\lambda)$ <i>.neb</i>	$(F_\lambda/F_\beta)_0$ <i>.all</i>	$(F_\lambda/F_\beta)_0$ <i>.neb</i>
3727	[O II]	0.370	0.391	2.006	2.090
3727	[O II]	0.370	0.391	1.469 ^e	1.458 ^e
3771	H11	0.338	0.347	0.028	0.034
3798	H10	0.319	0.323	0.043	0.050
3820	He I	0.305	0.304	0.009	0.009
3835	H9	0.296	0.293	0.081	0.086
3869	[Ne III]	0.276	0.268	0.176	0.172
3869	[Ne III]	0.276	0.268	0.152 ^e	0.151 ^e

3889	H8+HeI	0.266	0.254	0.233	0.231
3970	He+[Ne III]	0.226	0.207	0.217	0.221
4026	He I	0.202	0.180	0.018	0.017
4069	[S II]	0.186	0.161	0.011	0.014
4102	H δ	0.174	0.149	0.288	0.274
4340	H γ	0.104	0.081	0.515	0.488
4363	[O III]	0.099	0.076	0.015	0.012
4387	He I	0.093	0.071	0.005	0.004
4415	O II	0.086	0.065	0.005	0.004
4471	He I	0.074	0.055	0.044	0.042
4861	H β	0.000	0.000	1.000	1.000
4922	He I	-0.014	-0.016	0.015	0.014
4959	[O III]	-0.021	-0.022	0.871	0.873
5007	[O III]	-0.029	-0.029	2.661	2.653
5159	[Fe II]	-0.056	-0.052	0.006	0.008
5200	[N I]	-0.063	-0.059	0.007	0.008
5270	[Fe III]	-0.075	-0.070	0.007	0.006
5518	[Cl III]	-0.118	-0.110	0.004	0.004
5539	[Cl III]	-0.122	-0.114	0.003	0.003
5577	[O I]	-0.128	-0.120	0.056	0.058
5755	[N II]	-0.158	-0.150	0.005	0.005
5876	He I	-0.179	-0.171	0.135	0.137
6300	[O I]	-0.247	-0.245	0.029	0.029
6312	[S III]	-0.249	-0.247	0.007	0.006
6364	[O I]	-0.257	-0.256	0.009	0.008
6563	H α	-0.288	-0.291	2.879	2.859
6584	[N II]	-0.291	-0.295	0.310	0.304
6678	He I	-0.305	-0.311	0.035	0.035
6716	[S II]	-0.311	-0.317	0.107	0.105
6731	[S II]	-0.313	-0.320	0.076	0.077
7065	He I	-0.361	-0.375	0.023	0.024
7136	[Ar III]	-0.371	-0.386	0.100	0.099
7281	He I	-0.390	-0.409	0.006	0.005
7325	[O II]	-0.396	-0.416	0.015	0.014
7751	[Ar III]	-0.449	-0.479	0.020	0.017
8438	Pa18	-0.524	-0.568	0.004	0.006
8545	Pa15	-0.534	-0.581	0.001	0.004
8598	Pa14	-0.540	-0.587	0.004	0.006
8750	Pa12	-0.554	-0.605	0.005	0.007
8863	Pa11	-0.564	-0.617	0.010	0.011
9015	Pa10	-0.578	-0.633	0.019	0.021
9069	[S III]	-0.582	-0.639	0.193	0.167
9229	Pa9	-0.596	-0.655	0.020	0.022
9531	[S III] ^c	-0.620	-0.683	0.601	0.512
10028	He I	-0.655	-0.725	-	0.008
10049	Pa7	-0.657	-0.727	0.062	0.060
<hr/>					
<i>c</i> (H β)				1.01 \pm 0.08	1.00 \pm 0.08
<i>F</i> (H β) ₀ ^d				18.07 \pm 1.80	17.85 \pm 1.80

^a Line fluxes normalized to H β = 1.000. ^b *F*(H β)₀ fluxes in units of 10⁻¹¹ erg s⁻¹ cm⁻² arising from our 5'' \times 6.6' entrance slit. ^c Corrected with an estimated 6% and 8% contribution from unresolved Pa8 for *.all* and *.neb* respectively. ^d Dereddened with CCM89 extinction law for *R* = 4.2.

Our spectral resolution did not allow us to resolve Pa8 λ 9546 from [SIII] λ 9531. To estimate this contribution, we determined for each region the (*F*_{Pa8}/*F* β)₀ intrinsic values derived using our extinction law. These values turned out to be within \sim 5% of the theoretical values given by SH95. We found that [SIII] λ 9531 has to be decreased by \sim 6% to 8% for any region (both *.neb* and *.all*). In

Tables 2a – 2c we present the [SIII] λ 9531 line fluxes corrected by this Pa8 contribution, which will be used henceforth, and will be taken into account when estimating the S⁺⁺ and S abundance uncertainties.

The $c(\text{H}\beta) \approx 1$ values listed in Tables 2a – 2c consider only the Balmer decrement between H α and H β as explained above and ignore the possible underlying stellar absorption (or emission!) present in the observed spectrum. In contrast, the $c(\text{H}\beta) \approx 0.8$ values listed in Table 2 of Chapter III, were found fitting simultaneously the best $c(\text{H}\beta)$ and W_{abs} solutions using the brightest Balmer lines. It is worth noting that our de-reddened line fluxes *do not* depend on the assumed $c(\text{H}\beta)$ value, since we derived them interpolating over our observed $g(\lambda)$ function.

In Table 3 we present for each region the de-reddened Balmer and Paschen line ratios, $[F_{\lambda}/F_{\beta}]_0$ (Tables 2a – 2c) with respect to their theoretical values, $[F_{\lambda}/F_{\beta}]_{\text{theo}}$. The fit is reasonably good, within $\sim 10\%$ for the bright lines.

Table 3. Comparison of de-reddened and theoretical H I flux ratios for the Carina Regions. ^a

λ	Ion	CarNW .all	CarNW .neb	CarSE .all	CarSE .neb	CarSW .all	CarSW .neb
3771	H11	1.01	0.93	1.09	0.81	0.71	0.85
3798	H10	0.55	0.74	0.89	0.77	0.81	0.94
3835	H9	0.59	0.68	0.87	0.69	1.09	1.16
4102	H δ	1.12	1.08	1.09	1.09	1.10	1.05
4340	H γ	1.12	1.12	1.03	1.08	1.09	1.04
4861	H β	1.00	1.00	1.00	1.00	1.00	1.00
6563	H α	1.03	1.02	1.00	1.02	1.01	1.00
8598	Pa14	0.71	0.68	1.23	0.68	0.56	0.97
8750	Pa12	0.60	0.68	0.76	0.62	0.48	0.64
8863	Pa11	0.78	0.74	0.87	0.67	0.69	0.78
9015	Pa10	0.93	0.93	1.12	1.07	1.04	1.15
9229	Pa9	0.93	0.92	1.43	0.90	0.80	0.85
10049	Pa7	1.21	1.13	2.29	1.14	1.12	1.07

^a $[F_{\lambda}/F_{\beta}]_0 / [F_{\lambda}/F_{\beta}]_{\text{theo}}$ values for our 5th-order polynomial fit, using SH95 theoretical HI line ratios.

4.2.1 Comparison of extinction laws

In Figs. 1a – 1c we show our derived $f(\lambda).all$ and $f(\lambda).neb$ vs. $(1/\lambda)$ extinction law fits for each region. In each case, we fitted a smooth curve to the observed data, including the strong decline of the high Balmer lines. There are considerable differences in the derived $f(\lambda).all$ and $f(\lambda).neb$, especially for the CarNW and CarSE regions that contain most of the early O stars (Table 2a of Chapter II). These differences produce noticeable changes in the corresponding de-reddened fluxes, as can be seen in Tables 2a – 2c above.

In Fig. 1*d* we compare our derived $f(\lambda).neb$ for the CarSE region with different extinction laws found in the literature: *i)* $f(\lambda)$ adapted from the analytical fit given by CCM89 for $R = 4.2$; *ii)* $f(\lambda)$ adapted from the $E_{\lambda-V} / E_{B-V}$ vs. $(1/\lambda)$ graphs given by Thé, Bakker & Tjin A Djie (1980) for the three common stars in Tr 16 lying in our CarSE region, and *iii)* $f(\lambda)$ adapted from different average color excess ratios from the photometry of about 80 stars in Tr 16 given by Tapia et al. (1988).

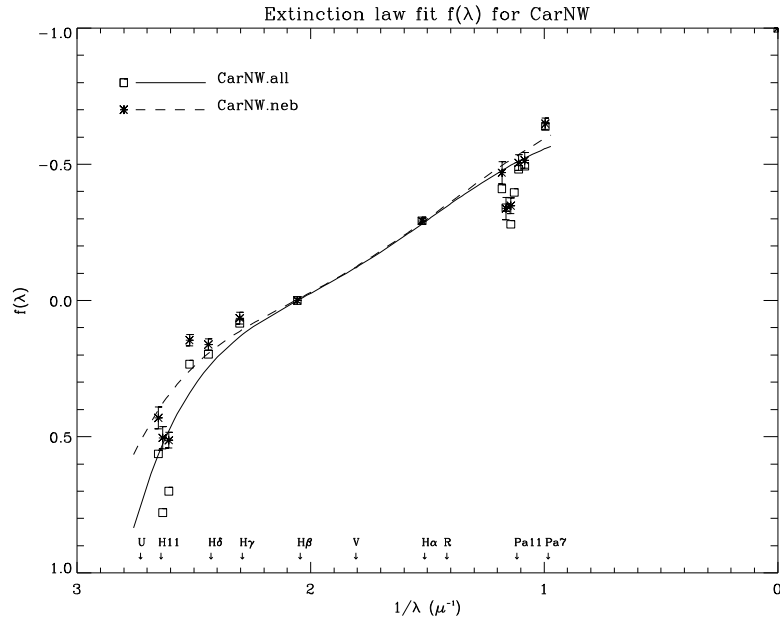


Fig. 1*a*. Derived *.all* and *.neb* extinction law fits for the CarNW region. We show the observational errors for the *.neb* case only.

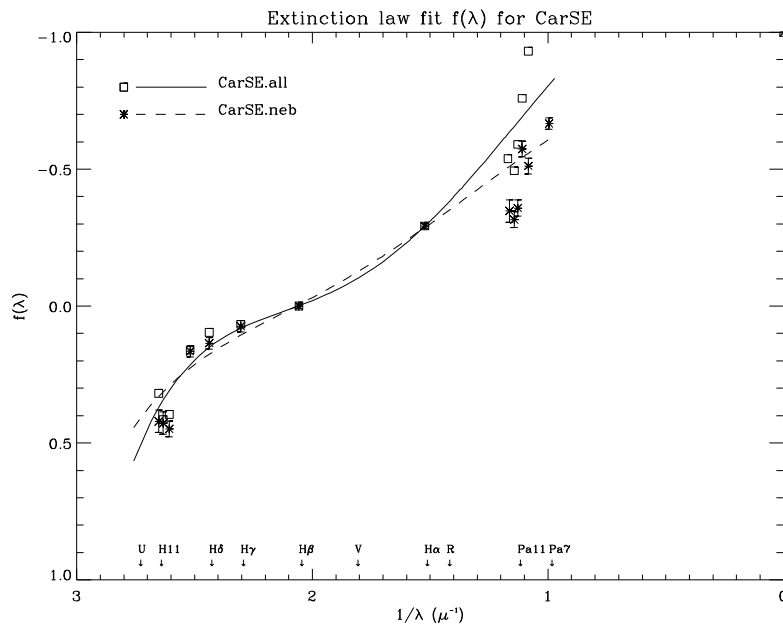


Fig. 1*b*. As Fig. 1*a* for the CarSE region.

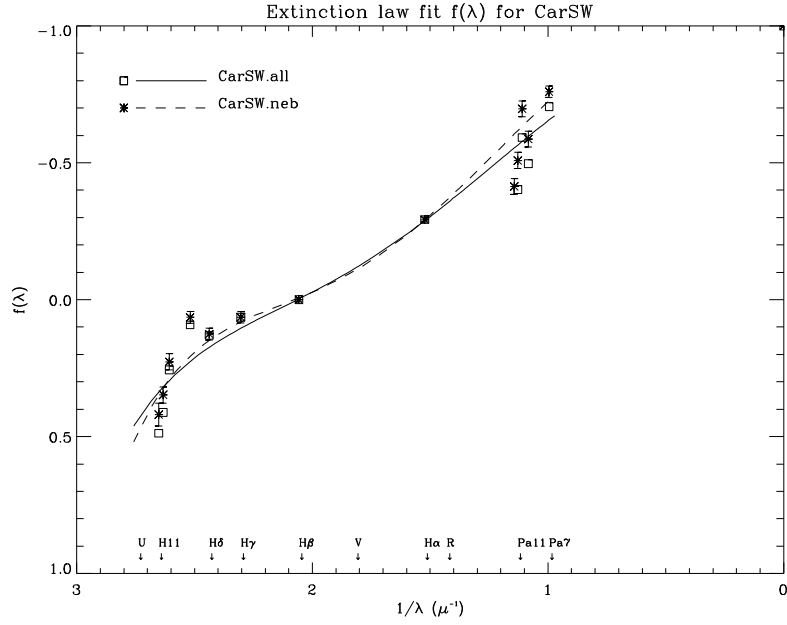


Fig. 1c. As Fig. 1a for the CarSW region.

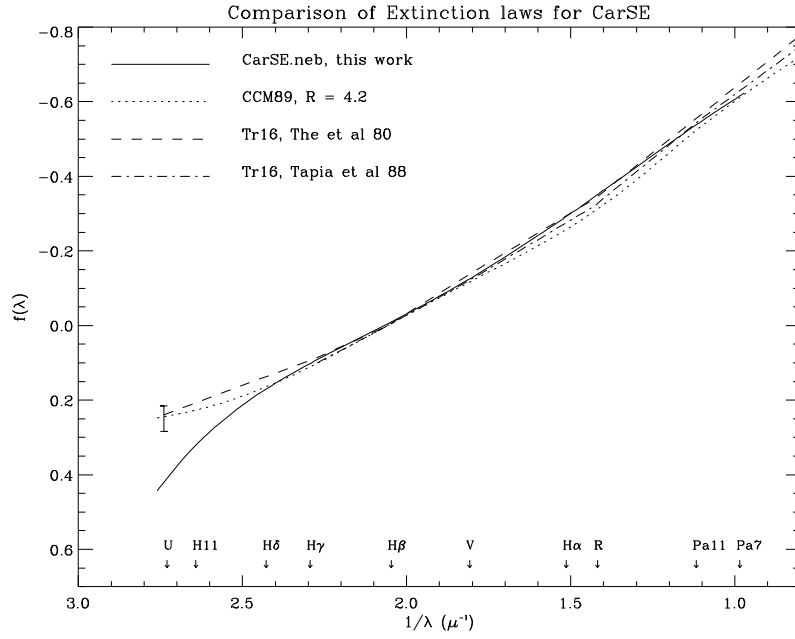


Fig. 1d. Comparison of our extinction law for the *.neb* CarSE region with those found in other studies. The error bar was derived from the uncertainties quoted by Thé, Bakker & Tjin A Djie (1980).

In Table 4 we summarize our results for the Carina regions and compare them with other determinations found in the literature.

To construct the $f(\lambda)$ function from Thé et al. (1980) we used the relation

$$f(\lambda) = \left(\frac{A_V}{A_{H\beta}} \right) \left[\frac{E_{\lambda-V}/E_{B-V}}{R} + 1 \right] - 1. \quad (13)$$

From their data, we obtained an average R value for 3 stars in common with our CarSE region: $R_{\text{Thé}} = 3.9 \pm 0.1$, in good agreement with our value $R_{\text{SE}} = 4.2 \pm 0.1$ (Table 4). Forte (1978) found an average $\langle E_{\text{B-V}} \rangle = 0.52$ for stars in Tr 14 and Tr 16, while Cudworth, Martin, & DeGioia-Eastwood (1993) report $\langle E_{\text{B-V}} \rangle = 0.50$ mag from photometry of stars in Tr 16, both in excellent agreement with our CarSE value: $E_{\text{B-V}} = 0.54$ mag. Although there is a $\Delta A_V \approx 0.20$ mag difference between Thé et al. A_V value and ours, we found that both extinction laws have the same slope in the blue: $(A_V/A_{\text{H}\beta})_{\text{SE}} = 0.88$, while $(A_V/A_{\text{H}\beta})_{\text{Thé}} = 0.87$.

Table 4. Comparison of extinction parameter in the Carina regions ^a

	----- Tr 14 -----		----- Tr 16 -----		----- Tr 16 -----	
	CarNW.all	CarNW.neb	CarSE.all	CarSE.neb	CarSW.all	CarSW.neb
$c(\text{H}\beta)\alpha\text{-}\beta$	1.03 \pm 0.08	1.02 \pm 0.08	0.73 \pm 0.14	1.01 \pm 0.08	1.01 \pm 0.08	1.02 \pm 0.08
$c(\text{H}\beta)_{\text{Wabs}}$	0.74 \pm 0.15	0.74 \pm 0.15	0.61 \pm 0.15	0.79 \pm 0.15	0.76 \pm 0.15	0.76 \pm 0.15
A_V	2.29 \pm 0.20	2.26 \pm 0.20	1.65 \pm 0.35	2.23 \pm 0.20 2.03 (Thé 80) 2.1 (Vázquez 96) 2.52 (Tapia 03) 2.21 \pm 0.15 (Gagné 11)	2.24 \pm 0.20 2.21 (Tapia 88) 2.06 (Tapia 03) 2.05 \pm 0.52 (Gagné 11)	2.24 \pm 0.20
$E_{\text{B-V}}$	0.57 \pm 0.10	0.54 \pm 0.10	0.30 \pm 0.10	0.54 \pm 0.10 0.52 \pm 0.10 (Forte 78) 0.50 \pm 0.10 (Cudworth 93)	0.51 \pm 0.07	0.48 \pm 0.07
R	4.0 \pm 0.1	4.1 \pm 0.1	5.4 \pm 0.2	4.2 \pm 0.1 3.9 \pm 0.1 (Thé 80) 4.1 \pm 0.1 (Tapia 88) 4.6 (Tapia 03)	4.3 \pm 0.1	5.0 \pm 0.20

^a Adapted from Thé, Bakker & Tjin A Djie (1980); Tapia et al. (1988); Cudworth, Martin, & DeGioia-Eastwood (1993); Vázquez et al. (1996); Tapia et al. (2003), and Gagné et al. (2011).

We used Eq. (13) to derive the extinction law $f(\lambda)$ from the color excess ratios given by Tapia et al. (1988). These authors found $A_V^{\text{Tapia}} = 2.21$ mag for stars in Tr 16, in excellent agreement with our derived value ($A_V = 2.23$ mag). Interpolating their reported color excess ratios we obtained, $A_\beta^{\text{Tapia}} = 2.50$ mag, and $c(\text{H}\beta)^{\text{Tapia}} = 1.00$, in very good agreement with our value. Our $R_{\text{SE}} = 4.2 \pm 0.10$ value for CarSE, is also in excellent agreement with the values derived by Tapia et al.: $R_{\text{Tapia}} = 4.1 \pm 0.1$. We see from Fig. 1d, that $f(\lambda)_{\text{Tapia}}$ and ours are very similar within the common λ range. Our results for CarNW are also in very good agreement with those reported by Vázquez et al. (1996) from CCD photometry of stars in Tr 14: $R_{\text{Vázquez}} \approx 4.1 \pm 0.6$ and $\langle A_V \rangle = 2.1$ mag (assuming a foreground $E_{\text{B-V}} \approx 0.33$; Vázquez, personal communication), as compared with our $R = 4.1$ and $A_V = 2.26$ mag derived values.

Tapia et al. 2003 presented new visual and NIR photometry results for the star clusters Tr 14 and Tr 15 and they confirmed the presence of widespread variations in the dust density and also in the dust size distribution leading to widely different values in the optical depth (as measured by A_V) and the shape of the extinction law (as measured by R) towards Tr 14 and Tr 16. They found no spatial patterns for these variations, or correlations with the spectral type or the distance, indicating true inhomogeneities within the clusters. We present their average values in Table 4 above.

Gagné et al. (2011) present an extensive x-ray study of the early stellar population in the Carina region, including a compilation of stellar parameters for the brightest stars. From the common stars within our Carina regions, we found that A_V varies from 2.0 – 2.4 for Tr 14, with an average $\langle A_V \rangle = 2.21 \pm 0.15$ (8 stars) and from 1.6 – 2.7 for Tr 16 with an average $\langle A_V \rangle = 2.05 \pm 0.53$ (7 stars). Povich et al. (2011) also used x-ray observations and IR SEDs for bright stars in the Carina clusters and found that the extinction law measured toward the OB stars has two components: $A_V = 1 - 1.5$ mag produced by foreground dust with $R_V = 3.1$, plus a contribution from local dust with $R_V > 4.0$. They found that the extinction derived from the B – V color excess (A_{V_EBV}), is consistent with that derived from the IR SED (A_{V_SED}) only for a high $R_V = 4.0$.

Although we found good agreement between the total visual extinction A_V , and the color excess E_{B-V} derived by other authors, our extinction law seems to be too steep in the blue side of the spectra as compared with other determinations (Fig. 1d). Given the errors associated with the high Balmer lines (H9, H10 and H11) used to derive the fit in this wavelength range, we decided better to un-redden the [OII] $\lambda 3727$ and [NeIII] $\lambda 3869$ lines using CCM89 extinction law with $R = 4.2$. This is important since [OII] $\lambda 3727$ is needed to calculate the degree of ionization of the nebula (O^{++}/O), which in turn will affect the ionization correction factors and the total abundances.

4.3 Physical Parameters: electron temperature and density

In this section we derive the electron density n_e , and electron temperature T_e , for our 3 Carina regions. We will use both the *.all* and the *.neb* spectra in order to study the possible effects of the stellar contribution in the integrated spectra. We computed n_e and T_e using specific line ratios which are sensitive both to n_e and to T_e by means of the *nebular* package within IRAF, which solve a 5-level atom (Shaw and Dufour 1995). For $n_e(\text{SII})$ we used the ratio $\lambda 6717/\lambda 6731$; for $n_e(\text{Cl III})$ we used $\lambda 5517/\lambda 5537$, assuming $T_e = 10^4$ K. For $T_e(\text{OIII})$ we used $(\lambda\lambda 4959+5007)/\lambda 4363$; for $T_e(\text{NII})$ we used $(\lambda\lambda 6548+6584)/\lambda 5755$; for $T_e(\text{OII})$ we used $(\lambda\lambda 3727+3729)/(\lambda\lambda 7320+7330)$; for $T_e(\text{SII})$ we used $(\lambda\lambda 6717+6731)/(\lambda\lambda 4068+4076)$; and for $T_e(\text{SIII})$ we used $(\lambda\lambda 9069+9532)/\lambda 6312$. Our results are summarized in Table 5 below. We corrected the line flux [OII] $\lambda 7325$ due to recombination using the expression given by Liu et al. (2000), which decreases the un-reddened line flux by about 5% for our

three regions. We found that the corrections of [NII] $\lambda 5755$ and [OIII] $\lambda 4363$ due to recombination were negligible.

We also built (n_e, T_e) diagnostic diagrams for selected temperature- and density-sensitive line ratios for each region (see Figs. 2a – 2c) using *Abelion* line-emissivities from Stasińska & Leitherer (1996). The n_e and T_e solutions derived with *Abelion* were the same as those derived using IRAF *nebular* package within 1%, except for $T_e(\text{OII})$ (with differences up to 10%) and $T_e(\text{SII})$ (with differences up to 30%).

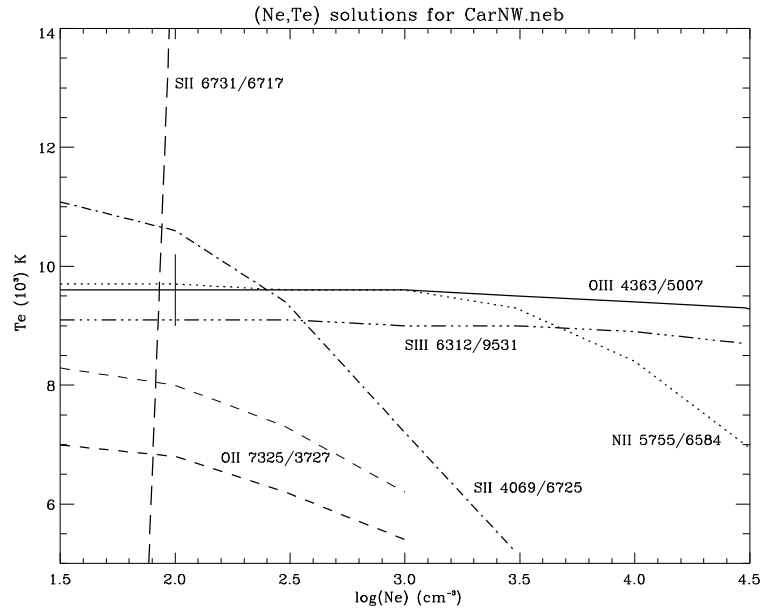


Fig. 2a. (n_e, T_e) diagram for selected emission line ratios for the CarNW.*neb* region derived using *Abelion* emissivities. For [OII] $\lambda\lambda 7325/3727$ we also show as a thin line, the corresponding curve if the de-reddening is done using CCM's standard extinction law with $R = 3.2$. The vertical bar shows a typical error for [OIII] $\lambda\lambda 4363/5007$ at $n_e = 10^2 \text{ cm}^{-3}$.

The wide spread shown by different line ratios for ions with similar ionization potentials, is larger than that attributable to the errors in the line intensities, the un-reddening procedure, or the atomic data, so that Figs. 2a – 2c are indicative of large-scale spatial density and temperature fluctuations within the nebula. The (n_e, T_e) diagram for CarSE.*neb* suggests even higher temperature variations across this region, although it presents higher uncertainties in the line ratios due to the strong contamination of η Car lines even in the *neb* spectra. For comparison, we also show as a thin line the [OII] $\lambda\lambda 7325/3727$ curve derived if the un-reddening is done using CCM89's extinction law with $R = 3.2$.

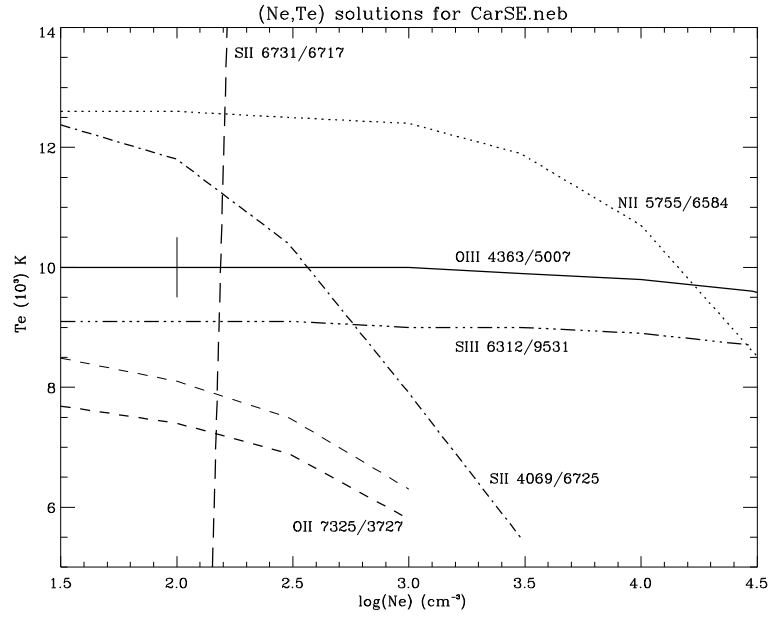


Fig. 2b. As Fig. 2a for the CarSE.neb region.

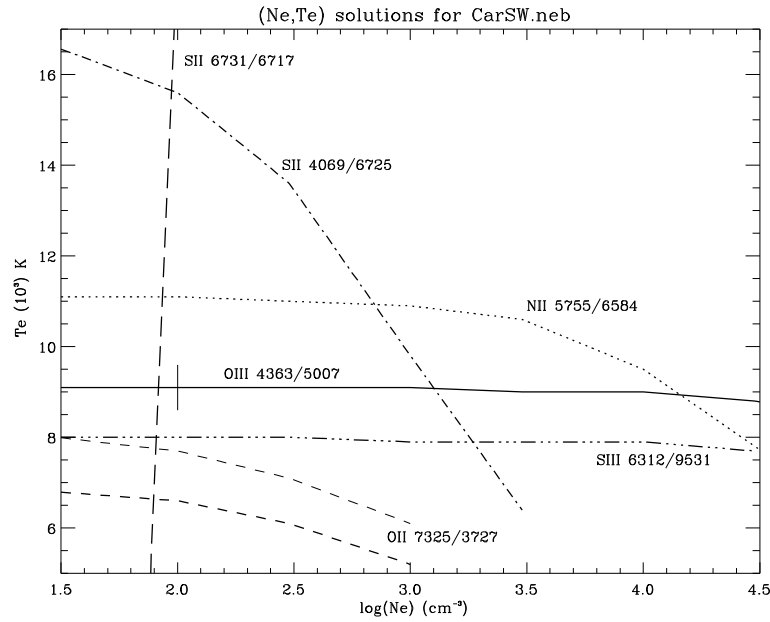


Fig. 2c. As Fig. 2a for the CarSW.neb region.

The electron density derived using the Chlorine lines $n_e(\text{Cl III})$ is definitively larger than that derived using Sulfur lines $n_e(\text{SII})$, and the differences are greater than what the uncertainties can account for. Since the [Cl III] lines originate in a higher excitation zone than the [SII] lines do, this may indicate a stratification in density, being higher closer to the ionizing sources. The [SII] ratio suggests an overall low-density regime for the whole nebula ($100 - 300 \text{ cm}^{-3}$) with a possible increment in CarSE. We will adopt $n_e(\text{SII})$ as a representative average for our scanned regions, and we used it to derive the electron temperatures listed in Table 5.

Table 5. Electron densities and electron temperatures for the three Carina regions. ^a

	CarNW. <i>all</i>	CarNW. <i>neb</i>	CarSE. <i>all</i>	CarSE. <i>neb</i>	CarSW. <i>all</i>	CarSW. <i>neb</i>
$n_e(\text{S II})$	$100^{+200}_{-...}$	$100^{+200}_{-...}$	$200^{+100}_{-...}$	$200^{+200}_{-...}$	$100^{+200}_{-...}$	$100^{+200}_{-...}$
$n_e(\text{Cl III})$	---	$300^{+2500}_{-...}$	4300 ± 3000	$1000^{+3000}_{-...}$	$1200^{+3500}_{-...}$	$500^{+2200}_{-...}$
$T_e(\text{O III})$	10.1 ± 0.6	9.7 ± 0.6	$(10.5)^{+11.0}_{-6.6}$ ^c	10.0 ± 0.6	9.7 ± 0.6	9.1 ± 0.6
$T_e(\text{N II})$	9.9 ± 0.9	9.8 ± 1.0	$(12.9)^{+5.3}_{-3.5}$ ^c	12.8 ± 1.6	11.3 ± 1.3	11.2 ± 1.2
$T_e(\text{O II})$ ^b	7.2 ± 0.6	7.9 ± 0.7	$9.4^{+0.9}_{-0.6}$	7.7 ± 0.6	7.3 ± 0.6	7.2 ± 0.5
$T_e(\text{S II})$	7.0 ± 0.8	7.0 ± 0.9	$10.2^{+2.3}_{-1.7}$	7.3 ± 0.9	8.0 ± 1.2	9.5 ± 1.7
$T_e(\text{S III})$	8.5 ± 0.7	9.2 ± 0.9	$(16.2)^{+3.1}_{-2.4}$	9.1 ± 0.8	8.0 ± 0.6	8.0 ± 0.6

^a Densities in cm^{-3} and temperatures in 10^3 K. ^b Corrected by recombination using the expression given by Liu et al. (2000). ^c Adapted from the *.neb* values

The T_e errors quoted in Table 5 correspond to the formal error propagation of the un-reddened line intensity ratios. Unfortunately, all the temperature-sensitive lines are very weak, only a few percent of $\text{H}\beta$, and consequently have very large uncertainties. From Table 5, we see that CarSE has a somewhat higher mean T_e as compared to the other two regions, although the errors are also much larger for this region. Due to the strong stellar contamination in the CarSE.*all* (and *.neb*!) spectrum, with strong wings in $\text{H}\gamma$, and too many [FeII] and [FeIII] lines (see Table 3a of Chapter II) we could not estimate a reliable $T_e(\text{OIII})$ nor $T_e(\text{NII})$ values for this regions. In what follows, we will adopt $T_{\text{OIII}} = 10.5$ kK and $T_{\text{NII}} = 12.9$ kK for CarSE.*all*, as inferred from the corresponding CarSE.*neb* values. Our derived T_{OIII} and n_e for CarSE.*neb* are in good agreement with the values reported by Faulkner & Aller (1965): $T_{\text{OIII}} = 10.2 \pm 0.7$ kK and $n_e = 620 \text{ cm}^{-3}$ and for the Carina nebula.

4.4 Ionic abundances

Having determined the electron temperature and density for our nebula, we proceed to estimate their ionic abundances. We will derive first the ionic and total abundances ignoring temperature fluctuations. Therefore our adopted temperatures will be upper limits to the real average temperatures, implying thus only lower limits to the derived ionic and total abundances (Peimbert & Torres-Peimbert 1977; PTP77). We will consider the corrections in the ionic and total abundances if temperature fluctuations are taken into account in Sec. 4.4.6 below.

The ionic abundance with respect to H^+ of the state of ionization $+m$ of element X, derived from its collisionally excited emission line at wavelength λ , is given by the expression:

$$\left(\frac{X_{\lambda}^{+m}}{\text{H}^+} \right) = \frac{\varepsilon[\text{H}\beta, T_e(\text{OIII})]}{\varepsilon(X_{\lambda}^{+m}, T_e)} \times \left(\frac{F_{\lambda}}{F_{\beta}} \right)_0, \quad (14)$$

where $\varepsilon(X_\lambda^{+m}, T_e, n_e)$ is the emissivity of ion X^{+m} as function of T_e and n_e , at wavelength λ , and $(F_\lambda/F_\beta)_0$ is the de-reddened line flux with respect to H β . We derived the ionic abundances using the *ionic* routine within the IRAF *nebular* package. We adopted a 2-zone model, in which we used $n_e(\text{SII})$ and $T_e^{\text{low}} = T_e(\text{NII})$ to compute the ionic abundances of O $^+$, N $^+$, S $^+$, and S $^{++}$ (the ‘‘low ionization’’ zone), and we used $n_e(\text{SII})$ and $T_e^{\text{high}} = T_e(\text{OIII})$ to compute the ionic abundances of O $^{++}$, Ne $^{++}$, Ar $^{++}$, and He $^+$ $\lambda 5876$ (the ‘‘high ionization’’ zone). We list in Table 6 our derived set of ionic abundances, where the quoted errors include the errors in the line intensities and electron temperatures.

Table 6. Ionic abundances relative to H $^+$ (in units of 10^{-6} , except for He $^+$) for the three Carina regions (without temperature fluctuations).

	CarNW.all	CarNW.neb	CarSE.all	CarSE.neb	CarSW.all	CarSW.neb
He $^+$ ($\lambda 5876$) ^a	0.091 ^{+0.021} _{-0.017}	0.091 ^{+0.021} _{-0.017}	0.120 ^{+0.024} _{-0.020}	0.091 ^{+0.019} _{-0.015}	0.095 ^{+0.019} _{-0.016}	0.098 ^{+0.022} _{-0.019}
O $^+$ ($\lambda 3727$) ^b	65.5 ^{+45.2} _{-25.4}	67.8 ^{+32.2} _{-24.5}	14.0 ^{+8.60} _{-5.24}	22.2 ^{+13.1} _{-7.90}	33.4 ^{+18.8} _{-11.4}	34.3 ^{+18.2} _{-12.2}
O $^{++}$ ($\lambda 5007$)	98.9 ^{+23.7} _{-19.9}	111 ^{+29.1} _{-20.9}	53.0 ^{+11.8} _{-10.0}	77.3 ^{+18.9} _{-15.8}	105 ^{+27.6} _{-19.8}	132 ^{+31.9} _{-27.5}
N $^+$ ($\lambda 6584$)	7.75 ^{+2.35} _{-1.70}	7.75 ^{+2.08} _{-1.86}	5.98 ^{+1.96} _{-1.43}	4.40 ^{+1.46} _{-1.06}	4.48 ^{+1.47} _{-1.06}	4.49 ^{+1.34} _{-1.08}
S $^+$ ($\lambda 6725$)	0.491 ^{+0.137} _{-0.101}	0.490 ^{+0.121} _{-0.112}	0.242 ^{+0.072} _{-0.053}	0.267 ^{+0.081} _{-0.059}	0.319 ^{+0.095} _{-0.070}	0.322 ^{+0.088} _{-0.072}
S $^{++}$ ($\lambda 9531$)	3.30 ^{+0.740} _{-0.570}	3.08 ^{+0.612} _{-0.581}	1.61 ^{+0.390} _{-0.310}	1.86 ^{+0.460} _{-0.360}	2.21 ^{+0.540} _{-0.420}	1.92 ^{+0.420} _{-0.370}
Ne $^{++}$ ($\lambda 3869$) ^b	16.6 ^{+5.80} _{-4.60}	18.9 ^{+6.10} _{-4.10}	6.43 ^{+1.70} _{-1.42}	9.95 ^{+3.00} _{-2.35}	17.5 ^{+5.70} _{-4.40}	22.9 ^{+6.70} _{-5.60}
Ar $^{++}$ ($\lambda 7136$)	1.02 ^{+0.160} _{-0.150}	1.09 ^{+0.193} _{-0.144}	0.838 ^{+0.124} _{-0.110}	0.904 ^{+0.148} _{-0.130}	0.993 ^{+0.167} _{-0.150}	1.15 ^{+0.180} _{-0.170}
O $^{++}$ /O	0.60 ^{+0.04} _{-0.06}	0.62 ^{+0.05} _{-0.07}	0.79 ^{+0.06} _{-0.09}	0.78 ^{+0.06} _{-0.09}	0.76 ^{+0.06} _{-0.08}	0.79 ^{+0.06} _{-0.09}

^a Derived using *Abelion* emissivities (Stasińska & Leitherer 1996). ^b Derived using the line intensities dereddened with CCM89 extinction law for $R = 4.2$

Given our available emission lines, we were able to determine the ionic abundances with respect to H $^+$ of O $^+$, O $^{++}$, N $^+$, S $^+$, and S $^{++}$ from two different lines. We found that O $^{++}(\lambda 5007)/\text{O}^{++}(\lambda 4363) \approx 1$, N $^+(\lambda 6584)/\text{N}^+(\lambda 5755) \approx 1$, and S $^+(\lambda 6725)/\text{S}^+(\lambda 4069) \approx 1$, within the errors. However, we found that O $^+(\lambda 3727)/\text{O}^+(\lambda 7325) = 1.9$ on average (with a much larger deviation for CarSE.all) and S $^{++}(\lambda 9531)/\text{S}^{++}(\lambda 6312) = 1.4$ on average. O $^+(\lambda 3727)$ is larger than O $^+(\lambda 7325)$ because we are using a higher $T_e(\text{NII})$ than $T_e(\text{OII})$, and the $\varepsilon(\lambda 7325)$ emissivity has a steeper dependence on T_e than $\varepsilon(\lambda 3727)$ does according to *Abelion*’s emissivities. The S $^{++}(\lambda 9531)/\text{S}^{++}(\lambda 6312)$ ratio can be explained with a similar argument. For all regions we found that that O $^0(\lambda 6300)$ is about 5% of (O $^+$ + O $^{++}$) and N $^0(\lambda 5200)$ is about 7% of N $^+$.

Dennefeld & Stasińska (1983; DS83) present S $^+$ and S $^{++}$ abundances for a sample of galactic and Magellanic Clouds HII regions, including the Carina nebula. They also found that S $^{++}(\lambda 9531)/\text{S}^{++}(\lambda 6312) = 1.3$ on average. Part of these differences may be explained by the uncertainties in the sulfur atomic data. Recent data for S $^{++}$ tend to decrease S $^{++}(\lambda 9531)$ while leaving S $^{++}(\lambda 6312)$ unchanged (DS83, García-Rojas et al. 2007).

Peimbert, Torres-Peimbert & Rayo (1978, PTPR78) presented observations of several slit positions within the Carina nebula. Our $c(\text{H}\beta) \approx 1$ values, are somewhat larger than those of PTPR78's, which vary from 0.65 to 0.94. However, note that these authors considered Whitford (1958) extinction law to find the reddening constant. PTPR78 also report a relatively low-density nebula, with $n_e \approx 300 \text{ cm}^{-3}$, with $T_{\text{NII}} = 9.6 \text{ kK} > T_{\text{OIII}} = 8.7 \text{ kK}$. They also report ionic abundances variations among different slit positions, as high as 0.46 dex for O^+ , 0.24 dex for O^{++} , 0.52 dex for N^+ , 0.40 dex for S^+ , 0.52 dex for S^{++} , and 0.27 dex for Ne^{++} .

4.5 Total abundances without temperature fluctuations

In order to estimate the total element abundances (with respect to H) we need to account for unseen ions, and define a set of ionization correction factors (ICF), such that $\text{X}/\text{H} = \Sigma(\text{X}^i/\text{H}^+) \times \text{ICF}(\text{X})$. One way to compute this contribution of unseen ions is to construct a detailed model of the nebula and to find its ionization structure. Instead, as a first approach, we will estimate the total abundances for our nebulae using the ICFs summarized by Kingsburgh & Barlow (1994; KB94) for O, N, S, Ne and Ar. We reviewed also the ICF for sulfur given by Izotov et al. (2006) for their medium- and high-metallicity regimes but we found that they are very similar to those of KB94. It is worth mentioning that these set of ICF was first proposed by Peimbert & Costero (1969) for O, N, Ne and Ar and by Stasińska (1978) for S. Except for sulfur, the derivation of these ICF relies on similarities of the ionization potentials of the species involved. For S, its derivation was based on photoionization models. In Carina as in many HII regions, O^+ and O^{++} comprise most of the oxygen with a negligible amount of O^{+3} , given that the ionization potential of O^{+3} is similar to that of He^{++} and there is no evidence of significant HeII line emission. There is also very little O^0 since the ionization potential for O^+ is the same as that for H^+ . The ICF summarized by KB94 are: $\text{O}/\text{H} = (\text{O}^+ + \text{O}^{++})/\text{H}^+$; $\text{N}/\text{H} = (\text{N}^+/\text{H}^+) \times (\text{O}/\text{O}^+)$; $\text{Ne}/\text{H} = (\text{Ne}^{++}/\text{H}^+) \times (\text{O}/\text{O}^{++})$; $\text{Ar}/\text{H} = (\text{Ar}^{++}/\text{H}^+) \times (\text{O}/\text{O}^{++})$, and $\text{S}/\text{H} = (\text{S}^+ + \text{S}^{++})/\text{H}^+ \times [1 - (1 - \text{O}^+/\text{O})^3]^{-1/3}$. The fractions of neutral oxygen or neutral nitrogen were assumed to be the same as that of neutral hydrogen, in which case the final abundance ratios with respect to hydrogen would not be affected.

Recently, Delgado-Inglada, Morisset, & Stasińska (2014; DI14) presented a set of new ICFs suited for physical conditions present in PNe and HII regions, derived by fitting a large grid of photoionization models considering different gas metallicities, stellar effective temperatures and SEDs, gas density distributions and the presence of dust grains. They also employed the latest transition probabilities and collisional strengths for the considered ions. DI14 tested their ICF verifying that the S/O, Ne/O and Ar/O ratios do not depend on the degree of ionization. At the other hand, N can be produced in the interiors of asymptotic giant stars, depending on the mass of the progenitor star, and a

trend of N/O with the degree of ionization would not be surprising. We adapted their ICF for the conditions of our Carina regions, with no HeII lines present and $w = O^{++}/O > 0.5$:

$$\frac{O}{H} = \frac{O^+ + O^{++}}{H^+}, \text{ if no HeII lines are present,} \quad (15)$$

$$\frac{N}{H} = \frac{N^+}{H^+} \left(\frac{O}{O^+} \right) \times 10^{-0.16w}, \quad w < 0.95, \quad (16)$$

$$\frac{S}{H} = \frac{S^+ + S^{++}}{H^+} \left(\frac{O}{O^+} \right) \times 10^{\left(\frac{-0.02 - 0.03w - 2.31w^2 + 2.19w^3}{0.69 + 2.09w - 2.69w^2} \right)}, \quad w < 0.95, \quad (17)$$

$$\frac{Ne}{H} = \frac{Ne^{++}}{H^+} \left(\frac{O}{O^{++}} \right) \times \left[w + 2.744(0.7 + 0.2w - 0.8w^2) \right], \quad w > 0.10, \quad (18)$$

$$\frac{Ar}{H} = \frac{Ar^{++}}{H^+} \times 10^{\left(\frac{0.05}{0.06+w} - 0.07 \right)}; \quad 0.05 < w \leq 0.50; \quad \frac{Ar}{H} = \frac{Ar^{++}}{H^+} \times 10^{\left(\frac{0.03w}{0.4-0.3w} - 0.05 \right)}, \quad 0.5 < w < 0.95, \quad (19)$$

In Table 7 we present our total abundances derived using both KB94's ICFs (most commonly used in the literature so far) and DI14's ICFs. We list only the average errors for each element, which are similar among the different regions. These errors were estimated propagating the errors in the ionic abundances (Table 6) and in the ICFs. We can conclude that *a*) the assigned error for O/H, Ne/H and Ar/H are quite large (more than 0.10 dex); *b*) there is not a clear trend between the *.neb* and *.all* total abundances, although the O/H, Ne/H and Ar/H *.neb* abundances seem to be larger than the *.all* ones by 0.06 dex on average; *c*) The S/H abundances derived with DI14's ICFs is basically the same as that derived with KB94's ICFs. However, the new ICFs of DI14 yield *decreased* N/H (by ≈ -0.12 dex), *decreased* Ar/H (by ≈ -0.07 dex) and *increased* Ne/H (by $\approx +0.27$ dex) abundances as compared to those derived using KB94's ICFs. Since there is no difference for O/H derived using DI14 or KB94 ICFs (both consider $ICF(O) = 1$), the differences in the N/O, S/O, Ne/O and Ar/O ratios go in the same direction as mentioned above: $(N/O)_{DI14} - (N/O)_{KB94} \approx -0.11$ dex, $(Ar/O)_{DI14} - (Ar/O)_{KB94} \approx -0.08$ dex, but $(Ne/O)_{DI14} - (Ne/O)_{KB94} \approx +0.27$ dex. Another way to analyze these results is comparing directly both sets of ICFs as given in the lower part of Table 7. We found that the $ICF(S)$ predicted by DI14 formulae is *smaller* than 1.00 if $w = O^{++}/O < 0.62$ in Eq. (17).

Table 7. Total abundances for the Carina regions: comparison of ICFs (without temperature fluctuations).^a

	NW.all		NW.neb		SE.all		SE.neb		SW.all		SW.neb		error
	KB94	DI14											
O/H	8.22	8.22	8.25	8.25	7.83	7.83	8.00	8.00	8.14	8.14	8.22	8.22	±0.14
N/H	7.29	7.19	7.31	7.21	7.46	7.33	7.29	7.17	7.27	7.15	7.34	7.21	±0.12
S/H	6.61	6.57	6.59	6.55	6.37	6.33	6.42	6.38	6.49	6.45	6.45	6.42	±0.11
Ne/H	7.44	7.75	7.48	7.79	6.91	7.16	7.11	7.36	7.36	7.63	7.46	7.71	±0.12
Ar/H	6.23	6.04	6.24	6.07	6.03	6.02	6.07	6.05	6.12	6.08	6.16	6.16	±0.14
log(N/O)	-0.93	-1.02	-0.94	-1.04	-0.37	-0.50	-0.70	-0.83	-0.87	-0.99	-0.88	-1.01	±0.26
log(S/O)	-1.60	-1.64	-1.66	-1.70	-1.46	-1.49	-1.58	-1.61	-1.66	-1.69	-1.77	-1.80	±0.25
log(Ne/O)	-0.78	-0.46	-0.77	-0.46	-0.92	-0.67	-0.89	-0.64	-0.78	-0.52	-0.76	-0.52	±0.26
log(Ar/O)	-1.99	-2.18	-2.01	-2.18	-1.80	-1.81	-1.93	-1.95	-2.03	-2.06	-2.06	-2.06	±0.28
ICF(N)	2.51	2.01	2.64	2.10	4.79	3.58	4.48	3.37	4.16	3.14	4.87	3.63	
ICF(S)	1.09	1.00	1.10	1.00	1.26	1.16	1.23	1.14	1.21	1.11	1.26	1.17	
ICF(Ne)	1.66	3.42	1.61	3.28	1.26	2.24	1.29	2.32	1.32	2.41	1.26	2.22	
ICF(Ar)	1.66	1.08	1.61	1.09	1.26	1.25	1.29	1.23	1.32	1.21	1.26	1.25	
O ⁺⁺ /O		0.60		0.62		0.79		0.78		0.76		0.79	

^a In units of $12 + \log(X/H)$, for $t^z = 0$. Columns 2, 4, 6, 8, 10 and 12 derived using Kingsburgh & Barlow (1994) ICFs. Columns 3, 5, 7, 9, 11 and 13 derived using Delgado-Inglada et al. (2014) ICFs.

We found that the CarNW and CarSW regions appear to have the same abundances, however the CarSE region, hosting η Car, seems to be under-abundant in O/H and Ne/H. The lower O/H in CarSE is consistent with other determinations for the nebula around η Car (eg. Davidson et al. 1986). At the other hand, all three regions present the same N/H, therefore CarSE has the highest N/O ratio, in agreement with the high N/O ratio reported for several condensations around η Car by Dufour et al. (1997) and Smith & Morse (2004) evidencing the modified chemical composition of the ejected material around η Car. Dufour et al (1997) found that, compared to Solar Neighborhood HII regions, the S2 and S3 sub-condensations of the η Carina ejecta, which consist of material ejected at very high velocities, has undergone extreme CNO-cycle processing such that essentially all of the C and O have been transformed into N. This is further evident by the 60 – 80% overabundance of He/H in these ejecta. The localized N/C and N/O ratios are 10^3 times higher than in the Sun or the local ISM (Dufour et al 1997). In our larger scans however, these differences are much diluted and we do not found such high N/O ratios.

At the other hand, the lower Ne/H in CarSE is in manly due to its lower $\text{Ne}^{++}/\text{H}^+$ observed in this region, as compared to CarNW and CarSW (Table 6). However, the $\text{Ne}^{++}/\text{H}^+$ ratio has large errors due to uncertainties in the reddening correction applied to the $[\text{NeIII}] \lambda 3869$ line flux in the blue part of the spectrum. If we correct the CarSE spectrum with our derived extinction law fit, instead of that of CCM89 with $R_V = 4.2$, the Ne/H is increased by ~ 0.05 dex, however we would obtain similar increments for the CarNW and CarSW regions.

Glover et al. (1998) present *HST FOS* spectroscopy of the bright ejecta in the homunculus around η Carina, which allowed them to kinematically resolve the emission arising in the J1 and J2 knots. They found that the temperature-sensitive ratio $[\text{NII}] \lambda 6584/\lambda 5755$ decreases in the contaminated (inherent + reflected) spectrum with respect to the pure nebular (inherent) spectrum, yielding a much higher contaminated temperature $T_e(\text{NII})_{\text{contaminated}}$ (similar to our *.all* temperature) than the inherent temperature $T_e(\text{NII})_{\text{inherent}}$ (similar to our *.neb* temperature). This temperature difference yields a smaller $(\text{N}^+/\text{H}^+)_{\text{contaminated}}$ abundance than the $(\text{N}^+/\text{H}^+)_{\text{inherent}}$ one. In our much wide-area integrated spectra, we found however that $(\text{N}^+/\text{H}^+)_{\text{.all}} > (\text{N}^+/\text{H}^+)_{\text{.neb}}$ in CarSE by 0.02 dex, which is not significant. Glover et al. (1998) stress the importance of considering this scattered light contamination in the derivation of ionic and total abundances, which is an issue we study in detail in Chapter VI.

In Table 8 we present our *.neb* total abundances and compare them with other determinations adapted from the literature. In column (2) we give the average of our 3 Carina regions (CarNW, CarSE and CarSW). However, as mentioned before, the CarSE region, containing η Car, have uncertain T_{OIII} and T_{NII} determinations, and we present in column (3) the average abundances of the CarNW and CarSW regions only, which we will consider as representative of the whole nebulae. Column (4) gives the average error for each element since they are similar for the 3 regions. The errors given for the ICFs are adapted from the formulae provided by DI14.

It is surprising the lack of “nebular work” for the Carina HII region itself, putting aside the extensive work on η Car, the *homunculus* and the condensations and jets around it. Faulkner & Aller (1965) presented low resolution spectroscopy of the Carina nebula and found $12 + \log(\text{O}/\text{H}) = 8.24 \pm 0.15$ in excellent agreement with our results. As mentioned before, Peimbert, Torres-Peimbert & Rayo (1978; PTPR78) presented observations of 8 slit positions around η Car, from which they derive the physical conditions and total abundances. Seven of these positions lie within our CarSE region and one of them lies in our CarSW region. However, they were able to measure $[\text{OIII}] \lambda 4363$ and $[\text{NII}] \lambda 5755$ line fluxes (needed to determine T_{OIII} and T_{NII}), only in 3 positions. These authors considered Whitford (1958) extinction law to de-redden the observed spectra and extrapolated their T_{NII} values for the regions where they did not count with a direct measurement. They used the canonical ICFs for O, N and Ne, but they consider for sulfur that $\text{S}/\text{H} = (\text{O}/\text{O}^+) \times (\text{S}^+ + \text{S}^{++})/\text{H}^+$, which usually yields

overestimated S/H values (Dennefeld & Stasińska 1983). The abundances' errors reported by PTPR78 are similar to ours.

Table 8. Total (*neb*) abundances for the Carina regions (without temperature fluctuations, $t^2 = 0$). ^a

	$\langle \text{Car} \rangle$ 3 regs.	$\langle \text{Car} \rangle$ 2 regs.	error	$\langle \text{PTPR78} \rangle^b$ w/ DI14 ICF	DS83 ^c w/ DI14 ICF	Orion E04 w/ DI14 ICF	$\langle \text{PTPR78} \rangle$ original	DS83 original	Orion E04 original
(1)	(2)	(3)	(4)	(5)	(6)	(7)	(8)	(9)	(10)
O	8.16	8.24	± 0.14	8.20	8.34	8.51	8.29	8.37	8.51
N	7.20	7.21	± 0.12	7.38	7.54	7.52	7.44	–	7.65
S	6.45	6.48	± 0.11	6.56	6.72	7.11	6.93	6.90	7.06
Ne	7.62	7.75	± 0.12	7.65	7.79	8.01	7.48	–	7.78
Ar	6.09	6.12	± 0.14	6.12	6.12	6.48	–	–	6.50
log N/O	-0.96	-1.03	± 0.26	-0.82	-0.80	-0.99	-0.85	–	-0.86
log S/O	-1.71	-1.75	± 0.25	-1.64	-1.62	-1.40	-1.36	-1.47	-1.45
log Ne/O	-0.54	-0.49	± 0.26	-0.55	-0.55	-0.50	-0.81	–	-0.73
log Ar/O	-2.06	-2.12	± 0.28	-2.09	-2.22	-2.03	–	–	-2.01
ICF(N)	3.03	2.87	± 1.15	2.13	1.72	4.19	–	–	5.62
ICF(S)	1.10	1.09	± 0.60	1.00	1.00	1.24	–	–	1.10
ICF(Ne)	2.60	2.75	± 0.20	3.87	4.10	2.07	–	–	1.23
ICF(Ar)	1.19	1.17	± 0.65	1.05	1.03	1.29	–	–	1.35
O^{++}/O	0.73	0.70	± 0.08	0.62	0.52	–	–	–	0.82
$c(\text{H}\beta)$	1.01	1.01	± 0.08	1.00	–	–	0.70	–	–
T_{OIII}	9.6	9.4	± 0.6	9.0	9.0	–	8.7	8.8	–
T_{NII}	11.3	10.5	± 1.2	10.5	8.9	–	9.6	8.9	–
$(\lambda 3727/\text{H}\beta)_0$	154.2	155.4	± 10.8	176.8	–	–	–	–	–
$(\lambda 5007/\text{H}\beta)_0$	254.5	273.1	± 10.6	196.5	–	–	–	–	–
$(\lambda 6584/\text{H}\beta)_0$	36.1	33.9	± 2.4	64.8	74.4	–	–	–	–
$(\lambda 6725/\text{H}\beta)_0$	19.3	19.1	± 1.9	27.8	29.2	–	–	–	–
$(\lambda 6312/\text{H}\beta)_0$	1.19	0.835	± 0.20	1.50	–	–	–	–	–
$(\lambda 9532\text{H}\beta)_0$	59.3	57.2	± 2.3	–	75.8	–	–	–	–
$(\lambda 3869/\text{H}\beta)_0$	13.8	15.8	± 2.2	8.77	–	–	–	–	–
$(\lambda 7136/\text{H}\beta)_0$	10.2	10.4	± 1.0	11.7	10.8	–	–	–	–
$\text{O}^+/\text{H}^+ (10^{-5})$	4.14	5.11	± 2.30	6.18	10.5	–	–	–	–
$\text{O}^{++}/\text{H}^+ (10^{-5})$	10.7	12.2	± 2.90	10.0	11.4	–	–	–	–
$\text{N}^+/\text{H}^+ (10^{-6})$	5.55	6.12	± 1.60	11.5	20.2	–	–	–	–
$\text{S}^+/\text{H}^+ (10^{-7})$	3.60	4.06	± 1.00	6.48	9.88	–	–	–	–
$\text{S}^{++}/\text{H}^+ (10^{-6})$	2.29	2.50	± 0.55	3.03	4.48	–	–	–	–
$\text{Ne}^{++}/\text{H}^+ (10^{-5})$	1.73	2.09	± 0.60	1.38	1.52	–	–	–	–
$\text{Ar}^{++}/\text{H}^+ (10^{-6})$	1.05	1.12	± 0.20	1.22	1.29	–	–	–	–

^a In units of $12 + \log(X/H)$. Electron temperatures in kK. Linear de-redden line flux ratios relative to $F\beta = 100$. ^b Average results for 3 slit positions within CarSE derived from PTPR78's *observed* fluxes following the same procedure as the one used

for our observations, for $t^2 = 0$. ^c Derived from the observed lines fluxes reported by DS83 for 1 slit position within CarSE, for $t^2 = 0$. ^d Derived from the ionic abundances reported by Esteban et al. (2004) for $t^2 = 0$, applying DI14's ICFs.

In order to make a fair comparison with our observations, we considered the *observed* fluxes for the 3 slit positions with complete observations given by PTPR78 and derived the $c(H\beta)$ reddening constant using CCM89 extinction law for $R_V = 4.2$, which is better suited for the Carina nebula than Whitford's extinction law (Sec. 4.4.2). We found $\langle c(H\beta) \rangle \approx 1.0$, in excellent agreement with our results (Tables 2a – 2c). We used these de-reddened fluxes to calculate the physical conditions, ionic abundances and total abundances following the same procedure that we used for our observations, and we report our results in column (5) of Table 8: The procedure followed is: *i*) we de-reddened their observed spectra using CCM89 extinction law for $R_V = 4.2$; *ii*) we used these de-reddened line fluxes to calculate the temperatures in the high and low ionization zones, T_{OIII} and T_{NII} , using the *temden* routine within IRAF. We found very good agreement with the corresponding temperatures derived using our spectra (Table 8). We used $n_e(\text{SII}) = 400 \text{ cm}^{-3}$ as estimated by PTPR78. *iii*) Using these temperatures and density we derived the ionic abundances for each region using the *ionic* routine within IRAF. *iv*) Finally, with these ionic abundances we calculated the corresponding total abundances using the ICFs given by DI14, just as we did with our spectra, and we present all the results in column (5) of Table 8. For comparison, we list PTPR78 original reported values in column (8) of Table 8.

Besides PTPR78 observations of the η Carina nebula, Dennefeld & Stasińska (1983; DS83) present visual and near IR observations for PTPR78's slit position 3a, lying within our CarSE region. DS83 obtained spectra for the nebula from $H\alpha \lambda 6563$ to $[\text{SIII}] \lambda 9532$, and considered PTPR78's observations for the blue part of the spectrum. As before, we considered the *observed* fluxes reported by DS83 and followed exactly the same procedure described above to rework PTPR78's observations. We present our results in column (6) of Table 8. In column (9) we present the original values reported by DS83. For comparison, we include in column (7) of Table 8 the total abundances for Orion computed from the ionic abundances reported by Esteban et al. (2004; E04) ignoring temperature fluctuations ($t^2 = 0$), but derived using the ICF's of DI14. The original values computed by E04 are also given in column (10) of Table 8.

We found that our N/H and S/H abundances are smaller by $\sim 0.2 - 0.3$ dex than those reported by PTPR78 and DS83. We tracked down the source of these differences and found that they are due to differences in the de-reddened fluxes (see Table 8). Our scan spectra represent an average over an area of about $7' \times 7'$ over the face of the nebula, while PTPR78 and DS83 narrow slit observations were located at 3 fixed bright zones a few arcmin away from η Car. We found that in general, our larger scans yields lower integrated fluxes of low-ionization ions, such as N^+ , S^+ , S^{++} and O^+ , and larger

integrated fluxes for high-ionization ions, such as O^{++} and Ne^{++} , as compared to the narrow slit observations.

For nitrogen, we tracked down the source of the difference and found that it is not due to differences in T_{NII} nor in the adopted $ICF(N)$, but to differences in the dereddened line fluxes. That is, $(F_{6584}/F\beta)_0^{Our} = 33.9$, while $(F_{6584}/F\beta)_0^{PTPR78} = 64.8$ (taking $F\beta = 100$), therefore our N/H is a factor of 1.5 smaller than that of PTPR78. In the case of DS83 observations, after normalizing their red-spectra to PTPR78's blue spectra, we found $(F_{6584}/F\beta)_0^{DS83} = 74.4$. On top of this, the derived low-ionization zone temperature from DS83 data is only $T_{NII} = 8.9$ kK, what yields a N^+/H^+ abundance a factor of 3.3 higher than ours. Considering that $ICF(N)_{DS83}$ is smaller than ours, it turns out that our total N/H abundance is still a factor of 2.1 lower than DS83's value. However, considering the uncertainties assigned to the total abundances, we conclude that the derived N/H is consistent among the three estimations.

For sulfur, we also found that the S/H discrepancy between our results and those derived using PTPR78 and DS83 spectra is mainly due to differences in the de-reddened line fluxes (see Table 8). Our S^+/H^+ and S^{++}/H^+ are both smaller than the corresponding values derived by PTPR78 and DS83, and, given that the $ICF(S)$ used are not too different, it turns out that our total S/H abundance is also smaller than theirs. This difference is not due to differences in the atomic parameters, since we are using the same ion emissivities stored within IRAF. Note however, that S/H is uncertain because the $[SIII] \lambda 9532$ may be affected by the process of sky subtraction, while $[SIII] \lambda 6312$ is usually a very faint line.

For neon, although $(F_{3869}/F\beta)_0^{Our}$ is a factor of 1.8 larger than $(F_{3869}/F\beta)_0^{PTPR78}$, we found $T_{OIII}^{Our} = 9.4$ kK, while $T_{OIII}^{PTPR78} = 9.0$ kK, such that $(Ne^{++}/H^+)_{Our}$ is a factor of 1.5 larger $(Ne^{++}/H^+)_{PTPR78}$. After correcting for the corresponding $ICFs$, we found reasonable agreement within the errors for the total Ne/H among our, PTPR78 and DS83 determinations.

For oxygen we found $(F_{3727}/F\beta)_0^{Our} = 155$ and $(F_{5007}/F\beta)_0^{Our} = 273$, while PTPR78 spectra yield a lower excitation nebula, with $(F_{3727}/F\beta)_0^{PTPR78} = 177$ and $(F_{5007}/F\beta)_0^{PTPR78} = 196$. Considering the corresponding electron temperatures, we found that $(O^+/H^+)_{Our}$ is a factor of 1.2 smaller than $(O^+/H^+)_{PTPR78}$, while $(O^{++}/H^+)_{Our}$ is a factor of 1.2 larger than $(O^{++}/H^+)_{PTPR78}$. Therefore, the total O/H abundance is in reasonable agreement within the errors for the 3 set of spectra (ours, PTPR78 and DS83).

In general, our abundances are 0.2 to 0.3 dex smaller than those found for Orion, with a larger deviation for S/H . The galactocentric distance for Orion is $R_G(\text{Orion}) = 8.8$ kpc (Esteban et al. 1998) and that for Carina is $R_G(\text{Carina}) = 8.1$ kpc (PTPR78), so we do not expect them to have such large

differences in chemical composition. According to the negative metallicity gradient derived by Deharveng et al. (2000) for HII regions in the Galaxy, the assigned O/H for Carina is $12 + \log(\text{O}/\text{H})_{\text{Deharveng}} = 8.50 \pm 0.05$, while that of Orion is 8.47 ± 0.05 . However our spectra indicate $\text{O}/\text{H} = 8.24 \pm 0.14$. The main reason for these differences is in the assigned electron temperatures: for the Carina regions we found $T_{\text{OIII}} = 9.4 \pm 0.6$ kK and $T_{\text{NII}} = 10.5 \pm 1.0$ kK, while Esteban et al (2004) used for Orion $T_{\text{high}} = 8.3 \pm 0.05$ kK and $T_{\text{low}} = 10.0 \pm 0.4$ kK.

Deharveng et al. (2000) compiled calculations of the electron temperature T_e , derived from radio recombination lines observations for a large number of galactic HII regions and found a galactic gradient in the sense that, the regions farther away from the center of the Galaxy tend to be hotter. However, by inspection of their reported figures, we found that there is a wide spread of T_e values, of at least ± 2.0 kK, at a given galactocentric distance. Therefore, our assigned temperatures for Carina are consistent with this spread of T_e and we trust our results that indicate that Carina is a low-metallicity HII region. In fact, Faulkner and Aller (1965) also found that O/H is 0.20 dex smaller in Carina than in Orion. Peimbert & Peimbert (2010) have shown that an important fraction of O atoms may be trapped into dust grains, so the total O/H gas-phase abundance should be increased by 0.10 ± 0.03 dex. Our results may suggest also that there is a higher dust-depletion of O atoms in Carina than in Orion, which has yet to be confirmed. Part of this difference may be related to the anomalous extinction law for the Carina region, with $R_V = 3.9 - 5.0$ (Sec. 4.2.1).

To better address the electron temperature issue, Garnett (1992) proposes to use a 3-zone scheme for the temperatures in HII regions. That is, use T_{NII} for N^+ , O^+ and S^{++} ; use T_{OIII} for O^{++} and Ne^{++} , but use an intermediate-zone temperature, given by $T_{\text{med}} = 0.83T_{\text{OIII}} + 1700$ (K) for S^{++} and Ar^{++} . We recalculated our S^{++} and Ar^{++} using this “improved” temperature and found that S^{++} increases by 0.12 dex on average for our three regions, and Ar^{++} decreases only by -0.01 dex, so this alleviate at least in part out low S/H abundance.

4.6 Total abundances considering temperature fluctuations

In this section, we estimate the temperature fluctuations in our Carina regions and their effect on the derived chemical abundances. The diagnostic diagrams shown in Figs. 2a – 2c, suggest the presence of considerable temperature and density variations in the Carina regions. Peimbert (1967) first introduced the root-mean-square temperature fluctuation parameter t^2 , as a measure of the quadratic deviation of the local electron temperature $T_e(\mathbf{r})$, with respect to the average temperature T_0 , weighted by the density of a given ion and integrated over the whole emitting volume. It is possible to estimate t^2 by comparing the temperature derived from a collisionally excited line, which is weighted towards higher temperatures, with the temperature derived from the ratio of the Balmer continuum to a Balmer line, or

from the ratio of a radio line to continuum observations, both of which sample lower temperature zones. The reason that this ratio depends upon the temperature is that the emission in the continuum, per unit wavelength interval, depends upon the width of the free-electron velocity-distribution, i.e., on T_e . It has been found that the temperature derived from the Balmer jump and the H β flux $T_e(\text{Bal})$, is typically ~ 1500 K *lower* than T_{OIII} derived from forbidden lines (Peimbert 1971; Liu & Danziger 1993, Peimbert & Peimbert 2011), suggesting the presence of temperature fluctuations. At the other hand, photoionization models of chemically homogeneous HII regions predict t^2 values typically in the 0.003 – 0.01 range, while observations yield t^2 values typically in the 0.02 – 0.06 range. (Peimbert & Peimbert, 2011), so an extra mechanism is required in the models to account for the observed t^2 values.

Our spectra start at about $\lambda 3500$, so we were able to measure the Balmer jump $\Delta(\text{Bal})_{\text{obs}}$, defined as the difference in the nebular continuum on both sides of the Balmer series limit at $\lambda 3646$ Å (see for example, Fig. 8b of Chapter II). As a first approach, we de-redden our spectra extrapolating our Carina extinction law (Tables 2a – 2c) down to this wavelength limit, however, since our extinction law was only defined down to H11, it predicted a very strong correction for $\lambda \leq 3700$ Å, giving us only upper limits for $\Delta(\text{Bal})_{\text{obs}}$.

Instead, we used the IRAF routine *deredden*, which is based on CCM89 extinction law, to correct our observed spectra for reddening, with the $c(\text{H}\beta)$ and R values listed in Tables 2a – 2c. We fitted the nebular de-reddened continuum underlying the high Balmer series (from $\lambda 4000$ down to $\sim \lambda 3760$ Å) and measured the intensity of the continuum on the both sides of the $\lambda 3646$ jump. In this way we derived $\Delta(\text{Bal})_{\text{obs}}$ values ($\text{erg cm}^{-2} \text{s}^{-1} \text{\AA}^{-1}$) for our 3 Carina regions. We define the observed Balmer discontinuity as $BD_{\text{obs}} = \Delta(\text{Bal})_{\text{obs}}/F(\text{H}\beta)_0$ (\AA^{-1}), where $F(\text{H}\beta)_0$ is the intrinsic H β flux ($\text{erg cm}^{-2} \text{s}^{-1}$) taken from Tables 2a – 2c. We present our results in Table 9 below, emphasizing the large uncertainties involved, $\sim 20\%$, arising from the process of fitting the continuum and the de-reddening correction applied. Another source of error in $\Delta(\text{Bal})_{\text{obs}}$ comes from the presence of starlight scattered by dust around $\lambda 3646$ in our *neb* spectra (Chapter VI). Since we are dealing with hot stars, (Table 2a of Chapter II), we expect the integrated stellar Balmer jump in absorption to be small, producing only a small negative contribution to $\Delta(\text{Bal})_{\text{obs}}$, that is within the errors arising from fitting the continuum (Liu et al. 1995). Consequently, we will neglect this effect, which in any case would increase the derived $\Delta(\text{Bal})_{\text{obs}}$ in a few percent.

At the other hand, it is possible to make a theoretical estimation of the Balmer electron temperature $T_e(\text{Bal})$, in terms of the observed Balmer jump and the H β intrinsic flux, taking into account all possible physical processes contributing both to the H β emission and to the continuum emission. To estimate this temperature we proceed as follow: first we model the dependence of the H β

emissivity upon temperature $\varepsilon_{\text{H}\beta}$ ($\text{erg cm}^{-3} \text{ s}^{-1}$) using the fits presented by Péquignot, Petitjean & Boisson (1991) for the case B H β effective recombination coefficient $\alpha_{\text{H}\beta}$ ($\text{cm}^{-3} \text{ s}^{-1}$),

$$\alpha_{\text{H}\beta} = 10^{-13} \times 0.668 t^{-0.507} / \left(1 + 1.221 t^{0.653} \right), \quad (20)$$

where the electron temperature is expressed as $t = T_e(\text{K})/10^4$. From this effective recombination coefficient, we calculate the H β emissivity ($\text{erg cm}^{-3} \text{ s}^{-1}$),

$$\varepsilon_{\text{H}\beta} = N_e N_{\text{H}^+} \alpha_{\text{H}\beta} h\nu_{\text{H}\beta} \quad (21)$$

where N_e and N_{H^+} are the electron and H $^+$ densities (cm^{-3}), and $h\nu_{\text{H}\beta}$ is the H β photon energy (erg). Péquignot et al. (1991) emissivities agree with those given by SH95 to within 1% for a given temperature.

The nebular continuum emissivity $\varepsilon_c(\lambda)$ ($\text{erg cm}^{-3} \text{ s}^{-1} \text{ \AA}^{-1}$), has in general the following components: *i*) recombination of electrons with excited H $^+$, *ii*) recombination of electrons with excited He ions, *iii*) bremsstrahlung emission produced by free-free transitions of electrons in the Coulomb fields of H and He ions, and *iv*) radiation produced by two-photon decay from the metastable $2^2\text{S}_{1/2}$ level of hydrogen. Using Brown & Mathews' (1970) formalism, we can write,

$$\varepsilon_c(\lambda) = \varepsilon_{\text{H}}(\lambda) + \varepsilon_{\text{HeI}}(\lambda) + \varepsilon_{\text{HeII}}(\lambda) + \varepsilon_{2q}(\lambda), \quad \text{or,} \quad (22)$$

$$\varepsilon_c(\lambda) = N_e N_{\text{H}^+} \left[\gamma_{\text{H}}(\lambda) + \frac{N_{\text{He}^+}}{N_{\text{H}^+}} \gamma_{\text{HeI}}(\lambda) + \frac{N_{\text{He}^{++}}}{N_{\text{H}^+}} \gamma_{\text{HeII}}(\lambda) + \frac{N_e}{N_{\text{H}^+}} \gamma_{2q}(\lambda) \right] \quad (23)$$

where the $\gamma(\lambda)$ terms ($\text{erg cm}^{-3} \text{ s}^{-1} \text{ \AA}^{-1}$) are the atomic continuum emission coefficients for each ion and include the contributions from both bound-free and free-free transitions. Our integrated spectra show no evidence of doubly ionized He for none of our objects, so we will neglect the term $\gamma_{\text{HeII}}(\lambda)$ in Eq. (23).

We can now define the theoretical Balmer discontinuity BD_{theo} (\AA^{-1}) as,

$$BD_{\text{theo}} = \left[\frac{\Delta(\text{Bal})}{F(\text{H}\beta)_0} \right]_{\text{theo}} = \frac{\Delta\varepsilon_c}{\varepsilon_{\text{H}\beta}}, \quad (24)$$

where $\Delta\varepsilon_c = [\varepsilon_c(\lambda_2) - \varepsilon_c(\lambda_1)]$, is the difference in the continuum emissivity on both sides of the Balmer discontinuity, and was calculated using Eq. (23).

We used the continuum coefficients tabulated by Brown & Mathews (1970) to calculate $\gamma_{\text{HI}}(\lambda)$, $\gamma_{\text{HeI}}(\lambda)$ and $\gamma_{2q}(\lambda)$ as function of temperature within the wavelength range used to derive $\Delta(\text{Bal})_{\text{obs}}$: $\lambda 3646^-$ to $\lambda 3760 \text{ \AA}$. In this wavelength interval, the main contributions to $\varepsilon_c(\lambda)$ come from the terms γ_{HI} and γ_{HeI} . Let us define the difference in a continuum coefficient at two wavelengths, $\Delta\gamma(\lambda_2 - \lambda_1) = \gamma(\lambda_2) - \gamma(\lambda_1)$. At $T_e = 10^4 \text{ K}$, $\Delta\gamma_{\text{HI}}(\lambda 3646^+ - \lambda 3646^-) = 5.29 \times 10^{-28} \text{ erg cm}^3 \text{ s}^{-1} \text{ \AA}^{-1}$, as measured at both sides of the Balmer jump. At the other hand, $\Delta\gamma_{\text{HI}}(\lambda 3760 - \lambda 3646^-)$ is only 3% smaller than $\Delta\gamma_{\text{HI}}(\lambda 3646^+ - \lambda 3646^-)$, so we consider $\Delta\varepsilon_{\text{HI}} \approx N_e N_{\text{H}^+} \Delta\gamma_{\text{HI}}(\lambda 3646^+ - \lambda 3646^-)$. The contribution from $\Delta\gamma_{\text{HeI}}(\lambda 3680^+ - \lambda 3680^-)$ at $T_e = 10^4 \text{ K}$ is 18% that of $\Delta\gamma_{\text{HI}}$. To compute the $\gamma_{2q}(\lambda)$ coefficient we used the simplified description of Osterbrock & Ferland (2006), which is valid for low density nebula. The two-photon continuum coefficient $\Delta\gamma_{2q}(\lambda 3760 - \lambda 3646^-)$, contributes only slightly, with $0.03 \times 10^{-28} \text{ erg cm}^3 \text{ s}^{-1} \text{ \AA}^{-1}$. To compute $\Delta\varepsilon_{\text{HeI}}$, we considered $N_{\text{He}^+}/N_{\text{H}^+} = 0.091$ (Table 6).

Considering the terms γ_{HI} , γ_{HeI} , and γ_{2q} , we found a power-law fit for the difference of the continuum emissivity as function of temperature ($\text{erg cm}^{-3} \text{ s}^{-1} \text{ \AA}^{-1}$),

$$\log [\Delta\varepsilon_c] = -36.87 \times 9.60 t^{-0.067}, \quad (25)$$

with a precision better than 1%, where t is in units of 10^4 K . With $\Delta\varepsilon_c$ from Eq. (25) and $\varepsilon_{\text{H}\beta}$ from Eq. (20) and (21), we found the following expression for the Balmer temperature $T_e(\text{Bal})$, as function of the Balmer discontinuity,

$$T_e(\text{Bal}) (\text{kK}) = 1.27 + 137 \times \left[\frac{\Delta(\text{Bal})}{F(\text{H}\beta)_0} (10^{-3} \text{ \AA}^{-1}) \right]^{-1.84}. \quad (26)$$

We present this relation in Fig. 3 and compare it with other determinations found in the literature and with observational data. We compare Liu et al. (1995) theoretical relation, $T_e(\text{Bal}) = 93.95 \times [\Delta(\text{Bal})/F(\text{H}\beta)_0 \text{ m\AA}^{-1}]^{-1.49} \text{ kK}$, with ours, assuming $F(\text{H}11)/F(\text{H}\beta) = 0.04$ (SH95). Liu et al. (1995) define their Balmer jump as $\Delta(\text{Bal}) = [i_c(\lambda 3861) - i_c(\lambda 3464)]$ so as to include the HeI continuum, and normalize it with respect to H11 at $\lambda 3771 \text{ \AA}$ to avoid the problem of reddening. We also show the fit given by Walter & Dufour (1994), $T_e(\text{Bal}) = 95.49 \times [\Delta(\text{Bal})/F(\text{H}\beta)_0 \text{ m\AA}^{-1}]^{-1.52} \text{ kK}$, and we can see that all three relations are very similar. In the upper part of Fig. 3, we indicate with three small arrows the measured Balmer discontinuity for our Carina regions. We list in Table 9 the derived $T_e(\text{Bal})$ for our Carina regions using our fit (Eq. 26), with computed errors not less than 30%.

In Fig. 3 we also compare our results with various observations found in the literature. As shown in the figure, the determination of $T_e(\text{Bal})$ is uncertain: for Orion, Liu et al. (1995) found $T_e(\text{Bal}) \approx 9.0 \text{ kK}$, while Peimbert (1967) reported $T_e(\text{Bal}) \approx 6.5 \text{ kK}$. These large variations correspond to systematic

errors in the process of evaluating $\Delta(Bal)_{\text{obs}}$ and BD_{theo} , as well as to real spatial T_e variations at different slit positions within the nebula.

Table 9. Balmer discontinuities, Balmer- and average-temperatures, and f^2 values for Carina ^a

	CarNW.neb	CarSE.neb	CarSW.neb
BD_{obs}^a	5.00 ± 1.00	4.58 ± 0.92	5.01 ± 1.00
$T_e(Bal)$	$8.1^{+2.4}_{-1.5}$	$9.3^{+2.4}_{-1.8}$	$8.1^{+2.4}_{-1.6}$
$T_e(\text{OIII})$	9.7 ± 0.6	10.0 ± 0.5	9.1 ± 0.5
$T_e(\text{NII})$	9.8 ± 0.9	12.8 ± 1.8	11.2 ± 1.2
$f^2(\text{O})$	$0.034^{+0.021}_{-0.034}$	$0.015^{+0.027}_{-0.015}$	$0.021^{+0.024}_{-0.021}$
$T_0(\text{O})$	$8.6^{+2.4}_{-1.5}$	$9.5^{+2.4}_{-1.8}$	$8.4^{+2.4}_{-1.6}$
$f^2(\text{N})$	$0.047^{+0.023}_{-0.036}$	$0.096^{+0.012}_{-0.022}$	$0.086^{+0.015}_{-0.031}$
$T_0(\text{N})$	$8.8^{+2.4}_{-1.5}$	$11.1^{+2.4}_{-1.8}$	$9.4^{+2.3}_{-1.6}$
$\langle f^2 \rangle$	$0.040^{+0.022}_{-0.034}$	$0.056^{+0.020}_{-0.019}$	$0.053^{+0.020}_{-0.026}$

^a Observed Balmer discontinuity $BD_{\text{obs}} = \Delta(Bal)_{\text{obs}}/F(\text{H}\beta)_0$ in 10^{-3} \AA^{-1} , where $F(\text{H}\beta)_0 = 38.8, 43.2,$ and $44.7 \times 10^{-11} \text{ erg cm}^{-2} \text{ s}^{-1}$, for CarNW, CarSE and CarSW, respectively. All temperatures are given in kK.

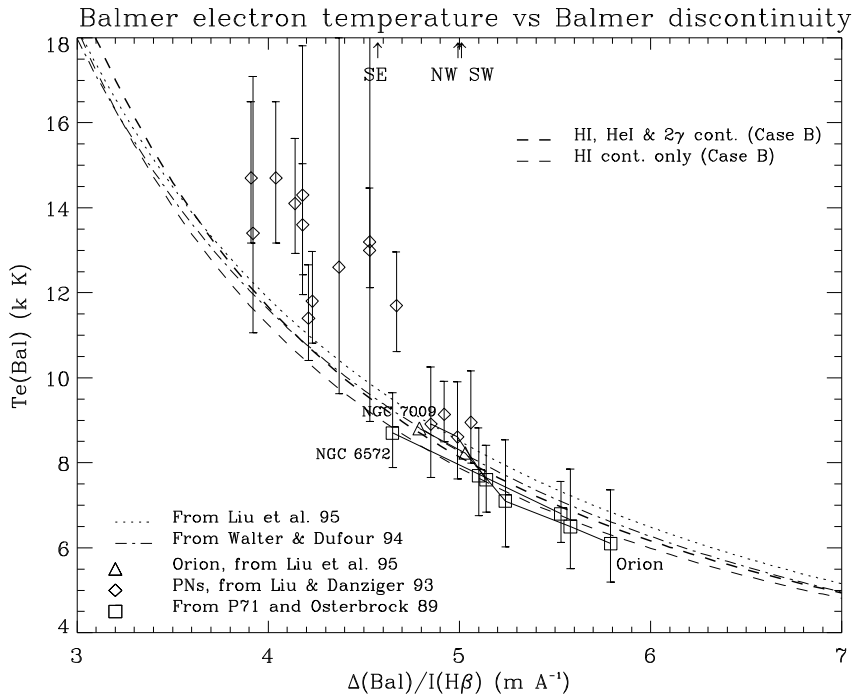


Fig. 3. Balmer electron temperature as function of the Balmer discontinuity (dashed lines) compared with other determinations from Liu et al. (1995) and Walter and Dufour (1994). Observations include: *i*) 3 slit positions in Orion from Liu et al. (1995); *ii*) 16 PNs from Liu & Danziger (1993), and *iii*) another 3 positions in Orion and 3 PNs from Peimbert (1967, 1971; P71), Peimbert & Torres-Peimbert (1971) and Osterbrock (1989). We joined with solid lines the different observations for Orion, NGC 6572 and NGC 7009. Note that most of Liu & Danziger (1993) PNs have higher $T_e(Bal)$ than predicted. The measured Balmer discontinuities for our 3 Carina regions are indicated with small arrows in the upper part of the figure.

Following Peimbert (1971) and Garnett (1992), we now relate $T_e(Bal)$ and the electron temperatures from the collisional excited lines $T_e(OIII)$ and $T_e(NII)$ with an average electron temperature T_0 , and the t^2 parameter for each ion: *i)* $T_e(OIII) = T_0^O + (45690 - 1.5T_0^O) t_{O}^2$; *ii)* $T_e(NII) = T_0^N + (34565 - 1.5T_0^N) t_{N}^2$, and *iii)* $T_e(Bal) = T_0^H (1 - 1.67 t_H^2)$, where T_0^O and T_0^N correspond to an *average* temperature in the high- and low-ionization zones respectively, and T_0^H is an overall average temperature. The different t^2 correspond to these different zones. With our computed values for $T_e(OIII)$, $T_e(NII)$, and $T_e(Bal)$ (Tables 5 and 9), we solved simultaneously equations *i)* and *iii)* (assuming $T_0^O = T_0^H$ and $t_O^2 = t_H^2$), and equations *ii)* and *iii)* (assuming $T_0^N = T_0^H$ and $t_N^2 = t_H^2$), and obtained the average temperatures T_0 and t^2 values shown in Table 9. The errors were computed formally considering the errors in $T_e(OIII)$, $T_e(NII)$ and $T_e(Bal)$. We found for Carina that t^2 is in the range 0.040–0.053, with typical errors about ± 0.024 .

For each *.neb* spectra, we recalculated the ionic abundances using the IRAF task *ionic* assuming our two-zone scheme, using now T_0^O for O^{++} , Ne^{++} , Ar^{++} , and He^+ , and T_0^N for N^+ , O^+ , S^+ and S^{++} , and the results are given in Table 10. We used these ionic abundances along with DI14's ICFs to estimate the total abundances (X/H), abundance ratios (X/O) and ICFs presented in the lower part of Table 10. The quoted errors consider the uncertainties in the electron temperatures and in the ICFs. We calculated the He^+/H^+ abundance given in Table 10 using *Abelion* emissivities from Stasińska & Leitherer (1996).

As in the previous section, in column (5) of Table 10 we present the results derived from the *observed* line fluxes presented by PTPR78 for the 3 slit positions within CarSE with measured $\lambda 4363$ and $\lambda 5755$ line fluxes. We dereddened their spectra using CCM89 extinction law with $R_V = 4.2$, and used it to find T_{OIII} and T_{NII} using the routine *temden* in IRAF. With these electron temperatures and their assumed $t^2 = 0.035$, we calculated the average low- and high-ionization temperatures, which turned out to be: $T_0^O = 7.8$ kK and $T_0^N = 9.8$ kK (about 1.5 kK smaller than our results). Finally, with these average temperatures we estimated the ionic abundances using the IRAF task *ionic* and with these, we derived the total abundances using DI14's ICFs.

As a further comparison, in Table 10 we also include the derived total abundances, abundance ratios and ICFs using the *observed* red spectra reported by DS83. We followed exactly the same procedure as with PTPR78 data. Finally, in the last column of Table 10 we present the total abundances for Orion derived from the ionic abundances from collisionally excited lines (CEL) presented by E04 for $t^2 = 0.022$, but using DI14's ICFs. In parenthesis we give the original values presented by E04.

Table 10. Ionic, total and relative abundances for the Carina regions including temperature fluctuations. ^a

	NW. <i>neb</i>	SE. <i>neb</i>	SW. <i>neb</i>	error	\langle PTPR78 \rangle ^b	DS83 ^c	Orion (E04) ^d
	(1)	(2)	(3)	(4)	(5)	(6)	(7)
log He ⁺ (λ 5876)	-1.06	-1.04	-1.03	\pm 0.03	-1.02	-	-
log O ⁺ (λ 3727)	-3.95	-4.42	-4.14	\pm 0.18	-4.10	-3.77	-
log O ⁺⁺ (λ 5007)	-3.76	-4.03	-3.74	\pm 0.10	-3.76	-3.69	-
log N ⁺ (λ 6584)	-4.98	-5.21	-5.15	\pm 0.12	-4.87	-4.57	-
log S ⁺ (λ 6725)	-6.19	-6.44	-6.31	\pm 0.09	-6.12	-5.89	-
log S ⁺⁺ (λ 9531)	-5.41	-5.62	-5.57	\pm 0.12	-5.40	-5.25	-
log Ne ⁺⁺ (λ 3869)	-4.49	-4.90	-4.48	\pm 0.12	-4.57	-4.52	-
log Ar ⁺ (λ 7136)	-5.83	-5.99	-5.85	\pm 0.07	-5.69	-5.72	-
O ⁺⁺ /O	0.61	0.71	0.71	\pm 0.05	0.68	0.55	-
O/H	8.45	8.12	8.40	\pm 0.17	8.41 \pm 0.09	8.57	8.67 \pm 0.04 (8.67-8.68)
N/H	7.33	7.21	7.28	\pm 0.15	7.53 \pm 0.09	7.69	7.60 \pm 0.09 (7.73-7.87)
S/H	6.66	6.46	6.53	\pm 0.14	6.69 \pm 0.17	6.84	7.29 \pm 0.04 (7.22-7.23)
Ne/H	8.03	7.53	7.95	\pm 0.15	7.89 \pm 0.09	8.07	8.17 \pm 0.07 (8.05-7.94)
Ar/H	6.20	6.07	6.22	\pm 0.17	6.37 \pm 0.09	6.30	6.62 \pm 0.05 (6.62-6.63)
N/O	-1.12	-0.90	-1.12	\pm 0.32	-0.88	-0.88	-1.07 (-0.94)
S/O	-1.80	-1.65	-1.87	\pm 0.31	-1.71	-1.75	-1.38 (-1.45)
Ne/O	-0.42	-0.59	-0.45	\pm 0.32	-0.52	-0.50	-0.50 (-0.62)
Ar/O	-2.25	-2.04	-2.18	\pm 0.34	-2.04	-2.27	-2.06 (-2.05)
ICF(N)	2.05	2.66	2.69	\pm 39%	2.51	1.80	4.34
ICF(S)	1.00*	1.05	1.05	\pm 54%	1.00	1.00*	1.25
ICF(Ne)	3.35	2.69	2.67	\pm 8%	1.86	3.87	2.04
ICF(Ar)	1.08	1.16	1.16	\pm 54%	1.14	1.05	1.30

^a Logarithmic ionic abundances relative to H⁺. The excitation degree O⁺⁺/O is linear. Total abundances given as 12 + log(X/H). ^b From PTPR78 *observed* fluxes, for $t^2 = 0.035$, using DI14's ICFs. Their S⁺⁺/H⁺ abundance is derived from [SIII] λ 6312. ^c From DS83 *observed* fluxes, for $t^2 = 0.035$, using DI14's ICFs. ^d From E04 for $t^2 = 0.022$, using DI14's ICFs. In parenthesis are given the original values reported by E04, and those recalculated by García-Rojas & Esteban (2007)

Considering temperature fluctuations decreases the assigned temperature of the emitting gas, and therefore the derived ionic and total abundances increase with respect to the case with no temperature fluctuations. For our $t^2 = 0.04$ – 0.05 values found for Carina, O/H increases on average by 0.30 dex, N/H by 0.13 dex, S/H by 0.21 dex, Ne/H by 0.39 dex and Ar/H by 0.09 dex. PTPR78 assumed $t^2 = 0.035$ as a representative average for Carina and report an increment of 0.21 dex for O/H.

As mentioned in the previous section, the temperatures assigned to the CarSE region have large uncertainties and its derivation may be affected by contaminating stellar features. Therefore, we will consider as representative abundances for the Carina regions those derived for CarNW and CarSW. Since the assigned average temperature for CarSE is higher than for CarNW and CarSW (Table 9), it turns out that CarSE present lower abundances than the other two regions.

Our O/H abundance derived from collisionally excited lines (CEL) for Carina is similar to that of PTPR78 and is similar within the errors to that derived by DS83. The value of $O/H = 8.57$ derived from DS83 data is larger than our value of 8.43, because DS83 report a higher [NII] $\lambda 6584$ line flux (Table 8), what yields a much smaller average electron temperature $T_0^N = 8.1$ kK, producing a much higher O^+ and therefore a higher O/H abundance. Our O/H value appears to be about -0.20 dex smaller than Orion's, and as commented in the previous section, about 0.10 dex may be explained by differences in the adopted electron temperatures. There remains an O/H deficiency of 0.10 dex in Carina as compared to Orion, that has to be further investigated, although it is still consistent with the spread of electron temperatures for a given galactocentric distances reported by Deharveng et al. (2000). Considering a dust-depletion of O atoms of 0.08 dex on average as suggested by Peimbert & Peimbert (2010), would increase our derived O/H to 8.65, which is very similar to the Orion value derived from CEL with $t^2 > 0$ (8.67).

It is worth mention that Simón-Díaz (2010) and Nieva and Simón-Díaz (2011) recalculated the abundances of early B-type stars in the Orion OB1 association and found $(O/H)_{B\text{-stars}} = 8.74 \pm 0.03$, $(N/H)_{B\text{-stars}} = 7.82 \pm 0.07$, and $(Ne/H)_{B\text{-stars}} = 8.09 \pm 0.05$, which are in very good agreement with those reported for the Sun by Asplund et al. (2009), $(O/H)_\odot = 8.73 \pm 0.05$, $(N/H)_\odot = 7.87 \pm 0.05$, $(Ne/H)_\odot = 7.97 \pm 0.10$. We see that O/H abundance for Orion derived with CEL and corrected for temperature fluctuations ($t^2 > 0$) and dust-depletion is now in very good agreement with the O/H abundance derived from B stars and the Sun.

Our N/H abundance appears to be 0.20–0.30 dex smaller than the value derived using PTPR78 and DS83 spectra. As mentioned in the previous section, this is mainly due to differences in the de-reddened [NII] $\lambda 6584$ line flux, which appears a factor of 2 smaller in our integrated spectra than in the fixed slit observations of PTPR78 and DS83. Nevertheless, note that the CarSE region has a higher N/O ratio as compared with CarNW and CarSW, in agreement with the nitrogen-rich gas found around η Car, which has an N/O ratio much higher than the general ISM (Dufour et al 1997, Smith & Morse 2004).

Our S/H appears also to be under-abundant with respect to the values derived from PTPR78 and DS83 spectra, however they are still consistent within the assigned errors. The reason for these

differences is in the de-reddened [SII] $\lambda 6725$ and [SIII] $\lambda 9532$ line fluxes. Our line fluxes are smaller than those derived from PTPR78 and DS83 and account for 0.15 dex of the difference. However when compared with Orion, we found a much smaller S/H abundance in Carina, by at least 0.20 dex, after considering the errors. The use of a larger ICF(S) in Orion than in Carina can account only for 0.09 dex of the difference. Nevertheless, recall that the [SIII] $\lambda 9532$ line flux has a large error due to the process of sky subtraction. This result however deserves further investigation. Note also that García-Rojas & Esteban (2007) recalculated Orion physical conditions and ionic abundances using updated atomic parameters from García-Rojas et al 2005. They found basically the same abundances (within 0.02 dex) except for sulfur, which was reduced from 7.29 to 7.20.

We derived a similar Ne/H abundance from our CarNW and CarSW spectra and with PTPR78 and DS83 spectra. This value appears to be ~ -0.10 dex smaller than Ne/H abundance for Orion derived with the new ICFs of DI14. Comparing the Ne/H abundances for Orion derived using the new ICFs with the Ne/H abundance of B stars and the Sun, indicates that the new ICFs may over-estimate the Ne/H abundance by about 0.1 dex. Our Ar/H abundance is consistent within the errors with that derived using PTPR78 and DS83 spectra. However it appears to be deficient by at least -0.10 dex when compared with that for Orion. Considering temperature fluctuations does not modify substantially the excitation parameter of the nebula, since we found for the CarNW and CarSW regions, $(O^{++}/O)_{I2=0} = 0.70 \pm 0.05$, while $(O^{++}/O)_{I2>0} = 0.66 \pm 0.05$.

Comparing Orion abundances derived with the new set of ICFs with the previous ones used by E04 (column 7 of Table 10), we confirm that the use of the new DI14's ICFs leaves O/H, S/H and Ar/H basically the same, but *decreases* the derived N/H abundance by -0.10 dex, while increases Ne/H by 0.10 dex.

4.8 Conclusions

We analyzed *spatially integrated* visual-NIR spectroscopy of 3 regions ($\sim 7 \times 7$ arcmin² each) in the northern part of the Carina Nebula. We derived an extinction law toward the Carina nebula by means of fitting the observed Balmer and Paschen line decrements. We confirm that the extinction is anomalous with an average ratio of total to selective extinction $\langle R_V \rangle = 4.4 \pm 0.4$, in agreement with previous determinations.

The logarithmic reddening correction constant $c(H\beta)$ is the same for the *.all* and *.neb* spectra, except for the CarSE region (hosting η Car), which yields a $c(H\beta).all$ about 0.25 dex *smaller* than $c(H\beta).neb$. At the other hand, when $c(H\beta)$ and the underlying stellar absorption equivalent width W_{abs} ,

are fitted simultaneously (Chapter III), the true $c(\text{H}\beta)$ values are about 0.20 smaller as compared with the case in which W_{abs} is ignored.

We calculated the physical conditions and the ionic and total abundances of O, N, S, Ne and Ar using both the *.all* and the *.neb* spectra in order to study the effect of the stellar component. The *.all* and *.neb* electron densities agree within the uncertainties, and indicate an overall low-density nebula with $n_e \approx 100 - 300 \text{ cm}^{-3}$. We found that the $T_e(\text{OIII}).all$ electron temperature is *larger* than $T_e(\text{OIII}).neb$ by about 500 K, although this difference is within the errors. For the CarSE region, which contains η Car, the broad $\text{H}\gamma$ line present in the *.all* (and still in the *.neb*) spectrum yields spuriously high values for the electron temperature. Besides this, there is a coincident $[\text{FeII}] \lambda 4363$ emission line (Damineli et al. 1998) affecting the true $[\text{OIII}] \lambda 4363$ line flux measurement. For the CarNW and CarSW regions, part of this difference in $T_e(\text{OIII})$ may be due to scattered stellar light that affects the measurement of $\text{H}\gamma$ and the faint $[\text{OIII}] \lambda 4363$ line flux in our mid-resolution spectra. This issue is further discussed in Chapter VI. For the electron temperature derived from the nitrogen lines, we found that $T_e(\text{NII}).all \approx T_e(\text{NII}).neb$ within the errors.

Excluding the CarSE region, the *.all* and *.neb* abundances are the same within the errors, although the O/H, N/H and Ar/H abundances appear to be approximately 0.05 dex *smaller* in the *.all* spectra than in the *.neb* ones.

We found that our scan-integrated spectra produces weaker de-reddened line fluxes for low ionization ions such as O^+ , N^+ and S^+ yielding smaller ionic abundances of these ions as compared with the ionic abundances derived from fixed slit observations found in the literature. At the other hand, our scan-integrated spectra yields stronger de-reddened line fluxes of high ionization ions such as O^{++} and Ne^{++} , yielding larger ionic abundances of these ions as compared to fixed slit observations. As a consequence, our integrated spectra suggest a nebula of higher excitation ($\text{O}^{++}/\text{O} = 0.70$), with a smaller N/H and S/H abundances as compared with fixed slit observations. These differences are not due to differences in the reddening corrections applied, atomic constants or use of ICFs, since all the observations were reduced following the same procedure.

Using the observed Balmer jump in emission, we estimated the Balmer electron temperature $T_e(\text{Bal})$ which allowed us to derive Peimbert's temperature fluctuation parameter t^2 for Carina. We found that t^2 is in the range 0.038–0.052, with typical errors of ± 0.024 . Considering temperature fluctuations increases O/H by 0.20–0.30 dex.

The t^2 -corrected abundances derived from collisional excited lines (CEL) for Carina are similar to those in Orion, although we found 0.1 dex smaller O/H and N/H abundances than previously

reported for Carina, in particular in the CarSE region, yielding higher N/O and S/O ratios for this region. S/H appears -0.45 dex under-abundant in Carina as compared to Orion, although the sulfur abundance has a large uncertainty, of ± 0.14 dex. About 0.10 dex of this difference is because Carina is claimed to be a hotter nebular than Orion, however this issue deserves further investigation, and accurate measurements of [OIII] and [NII] auroral lines are needed for the Carina region.

We compared the use of the new ICF from Delgado-Inglada et al. (2014; DI14) vs. the canonical formulae compiled by Kingsburgh & Barlow (1994; KB94) and found that both sets of ICF yield the same total abundances for O/H and S/H. However, the new ICF's yield smaller N/H (-0.11 dex) and Ar/H (-0.08 dex) and a much larger Ne/H ($+0.27$ dex) abundances than those derived using KB94's ICFs.

We estimate the root mean square density and filling factor of the nebula using radio continuum measurements and our observed $H\beta$ flux (see Appendix III), and found consistent values of $n_{\text{rms}} = 50 \pm 10 \text{ cm}^{-3}$, and $f = 0.2 \pm 0.1$ which can be used as an observational constrain when building photoionization models of the nebula.

Chapter V. M8 and M20 physical conditions and element abundances

5.1. Introduction

In this chapter we present the de-reddened *.all* and *.neb* spectra of our M8 and M20 subregions (Sec. 5.2) and derive their physical conditions (Sec. 5.3). In Sec. 5.4 we derive their ionic abundances and in Sec. 5.5 we calculate their total abundances ignoring temperature fluctuations and make a comparison with other estimations found in the literature. In Sec. 5.6 we estimate the ionic and total abundances including the effect of temperature fluctuations and in Sec. 5.7 we summarize our main results and conclusions.

5.2. Reddening corrections

As mentioned in Chapter II, we obtained spatially integrated spectra of the galactic HII regions M8 and M20 drifting the telescope over the face of the nebula for a given exposure time. We divided M8 in two subregions (M8-E and M8-W) and M20 in two subregions (M20-S and M20-N). Each sub-region corresponds to an area of about $7' \times 7'$ on the sky. The observed line intensities for each region are given in Chapter II and in this section we present their dereddened spectra. As explained in Chapter II, we made two extractions of the spectra: the *.all* spectra, which includes the emission of the gas and stars that crossed the slit during the scans and the *.neb* spectra, for which the “bright” stars were removed from the CCD before obtaining the 1D spectra (see details in Chapter II).

For M8, although there is evidence of an anomalous $R_V = 5.0$ extinction law toward the Hourglass (HG) in the center of the nebula, the extinction is normal beyond this central part (Sanchez & Peimbert 1991; SP91), so we considered the Cardelli, Clayton & Mathis (1989; CCM89) extinction law parameterized for $R_V = 3.1$ as given by Draine (2003), which is given in Table 1a. For M20 we considered the same extinction law. The fit provided by Draine (2003) for the CCM89 extinction law is in good agreement in the visual part of the spectrum with the extinction law given by Seaton (1979) and by Fitzpatrick (1999).

We derived the logarithmic reddening constant $c(H\beta)$ by adjusting the observed Balmer decrement for F_α/F_β , F_γ/F_β and F_δ/F_β to their theoretical case B values at $T_e = 10^4$ K and $n_e = 10^2$ cm⁻³ from Storey & Hummer (1995; SH95). We considered only these lines because they are the best-measured ones and any other bright line does not contaminate them. In our mid-low resolution spectra, H ϵ is blended with [NeIII] $\lambda 3970$, while H8 is blended with HeI $\lambda 3889$. Going further to the blue, the faint H9, H10 and H11 lines have much larger errors. In the red part of the spectra, the Paschen series is strongly affected by the process of sky subtraction. The adopted $c(H\beta)$ for each region is the average

derived from the 3 brightest Balmer line ratios and is given in Tables 1a and 1b for the M8 and M20 regions, respectively.

Having adopted a logarithmic reddening constant $c(H\beta)$ and an extinction law $f(\lambda)$, we derived the dereddened line fluxes using the common expression given in Eq. (5) of Chapter IV. The observed fluxes for M8 and M20 were given in Tables 3b and 3c of Chapter II, respectively, and here we present the dereddened *.all* and *.neb* line fluxes in Tables 1a and 1b for M8 and M20, respectively.

Table 1a. Dereddened $H\beta$ -normalized *.all* and *.neb* line fluxes for M8–E and M8–W subregions ^a

λ	Ion-ID	$f(\lambda)_{\text{CCM31}}$	M8-E. <i>all</i>	M8-E. <i>neb</i>	M8-W. <i>all</i>	M8-W. <i>neb</i>
			$F\lambda/F\beta_0$	$F\lambda/F\beta_0$	$F\lambda/F\beta_0$	$F\lambda/F\beta_0$
3727	[O II]	0.279	1.580	1.418	1.834	1.845
3771	H11	0.267	0.0181	0.0243	0.0224	0.0227
3798	H10 + He I	0.260	0.0263	0.0404	0.0394	0.0441
3835	H9	0.250	0.0417	0.0653	0.0675	0.0688
3869	[Ne III]	0.241	0.141	0.129	0.0967	0.0976
3889	H8 +HeI	0.236	0.188	0.194	0.174	0.182
3970	H ϵ + [Ne III]	0.215	0.190	0.207	0.199	0.212
4026	He I	0.201	0.0149	0.0174	0.0181	0.0178
4069	[S II]	0.190	0.0111	0.0102	0.0191	0.0152
4102	H δ	0.182	0.245	0.261	0.255	0.264
4340	H γ	0.122	0.493	0.490	0.484	0.482
4363	[O III]	0.117	0.0044	0.0049	0.0039	0.0054
4471	He I	0.091	0.0485	0.0468	0.0419	0.0447
4861	H β	0.000	1.000	1.000	1.000	1.000
4922	He I	-0.014	0.0128	0.0134	0.0126	0.0142
4959	[O III]	-0.022	0.839	0.844	0.686	0.665
5007	[O III]	-0.032	2.518	2.523	2.020	2.041
5200	[N I]	-0.074	0.0052	0.0058	0.0073	0.0068
5518	[Cl III]	-0.139	0.0045	0.0046	0.0044	0.0053
5539	[Cl III]	-0.143	0.0038	0.0029	0.0034	0.0035
5577	[O I]	-0.150	0.0216 ^b	0.0205 ^b	0.0182 ^b	0.0183 ^b
5755	[N II]	-0.184	0.0036	0.0044	0.0052	0.0056
5876	He I	-0.206	0.127 ^b	0.142 ^b	0.120 ^b	0.119 ^b
6300	[O I]	-0.278	0.0271	0.0308	0.0543	0.0570
6312	[S III]	-0.280	0.0083	0.0032	0.0072	0.0082
6364	[O I]	-0.289	0.0084	0.0092	0.0171	0.0170
6563	H α	-0.320	2.923	3.228	2.984	3.155
6584	[N II]	-0.323	0.452	0.497	0.657	0.687
6678	He I	-0.337	0.0354	0.0407	0.0366	0.0356
6716	[S II]	-0.342	0.0984	0.107	0.129	0.137
6731	[S II]	-0.344	0.0815	0.0914	0.118	0.125
7065	He I	-0.390	0.0248	0.0275	0.0248	0.0252
7136	[Ar III]	-0.400	0.113	0.128	0.111	0.116
7281	He I	-0.418	0.0080	0.0091	0.0050	0.0052
7325	[O II]	-0.423	0.0284	0.0306	0.0367	0.0371
7751	[Ar III]	-0.473	0.0281	0.0333	0.0245	0.0257
8467	Pa17	-0.544	0.0015	0.0021	0.0028	0.0025
8503	Pa16	-0.547	0.0028	0.0032	0.0036	0.0041
8545	Pa15	-0.551	0.0035	0.0050	0.0046	0.0051
8598	Pa14	-0.555	0.0048	0.0068	0.0053	0.0048
8750	Pa12	-0.568	0.0082	0.0107	0.0101	0.0100

8863	Pa11	-0.577	0.0134	0.0166	0.0141	0.0146
9015	Pa10	-0.590	0.0160	0.0211	0.0194	0.0187
9069	[S III]	-0.594	0.278	0.335	0.326	0.306
9229	Pa9	-0.606	0.0278	0.0341	0.0321	0.0304
9531	[S III]	-0.627	0.669	0.816	0.811	0.737
9712	HeI	-0.639	0.0030	0.0032	0.0029	0.0032
10018	HeI	-0.658	0.0140	0.0182	0.0139	0.0138
10049	Pa7	-0.660	0.0610	0.0762	0.0736	0.0695
$F(\text{H}\beta)_0$			1.40 ± 0.09^c	1.43 ± 0.09^c	1.69 ± 0.10^c	1.59 ± 0.10^c
$\langle c(\text{H}\beta) \rangle$			0.60 ± 0.16	0.45 ± 0.16	0.44 ± 0.10	0.44 ± 0.12

^a The estimated line flux errors are as follow: if $F\lambda / F\beta \geq 1.00$, then error = $\pm 4\%$; if $1.00 < F\lambda / F\beta \geq 0.50$, then error = $\pm 7\%$; if $0.50 < F\lambda / F\beta \geq 0.10$, then error = $\pm 10\%$; if $0.10 < F\lambda / F\beta \geq 0.02$, then error = $\pm 15\%$; if $0.02 < F\lambda / F\beta$, then error = $\pm 20\%$. ^b Upper limit due to inaccurate sky-subtraction. ^c $F(\text{H}\beta)$ flux in units of $10^{-10} \text{ erg cm}^{-2} \text{ s}^{-1}$.

Table 1b. Dereddened H β -normalized .all and .neb line fluxes for M20-S and M20-N subregions ^a

λ	Ion-ID	M20-S.all	M20-S.neb	M20-N.all	M20-N.neb
		$F\lambda / F\beta _0$			
3727	[O II]	3.534	3.175	3.768	3.491
3771	H11	0.0218	0.0306	0.0194	0.0147
3798	H10 + He I	0.0172	0.0397	0.0198	0.0271
3835	H9	0.0362	0.0644	0.0191	0.0365
3869	[Ne III]	0.0263	0.0185	0.0361	0.0243
3889	H8 + HeI	0.147	0.168	0.143	0.148
3970	H ϵ + [Ne III]	0.118	0.142	0.091	0.120
4069	[S II]	0.0185	0.0233	0.0264	0.0222
4102	H δ	0.231	0.248	0.225	0.247
4340	H γ	0.495	0.485	0.516	0.505
4363	[O III]	<0.0062	<0.0050	<0.0046	<0.0045
4471	He I	0.0271	0.0319	0.0298	0.0430
4861	H β	1.000	1.000	1.000	1.000
4922	He I	0.0082	0.0101	-	-
4959	[O III]	0.212	0.206	0.215	0.199
5007	[O III]	0.650	0.632	0.599	0.591
5200	[N I]	0.0149	0.0140	0.0205	0.0213
5518	[Cl III]	0.0052	0.0048	-	-
5539	[Cl III]	0.0027	0.0039	-	-
5577	[O I]	0.121 ^b	0.120 ^b	0.201 ^b	0.209 ^b
5755	[N II]	0.0094	0.0097	0.0095	0.0089
5876	He I	0.0887 ^b	0.0962 ^b	0.101 ^b	0.106 ^b
6300	[O I]	0.0854	0.0824	0.0310	0.0323
6364	[O I]	0.0241	0.0255	0.0072	0.0079
6563	H α	2.668	2.867	2.830	3.154
6584	[N II]	0.995	0.998	1.00	0.998
6678	He I	0.0245	0.0276	0.0260	0.0304
6716	[S II]	0.250	0.266	0.274	0.310
6731	[S II]	0.187	0.198	0.197	0.225
7065	He I	0.0135	0.0175	0.0137	0.0168
7136	[Ar III]	0.0746	0.0811	0.0744	0.0862
7325	[O II]	0.0255	0.0286	0.0287	0.0344
7751	[Ar III]	0.0105	0.0121	0.0127	0.0137
8467	Pa17	0.0024	0.0039	0.0024	0.0014
8503	Pa16	0.0034	0.0057	-	-

8545	Pa15	0.0043	0.0023	-	-
8598	Pa14	0.0043	0.0052	0.0031	0.0030
8750	Pa12	0.0118	0.0142	0.0065	0.0067
8863	Pa11	0.0104	0.0128	0.0118	0.0120
9015	Pa10	0.0106	0.0121	-	-
9069	[S III]	0.225	0.253	0.202	0.238
9229	Pa9	0.0234	0.0270	0.0207	0.0223
9531	[S III]	0.563	0.652	0.496	0.607
9712	HeI	0.0075	0.0071	-	-
10018	HeI	0.0261	0.0334	-	-
10049	Pa7	0.0569	0.0695	0.0465	0.0588
$F(\text{H}\beta)_0$		0.380 ± 0.024^c	0.395 ± 0.024^c	0.507 ± 0.032^c	0.527 ± 0.032^c
$\langle c(\text{H}\beta) \rangle$		0.64 ± 0.25	0.50 ± 0.11	0.83 ± 0.34	0.63 ± 0.23

^a The estimated line flux errors are as in Table 1a. ^b Upper limit due to inaccurate sky-subtraction. ^c $F(\text{H}\beta)$ flux in units of 10^{-10} erg cm⁻² s⁻¹.

For M8 we found a (*neb*) average reddening constant $\langle c(\text{H}\beta) \rangle = 0.44 \pm 0.14$, while Esteban et al (1999; E99) report $c(\text{H}\beta) = 0.85 \pm 0.05$ for one slit position located on a bright spot 12" south of the HG (position HGS of SP91). García-Rojas et al. (2007) report also a relatively high reddening: $c(\text{H}\beta) = 0.94 \pm 0.03$ for the same slit position. We see that our $7' \times 7'$ scan average sampled regions of much smaller reddening farther away from the HG. For M20 we found $c(\text{H}\beta) = 0.50 \pm 0.11$ for the southern regions (M20-S) and a higher reddening, $c(\text{H}\beta) = 0.63 \pm 0.23$, for the northern region (M20-N). These values are somewhat larger than the values reported by Hawley (1978): $c(\text{H}\beta) = 0.42 - 0.48$; Lynds & O'Neil (1985): $c(\text{H}\beta) = 0.45$; and García-Rojas et al. (2006): $c(\text{H}\beta) = 0.36$. These differences are expected since these authors used different slits positioned over bright spots within the nebula, while our scans sampled both regions of high and low extinction yielding an integrated average over the whole nebula.

We compared the Balmer line ratios derived from the dereddened line fluxes given in Tables 1a and 1b with their theoretical values from HS95 and found reasonable agreement within 10% for the bright Balmer and Paschen lines, with larger deviations (20% – 30%) for the weaker lines. We point out however, that our F_α/F_β , F_γ/F_β and F_δ/F_β observed ratios yielded $c(\text{H}\beta)$ values varying from 0.29 – 0.62 for M8 and from 0.37 – 0.77 for M20.

In Fig. 1 we present the comparison among the reddening constant derived from the spectra including the exciting stars, $c(\text{H}\beta)_{.all}$ and the spectra excluding them, $c(\text{H}\beta)_{.neb}$. We present the results of all our target objects, including Carina, M8, M20 and the 4 RCW objects mentioned in Chapter II. From this figure we see that, putting aside the CarSE region which contains the anomalous η Car, the *neb* spectra yield $c(\text{H}\beta)$ values 0.07 dex *smaller* on average than the *all* spectra. As we shall see below, these differences will propagate in the derivation of physical parameters and total abundances.

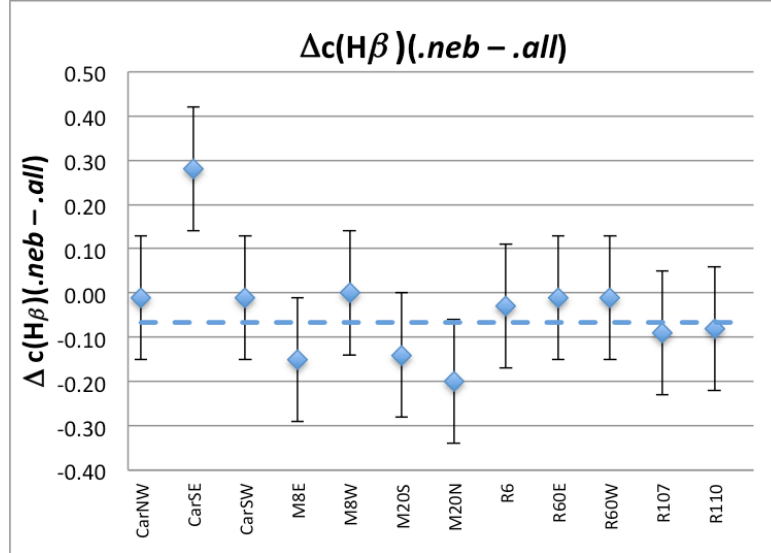


Fig. 1. Comparison of *.all* and *.neb* reddening constant $c(\text{H}\beta)$ for Carina, M8, M20 and the 4 RCW objects included in Chapter II. We show the average (*.neb* - *.all*) difference as a dashed line, excluding the CarSE region, hosting η Car, which shows an anomalous behavior.

5.3. Physical parameters: electron temperature and density

We derived the electron density n_e , and electron temperature T_e of the gas in our M8 and M20 subregions using the same procedure as described in Sec. 3.3 of Chapter IV. To compute the electron density we assumed $T_e = 10^4$ K; this is a good approximation given that these ratios have a weak dependence on T_e , especially at low densities ($\leq 600 \text{ cm}^{-3}$), according to the *Abelion* emissivities, kindly provided to us by G. Stasińska (eg. Stasińska & Leitherer, 1996). The chlorine lines are much fainter than the sulfur lines and always trace regions of higher density, indicating considerable density variations within the nebula. We present our results in Table 2. In what follows, we will consider $n_e(\text{SII})$ as representative of our wide scanned regions, and we will use it to estimate the electron temperature and ionic abundances. As can be seen from Table 2, the [SII] $\lambda\lambda 6731/6716$ line ratios for our nebula are close to their saturation limit, indicating that our integrated scans suggest nebulae of rather low density, $n_e \approx 400 \text{ cm}^{-3}$ for M8 and $n_e \approx 100 \text{ cm}^{-3}$ for M20.

We were able to determine the electron temperature from different line ratios mapping zones of high and low excitation. We used the ratio of nebular to auroral lines of several ions mentioned in Sec. 3.3 of Chapter IV to derive the electron temperatures $T_e(\text{OIII})$, $T_e(\text{NII})$, $T_e(\text{OII})$, $T_e(\text{SII})$, and $T_e(\text{SIII})$. We present our results in Table 2. The quoted errors correspond to the upper and lower limits derived using the uncertainties of the line fluxes involved, and turned out to be quite large, about ± 600 K, both for M8 and M20. Being M20 a nebula with relatively low excitation ($\text{O}^{++}/\text{O} < 0.20$, see below), we were able to measure only upper limits for $[F(\lambda 4363)/F\beta]_0$, so we could not derive an accurate T_{OIII} for M20. We looked for measurements of this line for this nebula in the literature and the only value we

found was that reported by García-Rojas et al. (2006; GR06). Other authors have reported only upper limits (eg. Hawley, 1978; Rodríguez, 1999). After comparing the spectra reported by GR06 for M20 and our spectra (see Table 5*b* below), we decided to use GR06 measurement of $[F(\lambda 4363)/F\beta]_0$ in order to have a more accurate determination of the electron temperature in the high ionization zone for this nebula.

Table 2. Electron densities and electron temperatures for M8 and M20 regions ^a

	M8-E.all	M8-E.neb	M8-W.all	M8-W.neb	M20-S.all	M20-S.neb	M20-N.all	M20-N.neb
$n_e(\text{SII})$	230^{+240}_{-180}	270^{+270}_{-190}	430^{+310}_{-240}	400^{+310}_{-210}	$80^{+170}_{-...}$	$80^{+190}_{-...}$	$35^{+175}_{-...}$	$45^{+185}_{-...}$
$n_e(\text{Cl III})$	1300^{+110}_{-840}	–	$690^{+910}_{-...}$	–	–	1000^{+1030}_{-800}	–	–
n_e (adopted)	200	300	400	400	100	100	50	50
T_{OIII}	$7.2^{+0.4}_{-0.3}$	$7.4^{+0.4}_{-0.3}$	$7.4^{+0.3}_{-0.4}$	$7.9^{+0.4}_{-0.4}$	$8.4^{+1.0}_{-0.8}$	$7.8^{+1.2}_{-0.7}$	$7.9^{+0.8}_{0.7}$	$7.8^{+0.8}_{-0.6}$
T_{NII}	$8.3^{+0.7}_{-0.6}$	$8.5^{+0.8}_{-0.7}$	$8.2^{+0.7}_{-0.6}$	$8.2^{+0.7}_{-0.6}$	$8.7^{+0.5}_{-0.4}$	$8.8^{+0.5}_{-0.4}$	$8.8^{+0.5}_{0.4}$	$8.6^{+0.4}_{-0.5}$
T_{OII}	$9.2^{+1.0}_{-0.8}$	$9.6^{+1.1}_{-0.9}$	$8.8^{+1.0}_{-0.7}$	$8.9^{+0.9}_{-0.8}$	$6.6^{+0.5}_{-0.4}$	$7.2^{+0.5}_{-0.5}$	$6.8^{+0.5}_{0.4}$	$6.7^{+0.6}_{-0.5}$
T_{SII}	$7.7^{+1.3}_{-0.9}$	$6.7^{+1.0}_{-0.7}$	$8.3^{+1.5}_{-1.2}$	$7.0^{+1.0}_{-0.8}$	$6.6^{+0.9}_{-0.7}$	$7.2^{+1.0}_{-0.9}$	$7.8^{+1.3}_{-1.0}$	$7.6^{+0.9}_{-0.8}$
T_{SIII}	$7.7^{+0.8}_{-0.5}$	$5.5^{+0.4}_{-0.3}$	$7.1^{+0.5}_{-0.5}$	$7.4^{+0.7}_{-0.5}$	–	–	–	–

^a Densities in cm^{-3} and temperatures in 10^3 K.

To derive T_{OII} we used the $F(\lambda 7325)_0$ line flux corrected for recombination using the expression provided by Liu et al. (2000). For M8, we found that the corrected line flux $F(\lambda 7325)_0^{\text{corr}}$ is about 4 – 8% smaller than the non-corrected value, while for M20, this correction amounts only to $\sim 1\%$. According to Liu et al. (2000), the [NII] $\lambda 5755$ line can also be affected by recombination, being this contribution a weak function of temperature and proportional to the N^{++}/H^+ abundance. García-Rojas et al. (2007) estimated N^{++}/H^+ in M8, using N^+/H^+ and ICF(N), and found that this contribution accounts only for 1% of the line intensity, so we will ignore this effect. For M20, due to its low excitation degree, we expect this contribution to be even smaller than in M8, and we will ignore it. Note however, that Tsamis et al. (2003) point out that ignoring this recombination contribution to the [NII] $\lambda 5755$ and [OII] $\lambda\lambda 7320+30$ line fluxes may lead to spuriously high values of T_{NII} and T_{OII} . For M17, Tsamis et al. (2003) estimated N^{++}/H^+ from recombination lines (RL) and found a much better agreement between the corrected T_{NII} and T_{OIII} . The [SIII] $\lambda 9532$ values given in Tables 1*a* and 1*b*, which are used to compute T_{SIII} and S^{++}/H^+ have a correction of 7% due to a blend with Pa8.

As we can see, the T_{NII} temperature in the low ionization zones tend to be smaller than the T_{OIII} temperature in the high ionization zone. This can be understood after the results presented by Stasińska

(1980), whom used photoionization models of metal-rich HII regions and found that the electron temperature increases outward as a function of radius, due to a combination of hardening of the radiation field with increasing optical depth, plus a stronger cooling from fine-structure lines of [OIII] in the inner parts of the nebula, where O^{++} dominates, yielding thus a lower temperature in the high ionization zone as compared to that of the low ionization zone. Given the uncertainties involved in the faint lines needed to compute T_{OII} , T_{SII} and T_{SIII} we will adopt T_{OIII} as the electron temperature in the high-ionization zone and T_{NII} as that in the low-ionization zone.

In Fig. 2 we present a comparison of the *.all* and *.neb* T_{OIII} and T_{NII} electron temperatures for our Carina, M8 and M20 regions. For clarity, we present only the error bars associated with T_{NII} , but they are similar for T_{OIII} . We present the average difference $\Delta T_e(.neb - .all)$ for T_{OIII} and T_{NII} as a horizontal dashed line (excluding the CarSE region). There is not a clear trend for $\Delta T_e(.neb - .all)$ among our objects. The actual difference depends on several factors including *a)* the spectral types of the embedded stars, *b)* the reddening procedure and the reddening constant applied for each object and *c)* the errors involved in measuring the faint [OIII] $\lambda 4363$ and [NII] $\lambda 5755$ line fluxes needed to estimate the electron temperatures. We conclude however that on average, $T_e(NII).all \approx T_e(NII).neb$. However, we see that $T_e(OIII).all$ is larger than $T_e(OIII).neb$ by about ~ 200 K on average.

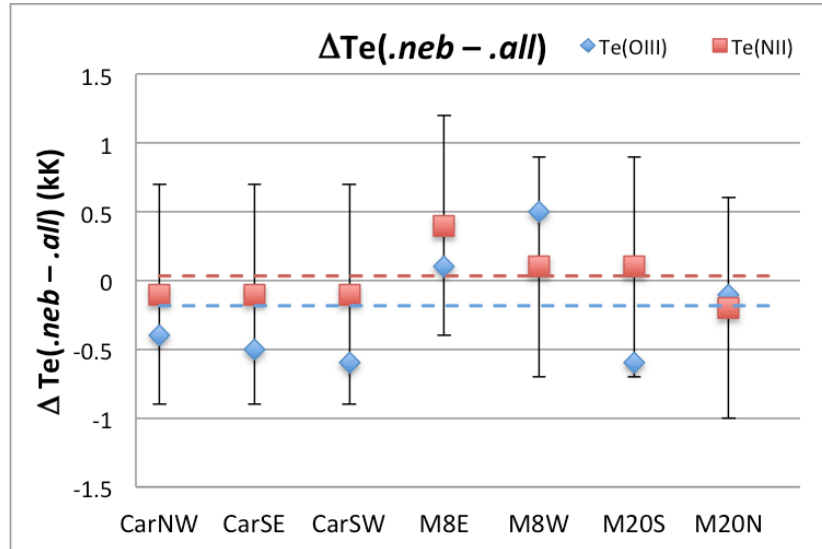


Fig. 2. Comparison of *.all* and *.neb* T_{OIII} and T_{NII} electron temperatures for Carina, M8 and M20. We show the average difference $\Delta T_e(.neb - .all)$ as a dashed line in each case.

5.4. Ionic abundances

We assumed a two-zone ionization scheme and derived the ionic abundances of O^+ , O^{++} , N^+ , S^+ , S^{++} , Ne^{++} and Ar^{++} relative to H^+ from the brightest collisional excited lines of these ions present in our

spectra following the same procedure as described in Sec. 3.4 of Chapter IV, and considering the temperatures and densities given in Table 2 above. We present our *.all* and *.neb* results in Table 3.

Table 3. *.all* and *.neb* ionic abundances relative to H^+ (in units of 10^{-6} , except for He^+) for M8 and M20 subregions (without temperature fluctuations).

	M8-E. <i>.all</i>	M8-E <i>.neb</i>	M8-W <i>.all</i>	M8-W <i>.neb</i>	M20-S <i>.all</i>	M20-S <i>.neb</i>	M20-N <i>.all</i>	M20-N <i>.neb</i>	Error
$He^+/H^+(\lambda 5876)^a$	0.0826	0.0869	0.0794	0.0760	0.0675	0.0710	0.0740	0.0719	20%
$O^+/H^+(\lambda 3727)$	155	112	189	178	250	216	267	260	46%
$O^{++}/H^+(\lambda 5007)$	326	306	231	176	44.4	59.2	53.4	56.6	22%
$N^+/H^+(\lambda 6584)$	15.7	14.9	22.8	23.0	27.0	28.2	27.9	33.2	27%
$S^+/H^+(\lambda 6725)$	0.723	0.712	1.03	1.06	1.45	1.50	1.50	1.82	25%
$S^{++}/H^+(\lambda 9532)$	5.16	5.63	5.96	5.50	3.54	4.00	3.05	3.92	21%
$Ne^{++}/H^+(\lambda 3869)$	68.3	57.9	40.3	29.0	5.78	5.86	10.7	7.70	27%
$Ar^{++}/H^+(\lambda 7136)$	2.54	2.76	2.30	1.98	1.07	1.44	1.27	1.52	15%

^a Derived using *Abelion* emissivities (Stasińska & Leitherer 1996).

The quoted errors for the ionic abundances (last column) were estimated considering both the errors in n_e and T_e , and the errors in the line fluxes. The exact errors are slightly different for each region but we give a representative average for each ion. For M8 we found that $S^{++}(\lambda 9532)$ and $S^{++}(\lambda 6312)$ agree within the uncertainties. However, for M20 we found that $S^{++}(\lambda 9532)$ is larger than $S^{++}(\lambda 6312)$ by a factor of ~ 2 . Dennefeld & Stasińska (1983) also found a similar behavior for a small sample of Galactic HII regions, although with smaller deviations. This difference may be due to uncertainties in the collisional strengths of sulfur as well as to errors in the line fluxes: [SIII] $\lambda 9532$ depends strongly on an accurate sky-subtraction procedure, while [SIII] $\lambda 6312$ is a very weak line, about 1% of $H\beta$, with a large observational error. Ignoring the Pa8 contribution to the [SIII] $\lambda 9532$ -line flux, leads to an S^{++}/H^+ abundance 0.07 dex larger than those reported in Table 3.

For the weak lines, such as [OIII] $\lambda 4363$ or [NII] $\lambda 5755$, the procedure used to measure the observed line fluxes has important consequences on the derived electron temperatures. We explored the effect of measuring the line flux using the IRAF task *splot a*) by fitting a Gaussian and using background fitting, and *b*) by measuring the total line flux under the line above a given continuum estimated by eye. We found that these two procedures may yield differences up to 300 – 400 K in the derived electron temperatures. At the other hand, according to IRAF emissivities, for temperatures in the 7 – 12 kK range, increasing T_{OIII} by 1.0 kK, yields reduced O^+/H^+ by 0.11 dex and reduced O^{++}/H^+

by 0.14 dex, yielding thus a reduced total O/H by 0.25 dex. This same T_e increment yields reduced N^+/H^+ and S^+/H^+ by 0.05 dex, reduced Ar^{++}/H^+ by 0.09 dex and reduced S^{++}/H^+ and Ne^{++}/H^+ by 0.15 dex. Therefore, these uncertainties in the assigned T_e prevent us to derive ionic abundances with a precision better than 0.05 – 0.1 dex.

5.5. Total abundances without temperature fluctuations

As commented in the previous chapter, in order to derive the total abundances we must account for the ionic abundances of unseen ions. In this section we derive the total abundances of O, N, S, Ne and Ar using the canonical ionization correction factors (ICFs) summarized by Kingsburgh & Barlow (1994; KB94) and the new ICFs presented by Delgado-Inglada et al. (2014; DI14), which are given in equations (15) – (19) of Chapter IV. We present our results in Table 4a for M8 and Table 4b for M20.

Table 4a. Total abundances for M8: comparison of ICFs (without temperature fluctuations).^a

	M8-E.all		M8-E.neb		M8-W.all		M8-W.neb		Error
	KB94	DI14	KB94	DI14	KB94	DI14	KB94	DI14	
O/H	8.68	8.68	8.62	8.62	8.62	8.62	8.55	8.55	±0.14
N/H	7.69	7.58	7.75	7.63	7.70	7.62	7.66	7.58	±0.12
S/H	6.82	6.78	6.87	6.83	6.87	6.84	6.84	6.82	±0.11
Ne/H	8.00	8.30	7.90	8.17	7.86	8.19	7.77	8.10	±0.12
Ar/H	6.57	6.46	6.58	6.51	6.62	6.38	6.60	6.31	±0.14
log(N/O)	-0.99	-1.10	-0.88	-0.99	-0.92	-1.01	-0.89	-0.97	±0.26
log(S/O)	-1.86	-1.90	-1.75	-1.79	-1.75	-1.78	-1.71	-1.73	±0.25
log(Ne/O)	-0.68	-0.39	-0.72	-0.45	-0.76	-0.43	-0.78	-0.45	±0.26
log(Ar/O)	-2.11	-2.22	-2.04	-2.11	-2.00	-2.24	-1.95	-2.24	±0.28
ICF(N)	3.10	2.42	3.73	2.85	2.22	1.81	1.99	1.66	
ICF(S)	1.13	1.02	1.18	1.08	1.06	1.00*	1.04	1.00*	
ICF(Ne)	1.48	2.90	1.37	2.57	1.82	3.83	2.01	4.32	
ICF(Ar)	1.48	1.13	1.37	1.18	1.82	1.05	2.01	1.02	
O^{++}/O		0.68		0.73		0.55		0.50	

^a In units of $12 + \log(X/H)$, for $t^2 = 0$. Columns 2, 4, 6, and 8 are derived using Kingsburgh & Barlow (1994)'s ICFs. Columns 3, 5, 7, and 9 are derived using Delgado-Inglada et al. (2014)'s ICFs. * Original expression gave ICF(S) < 1.

From Tables 4a and 4b we see that the new ICFs of DI14 yield basically the same O/H and S/H abundances as those derived using KB94's ICFs. However, as pointed out in the previous chapter, the N/H abundance is decreased by -0.10 dex for M8 but only by -0.03 dex for M20, which has a much

smaller excitation parameter. The “updated” Ne/H abundance is *increased* by about 0.30 dex both for M8 and M20, and the Ar/H abundance is *decreased* by -0.20 dex for M8 and by up to -0.60 dex for M20. We see that the differences between KB94– and DI14–derived abundances depend on the degree of ionization of the nebula, since $(\text{O}^{++}/\text{O})_{\text{M8}} = 0.50 - 0.73$, while $(\text{O}^{++}/\text{O})_{\text{M20}} = 0.18 - 0.22$.

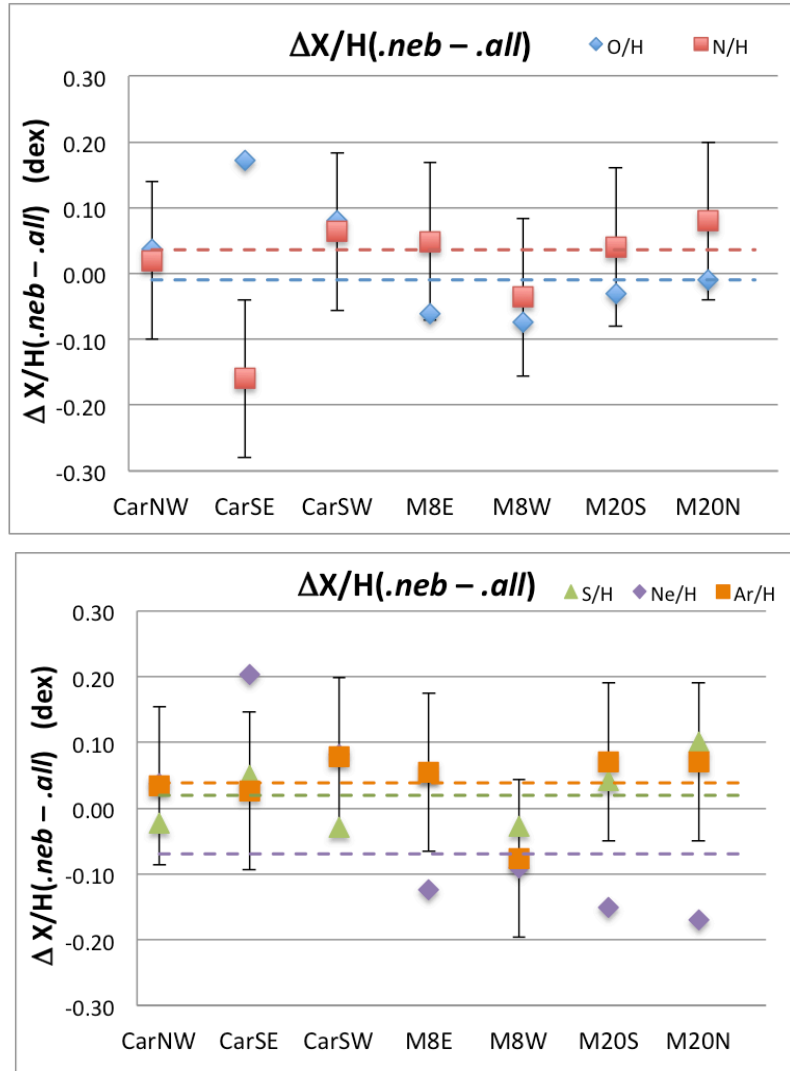
Table 4b. Total abundances for M20: comparison of ICFs (without temperature fluctuations).^a

	M20-S.all		M20-S.neb		M20-N.all		M20-N.neb		Error
	KB94	DI14	KB94	DI14	KB94	DI14	KB94	DI14	
O/H	8.47	8.47	8.44	8.44	8.51	8.51	8.50	8.50	± 0.14
N/H	7.50	7.48	7.56	7.52	7.52	7.50	7.61	7.58	± 0.12
S/H	6.70	6.70	6.74	6.74	6.66	6.66	6.76	6.76	± 0.11
Ne/H	7.58	7.91	7.43	7.76	7.81	8.13	7.63	7.96	± 0.12
Ar/H	6.85	6.20	6.83	6.27	6.88	6.25	6.93	6.32	± 0.14
log(N/O)	-0.97	-0.99	-0.88	-0.92	-0.98	-1.01	-0.89	-0.92	± 0.26
log(S/O)	-1.77	-1.77	-1.70	-1.70	-1.85	-1.85	-1.74	-1.74	± 0.25
log(Ne/O)	-0.89	-0.56	-1.01	-0.68	-0.70	-0.37	-0.87	-0.54	± 0.26
log(Ar/O)	-1.62	-2.27	-1.61	-2.17	-1.62	-2.25	-1.57	-2.18	± 0.28
ICF(N)	1.18	1.11	1.27	1.18	1.20	1.13	1.22	1.14	
ICF(S)	1.00	1.00*	1.00	1.00*	1.00	1.00*	1.00	1.00	
ICF(Ne)	6.63	14.0	4.65	10.0	6.00	12.7	5.59	11.9	
ICF(Ar)	6.63	1.47	4.65	1.29	6.00	1.41	5.59	1.38	
O ⁺⁺ /O		0.15		0.22		0.17		0.18	

^a In units of $12 + \log(\text{X}/\text{H})$, for $t^2 = 0$. Columns 2, 4, 6, and 8 are derived using Kingsburgh & Barlow (1994)’s ICFs. Columns 3, 5, 7, and 9 are derived using Delgado-Inglada et al. (2014)’s ICFs. * Original expression gave ICF(S) < 1.

In Figs. 3a and 3b we present the comparison between the *.all* and *.neb* total abundances of O/H and N/H (Fig. 3a) and S/H, Ne/H and Ar/H (Fig. 3b) for our Carina, M8 and M20 regions. As before, we show the average difference $\Delta\text{X}/\text{H}(\text{.neb} - \text{.all})$ for each element (excluding the uncertain CarSE region). For clarity, we show only the error bars of the N/H abundance (Fig. 3a) and of the Ar/H abundance (Fig. 3b). As with Fig. 2, there is not a clear trend for the $\Delta\text{X}/\text{H}(\text{.neb} - \text{.all})$ parameter among our objects. In average, the (O/H).*all* and (O/H).*neb* abundances are about the same. However, the (N/H).*all* abundance appears *smaller* on average than (N/H).*neb* abundance by ~ 0.05 dex. The S/H abundance appears unaffected between the *.all* and *.neb* spectra. However, our results indicate that (Ne/H).*all* is 0.07 dex *larger* on average than (Ne/H).*neb*, and (Ar/H).*all* appears 0.04 dex *smaller* on

average than $(\text{Ar}/\text{H})_{.neb}$. Note however the large uncertainties for the abundances given in Tables 4a and 4b.



Figs. 3a and 3b. Comparison of *.all* and *.neb* total abundances for Carina, M8 and M20. *Upper panel*: O/H and N/H. *Lower panel*: S/H, Ne/H and Ar/H. We show the average difference $\Delta X/H(.neb - .all)$ as a dashed line in each case (excluding CarSE).

In Table 5a we present a comparison of our derived average abundances for M8 ignoring temperature fluctuations ($t^2 = 0$), with recent determinations adapted from the literature. Esteban et al. (1999; E99) presented Echelle spectroscopy of one slit position located 12'' S of the Hourglass (the HGS position of Sánchez and Peimbert, 1991). Given the high resolution attained with their spectra, they were able to derive the ionic abundances of O^+ , O^{++} and C^{++} from recombination lines (RL) and from collisionally excited lines (CEL), and they compare both sets of abundances to derive values of the temperature fluctuation t^2 parameter introduced by Peimbert (1967). In order to make a fair comparison with our results, in Table 5a we present the total abundances derived using E99's CEL, $t^2 = 0$ ionic abundances and applying the new ICFs of DI14. For comparison, we also present E99's original

reported values. García-Rojas et al. (2007; GR07) obtained Echelle spectroscopy, with one of the 8.2-m VLT telescopes in Paranal, Chile, of the same position in M8 observed by E99. As with E99 data, we present the total abundances derived using their CEL, $t^2 = 0$ ionic abundances applying DI14's ICFs. We also include their original set of reported values. Finally, we include for comparison purposes Esteban et al. (2004; E04) CEL, $t^2 = 0$ abundances for Orion, recalculated using DI14's ICFs, and we also include their original reported values.

Table 5a. Comparison of total (*neb*) abundances for M8 (without temperature fluctuations, $t^2 = 0$).^a

	$\langle M8 \rangle^b$	error	E99 HGS ^c w/ DI14 ICF (4)	GR07 HGS ^d w/ DI14 ICF (5)	Orion E04 ^e w/ DI14 ICF (6)	E99 HGS original (7)	GR07 HGS original (8)	Orion E04 original (9)
(1)	(2)	(3)						
O	8.59	± 0.14	8.41	8.50	8.51	8.40 ± 0.15	8.51 ± 0.05	8.51 ± 0.03
N	7.60	± 0.12	7.46	7.58	7.52	7.62 ± 0.18	7.72 ± 0.03	7.65 ± 0.09
S	6.82	± 0.11	6.89	6.94	7.11	6.90 ± 0.10	6.94 ± 0.03	7.06 ± 0.04
Ne	8.13	± 0.12	7.49	7.93	8.01	7.68:	7.81 ± 0.12	7.78 ± 0.07
Ar	6.41	± 0.14	6.28	6.31	6.48	6.77:	6.52 ± 0.04	6.50 ± 0.05
log N/O	-0.98	± 0.26	-0.95	-0.93	-0.99	-0.78 ± 0.33	-0.79 ± 0.08	-0.86 ± 0.12
log S/O	-1.77	± 0.25	-1.51	-1.57	-1.40	-1.50 ± 0.25	-1.57 ± 0.08	-1.45 ± 0.07
log Ne/O	-0.45	± 0.26	-0.92	-0.58	-0.50	-0.72:	-0.70 ± 0.17	-0.73 ± 0.10
log Ar/O	-2.18	± 0.28	-2.13	-2.19	-2.03	-1.63:	-1.99 ± 0.09	-2.01 ± 0.08
ICF(N)	2.25	± 1.15	1.46	1.19	4.19	2.09	1.66	5.62
ICF(S)	1.04	± 0.60	1.00*	1.00*	1.24	1.01	1.01	1.10
ICF(Ne)	3.44	± 0.20	5.35	9.48	2.07	8.32	7.24	1.23
ICF(Ar)	1.10	± 0.65	1.09	1.27	1.29	3.39	2.04	1.35
O ⁺⁺ /O	0.61	± 0.08	–	–	–	0.41	0.23	–
$c(H\beta)$	0.44	± 0.014	–	–	–	0.85 ± 0.05	0.94 ± 0.03	–
T_{OIII}	7.6	± 0.6	–	–	–	8.0 ± 0.70	8.1 ± 0.14	–
T_{NII}	8.4	± 1.2	–	–	–	8.2 ± 0.90	8.5 ± 0.18	–
$(\lambda 3727/H\beta)_0$	163	± 6.5				163	210	
$(\lambda 5007/H\beta)_0$	228	± 9.1				124	95.5	
$(\lambda 4363/H\beta)_0$	0.52	± 0.10				0.37	0.29	
$(\lambda 6584/H\beta)_0$	59.2	± 4.1				77.7	102	
$(\lambda 5755/H\beta)_0$	0.50	± 0.10				0.73	0.95	
$(\lambda 6725/H\beta)_0$	23.0	± 2.3				14.8	21.2	
$(\lambda 9532/H\beta)_0$	77.7	± 5.4				–	59.2	
$(\lambda 3869/H\beta)_0$	11.3	± 1.1				2.64	3.75	
$(\lambda 7136/H\beta)_0$	12.2	± 1.2				10.1	10.0	

^a In units of $12 + \log(X/H)$. Electron temperatures are given in kK. Linear de-reddened line flux ratios relative to $F_{\beta} = 100$. ^b Average of our M8-E.neb and M8-W regions. ^c Adapted from E99's CEL, $t^2 = 0$ ionic abundances using DI14's ICFs. ^d Adapted from GR07 CEL, $t^2 = 0$ ionic abundances using DI14's ICFs. ^e Adapted from E04 CEL, $t^2 = 0$ ionic abundances for Orion using DI14's ICFs. * DI14 expression gives $ICF(S) < 1.0$.

Comparing E99 and GR07 results, we see that although both authors observed the same position within the nebula, GR07 derived in general larger abundances than E99, by about 0.10 dex on average, except for Ar, for which the tendency is reversed. However, note that E99 state that their Ar/H determination is uncertain, due to uncertainties in the applied ICF. The reason of these differences between E99's and GR07's abundances is not attributable to the adopted electron temperature, since both authors used basically the same temperatures. Comparing the original abundances given by these two authors (columns (8) and (9) of Table 5a), with the reported un-reddened line fluxes, we found that the differences in the reported abundances are due mainly to differences in the un-reddened line fluxes with respect to $H\beta$. Note also the large difference, of about 0.44 dex, in the Ne/H abundance derived using E99+DI14's ICFs and that derived using GR07+DI14's ICFs. This difference has two components: *a*) the dereddened line flux ($[NeIII] \lambda 3869$)₀ from GR07 is 0.15 dex larger than that from E99, and *b*) due to the lower excitation nebula reported by GR07: $(O^{++}/O)_{GR07} = 0.23 < 0.41 = (O^{++}/O)_{E99}$, the ICF(Ne) derived from GR07 abundances is 0.25 dex larger than that derived from E99 ones. We see the importance of have accurate line measurements.

From Tables 5a we see that our derived abundances agree within the errors with those reported by E99 and GR07. The agreement is better with the latest results presented by GR07. Note however that we found a larger Ne/H abundance, by about 0.20 dex, than the value reported by GR07. Tracking down the source of this difference, we found that it is not due to the adopted ICF(Ne), since our value is even smaller than that of GR07, but it is due to our larger $([NeIII] \lambda 3869/H\beta)_0$ dereddened line flux, which is a factor of 3 larger than the value reported by GR07.

Our S/H appears to be somewhat smaller than that reported by GR07. This result is unexpected since both our $([SII] \lambda 6725/H\beta)_0$ and $([SIII] \lambda 9532/H\beta)_0$ un-reddened line fluxes are larger than those reported by GR07. The reason of the discrepancy is in the ionic abundances employed. That is, although the single ionized abundance agree: $\langle S^+/H^+ \rangle_{Our} = 0.886 \times 10^{-6} \approx \langle S^+/H^+ \rangle_{GR07} = 0.851 \times 10^{-6}$, the double ionized abundances do not agree: $\langle S^{++}/H^+ \rangle_{Our} = 5.56 \times 10^{-6}$, while $\langle S^{++}/H^+ \rangle_{GR07} = 7.76 \times 10^{-6}$, which is a factor of 1.40 larger, explaining thus the 0.12 dex difference between our total (S/H) and that of GR07. The reason of this difference in S^{++}/H^+ is probably due to the updated atomic parameters used for sulfur within the IRAF task *ionic* used by GR07.

Table 5a also shows that the S/H abundance assigned to M8 is smaller, by about 0.1 dex than the S/H abundance found in Orion. However, as commented before this may be due to differences in the

atomic parameters employed as well as to uncertainties in measuring the extreme-red [SIII] $\lambda 9532$ emission line.

Table 5b. Comparison of total (*neb*) abundances for M20 (without temperature fluctuations, $t^2 = 0$).^a

	$\langle M20 \rangle^b$	error	GR06 ^c	Orion E04 ^d	GR06	Orion E04
	(2)	(3)	w/ DI14 ICF	w/ DI14 ICF	original	original
(1)	(2)	(3)	(4)	(6)	(7)	(9)
O	8.47	± 0.14	8.53	8.51	8.53 ± 0.06	8.51 ± 0.03
N	7.55	± 0.12	7.59	7.52	7.67 ± 0.05	7.65 ± 0.09
S	6.75	± 0.11	6.88	7.11	6.88 ± 0.05	7.06 ± 0.04
Ne	7.86	± 0.12	7.73	8.01	7.83 ± 0.16	7.78 ± 0.07
Ar	6.30	± 0.14	6.13	6.48	6.65 ± 0.06	6.50 ± 0.05
log N/O	-0.92	± 0.26	-0.93	-0.99	-0.86 ± 0.11	-0.86 ± 0.12
log S/O	-1.72	± 0.25	-1.64	-1.40	-1.65 ± 0.11	-1.45 ± 0.07
log Ne/O	-0.61	± 0.26	-0.80	-0.50	-0.70 ± 0.22	-0.73 ± 0.10
log Ar/O	-2.18	± 0.28	-2.39	-2.03	-1.88 ± 0.12	-2.01 ± 0.08
ICF(N)	1.16	± 1.15	1.10	4.19	1.32	5.62
ICF(S)	1.00	± 0.60	1.00*	1.24	1.00	1.10
ICF(Ne)	11.0	± 0.20	15.0	2.07	19.1	1.23
ICF(Ar)	1.34	± 0.65	1.52	1.29	3.02	1.35
O^{++}/O	0.20	± 0.08	-	-	0.14	-
$c(H\beta)$	0.56	± 0.17	-	-	0.36	-
T_{OIII}	7.8	± 0.6	-	-	7.8	-
T_{NII}	8.7	± 1.2	-	-	8.5	-
$(\lambda 3727/H\beta)_0$	334	± 13.4			320	
$(\lambda 5007/H\beta)_0$	61.2	± 4.3			58.9	
$(\lambda 4363/H\beta)_0$	<0.48	± 0.10			0.15	
$(\lambda 6584/H\beta)_0$	99.8	± 10.0			111	
$(\lambda 5755/H\beta)_0$	0.93	± 0.19			0.96	
$(\lambda 6725/H\beta)_0$	50.0	± 5.0			45.4	
$(\lambda 9532/H\beta)_0$	63.0	± 4.4			55.9	
$(\lambda 3869/H\beta)_0$	2.14	± 0.32			1.32	
$(\lambda 7136/H\beta)_0$	8.36	± 1.3			8.97	

^a In units of $12 + \log(X/H)$. Electron temperatures are given in kK. Linear de-redden line flux ratios relative to $F\beta = 100$. ^b Average of our M20-S.*neb* and M20-N.*neb* regions. ^c Adapted from GR06 CEL, $t^2 = 0$ ionic abundances using DI14's ICFs. ^d Adapted from E04 CEL $t^2 = 0$ ionic abundances for Orion using DI14's ICFs. * DI14 original expression gives $ICF(S) < 1.0$.

Regarding, M20, the group of García-Rojas et al. (2006; GR06) presented also Echelle spectroscopy obtained with one of the 8.2-m VLT telescopes in Paranal, Chile, for 1 slit position 20” North-East of the exciting star HD164492 in the center of M20. As in Table 5a, we compare in Table 5b our average (*neb*) abundances for M20 with those derived from GR06 (CEL) $t^2 = 0$ ionic abundances applying DI14’s ICFs. For comparison, we also include their original reported values.

From Table 5b we see that our abundances for M20 are similar to those derived by GR06 within the errors. As with M8, our S/H abundance appears to be somewhat smaller than that of GR06. Even though our dereddened $([\text{SII}] \lambda 6725/\text{H}\beta)_0$ and $([\text{SIII}] \lambda 9532/\text{H}\beta)_0$ line fluxes are somewhat larger than those reported by GR06, our derived ionic abundances are smaller: $\langle \text{S}^+/\text{H}^+ \rangle_{\text{our}} + \langle \text{S}^{++}/\text{H}^+ \rangle_{\text{our}} = (1.66 + 3.96) \times 10^{-6} = 5.62 \times 10^{-6}$, while $\langle \text{S}^+/\text{H}^+ \rangle_{\text{GR06}} + \langle \text{S}^{++}/\text{H}^+ \rangle_{\text{GR06}} = (1.48 + 6.17) \times 10^{-6} = 7.65 \times 10^{-6}$, which is a factor of 1.36 larger than our value and explains the 0.13 dex difference in the reported total S/H abundance. We conclude that the use of updated parameters for [SIII] used by GR06 and GR07 yields S^{++}/H^+ abundances ~ 0.05 dex larger than the transition probabilities and collision strengths contained in the IRAF task *ionic* (Shaw & Dufour, 1995).

For Ne/H, GR06 realized that that the common expression, $\text{ICF}(\text{Ne}) = \text{O}/\text{O}^{++}$ underestimates the total Ne/H in nebula of low degree of ionization, as it is the case for M20, because a considerable fraction of Ne^+ coexist with O^{++} (Torres-Peimbert & Peimbert 1977 and Peimbert et al. 1992). Instead of using this expression, GR06 used the prescriptions given by Torres-Peimbert & Peimbert (1977), and estimated that the $\text{ICF}(\text{Ne})$ should be 0.42 dex larger than that predicted by the common expression. From our Table 4b, we found that the new ICF of DI14 predicts a $\text{ICF}(\text{Ne})$ 0.33 dex larger than that predicted by the common expression, and this explains why the original Ne/H value reported by GR06 (column 7 of Table 5b) is larger than the value derived using DI14’s $\text{ICF}(\text{Ne})$ (column 4 of Table 5b).

Comparing Tables 5a for M8 and 5b for M20, we see that M8 present somewhat higher abundances than M20, by about 0.09 dex on average, except for Ne/H, which seems to be overestimated by 0.17 dex in M8 as compared to M20. As commented in Chapter IV, the N/O ratio derived using DI14’s ICFs is 0.10 dex smaller than the N/O ratio derived using the common ICFs. At the other hand, the Ne/O ratio derived using the “updated” ICFs of DI14 is about 0.11 dex larger than the Ne/O ratio derived using the common ICFs.

5.6. Total abundances including temperature fluctuations

As mentioned in the previous chapter, there is ample evidence of the presence of density and temperature fluctuations within HII regions. Recent works, such as GR07, have derived t^2 values from

different methods, including *a*) matching the O^{++}/H^+ , O^+/H^+ , or C^{++}/H^+ abundances derived from collisional excited lines (CEL) to those derived from recombination lines (RL), *b*) adjusting the He^+/H^+ abundance derived from several HeI lines and *c*) by comparing the HI Balmer or Paschen temperature with another temperature derived from forbidden lines.

Peimbert (1967) and Peimbert and Costero (1969) presented a formalism that allows to estimate an average low-ionization temperature T_0^{low} , an average high-ionization temperature T_0^{high} , and their corresponding temperature fluctuation parameters, t^2_{low} and t^2_{high} , in terms of the low-ionization temperature T_{NII} , the high-ionization temperature T_{OIII} , and the Balmer temperature T_{Bal} , this last one, being derived from the Balmer jump in emission observed in the nebula.

We attempted to derive the t^2 parameter measuring the ratio of the Balmer jump in emission to the de-reddened $H\beta$ flux from our *neb* M8 and M20 observed spectra, following the procedure described in Sec. 3.6 of Chapter IV. That is, using the IRAF task *splot* we measured by eye the continuum at $\lambda 3600$ and $\lambda 3680$, so to have a good spectral base to measure the Balmer jump. We then dereddened these measurements extrapolating CCM89 $R_V = 3.1$ extinction law at these wavelengths and obtained the Balmer discontinuity: $BD = \Delta i(\text{Bal})_0 / F(H\beta)_0$ for our spectra, where $\Delta i(\text{Bal})_0 = i(\lambda 3600)_0 - i(\lambda 3680)_0$, and $F(H\beta)_0$ is the dereddened flux at $H\beta$. However, given the large uncertainties present in measuring the continuum fluxes at these wavelengths in our spectra and the possible contamination due to scattered light at these blue wavelengths, we got very low values of the Balmer discontinuity BD , in the range $1.3 - 2.2 \times 10^{-3} \text{ \AA}^{-1}$, yielding unreasonable high values for the Balmer temperature $T_e(\text{Bal})$, either by means of Eq. (26) of Chapter IV, or using the formula provided by Liu et al. (1995).

In order to estimate the average temperatures T_0^{low} and T_0^{high} in M8, we used the derived $T_{\text{Bal}} = 7.1 \pm 0.11$ kK calculated by GR07. For M20 we used the $T_e(\text{HI}) = 7.3 \pm 2.5$ kK value reported by Reifenstein et al. (1970) from radio recombination lines. We decided not to use the Balmer temperature reported by GR06 for M20, $T_{\text{Bal}} = 6.0 \pm 1.3$ kK, since it predicted too low average temperatures and therefore, too high ionic and total abundances for this nebula. We used the prescriptions given by Peimbert (1971) and Garnett (1992) with these HI temperatures (see Sec. 3.6 of Chapter IV) and our derived T_{NII} and T_{OIII} temperatures (given in Table 2 above) to calculate the low- and high-average temperatures and t^2 parameters presented in Table 6 below. For M8, our average t^2 parameter is $\langle t^2 \rangle = 0.024 \pm 0.021$, while E99 adopted $t^2 = 0.032 \pm 0.019$, and GR07 preferred $t^2 = 0.040 \pm 0.004$. Note however that GR07 found $t^2 = 0.022 \pm 0.015$ comparing T_{Bal} with T_{FL} (forbidden lines). For M20, our average t^2 parameter is $\langle t^2 \rangle = 0.024 \pm 0.021$, while GR06 adopted $t^2 = 0.029 \pm 0.007$.

Table 6. Estimation of high and low average temperatures and t^2 temperature fluctuation parameter.

	M8-E. <i>neb</i>	M8-W. <i>neb</i>	M20-S. <i>neb</i>	M20-N. <i>neb</i>
T_{OIII} (kK)	7.3 \pm 0.3	7.9 \pm 0.4	7.8 \pm 1.0	7.8 \pm 0.7
T_{NII} (kK)	8.6 \pm 0.8	8.3 \pm 0.6	8.8 \pm 0.4	8.6 \pm 0.4
$T_{\text{Bal}} / T_{\text{e}}(\text{HI})$ (kK) ^a	7.1 \pm 0.11	7.1 \pm 0.11	7.3 \pm 2.5	7.3 \pm 2.5
T_0^{high} (kK)	7.1 \pm 0.2	7.3 \pm 0.2	7.4 \pm 1.2	7.4 \pm 1.1
t^2_{high}	0.0043 \pm 0.0042	0.017 \pm 0.006	0.011 \pm 0.008	0.011 \pm 0.008
T_0^{low} (kK)	7.6 \pm 0.4	7.5 \pm 0.3	7.8 \pm 1.0	7.8 \pm 1.0
t^2_{low}	0.042 \pm 0.020	0.033 \pm 0.014	0.041 \pm 0.011	0.036 \pm 0.010
$\langle t^2 \rangle$	0.023 \pm 0.021	0.025 \pm 0.008	0.026 \pm 0.020	0.023 \pm 0.018

^a For M8, T_{Bal} taken from GR07. For M20, $T_{\text{e}}(\text{HI})$ adapted from Reifenstein et al. (1970).

We recalculated our M8 and M20 ionic and total abundances including temperature fluctuations according to the average T_0^{high} and T_0^{low} temperatures given in Table 6, and we present our results in Table 7a and 7b for M8 and M20, respectively.

From Table 7a for M8, as mentioned for the $t^2 = 0$ abundances, we see that although E99 and GR07 observed the same position 12'' S of the Hourglass, there are considerable differences in the ionic and total abundances. For example, the excitation parameter reported by E99 is $\text{O}^{++}/\text{O} = 0.48$, while GR07 report $\text{O}^{++}/\text{O} = 0.28$. Comparing their results with our observations, we see that our $7' \times 7'$ average integrated scan indicate a somewhat higher excitation nebula, with $\text{O}^{++}/\text{O} = 0.45 - 0.62$.

Except for O^{++}/H^+ , all ionic abundances from GR07 are about 0.20 dex larger than those reported by E99. Due to these increased ionic abundances, the total abundances reported by GR07 are about 0.14 dex larger than those reported by E99 (except for Ar/H, which is uncertain in E99's results). These are very large differences, especially since they correspond to the same observing position within the nebula. Looking at their reported values, we conclude that these differences correspond to differences in the adopted average temperatures in the low- and high-ionizations zones, since E99 used $T_{\text{NII}} = 8.7 \pm 1.0$ kK, $T_{\text{OIII}} = 8.1 \pm 0.7$ kK and $t^2 = 0.032 \pm 0.019$, while GR07 used basically the same temperatures, $T_{\text{NII}} = 8.5 \pm 0.15$ kK, $T_{\text{OIII}} = 8.1 \pm 0.12$ kK but $t^2 = 0.040 \pm 0.004$. It calls our attention that, neither E99 nor GR07, give their adopted final average low- and high-temperature used to re-compute their ionic abundances including temperature fluctuations. Another factor that contributed to the ionic abundances differences between E99 and GR07 are the dereddened line fluxes employed (see Table 5a).

Table 7a. Ionic, total and relative abundances for M8 including temperature fluctuations. ^a

	M8-E. <i>neb</i>	M8-W. <i>neb</i>	Error	E99+DI14 ^b	GR07+DI14 ^c	E99 original	GR07 original
	$t^2 = 0.023$	$t^2 = 0.025$		$t^2 = 0.032$	$t^2 = 0.040$	$t^2 = 0.032$	$t^2 = 0.040$
	(1)	(2)	(3)	(4)	(5)	(6)	(7)
log O ⁺ ($\lambda 3727$)	8.33	8.49	± 0.18			8.31	8.58 ± 0.07
log O ⁺⁺ ($\lambda 5007$)	8.54	8.39	± 0.10			8.27	8.18 ± 0.07
log N ⁺ ($\lambda 6584$)	7.34	7.50	± 0.12			7.42	7.67 ± 0.04
log S ⁺ ($\lambda 6725$)	6.01	6.16	± 0.09			5.89	6.10 ± 0.07
log S ⁺⁺ ($\lambda 9531$)	6.88	6.85	± 0.12			7.04	7.25 ± 0.07
log Ne ⁺⁺ ($\lambda 3869$)	7.83	7.64	± 0.12			7.03	7.30 ± 0.07
log Ar ⁺ ($\lambda 7136$)	6.48	6.40	± 0.07			6.44	6.48 ± 0.05
O ⁺⁺ /O	0.62	0.45	± 0.05			0.48	0.28
O/H	8.75	8.74	± 0.17	8.59 ± 0.15	8.73 ± 0.05	8.60 ± 0.15	8.73 ± 0.05
N/H	7.66	7.69	± 0.15	7.63 ± 0.18	7.77 ± 0.06	7.78 ± 0.18	7.96 ± 0.06
S/H	6.93	6.93	± 0.14	7.07 ± 0.10	7.28 ± 0.06	7.12 ± 0.10	7.28 ± 0.06
Ne/H	8.35	8.33	± 0.15	7.69 ± 0.20	8.18 ± 0.13	7.95:	8.03 ± 0.13
Ar/H	6.52	6.40	± 0.17	6.46 ± 0.11	6.56 ± 0.07	6.97:	6.69 ± 0.07
N/O	-1.09	-1.05	± 0.32	-0.97 ± 0.33	-0.96 ± 0.11	-0.82 ± 0.33	-0.77 ± 0.11
S/O	-1.82	-1.82	± 0.31	-1.52 ± 0.25	-1.45 ± 0.11	-1.48 ± 0.25	-1.45 ± 0.11
Ne/O	-0.40	-0.42	± 0.32	-0.91 ± 0.35	-0.54 ± 0.18	-0.65:	-0.70 ± 0.18
Ar/O	-2.23	-2.35	± 0.34	-2.13 ± 0.26	-2.17 ± 0.12	-1.63:	-2.04 ± 0.12
ICF(N)	2.09	1.54	$\pm 39\%$	1.60	1.26	2.29	1.95
ICF(S)	1.00*	1.00*	$\pm 54\%$	1.00*	1.00*	1.00	1.00
ICF(Ne)	3.30	4.86	$\pm 8\%$	4.53	7.67	8.31	5.37
ICF(Ar)	1.09	1.00	$\pm 54\%$	1.05	1.19	3.39	1.62

^a Logarithmic ionic and total abundances given as $12 + \log(X^{+i}/H^+)$. The excitation degree O⁺⁺/O is linear. ^b From E99's ionic abundances for $t^2 = 0.032$ and DI14's ICFs. ^c From GR07's ionic abundances for $t^2 = 0.040$ and DI14's ICFs.

We tested the temperature dependence of the ion emissivities within the IRAF-*nebular* package for a hypothetical nebula with $n_e = 100 \text{ cm}^{-3}$ and $T_e = 8.0 \text{ kK}$ and found that increments (or decrements) of T_e in 1.0 kK around 8.0 kK produce decrements (or increments) of 0.28 dex in O⁺/H⁺; of 0.22 dex in O⁺⁺/H⁺; of 0.17 dex in N⁺/H⁺; of 0.16 dex in S⁺/H⁺; of 0.13 dex in S⁺⁺/H⁺; of 0.28 dex in Ne⁺⁺/H⁺; and of 0.15 dex in Ar⁺⁺/H⁺. Likewise, considering DI14's ICFs, we found that an increment (or decrement) of T_e in 1.0 kK around 8.0 kK produce a decrement (or increment) 0.26 dex in O/H; of 0.15 dex in N/H; of 0.14 dex in S/H; of 0.30 dex in Ne/H; and of 0.15 dex in Ar/H. As it is widely know, we see that the derived (CEL) ionic and total abundances are *very* sensitive to the adopted electron temperature.

Comparing our integrated abundances with those reported by GR07 for M8, we see that there is good agreement for O/H, N/H and Ar/H within the errors. However, for S/H, our value is 0.35 dex

smaller than GR07's, although it is similar to the value reported by E99 within the errors. As commented before, this difference in S/H is due in part to the updated [SIII] atomic data used by GR07 and to uncertainties in the [SIII] $\lambda 9532$ line intensity, which may be affected by atmospheric H₂O absorption and OH emission bands (Stevenson, 1994).

Our Ne/H is 0.16 dex larger than the value reported by GR07, although it is barely consistent within the errors. The reason of this difference is *not* in the adopted ICF(Ne), since our ICF(Ne) is 50% smaller than that of GR07, but it is in the much higher ([NeIII] $\lambda 3869/H\beta$)₀ dereddened line intensity that we measured, as compared to that reported by GR07 (see Table 5a).

Table 7b. Ionic, total and relative abundances for M20 including temperature fluctuations.^a

	M20-S. <i>neb</i> $t^2 = 0.026$ (1)	M20-N. <i>neb</i> $t^2 = 0.023$ (2)	Error (3)	GR06+DI14 ^b $t^2 = 0.029$ (4)	GR06 original $t^2 = 0.029$ (5)
log O ⁺ ($\lambda 3727$)	8.60	8.63	± 0.18		8.59 ± 0.08
log O ⁺⁺ ($\lambda 5007$)	7.87	7.85	± 0.10		7.90 ± 0.10
log N ⁺ ($\lambda 6584$)	7.61	7.65	± 0.12		7.67 ± 0.05
log S ⁺ ($\lambda 6725$)	6.33	6.38	± 0.09		6.29 ± 0.06
log S ⁺⁺ ($\lambda 9531$)	6.72	6.69	± 0.12		7.09 ± 0.10
log Ne ⁺⁺ ($\lambda 3869$)	6.89	7.00	± 0.12		6.80 ± 0.10
log Ar ⁺ ($\lambda 7136$)	6.23	6.25	± 0.07		6.36 ± 0.05
O ⁺⁺ /O	0.16	0.14	± 0.05		0.17
O/H	8.68	8.70	± 0.17	8.67 ± 0.05	8.67 ± 0.07
N/H	7.66	7.70	± 0.15	7.72 ± 0.06	7.83 ± 0.07
S/H	6.87	6.87	± 0.14	7.15 ± 0.06	7.12 ± 0.09
Ne/H	8.02	8.17	± 0.15	7.90 ± 0.13	7.97 ± 0.18
Ar/H	6.39	6.43	± 0.17	6.51 ± 0.07	6.70 ± 0.11
N/O	-1.02	-1.00	± 0.32	-0.95 ± 0.11	-0.84 ± 0.14
S/O	-1.81	-1.83	± 0.31	-1.52 ± 0.11	-1.55 ± 0.16
Ne/O	-0.66	-0.55	± 0.32	-0.77 ± 0.18	-0.70 ± 0.25
Ar/O	-2.29	-2.27	± 0.34	-2.16 ± 0.12	-1.97 ± 0.18
ICF(N)	1.12	1.11	$\pm 39\%$	1.13	1.45
ICF(S)	1.00*	1.00*	$\pm 54\%$	1.00*	0.925!
ICF(Ne)	13.5	14.8	$\pm 8\%$	12.5	14.8
ICF(Ar)	1.45	1.51	$\pm 54\%$	1.41	2.19

^a Logarithmic ionic and total abundances given as $12 + \log(X^+/H^+)$. The excitation degree O⁺⁺/O is linear. ^b From GR06's ionic abundances for $t^2 = 0.029$ and DI14's ICFs.

Regarding the comparison of our M20 results with those reported by GR06, we found an excellent agreement among the ionic abundances listed in Table 7b, except again, for S⁺⁺/H⁺, which is

0.38 dex smaller than the value reported by GR06. This difference is not due to the $([\text{SIII}] \lambda 9532/\text{H}\beta)_0$ line intensities employed (Table 5*b*), which explains only 0.05 dex of the difference, but to the updated atomic data for [SIII] employed by GR06 and García-Rojas et al. (2005). This difference in the S^{++}/H^+ ionic abundance is responsible for 0.28 dex of the difference between our integrated S/H and the value derived from GR06 results (column 4 of Table 7*b*).

Comparing our Ne/H abundance for M20-S and M20-N, we see that $(\text{Ne}/\text{H})_{\text{M20-N}}$ is 0.15 dex larger than $(\text{Ne}/\text{H})_{\text{M20-S}}$, which however is still within the assigned errors. The reason of this difference is mostly due to the difference in the dereddened line intensity, since $([\text{NeIII}] \lambda 3869/\text{H}\beta)_0$ in M20-N is 0.12 dex larger than in M20-S, and also to the different ICF(Ne) employed.

Our derived Ar/H abundance is 0.10 dex smaller than the value derived from GR06 ionic abundance, but still within the errors. As mentioned before, GR06 derived a relatively low Balmer temperature $T_{\text{Bal}} = 6.0 \pm 1.3$ kK, corresponding to a relatively high $t_{\text{Bal}}^2 = 0.049$ value for M20. Therefore, part of the difference in the Ar/H abundance is because GR06 considered a smaller average temperature in the high-ionization zone used to compute $\text{Ar}^{++}/\text{H}^+$ including temperature fluctuations.

Finally, comparing our M8 and M20 $t^2 > 0$ total abundances with those recalculated from the $t^2 > 0$ ionic abundances given by GR07 and GR06, respectively, we conclude that our integrated spectra yield the same O/H abundances as those derived from fixed slit observations. However for nitrogen, our integrated spectra indicates N/H abundances ~ 0.06 dex smaller than the abundances derived from fixed slit observations. At the other hand, our integrated spectra seem to indicate Ne/H abundances that are ~ 0.20 dex larger than those derived using fixed slit observations.

To finish this section, in Table 8 we present a comparison of the average N/O and Ne/O abundance ratios derived for our Carina, M8, and M20 regions, along with the most recent determinations found in the literature for these objects. We also include the abundance ratios derived from B stars in the Orion star-forming region (Nieva & Simón-Díaz, 2011), and the corresponding values for the Sun (Asplund, et al. 2009). Our N/O ratio appears to be 0.10 dex smaller than the N/O ratio derived from B stars and 0.15 dex smaller than the N/O ratio derived for the Sun. However, they are still consistent within the errors. Our Ne/O ratio appears to be 0.15 dex larger than the ratio derived from B stars, and 0.26 dex larger than the ratio derived for the Sun. The N/O ratio derived from the observations found in the literature using the new ICFs from DI14's, is consistent with the ratio derived from B stars and for the Sun. The Ne/O ratio derived from observation found in the literature is consistent with the ratio derived for B stars, but is 0.14 dex smaller than the ratio derived for the Sun. From Table 8 we conclude that the ICFs of DI14 seem to overestimate the Ne/H abundance, except in the case of low excitation nebula (as in M20).

Table 8. Comparison of abundance ratios. ^a

	$\langle \text{Car} \rangle$	$\langle \text{M8} \rangle$	$\langle \text{M20} \rangle$	B stars ^b	Sun ^c
N/O	-1.05 -0.88 ^d	-1.07 -0.96 ^e	-1.01 -0.95 ^f	-0.92	-0.86
Ne/O	-0.49 -0.52 ^d	-0.41 -0.54 ^e	-0.61 -0.77 ^f	-0.65	-0.76

^a Typical error for our abundance ratios are ± 0.30 dex. ^b From Nieva & Simón-Díaz (2011). ^c From Asplund et al. (2009). ^d From Peimbert et al. (1978), recalculated using DI14's ICFs. ^e From García-Rojas et al. (2007), recalculated using DI14's ICFs. ^f From García-Rojas et al. (2006), recalculated using DI14's ICFs.

5.7 Conclusions

In this chapter we presented the *.all* and *.neb* dereddened line intensities for our M8-E, M8-W, M20-S and M20-N subregions. We found that the logarithmic reddening constant derived including the exciting stars is larger than excluding them: for M8 we found on average that $c(\text{H}\beta).all = 0.52 \pm 0.13$, while $c(\text{H}\beta).neb = 0.44 \pm 0.14$. Likewise, for M20 we found $c(\text{H}\beta).all = 0.74 \pm 0.30$, while $c(\text{H}\beta).neb = 0.56 \pm 0.17$. Considering all our target objects: Carina, M8, M20 and the 4 RCW objects mentioned in Chapter II, we found that $c(\text{H}\beta).all$ is on average 0.07 dex larger than $c(\text{H}\beta).neb$. This difference may have consequences on the physical parameters and element abundances derived for giant extragalactic HII regions where the embedded exciting stars cannot be removed from the integrated spectra.

For M8, our integrated $c(\text{H}\beta)$ is smaller than the corresponding value derived from fixed slit observations adapted from the literature. However, for M20, our integrated $c(\text{H}\beta)$ is similar to that derived from several slit positions within the nebula as reported in the literature. Regarding the density, our integrated scans suggest nebulae of rather average low density, $n_e \approx 400 \text{ cm}^{-3}$ for M8 and $n_e \approx 100 \text{ cm}^{-3}$ for M20.

Comparing the *.all* and *.neb* electron temperatures derived in Carina, M8 and M20, we found that on average, $T_e(\text{OIII}).all$ (including the exciting stars) is 200 K *larger* than $T_e(\text{OIII}).neb$ (excluding the exciting stars). Although the assigned error for $T_e(\text{OIII})$ is about ± 600 K, this 200 K increment between the *.all* and *.neb* electron temperatures will tend to yield *.all* abundances about 0.05 dex smaller than the true *.neb* abundances.

We found that the procedure used to measure the faint auroral lines $[\text{OIII}] \lambda 4363$ and $[\text{NII}] \lambda 5755$ has a strong impact on the derived T_e and ionic abundances, that prevent us to estimate the ionic and total abundances with a precision better than 0.05 – 0.10 dex.

As mentioned in Chapter IV, we found that the use of the new ICF's presented by Delgado-Inglada et al. (2014) leaves the O/H and S/H abundances unchanged with respect to the values derived using KB94's common ICFs. However, the "updated" N/H value appears to be decreased by -0.10 dex in M8, while the "updated" Ne/H abundance is increased by 0.30 dex both in M8 and in M20, with respect to the values derived using the common ICFs.

We found that $(\text{O}/\text{H})_{.all} \approx (\text{O}/\text{H})_{.neb}$, and $(\text{S}/\text{H})_{.all} \approx (\text{S}/\text{H})_{.neb}$, although both $(\text{N}/\text{H})_{.all}$ and $(\text{Ar}/\text{H})_{.all}$ appear 0.05 dex *smaller* on average than the corresponding $(\text{N}/\text{H})_{.neb}$ and $(\text{Ar}/\text{H})_{.neb}$ values. However, we also found that $(\text{Ne}/\text{H})_{.all}$ is 0.07 dex *larger* on average than $(\text{Ne}/\text{H})_{.neb}$. The cause of these differences is due to differences in the *.all* and *.neb* reddening and temperatures applied. Note however, that our abundances errors are about ± 0.12 dex, so we cannot establish a definitive trend among the *.all* and *.neb* total abundances.

Our M8 derived abundances are in good agreement with those reported by García-Rojas et al. (2007; GR07). However, we found a Ne/H abundance 0.20 dex larger than that reported by GR07. This is not due to the ICF(Ne) employed, but to our larger dereddened $([\text{NeIII}] \lambda 3869/\text{H}\beta)_0$ line flux ratio. As with the Carina spectra discussed in Chapter IV, our integrated spectra for M8 appears to favor the detection of high-excitation lines such as $([\text{OIII}] \lambda 5007)_0$ and $([\text{NeIII}] \lambda 3869)_0$, while decreases low-excitation lines such as $([\text{OII}] \lambda 3727)_0$ and $([\text{NII}] \lambda 6584)_0$, as compared to fixed slit position observations. For M20, which is a much lower excitation nebula, we do not see this trend, although our Ne/H abundance is also 0.20 dex larger than that reported by GR06 from fixed slit observations.

Our average N/O ratio for M8 and M20, $\langle \text{N}/\text{O} \rangle_{\text{Our}} = -1.04$ is in good agreement with that derived for M8 and M20 by the group of García-Rojas et al., $\langle \text{N}/\text{O} \rangle_{\text{GR}} = -0.96$, which is also in very good agreement with the ratio derived for B stars in the Orion region by Nieva & Simón-Díaz (2011): $\langle \text{N}/\text{O} \rangle_{\text{B-Stars}} = -0.92$.

Comparing the Ne/O ratio derived for our objects with similar studies found in the literature, with B stars in the Orion star-forming region and with the Sun, it seems we may be overestimating the Ne/O ratio in M8, since we found $\langle \text{Ne}/\text{O} \rangle_{\text{M8 Our}} = -0.41$. It appears then that the new ICFs proposed by Delgado-Inglada et al. (2014) may be overestimating the Ne/H abundance by $0.10 - 0.15$ dex, except in nebula of low excitation ($\text{O}^{++}/\text{O} < 0.20$) as is the case of M20.

Chapter VI. Scattered light in the spectra of HII regions

6.1 Introduction - Dust within HII regions

The existence of dust within HII regions is exemplified by the presence of dark lanes and dark globules silhouetted against bright diffuse nebular emission. The observed non-correspondence between the $H\alpha$ emission and the radio brightness distribution is also an indication of the presence of dust within an HII region. Even more, there are some HII regions which do not have a visual counterpart and that are detected only at radio and IR wavelengths. Dust is mixed with the gas in the ISM, so it is expected an appreciable amount of dust in the original gas where the HII region was born. However, once the O stars are formed, dust will tend to be destroyed, either by sputtering with gas atoms or by evaporation once the grain's surface attain a high temperature due to absorption of incident UV radiation from the hot stars. This would tend to erode loosely bound ice grains, leaving behind a large fraction of refractory core particles, and this would lead to sub-normal values of the dust-to-gas ratio *inside* the HII region as compared to the general ISM, as has been found for the Orion nebula (O'Dell & Hubbard 1965; OH65).

The presence of dust within the HII regions alters significantly the physical processes taking place within the nebula. Absorption of ionizing photons by dust will alter the ionization equilibrium, and the Balmer decrement will be affected because blue wavelengths are more absorbed than the red ones. Dust grains will absorb $Ly\alpha$ trapped photons and continuum UV photons and will re-radiate them in the IR, so the general IR emission for the HII region would appear arising from an extended HII region rather than from localized spots within the nebula. Dust will compete effectively for $Ly\alpha$ photons and the overall ionization balance will decrease, yielding a smaller ionization-bounded HII region. The chemical composition of the nebula, traced by the O/H abundance, may also be affected by the presence of dust within the nebula, since an important fraction of O-atoms may be depleted onto dust grains, reaching fractions as high as 50 – 60% of the total O/H abundance (Peimbert & Peimbert 2010).

Dust within a HII region will also affect the dynamic behavior of the nebulae. Radiation pressure on the dust may produce grain drifting through the gas leading to separation of large and small dust grains within the nebula. This will affect also the general expansion of the nebula by the strong electrostatic coupling of the dust particles to the gas, and the radiation pressure effects would be stronger closer to the ionizing star and on larger grains. Line splitting and other velocity features can partially be attributed to the interaction of ionizing radiation with dust particles (Henney 1998). There is also evidence of strong IR excess around $10\ \mu\text{m}$ due to thermal emission by hot dust when compared

to the gaseous contribution predicted by IR radiation from free-free, free-bound and bound-bound transitions in the H–He plasma, as in the nebula W3(A) (Wynn-Williams et al. 1972).

In this chapter we present an analysis of the *.all* and *.neb* line intensities, continuum fluxes and equivalent widths in the presence of scattered light in our integrated *.all* and *.neb* spectra of Carina, M8 and M20. In Sec. 6.2 we present evidence of scattered light in Galactic HII regions, and in Sec. 6.3 we derive the fraction of scattered light present in our spectra. In Sec 6.4 we compare the scattered continuum with the stellar continuum in each nebula. In Sec. 6.5 we study the dependence of the scattered continuum on wavelength, and in Sec. 6.6 we investigate the effects of the scattered light on the derivation of reddening, electron temperatures, and ionic and total abundances. In Sec. 6.7 we use simple arguments to relate the scattered continuum to the observed reddening. In Sec. 6.8 we comment on the relation between the gas-to-dust ratio and the fraction of scattered light. Our conclusions are presented in Sec. 6.9.

In Appendix IV we present an attempt to relate the derived scattered continua colors with the sizes and types of grains that composes our studied nebulae. And in Appendix V we present a review of models for dusty nebula and discuss some implications of the scattered light in GEHRs.

6.2 Evidence of scattered light within HII regions

There is considerable evidence of the presence of scattered light in the observed spectrum of diffuse nebula. From the theoretical point of view, and depending on the assumed geometry of the emitting layers, the emission line profile and polarization may indicate the presence of scattered light (Henney 1998). For the Orion Extended Nebula (OEN), O’Dell & Goss (2009) found that the $H\beta$ surface brightness derived from optical spectroscopy $S(H\beta)_{\text{vis}}$, is a factor of 1 – 2 larger than the corresponding value derived from radio observations for the same regions $S(H\beta)_{\text{rad}}$, indicating the presence of a scattered component which increases with distance from the ionizing star θ^1 Ori C.

Another strong evidence of scattered light present in the nebula is the fact that the diffuse optical continuous emission observed in many HII regions is larger than what pure nebular-atomic processes can account for. That is, the observed equivalent width at $H\beta$ cannot be explained by atomic processes only in a nebula free of dust, therefore suggesting the presence of an additional source of continuum. Recently, O’Dell et al. (2013) found that 20% of the continuum light at $\lambda 4861$ in the PN NGC 6720 comes from scattered light arising in the dense photo-dissociation region lying *outside* the ionization front.

In Fig. 1a we plot the observed $\lambda 4861$ Å continuum flux i_{4861}^{obs} vs. the observed $H\beta$ flux F_{β}^{obs} , for 16 Galactic H II regions (open squares) adapted from the literature, as well as our 7 nebulae (filled circles = *.neb* and open circles = *.all*). For Orion we have joined the average from OH65 and from Costero & Peimbert (1970; CP70). We joined M8 and M20 averages from O’Dell, Hubbard & Peimbert (1966; OHP66) to our values. We also plotted 27 Galactic HII regions (asterisks) from integrated photometry by Copetti (2000), who used aperture diameters from 1.7’ to 6.7’. Copetti’s observations could be compared to our *.all* spectra since they encompassed both most of the nebulae and their exciting stars. Note that different objects were observed with different slit/apertures and suffer different amounts of extinction. Even considering a single nebula, observations at different spots within the nebulae present variations in both parameters, with variations in F_{β}^{obs} up to 2.6 dex for Orion. In Fig. 1a, all nebulae except a few (NGC 1499, NGC 7000, and IC 5067 – 70) show an excess of the continuum above that expected from purely atomic processes i_{4861}^{a} , indicated by straight lines at 3 different temperatures (see Sec. 6.3 below). For the *.neb* observations (ours and the open squares), this is evidence of an added continuum component due to stellar continuum scattered by dust grains. The actual shift $i_{4861}^{\text{obs}} - i_{4861}^{\text{a}}$ at a given F_{β}^{obs} , depends on the nature and the amount of scattering particles, and on the density of the radiation field as seen from the nebula. Therefore, the observed shift is not linearly related to the actual dust content within each nebula.

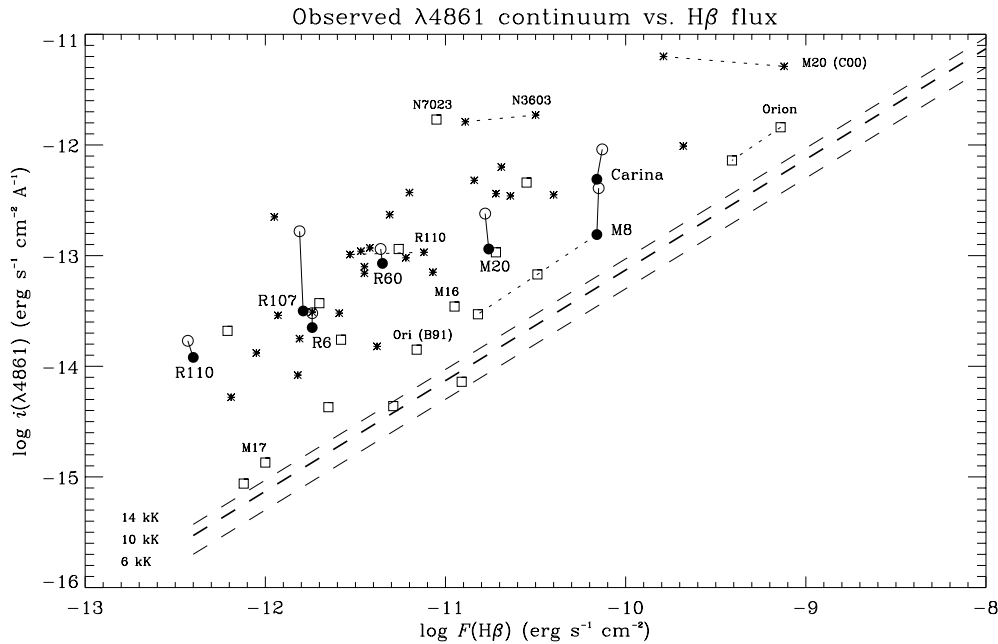


Fig. 1a. Observed $\lambda 4861$ Å continuum vs. $H\beta$ flux for several Galactic H II regions (open squares) adapted from the literature: OH65 (Orion), OHP66 (M8, M20 and M16), Krishna Swamy & O’Dell (1966; open squares), Baldwin et al. (1991; Orion), PTPR92 (M17), and Copetti (2000; asterisks). For our regions, *.neb* = filled circles, *.all* = open circles. Straight lines give the “pure atomic” continuum at 3 different temperatures.

Comparing Copetti's photometry with the rest of the *neb* observations, we see that his integrated aperture observations present a continuum that is 1.4 dex larger on average, with respect to the atomic continuum. This is due to the added continuum from the embedded stars; however from our *neb* and *all* observations (see Sec. 6.4 below), we know that only $\sim 0.4 - 0.6$ dex is due to the stellar contribution, therefore the rest must be due to scattered continuum. Our *neb* observations tend to present a higher i_{4861}^{obs} (at given F_{β}^{obs}) than the fixed-slit observations of other Galactic HII regions (open squares), indicating probably a remaining background and foreground stellar continuum still present in the *neb* spectra, as discussed in Chapter II.

In order to eliminate the reddening and slit-coverage factors, we present in Fig. 1b the dereddened $\lambda 4861$ Å continuum surface brightness s_{4861}^0 vs. the dereddened $H\beta$ surface brightness S_{β}^0 , for a subset of the above nebula (same scale and symbols) for which we had the entrance slit or diaphragm aperture and the reddening constant. In this plot the nebulae present a smaller spread, with Orion, NGC 3603, M17 and Carina being among the brightest nebulae. The corrections for slit-entrance and reddening for a given nebula only produce displacements parallel to the atomic continuum line since $\log S_{\beta}^0 = \log F_{\beta}^{\text{obs}} + c(H\beta) - \log \Omega_{\text{slit}}$, and $\log s_{4861}^0 = \log S_{\beta}^0 - \log W_{\beta}$, where the reddening constant $c(H\beta)$, the entrance slit Ω_{slit} (in arcmin²) and the equivalent width W_{β} (in Å) are constants for each observation, so the suggested fraction of scattered continuum remains the same. We see that most of the Galactic HII regions observed with slits that cover only a fraction of the nebula and that were positioned close to the ionizing stars show an important contribution of scattered continuum.

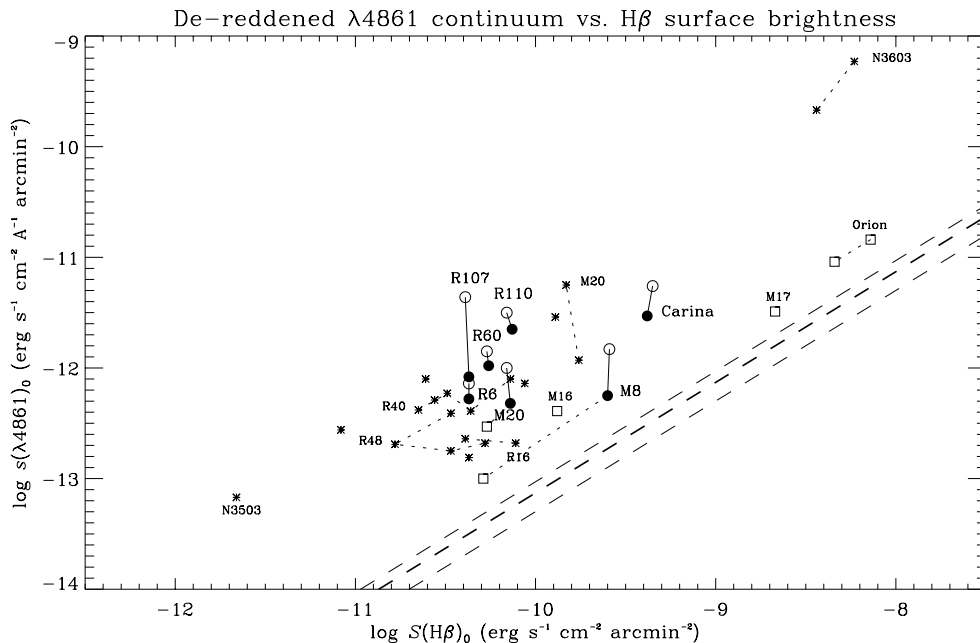


Fig. 1b. Dereddened $\lambda 4861$ Å continuum surface brightness vs. $H\beta$ surface brightness for some of the nebulae in Fig. 1a. Same symbols and lines as in Fig. 1a.

The spatial distribution of reflected light does not follow necessarily the distribution of the line emission or that of the atomic continuum, even if the dust and gas are well mixed. On one hand, gas emission depends on the gas density n_g^2 , and is affected by density gradients and inhomogeneities. On the other hand, scattered light tends to be more centrally peaked due to the r^{-2} dependence of the stellar flux. It is thus expected that scattered light will in general be confined to the inner parts of the HII regions. However, in the Orion nebulae, it seems to be an under-abundance of dust (that is, a high gas-to-dust ratio) in the inner regions ($\sim 1'$) and a possible over-abundance in the outer regions (O'Dell & Harris 2010). This apparent increment of the dust density as function of distance in Orion may be due to *a*) radiation pressure on dust grains and *b*) a change in the albedo of the scattering particles: grains retaining their icy-mantles in the outer region would have a relatively high albedo, whereas in the inner regions, the mantles could be evaporated, leaving a smaller refractory particle with a lower albedo (Martin 1978). Additional evidence of dust-scattered starlight in Orion was given by Peimbert & Goldsmith (1972) whom detected HeII $\lambda 4686$ in *absorption* over the nebular continuum, indicating the presence of scattered starlight from the main ionizing sources θ^1 Ori and θ^2 Ori in the nebular spectra.

The presence of scattered light could have several implications. As we shall see in Sec. 6.5 below, the line and continuum scattered component increases towards the blue and produce observed F_α/F_β line flux ratios which are underestimated if scattering is not taken into account (O'Dell & Harris 2010, Simón-Díaz et al. 2011). This would yield in turn, underestimated reddening corrections to the observed spectra. At the other hand, the electron temperatures derived from collisional excited lines such as $T_e(\text{OIII})$, $T_e(\text{NII})$ and $T_e(\text{SII})$, all involve the ratio of a nebular to an auroral line (e.g. $\lambda 5007/\lambda 4363$), and this *bluing* of scattered light would artificially enhance the auroral line, yielding an overestimated T_e if scattering is not taken into account. Then, to account for the observed line fluxes, the ion abundances derived from collisional excited lines (CEL; e.g. O^+ and O^{++}) would tend to be underestimated in the presence of scattering. This behavior goes in the right direction to compensate at least in part the so-called Abundance Discrepancy Factor (ADF) found in several well studied nebulae, for which the ionic abundances derived from CEL are about a factor of 2 smaller than those derived from optical recombination lines (RL) in HII regions (Torres-Peimbert et al. 1980, Peimbert et al. 1993, García-Rojas & Esteban 2007 and references there in).

6.3 Scattered continuum

Our observed *.neb* continua $i_{.neb}^{\text{obs}}$, have in principle the following contributions: *i*) atomic processes such as recombination of H and He ions, and free-free and two-photon continuum (see below), which we will call hereafter the *atomic continua*, i^a ; *ii*) dust scattered light originating mainly in the stars within the nebula, i^d ; *iii*) continuum from background or foreground faint stars that crossed our slit during the drift observations and that were *not* removed from the *.neb* spectra; *iv*) continuum

from bright stars inaccurately removed from the CCD when constructing the *.neb* spectra; *v*) sky continua due to inaccurate sky subtraction; *vi*) scattered light inside the spectrograph and *vii*) electron scattering. The observed *.all* spectra, besides all these contributions (except *iv*) are obviously affected by the continua of the bright stars that crossed the slit during the scans, i^* . All continua hereafter will be measured in $\text{erg s}^{-1} \text{cm}^{-2} \text{\AA}^{-1}$. Sánchez (1990) showed that electron scattering is negligible (less than 0.4% of i^*) for plasma at the T_e and N_e expected in typical HII regions and will be ignored. The continuum from scattered light inside the spectrograph was already corrected during data reductions (Chapter II).

As explained in Chapter II, to construct our *.neb* spectra we “removed” from the CCD only those stars whose continuum at $\lambda 4861 \text{\AA}$ was brighter than $\sim 5\%$ of the nebular $H\beta$ emission around the star on the CCD. Therefore, some faint stars were left even in the *.neb* spectra. From inspection of the scanned regions and their corresponding integrated spectra, we estimate that these non-removed dim stars may contribute up to $\sim 10\%$ of the observed *.neb* continuum in the Carina regions, which has the highest projected density of stars, and less than 10% in M8 and M20, where there are only a few bright stars. Sky subtraction was performed as best as possible, and we estimate that the sky contribution is smaller than 5 – 10% in our spectra. In any case, this sky contribution would tend to redden the observed continuum, which turned out to be quite blue.

Finally, we have two additional sources of uncertainty introduced by the procedure used to remove the selected stars, as explained in Chapter II. The slit was aligned N–S and the dispersion ran along the E – W direction. To “remove” a selected stellar spectra from the CCD, we used a rectangle formed by the pixels occupied by the spectra (usually from 3 to 10 pixels wide and 576 pixels long). In order to *do not* remove the nebular emission originating within this rectangle (both nebular continuum and emission lines), we “filled up” this rectangle by interpolating at each λ , the values of the nebular emission arising from strips 2 – 3 pixels wide above (N) and below (S) the rectangle. After removal of the selected stars, we examined the 2-D *.neb* spectra by making cuts at different wavelengths to check whether the nebular emission interpolation was satisfactory (see Figs. 6a – 6b of Chapter II). This procedure, however, carried the following uncertainties: *i*) the spectra of the brightest stars did not occupied the same number of pixels all along the dispersion, but marked usually a wider spectrum towards the blue, and *ii*) the CCD was not *exactly* aligned along the dispersion, so that a dim star left a spectrum that ran slightly diagonal along the two borders of the CCD, shifted about 3 – 4 pixels from one side to the other. To construct the *.neb* spectra, we removed the same rectangle from each of the B, Y and R spectral ranges. We estimate that $i_{.neb}^{\text{obs}}$ may have a stellar contribution up to 5 – 10% due these errors introduced in the process of removing the bright stars, specially in the crowded Carina regions, where bright stars with similar declination produced rectangles on the CCD that either

intersected each other, or were uncomfortably close in declination, affecting thus the aforementioned nebular interpolation.

Keeping all these possible contributions in mind, we will consider hereafter that the observed *.neb* continua is given by:

$$i_{.neb}^{\text{obs}} = i^{\text{a}} + i^{\text{d}}, \quad (1)$$

while the observed *.all* continua would be given by:

$$i_{.all}^{\text{obs}} = i^{\text{a}} + i^{\text{d}} + i^* = i_{.neb}^{\text{obs}} + i^*. \quad (2)$$

To estimate the atomic continua we proceeded as follow. As mentioned in Chapter III, for an ideal homogeneous isothermal nebula free of dust, the nebular continuum emissivity $\varepsilon_c(\lambda)$, has the following contributions: *i*) recombination of electrons with H^+ , *ii*) recombination of electrons with He ions, *iii*) bremsstrahlung emission produced by free-free transitions of electrons in the Coulomb fields of H and He ions, and *iv*) radiation produced by two-photon decay from the metastable $2^2\text{S}_{1/2}$ level of hydrogen. Using Brown & Mathews' (1970) formalism, we can write the nebular continuum emissivity as given in Eqs. (22) and (23) of Chapter III, where the $\gamma(\lambda)$ coefficients (in $\text{erg cm}^3 \text{ s}^{-1} \text{ \AA}^{-1}$) are the atomic continuum emission coefficients for HI, HeI and HeII, and include contributions from both bound-free and free-free transitions, as well as two-photon emission from HI. We used the atomic continuum emission coefficients, γ_i computed by Brown & Mathews (1970) to estimate i_{λ}^{a} . We will ignore the contribution from γ_{HeII} in Eq. (23) of Chapter IV since $\text{He}^{++}/\text{H}^+$ is negligible in our spectra. Therefore, the effective atomic continuum emission coefficient can be written as:

$$\gamma_{\text{eff}} = \gamma_{\text{HI}} + \gamma_{2q} + (0.1) \gamma_{\text{HeI}} \quad (3)$$

where we have assumed an average fraction $\text{He}^+/\text{H}^+ = 0.1$. We used Brown & Mathews (1970) $\gamma_{\text{HI}}(\lambda)$, $\gamma_{2q}(\lambda)$ and $\gamma_{\text{HeI}}(\lambda)$ coefficients (as function of λ and T_e), given in $\text{erg cm}^3 \text{ s}^{-1} \text{ Hz}^{-1}$, and transformed them for convenience to $\text{erg cm}^3 \text{ s}^{-1} \text{ \AA}^{-1}$ (multiplying them by c/λ^2). Fig. 2a shows these γ_i coefficients, for $N_e \ll 10^4 \text{ cm}^{-3}$, at $T_e = 6, 10$ and 14 kK . At a given temperature, we interpolated these γ_i coefficients at every few hundred angstroms to compute γ_{eff} , shown in Fig. 2b, and from this plot, we interpolated γ_{eff} at $\text{H}\delta$, $\text{H}\gamma$, $\text{H}\beta$ and $\text{H}\alpha$, which are given in Table 1a.

We computed the $\text{H}\beta$ emissivity, $\varepsilon_{\text{H}\beta} = N_e N_{\text{H}^+} \alpha_{\text{H}\beta}^{\text{eff}} \times h\nu_{\text{H}\beta}$ (in $\text{erg cm}^{-3} \text{ s}^{-1}$), using the fits presented by Pèquignot, Petitjean & Boisson (1991) to estimate the case B $\text{H}\beta$ effective recombination coefficient $\alpha_{\text{H}\beta}^{\text{eff}}$, as function of temperature, which is given in Eq. (20) of Chapter III.

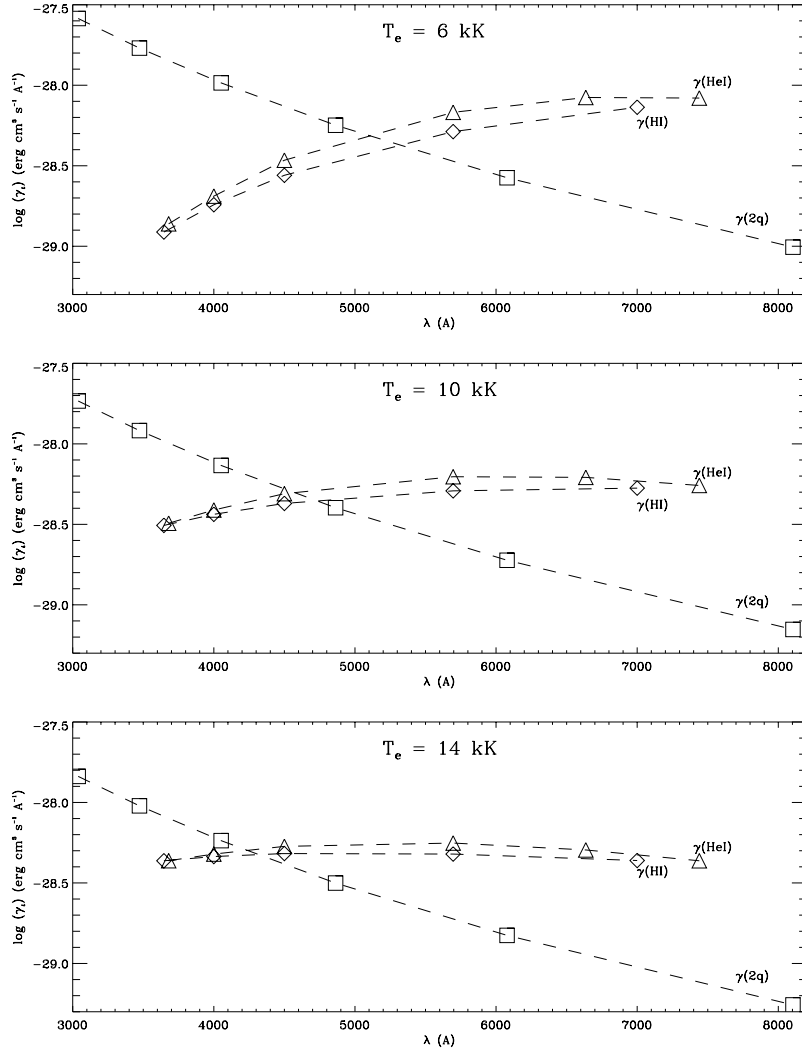


Fig. 2a. Logarithmic atomic continuum emission coefficients $\log(\gamma_i)$ ($\text{erg cm}^3 \text{s}^{-1} \text{\AA}^{-1}$) as function of wavelength λ (\AA), for $N_e \ll 10^4 \text{ cm}^{-3}$ (adapted from Brown & Mathews (1970)).

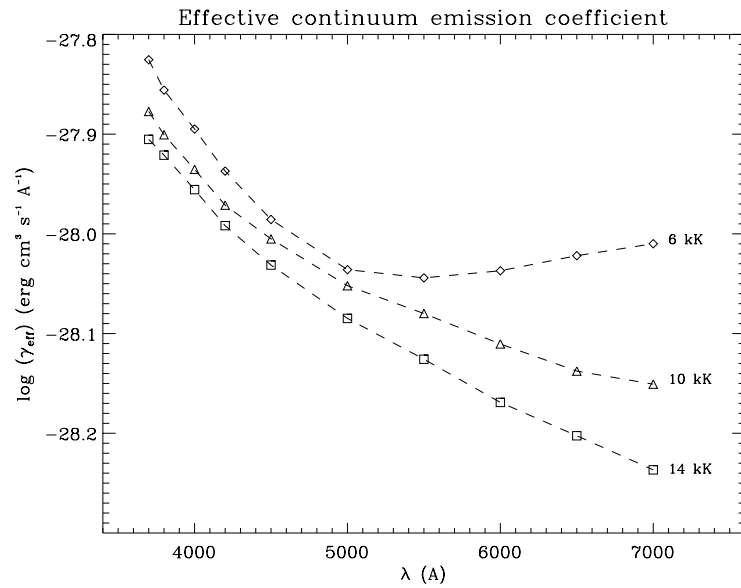


Fig. 2b. Effective atomic continuum emission coefficient, $\gamma_{\text{eff}} \approx \gamma_{\text{HI}} + \gamma_{2q} + (0.1) \gamma_{\text{HeI}}$, for $N_e \ll 10^4 \text{ cm}^{-3}$, at three different temperatures (adapted from Brown & Mathews 1970).

Table 1a. Effective atomic continuum emission coefficients and predicted atomic equivalent widths, W_λ^a

		$\log \gamma_{\text{eff}}^a$			$\log i_\lambda^a / F(\text{H}\beta)_0 (\text{\AA}^{-1})$			
		6	10	14	6	10	14	8 ^d
T_e (kK)								
H δ	4102	-27.916	-27.952	-27.972	-3.192	-3.042	-2.933	-3.115
H γ	4340	-27.960	-27.988	-28.010	-3.236	-3.078	-2.971	-3.150
H β	4861	-28.022	-28.040	-28.070	-3.298	-3.130	-3.031	-3.205
H α	6563	-28.020	-28.139	-28.206	-3.296	-3.229	-3.167	-3.255
$\log \alpha_{\text{H}\beta}^{\text{eff}} h\nu_\beta^b$		-24.724	-24.910	-25.039				

		$F(\lambda)/F(\text{H}\beta)_0$			W_λ^a		
		6	10	14	6	10	14
T_e (kK)							
H δ	4102	0.253	0.259	0.261	394	285	224
H γ	4340	0.460	0.468	0.471	793	560	441
H β	4861	1.00	1.00	1.00	1990	1350	1070
H α	6563	2.896	2.850	2.794	5730	4830	4100

^a Effective continuum emission coefficient, γ_{eff} (in $\text{erg cm}^3 \text{s}^{-1} \text{\AA}^{-1}$), interpolated from Fig. 2b. ^b Effective H β recombination coefficient (in $\text{erg cm}^3 \text{s}^{-1}$) from Pèquignot et al. (1991). ^c Intrinsic case B line ratios from Storey & Hummer (1995). ^d Adapted from Sánchez & Peimbert (1991) for $T_e = 8$ kK.

With these parameters we computed the ratio $i_\lambda^a / F(\text{H}\beta)_0 = \gamma_{\text{eff}} / (\alpha_{\text{H}\beta}^{\text{eff}} \times h\nu_{\text{H}\beta})$. Finally, we used Storey & Hummer (1995; SH95) case B Balmer intrinsic line ratios to compute the ratio $i_\lambda^a / F(\lambda)_0$, which is the inverse of the predicted atomic equivalent width, W_λ^a , expected from an hypothetical nebula free of dust. The intrinsic Balmer line decrements are almost insensitive to T_e and N_e in the range expected for HII regions. We present our results in Table 1a and Fig. 2c. Our results indicate that at $T_e = 10$ kK, we should expect a pure atomic equivalent width at H β , $W_\beta^a \approx 1350$ Å. O’Dell, Hubbard & Peimbert (1966; OHP66) used Seaton (1960) continuum coefficients and obtained $W_\beta^a \approx 1150$ Å, while Sánchez & Peimbert (1991) found $W_\beta^a \approx 1600$ Å at $T_e = 8$ kK, which agree with our results (Table 1a). O’Dell et al. (2013) found that at 10 kK, $W_\beta^a = 1400$ Å for a pure H nebula and $W_\beta^a = 935$ Å for nebula with He/H = 0.12 and He⁺⁺/He = 0.70 (suited values for the PN NGC6720 they studied).

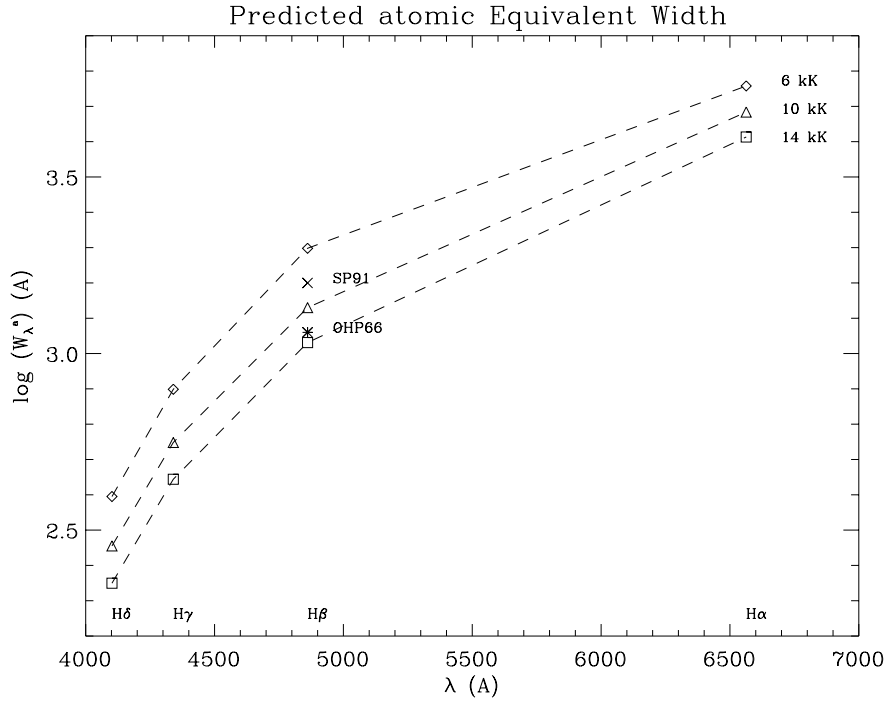


Fig. 2c. Predicted atomic equivalent width W_λ^a for Balmer lines as function of T_e . The cross gives the value computed by Sánchez and Peimbert (1991) at 8 kK, and the asterisk that by OHP66 at 10 kK.

As commented in Chapter III, we built further integrated spectra of our target nebulae, Car Reg, M8 Reg and M20 Reg, adding λ to λ the spectra of the individual sub-regions for each nebula. We will use the Balmer line fluxes F_λ and equivalent widths W_λ for these regions presented in Tables 1a and 1b of Chapter III, which have an estimated statistical error of about 5%, as explained in Chapter III.

Now we can estimate the contribution of the scattered continuum i^d , present in $W_\lambda^{.neb}$ for Car Reg, M8 Reg and M20 Reg. Knowing this contribution, we can also estimate the contribution of the integrated stellar continuum i^* , present in $W_\lambda^{.all}$. We also can estimate the color of i^d , which bears information about the properties of the scattering particles. We used $T_e = 9.5, 8.2$ and 8.7 kK for Car Reg, M8 Reg and M20 Reg, respectively, based on our T_{OIII} and T_{NII} determinations (Chapters IV and V), as well as other T_e determinations for these objects found in the literature. We used Fig. 2c to assign an atomic W_λ^a for each nebula according to its temperature, and we present our results in Table 1b.

Using the fact W_λ is practically not affected by extinction ($W_\lambda^{obs} = W_\lambda^0$), we can show that the fraction of scattered continuum to the *.neb* continuum is given by:

$$\mathcal{X}_\lambda^d \equiv \left(\frac{i_\lambda^d}{i_\lambda^a + i_\lambda^d} \right) = 1 - \left(\frac{W_\lambda^{.neb}}{W_\lambda^a} \right) \quad (4)$$

Table 1b. *.neb*, *.all* and atomic Equivalent Widths, and scattered and stellar continuum fractions

	$W_{\lambda}^{.neb}$ (Å)			$W_{\lambda}^{.all}$ (Å)			r^a		
	Car Reg	M8 Reg	M20 Reg	Car Reg	M8 Reg	M20 Reg	Car Reg	M8 Reg	M20 Reg
4102 (H δ)	18.2	75.5	21.4	12.0	23.0	7.90	0.87	1.05	1.22
4340 (H γ)	45.9	161	50.4	27.8	53.8	21.2	0.88	1.00	1.08
4861 (H β)	141	450	150	82.0	174	68.7	0.93	0.97	1.03
6563 (H α)	816	1990	790	464	1080	452	0.98	1.00	1.00
	W_{λ}^a (Å)			χ^d ^b			χ^* ^c		
	Car Reg	M8 Reg	M20 Reg	Car Reg	M8 Reg	M20 Reg	Car Reg	M8 Reg	M20 Reg
4102 (H δ)	297	330	317	0.939	0.771	0.932	0.426	0.680	0.550
4340 (H γ)	585	655	627	0.922	0.754	0.920	0.467	0.666	0.546
4861 (H β)	1416	1607	1531	0.900	0.720	0.902	0.459	0.625	0.528
6563 (H α)	4932	5212	5105	0.836	0.618	0.845	0.443	0.458	0.428

^a Parameter $r = F_{\lambda}^{.neb}/F_{\lambda}^{.all}$. ^b Fraction of scattered continuum to *.neb* continuum $\chi^d = i_{\lambda}^d / (i_{\lambda}^a + i_{\lambda}^d)$. ^c Fraction of stellar continuum to *.all* continuum $\chi^* = i_{\lambda}^* / (i_{\lambda}^a + i_{\lambda}^d + i_{\lambda}^*)$. The errors for χ^d are ± 0.01 , for H α to H δ , and the errors for χ^* are ± 0.07 for H α and H β , ± 0.11 for H γ and ± 0.16 for H δ .

At the other hand, the proportion of stellar continuum to the *.all* continuum is given by:

$$\chi_{\lambda}^* \equiv \left(\frac{i_{\lambda}^*}{i_{\lambda}^a + i_{\lambda}^d + i_{\lambda}^*} \right) = 1 - r \left(\frac{W_{\lambda}^{.all}}{W_{\lambda}^{.neb}} \right) \quad (5)$$

where $r = F_{\lambda}^{.neb}/F_{\lambda}^{.all}$. Using the $W_{\lambda}^{.neb}$, $W_{\lambda}^{.all}$, W_{λ}^a and r -values given in Table 1b, we computed the continuum fractions χ^d and χ^* given in the lower part of Table 1b. The errors assigned to χ^d and χ^* were estimated considering a 4% error in the EWs and r parameter of H α and H β , a 7% error for H γ and a 10% error for H δ . According to these results, most of the observed continuum in our nebulae is due to scattered light, reaching at H β , $\chi^d = 90 \pm 1\%$ for Carina and M20 and $\chi^d = 70 \pm 1\%$ for M8. Considering temperatures 800 K smaller than the assumed values would decrease the derived χ^d by 2%.

Note that the assigned χ^d values for Carina should be considered only as upper limits, with a larger uncertainty of about ± 10 – 15% , because the Carina regions have an important contribution from background and foreground dim stars which were *not* removed from the CCD when we built the *.neb* spectra, which may be an important contribution to the observed continuum at H β . Even with this dim-star correction, i^d remains the main source of the continuum in our program spectra.

OHP66 report measurements of the continuum surface brightness at $\lambda 4861$, $s_c(\lambda 4861)$ ($\text{erg s}^{-1} \text{cm}^{-2} \text{\AA}^{-1} \text{ster}^{-1}$) and the $\text{H}\beta$ surface brightness, $S(\text{H}\beta)$ ($\text{erg s}^{-1} \text{cm}^{-2} \text{ster}^{-1}$) at several slit position close and within our scanned regions for M8 and M20. From these measurements, and their computed $W\lambda^a = 1150 \text{\AA}$, we derive at $\text{H}\beta$, $\chi_{\text{OHP66}}^d = 0.85$ for M20, in very good agreement with our results, although $\chi_{\text{OHP66}}^d = 0.51$ for M8, which is 29% smaller than our estimated value. Sánchez & Peimbert (1991; SP91) present mid-resolution continuum and line spectro-photometry of 6 bright spots in M8 within $1.5'$ of the exciting stars Her 36 and 9 Sgt, which fall inside our M8-E and M8-W subregions. We derived from their observations, $\chi_{\text{SP91}}^d = 0.62$ which is an intermediate value between our result (0.72) and that derived from OHP66 observations (0.51). García-Rojas et al. (2006; GR06) present line and continuum deep observations of one bright slit position in M20, $20''$ from the exciting star HD164492. Interpolating over their reported continuum observations, we found $\chi_{\text{GR06}}^d = 0.89, 0.95, 0.97$ and 0.97 for $\text{H}\alpha$, $\text{H}\beta$, $\text{H}\gamma$ and $\text{H}\delta$, respectively, in reasonable good agreement with our results.

We also performed the same procedure described above to estimate χ^d for each of our M8-E, M8-W, M20-S and M20-N subregions. For M8 we found at $\text{H}\beta$ that $\chi_{\text{M8-E}}^d = 0.75$, while $\chi_{\text{M8-W}}^d = 0.64$. Similarly, for M20 we found that $\chi_{\text{M20-S}}^d = 0.86$, while $\chi_{\text{M20-N}}^d = 0.89$. This implies a larger dust content in M8-E which corresponds well with the huge dark lane crossing in the middle of M8-E, as can be seen in Fig. 3b of Chapter II. At the other hand, our results and those of OHP66 support the idea that M20 has a larger dust content as compared with M8, with an effective gas to dust ratio $(N_{\text{H}}/N_{\text{d}} \sigma_{\lambda}) = 4 \times 10^{20} \text{cm}^{-2}$, which is a factor of 5 smaller than that found in the average ISM (OHP66).

6.4 Comparison between scattered continuum and stellar continuum

In Fig. 3 we present the relation between the fraction of dust-scattered continuum χ^d , derived from the *.neb* spectra, with the fraction of the stellar continuum χ^* , derived from the *.all* spectra for our Carina, M8 and M20 subregions and integrated spectra. To build these charts we used Eqs. 4 and 5, along with the atomic equivalent widths $W\lambda^a$, given in Table 1b and the $W\lambda^{.neb}$ and $W\lambda^{.all}$ equivalent widths given in Tables 1a and 1b of Chapter III. The estimated errors are ± 0.10 for χ^d , and ± 0.15 for χ^* .

Two main conclusions can be drawn from these figures: *a)* For the M8 and M20 spectra, the fraction of scattered continuum correlates with the fraction of stellar continuum, indicating the stellar origin of the scattered light. For the Carina subregions, in particular for the CarSE region, containing η Car, we see that χ^d increases while χ^* remains fairly constant. Even though we are dealing the fractions of scattered and stellar *continuum*, this behavior may be due to contamination of the continuum measurements from the Balmer lines appearing in emission for this spectrum. *b)* The fraction of

scattered continuum for all three nebulae increases with decreasing wavelength, showing that the albedo of the scattering particles increases towards the blue.

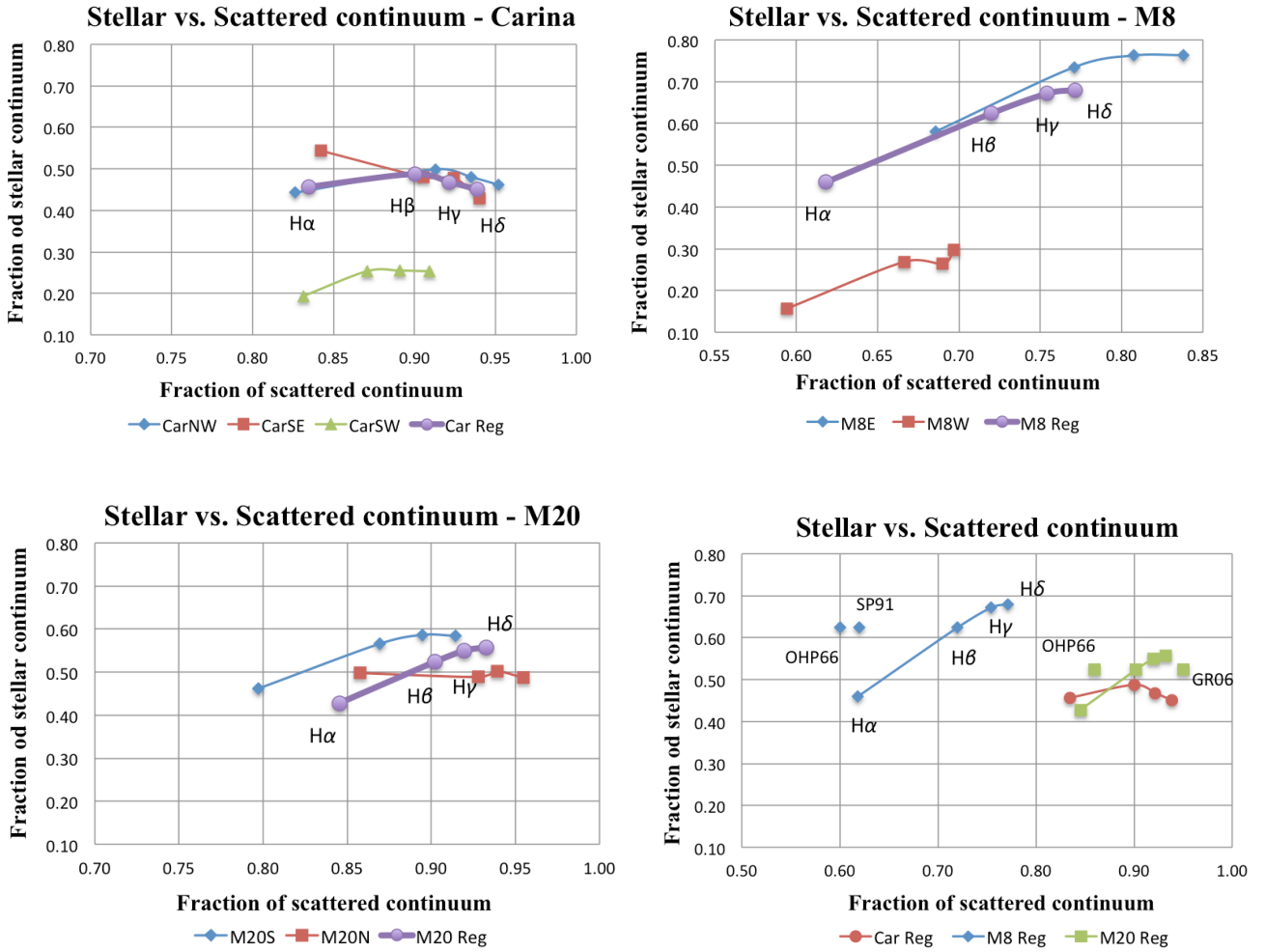


Fig. 3. Relation between the fraction of stellar continuum χ^* and the fraction of scattered continuum χ^d for our individual subregions (first three panels) and for our integrated spectra (lower right panel), where we include also other measurements of χ^d at $H\beta$ for M8 and M20 adapted from the literature.

Observations of GEHRs and HIIGs have also shown that observed W_β are much lower than the theoretical expectation (e.g. Searle, 1971; McCall, Rybski & Shields, 1985; Kobulnicky, et al. 1999; Kehrig et al. 2004; Bresolin et al. 2005; Guseva et al. 2011). The usual interpretation is that an underlying population of stars older than the stars responsible for the ionization contribute to the observed continuum but do not contribute to the $H\beta$ emission, decreasing so the observed W_β . Our spatially integrated spectroscopy shows that this tendency ($W_\beta > W_\beta^a$) is also present in Galactic HII regions, however in our nebula, the additional continuum component is due mainly to dust-scattered starlight. This t^d contribution of scattered starlight should be taken into account when interpreting the observed Balmer W_λ in GEHRs of spiral and irregular galaxies observed with slits or diaphragms that do not encompass the whole emitting region.

6.5 Scattered continua colors

We now turn our attention to the wavelength dependence of the scattered continuum. From the observed Balmer F_λ and W_λ for Car Reg, M8 Reg and M20 Reg given in Tables 1a and 1b of Chapter III, we computed at each λ , both the *.neb* and *.all* observed continuum, $i_\lambda^{\text{obs}} = F_\lambda^{\text{obs}} / W_\lambda$. From these, we obtained the observed continuum surface brightness, $s_\lambda^{\text{obs}} = i_\lambda^{\text{obs}} / \Omega_S$, with the solid angle, $\Omega_S = 3 \Omega_{\text{slit}} = 1.63 \text{ arcmin}^2$ for Car Reg (3 added subregions), and $\Omega_S = 2 \Omega_{\text{slit}} = 1.08 \text{ arcmin}^2$ for M8 Reg and M20 Reg (2 added subregions each). We used the fractions χ^d and χ^* given in Table 1b above, to estimate the observed scattered continuum surface brightness, $s_{\text{obs}}^d = \chi^d s_{\text{obs}}^{\text{.neb}}$, the atomic continuum surface brightness, $s_{\text{obs}}^a = (1 - \chi^d) s_{\text{obs}}^{\text{.neb}}$ and stellar continuum surface brightness, $s_{\text{obs}}^* = \chi^* s_{\text{obs}}^{\text{.all}}$. We de-reddened each of these continua using: $\log s_\lambda^0 = \log s_\lambda^{\text{obs}} + c(\text{H}\beta) (f_\lambda + 1)$, with $c(\text{H}\beta)_{\text{.neb}} = 0.99, 0.59$ and 0.65 for Car Reg, M8 Reg and M20 Reg, respectively, as derived from the observed $\text{H}\alpha/\text{H}\beta$ ratios given in Tables 1a and 1b of Chapter III. For Car Reg we used an extinction law f_λ obtained by averaging our CarNW, CarSE and CarSW f_λ polynomial fits derived in Chapter IV, and for M8 Reg and M20 Reg we used CCM89 extinction law with $R = 3.1$. We present these observed and de-reddened continua surface brightness in Table 2a and compare them in Figs. 4a and 4b below.

As can be seen from Fig. 4a, a) most of the *.neb* continuum is due to scattered light with a minor contribution from the atomic continuum (especially for Car Reg and M20 Reg), and b) the bluing of the de-reddened *.neb* continuum is therefore due to the bluing of the scattered continuum. In the upper panel of Fig. 4a, we include for comparison the de-reddened continuum (solid line) and scattered (dashed line) surface brightness derived for Orion by OH65. We see that Orion is intrinsically brighter than Carina and that its continuum has also a very strong scattered component.

In the middle panel of Fig. 4a we show for M8 the average de-reddened total “*.neb*” and scattered continuum adapted from SP91. This average was computed from 6 fixed-slit positions around and including the Hourglass (HG), sampling an area of about 5 arcmin^2 . At the other hand, our M8 Reg integrated spectra (also centered on the HG), represents an average over more than 80 arcmin^2 . This difference in sampled area explains the stronger total– and scattered–continua surface brightness reported by SP91, whose slit observations were centered on the brightest spots. As mentioned before, SP91 also found that the HG contributes with $\sim 70 - 80\%$ of the observed continuum at a given wavelength within the considered spectral range.

Table 2a. Observed and de-reddened continuum surface brightness components. ^a

λ	$\log s_{\lambda}^{\text{obs}}$						$\log s_{\lambda}^0$					
	Car Reg		M8 Reg		M20 Reg		Car Reg		M8 Reg		M20 Reg	
	<i>.neb</i>	<i>.all</i>	<i>.neb</i>	<i>.all</i>	<i>.neb</i>	<i>.all</i>	<i>.neb</i>	<i>.all</i>	<i>.neb</i>	<i>.all</i>	<i>.neb</i>	<i>.all</i>
H δ	-12.37	-12.13	-12.73	-12.23	-12.82	-12.47	-11.20	-10.96	-12.00	-11.50	-12.02	-11.68
H γ	-12.43	-12.16	-12.77	-12.29	-12.88	-12.53	-11.34	-11.07	-12.08	-11.60	-12.13	-11.78
H β	-12.52	-12.25	-12.85	-12.42	-12.97	-12.65	-11.53	-11.26	-12.25	-11.83	-12.32	-12.00
H α	-12.54	-12.29	-12.86	-12.59	-13.05	-12.80	-11.84	-11.59	-12.44	-12.17	-12.59	-12.35

λ	$\log s_{\text{obs}}^a$			$\log s_{\text{obs}}^d$			$\log s_{\text{obs}}^{*}$		
	Car	M8	M20	Car	M8	M20	Car	M8	M20
H δ	-13.59	-13.37	-13.97	-12.39	-12.84	-12.85	-12.49	-12.40	-12.73
H γ	-13.53	-13.37	-13.97	-12.47	-12.89	-12.91	-12.49	-12.47	-12.79
H β	-13.52	-13.40	-13.97	-12.57	-12.99	-13.02	-12.59	-12.63	-12.92
H α	-13.34	-13.28	-13.87	-12.62	-13.06	-13.12	-12.65	-12.93	-13.17

λ	$\log s_0^a$			$\log s_0^d$			$\log s_0^{*}$		
	Car	M8	M20	Car	M8	M20	Car	M8	M20
H δ	-12.43	-12.64	-13.18	-11.23	-12.11	-12.06	-11.33	-11.67	-11.94
H γ	-12.44	-12.68	-13.22	-11.38	-12.21	-12.16	-11.39	-11.78	-12.04
H β	-12.53	-12.80	-13.32	-11.58	-12.39	-12.37	-11.60	-12.03	-12.27
H α	-12.63	-12.86	-13.41	-11.91	-12.65	-12.66	-11.94	-12.51	-12.71

^a (top) Car Reg, M8 Reg and M20 Reg *.neb* and *.all* observed (s_{λ}^{obs}) and de-reddened (s_{λ}^0) continuum surface brightness (in $\text{erg s}^{-1} \text{cm}^{-2} \text{\AA}^{-1} \text{arcmin}^{-2}$); (middle) atomic (s^a), scattered (s^d) and stellar (s^*) observed and (bottom) de-reddened components.

In the lower panel of Fig. 4a we show for comparison the average de-reddened continuum and scattered continuum surface brightness for 2 subregions within M17 adapted from Peimbert, Torres-Peimbert & Ruiz (1992: PTPR92), whom also report that 50 – 65% of the observed continua at $\lambda 4200 \text{ \AA}$ in M17 is due to scattered light.

Let us define a de-reddened continuum color index, $\psi(\lambda_1/\lambda_2) = \log(i_{\lambda_1}^0 / i_{\lambda_2}^0)$. In terms of this index, our results for M8 Reg give, $\psi(\lambda 6400/\lambda 4200)^{\text{neb}} = -0.40 \pm 0.03$ and $\psi(\lambda 6400/\lambda 4200)^d = -0.46 \pm 0.03$, while the derived values adapted from SP91 are -0.34 and -0.44 , respectively. The quoted errors are estimated from the uncertainties assigned to the continuum fluxes, which in turn depend on the uncertainties in the fluxes and the equivalent widths. We see that our colors are similar within the errors with those derived by SP91, although our *.neb* color appears bluer (steeper) than SP91's.

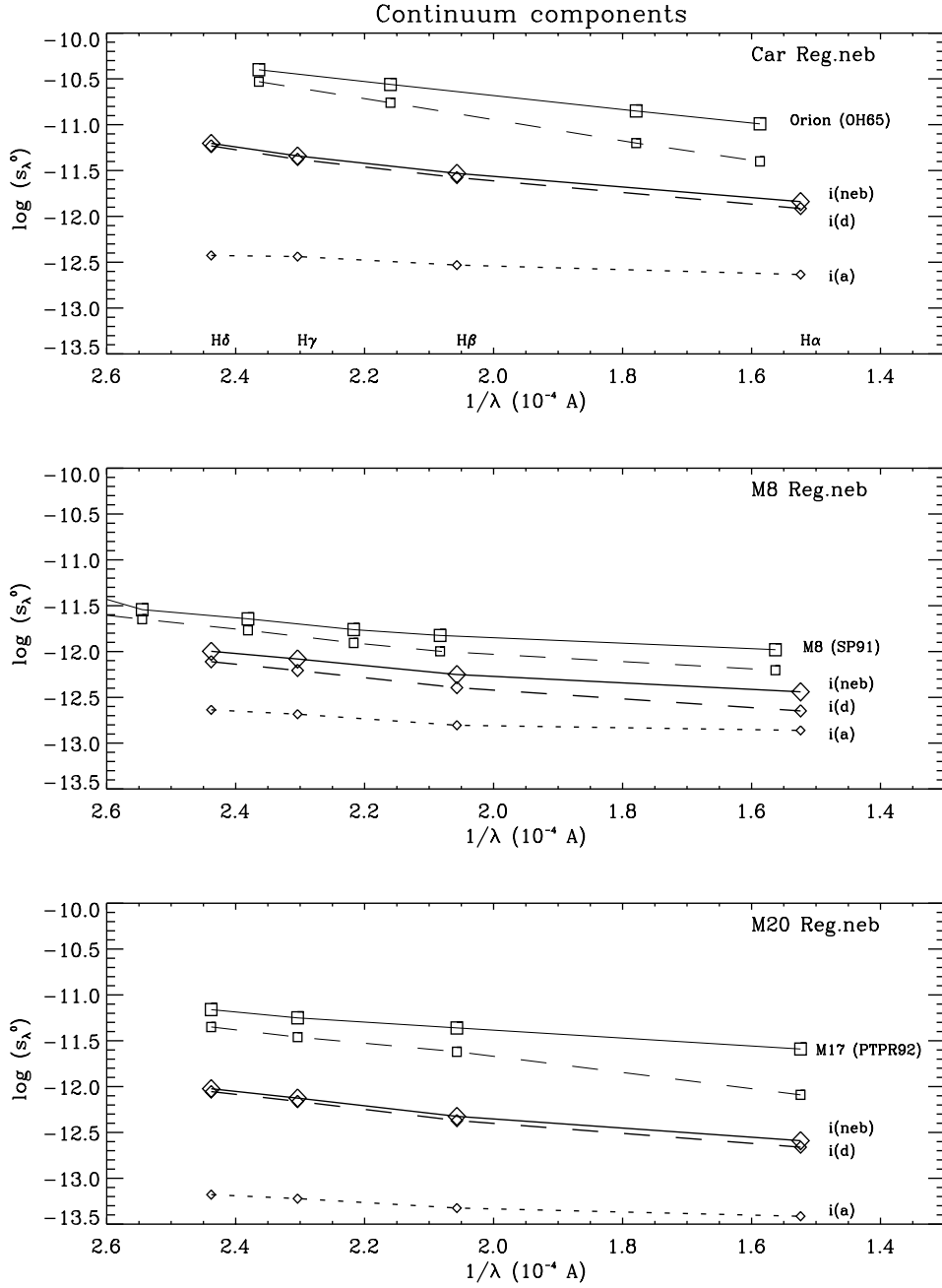


Fig. 4a. Comparison of de-reddened *neb* (solid line), scattered (long dashed line) and atomic (short dashed line) continuum surface brightness (in $\text{erg s}^{-1} \text{cm}^{-2} \text{\AA}^{-1} \text{arcmin}^{-2}$) for Car Reg (*top*), M8 Reg (*middle*) and M20 Reg (*bottom*). We show the average “*neb*” and scattered continuum in Orion, M8 and M17, adapted from OH65, SP91 and PTPR92, respectively.

In the upper part of Table 2b below, we present our de-reddened *neb*, *all*, scattered and stellar continuum colors $\psi(\text{H}\alpha/\text{H}\beta)$ and $\psi(\text{H}\alpha/\text{H}\delta)$ for our three nebulae, which we have plotted in the upper panel of Fig. 4b. For Car Reg, we found $\psi(\text{H}\alpha/\text{H}\delta)^{\text{neb}} \approx \psi(\text{H}\alpha/\text{H}\delta)^{\text{all}} = -0.64 \pm 0.07$. However for M20 Reg (O7V), and especially for M8 Reg (O4V), the *all* continuum colors are bluer (steeper) than the *neb* ones, as expected, with $\psi(\text{H}\alpha/\text{H}\delta)^{\text{all}} = -0.67 \pm 0.07$, while $\psi(\text{H}\alpha/\text{H}\delta)^{\text{neb}} = -0.44 \pm 0.07$, revealing the nature of the early star (HD164794) embedded in M8.

Table 2b. Color of de-reddened continuum ^a

	<i>.neb</i>			<i>.all</i>				
	Car Reg	M8 Reg	M20 Reg	Car Reg	M8 Reg	M20 Reg		
$\psi(\text{H}\alpha/\text{H}\beta)$	-0.31	-0.19	-0.27	-0.33	-0.34	-0.35		
$\psi(\text{H}\alpha/\text{H}\delta)$	-0.64	-0.44	-0.57	-0.63	-0.67	-0.67		
	Scattered			Stellar				
	Car Reg	M8 Reg	M20 Reg	Car Reg	M8 Reg	M20 Reg		
$\psi(\text{H}\alpha/\text{H}\beta)$	-0.33	-0.26	-0.29	-0.34	-0.48	-0.44		
$\psi(\text{H}\alpha/\text{H}\delta)$	-0.68	-0.54	-0.60	-0.61	-0.84	-0.77		
----- <i>.neb</i> -----								
	Car Reg	M8 Reg	M20 Reg	Orion OH65	M8 SP91	M20 GR06	M17 PTPR92	
$\psi(\lambda 4230/\lambda 4630)$	+0.17	+0.15	+0.16	+0.16	+0.15	+0.15	+0.10	
$\psi(\lambda 5260/\lambda 4630)$	-0.24	-0.15	-0.23	-0.29	-0.11	-0.22	-0.17	
$\psi(\lambda 6300/\lambda 4630)$	-0.34	-0.22	-0.33	-0.43	-0.19	-0.53	-0.25	
----- <i>scattered</i> -----								
	Car Reg	M8 Reg	M20 Reg	Orion OH65	M8 SP91	M20 GR06	M17 PTPR92	
$\psi(\lambda 4230/\lambda 4630)$	+0.19	+0.14	+0.18	+0.23	+0.14	+0.14	+0.14	
$\psi(\lambda 5260/\lambda 4630)$	-0.25	-0.21	-0.22	-0.44	-0.17	-0.21	-0.31	
$\psi(\lambda 6300/\lambda 4630)$	-0.38	-0.30	-0.32	-0.64	-0.26	-0.57	-0.48	

^a De-reddened continuum color index, defined as, $\psi(\lambda_1/\lambda_2) = \log(i_{\lambda_1}^0/i_{\lambda_2}^0)$. The estimated uncertainty is about ± 0.04 dex for the “red colors” $\psi(5260/4630)$ and $\psi(6300/4630)$, and ± 0.05 for the “blue one” $\psi(4230/4630)$. We include also data adapted from the literature (see text).

For Carina, our results indicate that i^d is somewhat bluer than i^* , with $\psi(\text{H}\alpha/\text{H}\delta)^d = -0.68 \pm 0.07$, and $\psi(\text{H}\alpha/\text{H}\delta)^* = -0.61 \pm 0.07$. However, for M8 and M20 we found an opposite trend, with $\psi(\text{H}\alpha/\text{H}\delta)^d = -0.54 \pm 0.07$, and $\psi(\text{H}\alpha/\text{H}\delta)^* = -0.84 \pm 0.07$ for M8, while $\psi(\text{H}\alpha/\text{H}\delta)^d = -0.60 \pm 0.07$, and $\psi(\text{H}\alpha/\text{H}\delta)^* = -0.77 \pm 0.07$ for M20. These differences may be related to differences in the size distribution, albedo, and geometric distribution of the scattering particles present in Carina as compared to those in M8 or M20. This is consistent with the “flatter” extinction law (with $R_V \approx 5$) derived for Carina in Chapter IV, in the sense that the scattered component tends to bluish the final emitted spectrum (Mathis, 1983). For our three nebulae, we found that the scattered continuum colors are

somewhat bluer than the *.neb* ones, evidencing the scattering properties of the dust particles present in each nebula.

In the lower panel of Fig. 4*b* we compare the de-reddened scattered continuum surface brightness (s_0^d) for Car Reg, M8 Reg and M20 Reg. For all three nebulae we found, $\psi(\text{H}\alpha/\text{H}\delta)^d \approx -0.61 \pm 0.07$, although Carina has $s_\lambda^d \approx 0.75$ dex brighter than M8 or M20.

O'Dell and collaborators started long ago a program aimed to study the scattering properties of particles in several Galactic nebulae by observing their scattered light. OH65 presented photoelectric spectrophotometry of 5 regions in Orion, and used Seaton (1960) atomic emission coefficients to compute the atomic continuum i_λ^a at each region, assuming a constant $T_e = 8$ kK. From their reported $i_\lambda^{.neb}$ and i_λ^a values it can be concluded that: *i*) the scattered continuum component ($i_\lambda^d = i_\lambda^{.neb} - i_\lambda^a$) comprises on average from 38% (at $\lambda 8000$ Å) to 84% (at $\lambda 4230$ Å) of the observed continuum; *ii*) the fraction of scattered light, $i_\lambda^d/i_\lambda^{.neb}$ at any given λ increases outward from the Trapezium; and *iii*) for a given region, i_λ^d increases toward the blue. These authors compared the de-reddened i_λ^d colors with those derived from the integrated light of the 4 bright members of the Trapezium (mainly θ^1 Ori) and found reasonable agreement, with $\psi(\lambda/\lambda 4630)_0^d - \psi(\lambda/\lambda 4630)\theta^1\text{Ori}_0 \leq +0.05$ dex for $\lambda < 5620$ Å. This difference is within the errors, and suggests a stellar origin for i_λ^d . This comparison however, is hampered by errors in the derived and variable reddening for each region, as well as for θ^1 Ori.

For comparison, in the lower panel of Fig. 4*b* we show the average de-reddened (*.neb*) and scattered continuum surface brightness of the 3 innermost subregions in Orion adapted from OH65. To de-redden their observed continua we used for each region their reported $c(\text{H}\beta)$ values and applied Orion's extinction law (CP70). We also present the results for M8 and M17 adapted from SP91 and PTPR92, respectively.

In the lower part of Table 2*b* we present the de-reddened continuum color indices $\psi(\lambda 4230/\lambda 4630)$, $\psi(\lambda 5260/\lambda 4630)$, and $\psi(\lambda 6300/\lambda 4630)$, both *.neb* and scattered, for our three nebulae and compare them with those of Orion (OH65), M8 (SP91), M20 (GR06), and M17 (PTPR92). For M8, there is good agreement between our scattered-continuum colors and those derived by SP91, although ours tend to be a little bit bluer. Since we sampled a much larger area away from the HG than SP91 did, this trend is consistent with a similar behavior found in Orion by OH65 and in the Extended Orion Nebula (EON) by O'Dell & Harris (2010), in the sense that the de-reddened scattered continua become bluer farther away from the Trapezium.

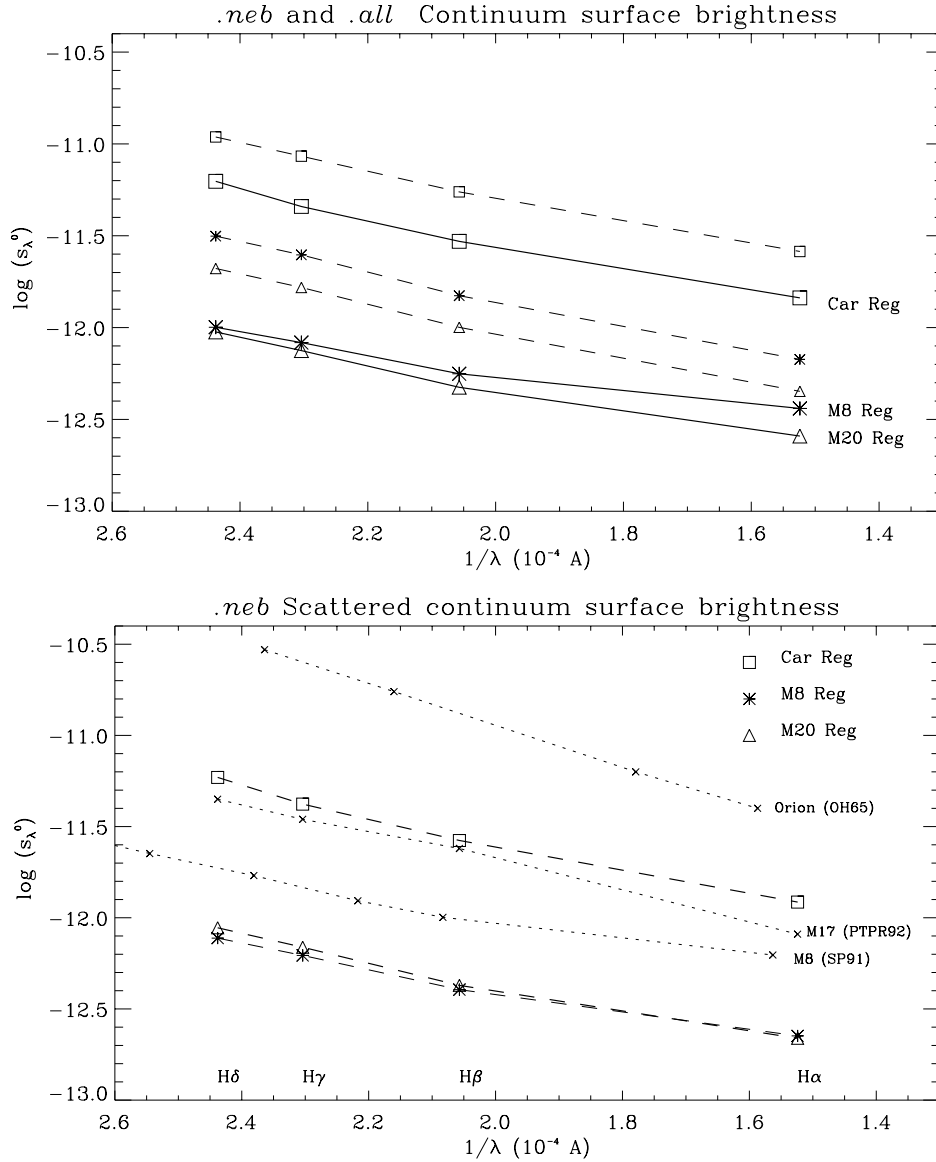


Fig. 4b. (Top) *.neb* (solid line) and *.all* (dashed line) de-reddened continuum surface brightness for Car Reg, M8 Reg and M20 Reg (in $\text{erg s}^{-1} \text{cm}^{-2} \text{\AA}^{-1} \text{arcmin}^{-2}$). (Bottom) Comparison of de-reddened scattered continuum surface brightness for Car Reg, M8 Reg and M20 Reg (same units), including for comparison Orion (OH65), M8 (SP91) and M17 (PTPR92).

For M20 Reg, we found very good agreement between our de-reddened continuum colors and those of GR06 for $\psi(\lambda 4230/\lambda 4630)$ and $\psi(\lambda 5260/\lambda 4630)$. However, for the reddest color, we found $\psi(\lambda 6300/\lambda 4630) = -0.32$, while the continuum color derived from the spectra presented by GR06 is $\psi(\lambda 6300/\lambda 4630) = -0.48$. This difference is beyond the assigned errors and is mainly due to differences in the applied reddening law, $c(\text{H}\beta) \times (f_{\lambda 1} - f_{\lambda 2})$; we used CCM89 with $R = 3.1$, while GR06 used Seaton (1979). Also note that our value is an average over a much wider area, while the value derived from GR06's results correspond only to one small slit placed very close to the exciting star. Comparing the average red color of our three integrated nebula, $\langle \psi(\lambda 6300/\lambda 4630) = -0.33 \rangle$, with the average of the

other nebular given in Table 2b, $\langle \psi(\lambda 6300/\lambda 4630) = -0.49 \rangle$, it seems that integrating the spectra over a wider area yields less steep scattered continua in the red part of the spectrum, as compared to that derived from small slit observations.

Finally, from Table 2b, we see that the scattered continua for the 5 nebulae in Table 2b, are bluer than the *neb* continua: $\psi(\lambda_1/\lambda_2)^d < \psi(\lambda_1/\lambda_2)^{neb}$, indicating that the albedo times the average extinction cross section [$\omega_\lambda \kappa_d^{ext}(\lambda)$] of the scattering particles increases at shorter wavelengths.

An important application of the scattered component present in the nebular spectra of gaseous nebula has been given by Peimbert, Storey & Torres-Peimbert (1993) in the determination of O^+/H^+ abundances in Orion from *recombination lines*. From the estimated scattered-continuum contribution in Orion [$i_\lambda^d/(i_\lambda^a + i_\lambda^d) \approx 75\%$ at $\sim \lambda 4530 \text{ \AA}$], along with the combined stellar equivalent widths in absorption W_{abs}^* , observed in the 4 members of θ^1 Ori, these authors estimated the expected equivalent width nebular contribution in absorption $W_{abs}^{neb} = W_{abs}^* \times i_\lambda^d/(i_\lambda^a + i_\lambda^d)$, that has to be subtracted from the observed nebular equivalent widths in emission W_{emi}^{neb} , in order to correct the weak OI $\lambda\lambda 4414\text{--}4417$, $\lambda\lambda 4639\text{--}4642$, and $\lambda\lambda 4649\text{--}4650$ line blends (with [FeII], NIII and CIII, respectively) before attempting an accurate abundance determination using these faint OI lines.

Another important application of the scattered continua contribution appears in accurate determinations of the extinction and He/H abundances. From the knowledge of $i_\lambda^d/i_\lambda^{neb}$ and W_{abs}^* at the pertinent Balmer and HeI lines (eg. $\lambda 4472$, $\lambda 5876$ and $\lambda 6678$), PTPR92 found for M17 that the $H\beta$ and $H\gamma$ *nebular* equivalent widths in emission should be *decreased* by an underlying stellar correction of $\sim 2 \text{ \AA}$, while for the HeI lines this correction amounts only to $\sim 0.4 \text{ \AA}$. For nebula with high W_λ in emission, this is usually a very small correction, of a few percent, however it must be taken into account when interpreting integrated weak HeI spectra of GEHRs and HIIGs with significant embedded stellar populations (eg. Olive & Skillman, 2001).

6.6. Effects of scattered light on derived reddening, physical conditions and element abundances

As commented before, O'Dell & Harris (2010) presented a detailed paper pointing out the importance of the scattered light on the observed spectra of the Extended Orion Nebula (EON). They found that except at very high spectroscopic resolution, the observed lines are a blend of the original and the scattered light, with shorter wavelengths being artificially enhanced. They suggest that this could explain the unrealistic low $c(H\beta)$ values derived for several regions within the EON, with zones far away from the trapezium ($r \geq 5$) where the F_α/F_β ratio falls even *below* its theoretical limit of 2.85. Similar results were reported in M43 by Simón-Díaz et al. (2011) and in the HIIG NGC 4214 by Maíz-

Apellániz et al. (1998). In this section we present an analysis of the effects of the scattered light on the derived reddening, physical conditions and abundances of our nebulae.

The scattering of dust particles should affect also the line emission from the gas. If the dust albedo were $w_\lambda = 1$ at all wavelengths, the scattering should not affect the total emission line fluxes from the whole nebula, nor the line flux ratios. Scattering would only shift the apparent source of photons within the nebula. However, in general $w_\lambda < 1$ (although it is relatively high) and increases toward shorter wavelengths, as suggested by our observations (Sec. 6.5) and by Mathis (1983) models. Therefore, the standard un-reddening correction procedure, which assumes that all of the absorption and reddening occurs *outside* the nebula, should be corrected in order to include the contribution of scattering of line emission within the nebula. However, as we shall see below, the effects of scattering on the observed spectra and on the derived reddening tend to cancel out. Also, Osterbrock & Ferland (2006) comment that model numerical calculations show that the correction for this in-situ dust scattering of line emission is small and does not alter significantly the correct line emission intensity ratios.

6.6.1 Effects of scattering on the derived reddening

We found in Sec. 6.2 that the fraction of scattered light increases at shorter wavelengths, with values for Car Reg (as example) as high as $\chi^d = 0.83 \pm 0.01$, 0.90 ± 0.01 , 0.92 ± 0.01 and 0.94 ± 0.01 for H α , H β , H γ and H δ , respectively (Table 1b). In this section we will estimate the effect of the scattered light on the derived reddening constant. For each of our program spectra (CarNW.*neb*, CarSE.*neb*, etc.), we estimated a “corrected” F_λ/F_β Balmer ratio considering the scattering contribution through the relation

$$\left(\frac{F_\lambda}{F_\beta}\right)_{corr} = \left(\frac{F_\lambda}{F_\beta}\right)_{obs} \times \left(\frac{\chi_\beta}{\chi_\lambda}\right). \quad (6)$$

In this way, we compensate for the *relative* bluing of the scattered contribution among the different Balmer lines. We calculated thus two values for the reddening constant: $c(\text{H}\beta)_{obs}$, derived using the *observed* Balmer fluxes, and $c(\text{H}\beta)_{corr}$, derived using the *scattering-corrected* Balmer fluxes. For each nebula, we estimated $c(\text{H}\beta)$ using the (F_α/F_β) , (F_γ/F_β) and (F_δ/F_β) ratios along with SH95 theoretical case B line ratios at 10 kK and 100 cm^{-3} . In order to test only the effects of the scattered light on the derived reddening, physical conditions and total abundances, in this section we dereddened all our program spectra using the derived $c(\text{H}\beta)$ and the same CCM89 extinction law with $R = 3.1$ (as parameterized by Draine 2003) for all our nebulae, in contrast to the more detailed analysis that we carried out in Chapters IV for Carina and Chapter V for M8 and M20. We summarize our results in Table 3 and Fig. 5.

Table 3. Reddening constants with and without correction for scattering

	$c(\text{H}\beta)_{\text{obs}}$	$c(\text{H}\beta)_{\text{corr}}$
Car NW	0.78 ± 0.09	0.88 ± 0.10
Car SE	0.71 ± 0.10	0.80 ± 0.11
Car SW	0.65 ± 0.11	0.72 ± 0.11
Car Reg	0.72 ± 0.10	0.81 ± 0.11
M8 E	0.43 ± 0.09	0.59 ± 0.09
M8 W	0.40 ± 0.07	0.53 ± 0.09
M8 Reg	0.41 ± 0.07	0.58 ± 0.08
M20 S	0.48 ± 0.06	0.59 ± 0.06
M20 N	0.61 ± 0.12	0.68 ± 0.14
M20 Reg	0.50 ± 0.07	0.57 ± 0.07

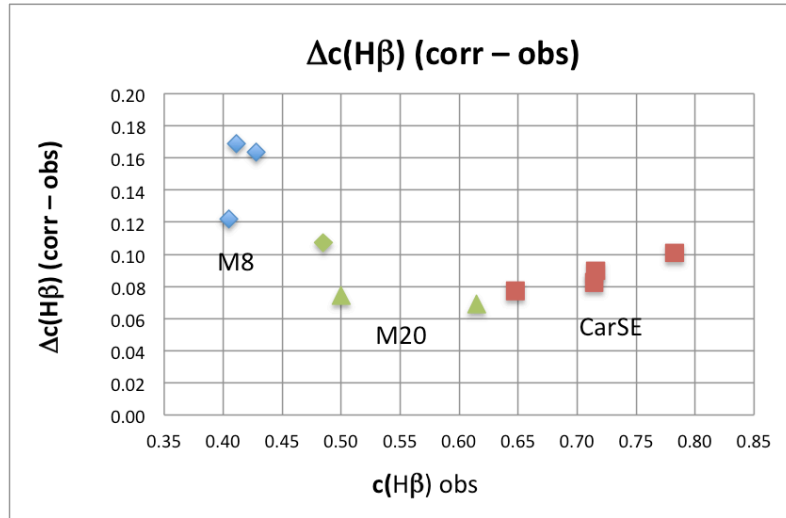


Fig. 5. Difference in the *scattering-corrected* reddening constant and the un-corrected one, $c(\text{H}\beta)_{\text{corr}} - c(\text{H}\beta)_{\text{obs}}$ as function of $c(\text{H}\beta)_{\text{obs}}$ for Carina (red squares), M8 (blue diamonds) and M20 (green triangles). We include also the integrated spectra Car Reg, M8 Reg and M20 Reg. We indicate the position of the CarSE region, which includes η Car.

The uncertainties in $c(\text{H}\beta)$ were estimated considering the uncertainties in the observed line fluxes and the differences among the $c(\text{H}\beta)$ values derived from different Balmer line ratios. We found that $c(\text{H}\beta)_{\text{corr}}$ is larger than $c(\text{H}\beta)_{\text{obs}}$ by 0.11 on average, with differences up to 0.17 for M8. These differences in $c(\text{H}\beta)$ will propagate in the dereddened spectra and in the physical conditions and abundances derived for the gas. The $c(\text{H}\beta)_{\text{corr}}$ is larger than the $c(\text{H}\beta)_{\text{obs}}$, because when we correct the

observed Balmer lines for scattering, we decrease $H\beta$ with respect to $H\alpha$, yielding thus a higher reddening constant.

6.6.2 Effects of scattering on the derived temperatures

In order to study the effects of the scattered light on the derived physical conditions and ionic abundances, we considered 3 sets of spectra: *a) observed spectra*: we dereddened our observed spectra using the uncorrected $c(H\beta)_{\text{obs}}$; *b) $c(H\beta)$ -corrected spectra*: we dereddened our observed spectra using the scattering-corrected $c(H\beta)_{\text{corr}}$ and *c) full-corrected spectra*: before de-reddening the spectra with $c(H\beta)_{\text{corr}}$, we created an *observed spectra corrected for scattering* using a factor $(\chi^{\text{d}\beta} / \chi^{\text{d}\lambda})$ at each λ , by interpolating and extrapolating the $\chi^{\text{d}\lambda}$ values derived from the Balmer lines. That is, we considered that the *observed* line spectrum is also affected by scattering, which artificially enhances the blue lines with respect to the red ones. For each program spectrum, we used the $\chi^{\text{d}\lambda}$ values derived from the Balmer lines to build a linear fit of $\chi^{\text{d}\lambda}$ as function of λ (with correlations coefficients $R \approx 0.99$), which was used to correct for scattering the observed line spectrum. This adjustment is small for lines close to $H\beta$, but amounts to correction factors in the range: $(\chi^{\text{d}\beta} / \chi^{\text{d}\lambda}) = 0.942$ for [OII] $\lambda 3727$ and $(\chi^{\text{d}\beta} / \chi^{\text{d}\lambda}) = 1.34$ for [SIII] $\lambda 9532$. As before, we dereddened all our spectra using CCM89 extinction law with $R = 3.1$ as parameterized by Draine (2003).

With these 3 set of spectra, we derived the dereddened line ratios for the [OIII] $F(\lambda\lambda 4959+5009)/F(\lambda 4364)$ lines and for the [NII] $F(\lambda\lambda 6548+6584)/F(\lambda 6755)$ lines. We used IRAF *nebular* routine to estimate the temperatures in the high excitation zone $T_e(\text{OIII})$, and in the low excitation zone $T_e(\text{NII})$, considering the electron density derived from the [SII] $F(\lambda 6716)/F(\lambda 6731)$ line ratio. We present our results in Table 4 and Fig. 6. The quoted errors correspond to the errors assigned to the line flux ratios.

As we can see, the *$c(H\beta)$ -corrected* spectra yield $T_e(\text{OIII})$ temperatures 120 K larger on average than the temperature derived ignoring the scattering effects. This is due to the larger reddening correction applied when scattering effects are considered, increasing the auroral lines (say) $F(\lambda 4363)$ with respect to the nebular lines $F(\lambda\lambda 4959+5007)$. However, the *full-corrected* spectra yield back basically the same $T_e(\text{OIII})$ temperatures as those derived ignoring the scattering effects. That is, the effect of de-reddening the spectra with a larger reddening correction, is compensated with the effect of decreasing the observed $F(\lambda 4363)$ with respect to $F(\lambda\lambda 4959+5007)$ due to scattering.

Table 4. Electron temperatures considering scattering effects derived with the $c(\text{H}\beta)_{\text{obs}}$ -spectra (*obs*), with the $c(\text{H}\beta)$ -corrected spectra (*corr1*) and with the *full-corrected* spectra (*corr2*)

	$n_e(\text{SII})$ cm^{-3}	$T_e(\text{OIII})_{\text{obs}}$ (kK)	$T_e(\text{OIII})_{\text{corr1}}$ (kK)	$T_e(\text{OIII})_{\text{corr2}}$ (kK)	$T_e(\text{NII})_{\text{obs}}$ (kK)	$T_e(\text{NII})_{\text{corr1}}$ (kK)	$T_e(\text{NII})_{\text{corr2}}$ (kK)
Car NW	100	10.0 ± 0.5	10.1 ± 0.5	10.0 ± 0.5	10.2 ± 0.7	10.4 ± 0.7	10.2 ± 0.7
Car SE	200	13.8 ± 1.0	14.0 ± 1.0	13.8 ± 1.0	15.2 ± 1.5	15.4 ± 1.6	15.0 ± 1.5
Car SW	100	9.7 ± 0.5	9.8 ± 0.5	9.7 ± 0.5	11.5 ± 1.0	11.7 ± 0.9	11.5 ± 1.0
Car Reg	100	11.4 ± 0.7	11.5 ± 0.7	11.4 ± 0.7	12.7 ± 1.0	12.9 ± 1.1	12.6 ± 1.0
M8 E	300	8.1 ± 0.4	8.2 ± 0.4	8.2 ± 0.4	9.3 ± 0.6	9.5 ± 0.6	9.2 ± 0.6
M8 W	400	8.9 ± 0.4	9.0 ± 0.4	8.9 ± 0.4	9.2 ± 0.6	9.3 ± 0.6	9.2 ± 0.6
M8 Reg	300	8.5 ± 0.4	8.6 ± 0.4	8.5 ± 0.4	9.2 ± 0.6	9.4 ± 0.6	9.2 ± 0.6
M20 S	100	11.9 ± 0.7	12.0 ± 0.7	11.8 ± 0.7	8.6 ± 0.5	8.7 ± 0.5	8.5 ± 0.5
M20 N	50	11.6 ± 0.7	11.8 ± 0.7	11.6 ± 0.7	9.4 ± 0.6	9.5 ± 0.6	9.3 ± 0.6
M20 Reg	100	11.7 ± 0.7	11.9 ± 0.7	11.7 ± 0.7	9.2 ± 0.6	9.3 ± 0.6	9.2 ± 0.6

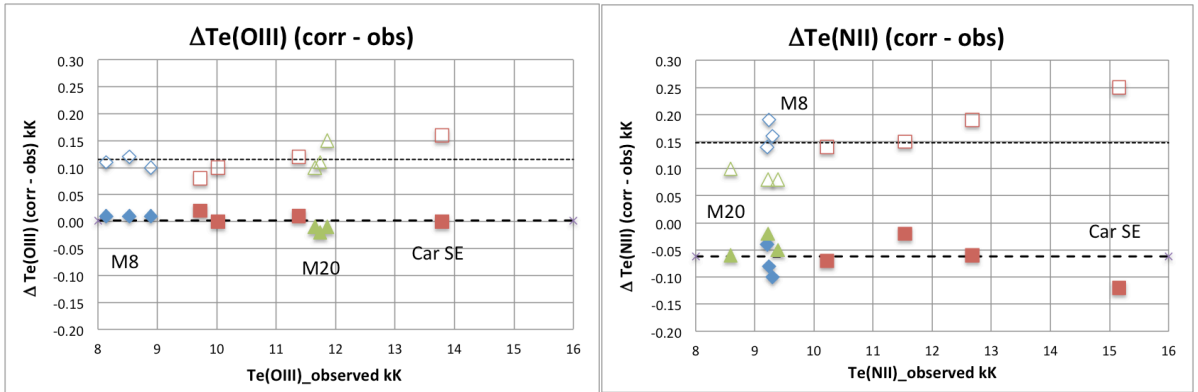


Fig. 6. (*Left panel*) Difference in the corrected and un-corrected electron temperature, $T_e(\text{OIII})_{\text{corr}} - T_e(\text{OIII})_{\text{obs}}$ derived with the $c(\text{H}\beta)$ -corrected spectra (open symbols) and with the *full-corrected* spectra (filled symbols) as function of $T_e(\text{OIII})_{\text{obs}}$. Red squares for Carina, blue diamonds for M8 and green triangles for M20. We indicate the average difference in each case by a dashed horizontal line. We also indicate the position of the CarSE region, which contains η Car. (*Right panel*) The same for the $T_e(\text{NII})$ temperature.

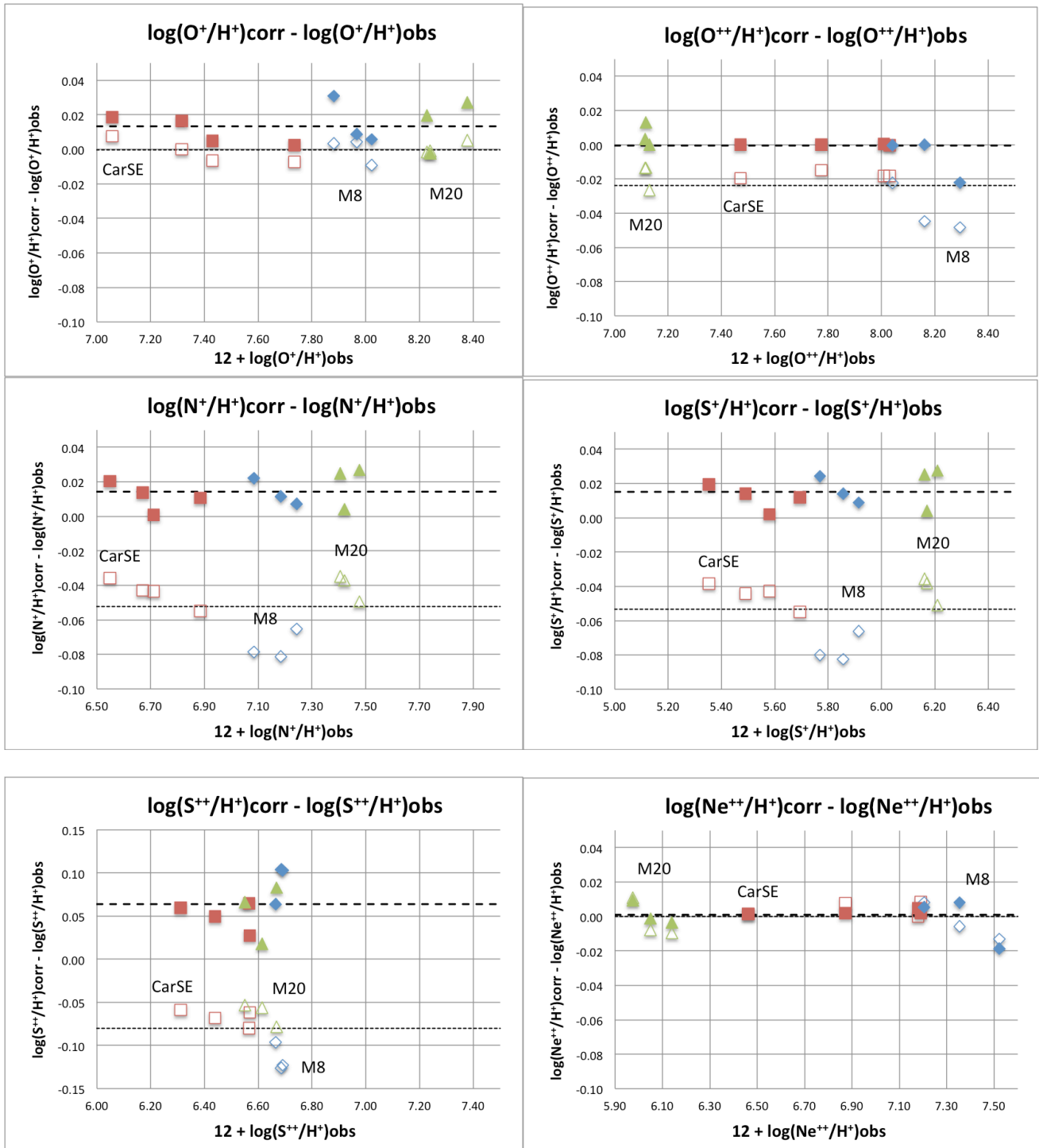
For the $T_e(\text{NII})$ temperature, the $c(\text{H}\beta)$ -corrected spectra yield $T_e(\text{NII})$ temperatures 150 K larger on average than the temperature derived ignoring scattering effects. However, the *full-corrected* spectra yield temperatures only about 60 K *smaller* than those derived ignoring scattering effects. In this case, the effect of increasing the observed $F(\lambda 6584)$ with respect to $F(\lambda 5755)$ due to scattering, has a stronger impact than de-reddening the spectra with a higher $c(\text{H}\beta)_{\text{corr}}$. For the CarSE regions,

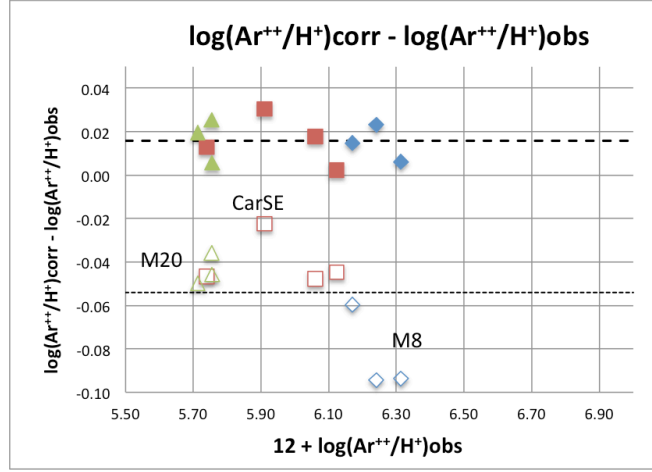
containing η Car, the temperatures are probably overestimated due to contamination of the faint $F(\lambda 4364)$ and $F(\lambda 5755)$ line fluxes. This region presents also the highest errors.

We point out that Simón-Díaz et al. (2011) found evidence of scattered nebular light affecting the emission spectra of M43. They corrected their observed spectra for this diffuse emission and calculated $T_e(\text{OII})$ using the standard lines for this ion and found for 2 apertures that the corrected temperature is *smaller* than the non-corrected one, with an average difference: $T_e(\text{OII})_{\text{Corr}} - T_e(\text{OII})_{\text{NC}} \approx -410$ K, which go in the opposite direction as the T_e differences found by us. The reason is because we are using different lines and ions, and the effect of correcting for scattering the observed spectra and the derived reddening, depend on the wavelength of the considered lines and also on the geometry and distribution of the scattering particles.

6.6.3 Effects of scattering on derived ionic and total abundances

These small differences in temperature will propagate in the derived ionic and total abundances, in particular in the *full-corrected* spectra as shown below. As before, we used *a)* the “*observed spectra*”, *b)* the *c(H β)-corrected* spectra and *c)* the *full-corrected* spectra with the IRAF *nebular* package to calculate the ionic abundances with respect to H^+ of $\text{O}^+(\lambda 3727)$, $\text{O}^{++}(\lambda 5007)$, $\text{N}^+(\lambda 6584)$, $\text{S}^+(\lambda 6725)$, $\text{S}^{++}(\lambda 9531)$, $\text{Ne}^{++}(\lambda 3869)$, and $\text{Ar}^{++}(\lambda 7136)$ using as usual $T_e(\text{NII})$ for ions in the low excitation zone (O^+ , N^+ , S^+ , and S^{++}) and $T_e(\text{OIII})$ for ions in the high excitation zone (O^{++} , Ne^{++} , and Ar^{++}). We present our results graphically in Figs. 7a – 7g, which show the difference in the logarithm of the ionic abundance corrected for scattering effects (*corr*) minus the ionic abundances ignoring these effects (*obs*), $\log(X^{+i}/\text{H}^+)_{\text{corr}} - \log(X^{+i}/\text{H}^+)_{\text{obs}}$ as function of $\log(X^{+i}/\text{H}^+)_{\text{obs}}$. We present both the results derived with the *c(H β)-corrected* spectra and the corresponding temperatures (open symbols), and the results derived with the *full-corrected* spectra and the corresponding temperatures (filled symbols). The spanning of the axes in each figure are the same so to help the comparison among different ions. We also show the average difference in each case as a horizontal dashed line.





Figs. 7a – 7g. Difference in the logarithm of the *scattering-corrected* ionic abundance (*corr*) minus the observed ionic abundance (*obs*), $\log(X^{+i}/H^+)_{\text{corr}} - \log(X^{+i}/H^+)_{\text{obs}}$, as function of $\log(X^{+i}/H^+)_{\text{obs}}$. We show the results derived with the *c(H β)-corrected* spectra and the corresponding T_e 's (open symbols) and those derived with the *full-corrected* spectra and the corresponding T_e 's (filled symbols). Same symbols as in Figure 6.

In Table 5 we present the average errors (column 2) in our calculated ionic abundances for our nebula. These errors come from propagating the errors in the electronic temperatures and in the line fluxes within IRAF. We also give the average of the logarithmic differences $\Delta(X^{+i}/H^+)(\text{corr} - \text{obs}) = \log(X^{+i}/H^+)_{\text{corr}} - \log(X^{+i}/H^+)_{\text{obs}}$ for each ion, both for the *c(H β)-corrected* case (*corr1*) and for the *full-corrected* case (*corr2*).

Table 5. Ionic and total abundances average errors and average *scattering-corrected* and un-corrected logarithmic differences^a

	error	$\Delta(X^+/H^+)$	$\Delta(X^+/H^+)$	$\Delta(X^+/H^+)$		error	$\Delta(X/H)$	$\Delta(X/H)$	$\Delta(X/H)$
		(<i>corr1</i> – <i>obs</i>)	(<i>corr2</i> – <i>obs</i>)	(<i>corr</i> – <i>obs</i>)			(<i>corr1</i> – <i>obs</i>)	(<i>corr2</i> – <i>obs</i>)	(<i>corr</i> – <i>obs</i>)
	(dex)	(dex)	(dex)	(dex)	(6)	(dex)	(dex)	(dex)	(dex)
(1)	(2)	(3)	(4)	(5)	(6)	(7)	(8)	(9)	(10)
O^+/H^+	± 0.13	-0.001	+0.013	+0.135	O/H	± 0.12	-0.013	+0.005	+0.085
O^{++}/H^+	± 0.09	-0.024	-0.001	-	N/H	± 0.06	-0.065	+0.006	+0.050
N^+/H^+	± 0.10	-0.052	+0.014	+0.095	S/H	± 0.08	-0.079	+0.055	+0.065
S^+/H^+	± 0.10	-0.053	+0.015	+0.095	Ne/H	± 0.14	+0.011	+0.014	-
S^{++}/H^+	± 0.08	-0.080	+0.064	+0.045	Ar/H	± 0.14	-0.043	+0.022	-
Ne^+/H^+	± 0.11	+0.000	+0.009	-	N/O		0.89	1.00	
Ar^+/H^+	± 0.11	-0.054	+0.016	-	S/O		0.86	1.12	
					Ne/O		1.06	1.00	
					Ar/O		0.93	1.04	
					O^+/O		1.03	1.02	
					O^{++}/O		0.97	0.99	

^a For ionic and total abundances, $\Delta(\text{corr} - \text{obs}) = \log(X^{+i}/H^+)_{\text{corr}} - \log(X^{+i}/H^+)_{\text{obs}}$. For abundance ratios, entries give $(X/O)_{\text{corr}}/(X/O)_{\text{obs}}$. Columns (1) – (4) and (6) – (9) from this work. Columns (5) and (9) taken from Simón-Díaz et al. (2011) for M43.

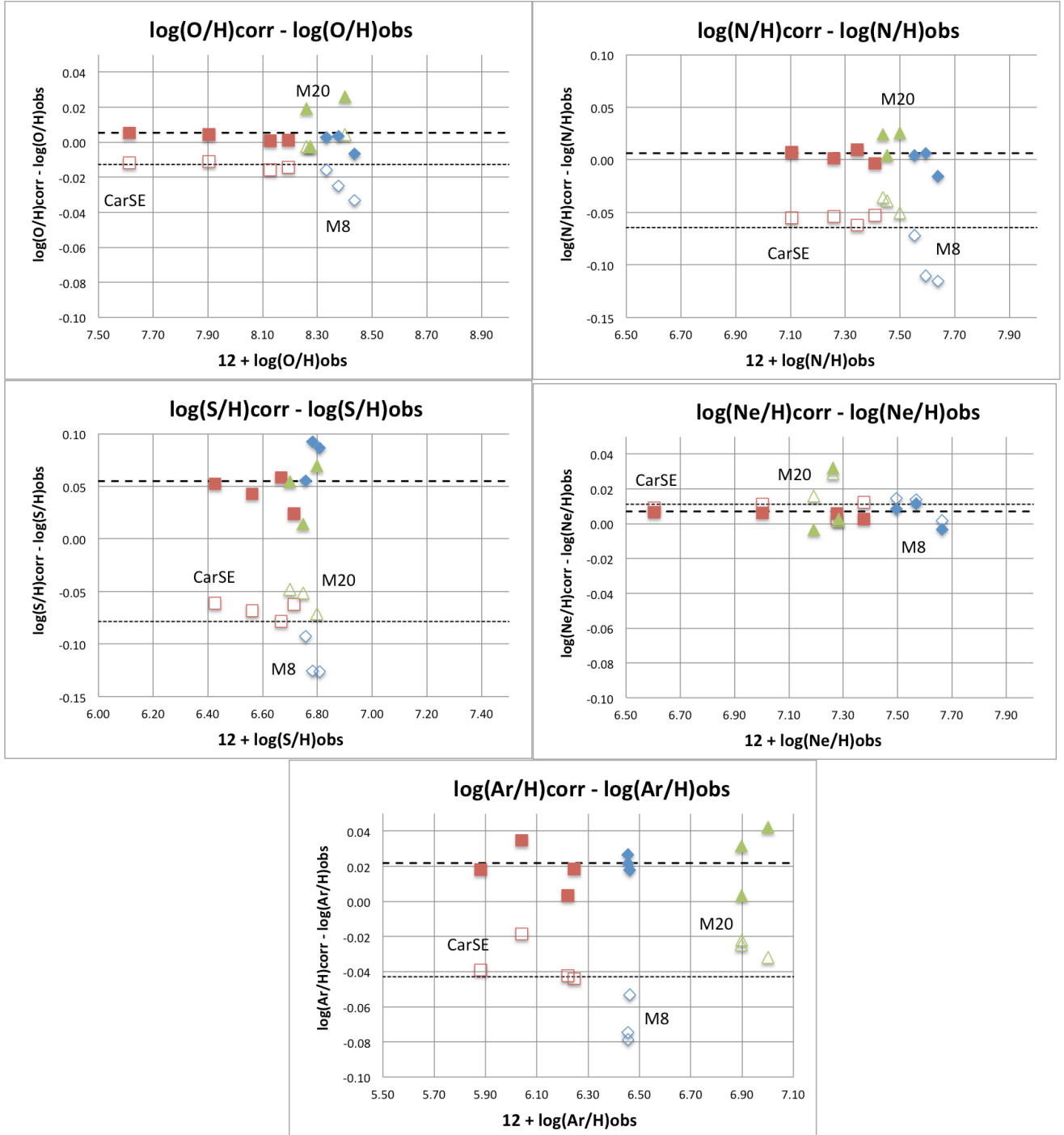
We found that the ionic abundances derived using the *c(H β)-corrected* spectra and the corresponding electron temperatures (*corr1*), are *smaller* than the ionic abundance derived ignoring the scattering effects (*obs*). This is mainly due because the corrected temperatures $T_e(\text{corr1})$, are about 100 K larger than the “observed” temperatures $T_e(\text{obs})$. For the O⁺ and Ne⁺⁺ abundances, derived using lines at the blue side of the spectrum ($\lambda 3727$ and $\lambda 3869$, respectively) we found $\Delta(\text{corr1} - \text{obs}) \approx 0$. This is due because, at one side, increasing T_e yields decreased ionic abundances, but at the other side, increasing *c(H β)* increases the corrected line flux of these blue lines, increasing thus the ionic abundances, and both effects cancel out. For O⁺⁺, we found $\Delta(\text{corr1} - \text{obs}) \approx -0.02$ dex, with even larger differences (~ -0.05 dex) for ions such as N⁺, S⁺, S⁺⁺, and Ar⁺⁺.

For the ionic abundances derived using the *full-corrected* spectra and the corresponding electron temperatures (*corr2*), which we consider to be the more realistic case, we found a different pattern. The corrected and “observed” electron temperatures are the same, $T_e(\text{corr2}) = T_e(\text{obs})$, and the higher reddening applied, $c(H\beta)_{\text{corr}} > c(H\beta)_{\text{obs}}$, tends to cancel out somehow the correction applied to the *scattering-corrected* spectra, which diminished the fluxes on the blue side of the spectrum and increased the fluxes on the red side. The corrected ionic abundances (*corr2*) are a little bit *larger* than the “observed” ones, with $\Delta(\text{corr2} - \text{obs}) \approx 0$ for O⁺⁺, $\Delta(\text{corr2} - \text{obs}) \approx +0.015$ dex for O⁺, N⁺, S⁺, and Ar⁺⁺. Due to the larger *scattering-correction* applied at [SIII] $\lambda 9531$, we found $\Delta(\text{corr2} - \text{obs}) \approx +0.064$ for S⁺⁺.

Summarizing, we found that both our *corr1* and *corr2* scattering corrections for the ionic abundances are small and well within our assigned errors. In Table 5 we also include the ionic abundance differences reported by Simón-Díaz et al. (2011) for M43. Since this is a low excitation HII region, they were able to use only $T_e(\text{OII})$, which yielded differences as high as $\Delta(\text{corr} - \text{obs}) = +0.14$ dex for O^{+/H⁺}, +0.10 for N^{+/H⁺} and S^{+/H⁺}, and +0.06 for S^{++/H⁺}. Therefore, we consider that this scattering-contribution has to be taken into account when deriving precision abundances from collisional excited lines in blister nebula. Simón-Díaz et al. (2011) also concluded that considering scattering effects may yield corrected ionic abundance increased by 0.05 – 0.15 dex.

Now we focus on the effects of the scattered light on the total abundances. We adopted the ICFs given by KB94 (see Sec. 4.5 of Chapter IV). As before, we calculated the total abundances considering *a*) the “observed” ionic abundances (without any correction), *b*) the *c(H β)-corrected* ionic abundances and their corresponding ICFs (*corr1*), and *c*) the *full-corrected* ionic abundances and their

corresponding ICFs (*corr2*). We present graphically our results in Figs. 8a – 8e in terms of the logarithmic difference $\Delta(X/H)(corr - obs) = \log(X/H)_{corr} - \log(X/H)_{obs}$, both for the *corr1* abundances (open symbols) and for the *corr2* abundances (filled symbols). We also show the average differences in each case with a horizontal dashed line, and we summarize our results in the right side of Table 5, where we present the average errors of our total abundances (column 6) derived from the errors in the ionic abundances and in the ICFs.

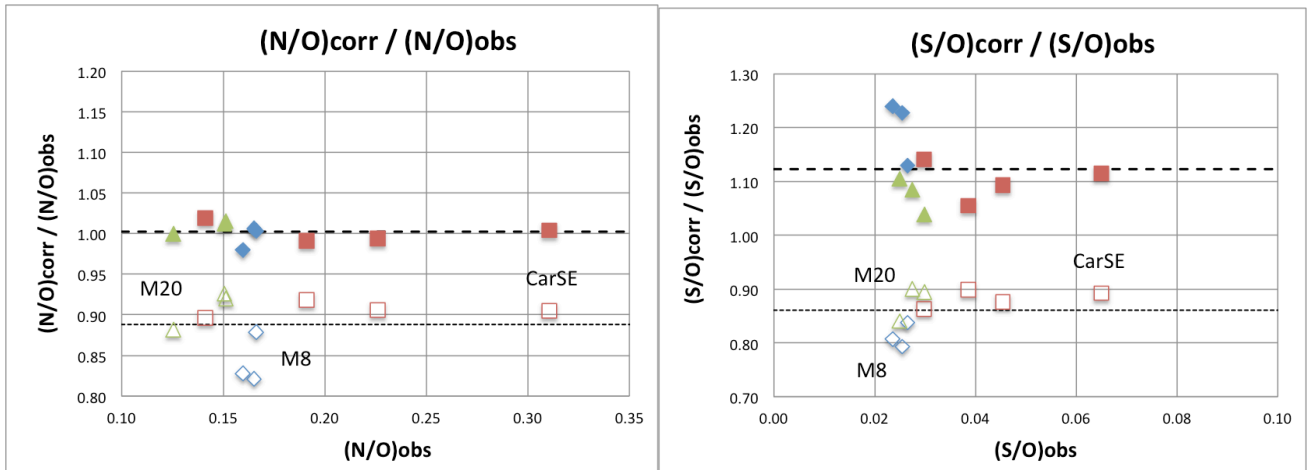


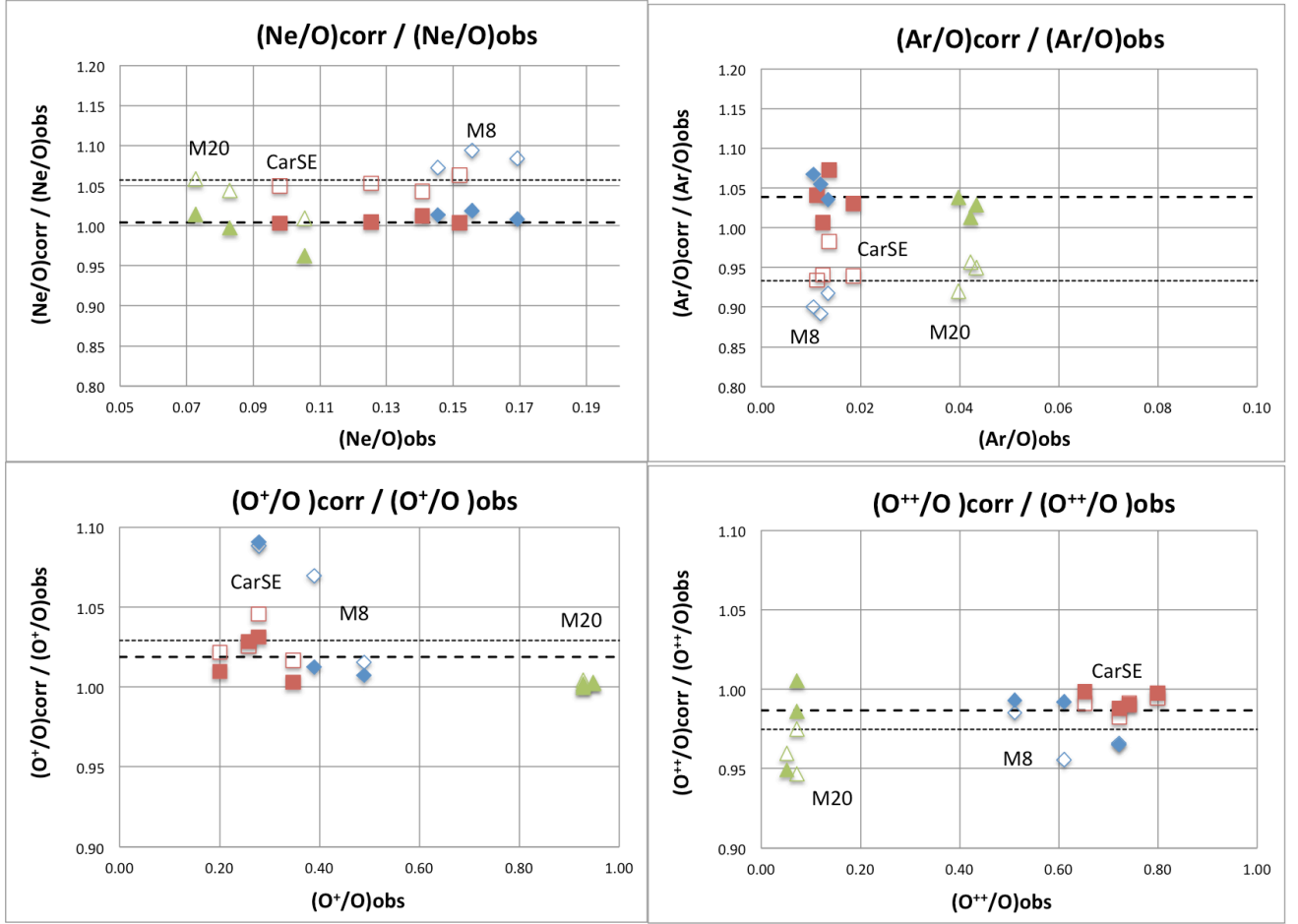
Figs. 8a – 8e. Difference in the logarithm of the *scattering-corrected* total abundance (*corr*) minus the “observed” total abundance (*obs*), $\log(X/H)_{corr} - \log(X/H)_{obs}$, as function of $\log(X/H)_{obs}$. We show the results derived with the

$c(\text{H}\beta)$ -corrected ionic abundances and the corresponding ICFs (open symbols) and those derived with the *full-corrected* ionic abundances and the corresponding ICFs (filled symbols). Same symbols as in Figure 6.

Several conclusions can be drawn from these plots. Considering first the (*corr1* – *obs*) differences, we found that the scattering effects due only to changes in the applied reddening ($c(\text{H}\beta)_{\text{corr}}$), yields *smaller* abundances for N/H (–0.06 dex) and for S/H (–0.08 dex) than the observed ones. However, the *full-corrected* procedure yields (*corr2* – *obs*) total abundances very similar to the observed ones. The *full-corrected* abundances are only a little bit larger than the *observed* ones, about +0.01 dex for O/H, N/H and Ne/O, whit larger differences for Ar/H (+0.02 dex) and S/H (+0.06 dex). However, this larger discrepancy for sulfur deserves a more detailed treatment of the scattered light contribution in the far-red line [SIII] $\lambda 9531$. The reason that the *full-corrected* abundances are basically the same as the *observed* ones is that *a*) the *full-corrected* temperatures are the same as the observed ones (Table 4) and *b*) the larger reddening applied ($c(\text{H}\beta)_{\text{corr}} > c(\text{H}\beta)_{\text{obs}}$) is compensated by the line-scattering correction applied to the observed spectra (Eq. 6). In Table 5 we also include the total abundance differences for M43 found by Simón-Díaz et al. (2011), whom report differences as high as $\Delta(X/H)(\text{corr2} - \text{obs}) = +0.09$ dex for O/H; +0.05 dex for N/S and +0.07 dex for S/H, which are larger that their reported errors of ± 0.05 dex, ± 0.04 dex and ± 0.03 dex, respectively. We conclude that scattering effects has to be carefully evaluated when estimating accurate ionic and total abundances.

Finally, in Figs. 9a – 9f and in the right-side of Table 5, we compare the $(X/O)_{\text{corr}} / (X/O)_{\text{obs}}$ ratio for N/O, S/O, Ne/O and Ar/O. The *corr1* set of values (open symbols) suggests N/O and S/O ratios about 10% smaller than the observed ones. However, the *full-corrected* values give basically the same X/O ratios, except for S/O, which is increased by about 10%. As expected, the excitation parameters O^+/O and O^{++}/O are the same for the *full-corrected* values as for the observed ones.





Figs. 9a – 9f. (a – d) Comparison of the $(X/O)_{\text{corr}}$ ratio corrected for scattering effects as compared to the $(X/O)_{\text{obs}}$ observed ratio ignoring these effects, for the N/O, S/O, Ne/O and Ar/O ratios. Open symbols for $c(\text{H}\beta)$ -corrected ratio, and filled symbols for *full-corrected* ratios. (e – f) Same as before, for the excitation fractions O^+/O and O^{++}/O . In each case we show the average value by the horizontal dashed lines. Same symbols as in Fig. 6.

6.7 Relation between reddening and scattering

In this section we look for a relation between the fraction of scattered light χ^d and the observed reddening. The observed flux from a Galactic H II region may be affected by at least two sources of extinction: *i*) extinction due to foreground dust in our own Galaxy, A_{gal} and *ii*) extinction due to dust inside the HII region, A_{int} , so in general, $A_{\beta}^{\text{tot}} = A_{\beta}^{\text{int}} + A_{\beta}^{\text{gal}}$. In the case of GEHRs we should also consider a contribution from “external” extinction in the host galaxy. This latter extinction can be very non-uniform, and in this case, the extinction derived from the Balmer decrement A_{β}^{Bal} , will be strongly weighted by the zones of low extinction. This may explain at least in part, why the radio-derived extinction, A_{β}^{rad} in GEHRs is larger than A_{β}^{Bal} (eg. Melnick 1979, Israel & Kennicutt 1980).

The problem of dust scattering within a dusty radiated plasma, or scattering by dust inside a uniform (or clumpy) slab close to an emitting source is difficult because it involves a detailed knowledge of the dust properties and its composition, as well as the geometric distribution of the dust, gas and stars within the nebulae (see Appendix IV). Substantial contributions to this problem have been made by Mathis (1970, 1971, 1972, 1983; M83), Natta & Panagia (1984), Caplan & Deharveng (1986; CD86), Bruzual, Magris & Calvet (1988), Witt, Thronson & Capuano (1992), Calzetti, Kinney & Storchi-Bergmann (1994: CKS94; 1996), Henney (1994, 1998) and Calzetti (1997, 2001).

For a given nebula with known gas and dust distributions, it is possible to estimate A_{β}^{int} by constructing a detailed model and using the observed scattered continuum. Mathis (1970) constructed dusty models for Orion and based on continuum observations found that $c(\text{H}\beta)^{\text{int}}$ comprises up to 84% of $c(\text{H}\beta)^{\text{tot}}$. This result is consistent with those of derived by O’Dell, Walter & Dufour (1992) whom compared 21 cm VLA continuum maps and extinction-corrected images of Orion. They compared N_{HI} column densities with derived $c(\text{H}\beta)$ values and found that most of the extinction in Orion arises in a neutral lid lying on the near side of the nebula, which is responsible for most of the observed extinction, so that $c(\text{H}\beta)^{\text{tot}} = c(\text{H}\beta)^{\text{int}} + c(\text{H}\beta)^{\text{gal}} = 0.80$, with $c(\text{H}\beta)^{\text{int}} \approx 17\%$ of $c(\text{H}\beta)^{\text{tot}}$. Their results are consistent with a dust scattering cross section per hydrogen atom of $\sigma \approx 5 \times 10^{22} \text{ cm}^2$. Cox, Deharveng & Caplan (1987) compared the extinction of three Galactic HII regions derived from HI data and from the color excess of their exciting stars and report, $A_{\text{V}}^{\text{int}}/A_{\text{V}}^{\text{tot}}$ ratios in the range 0.24 – 0.50.

An direct method to estimate the amount of internal reddening would be to measure the reddening over the nebula and also in regions close to it but *outside* its main body, so the difference would give the local reddening. Sánchez & Peimbert (1991) report $c(\text{H}\beta)^{\text{int}} \approx 0.55 c(\text{H}\beta)^{\text{tot}}$ from slit observations of M8.

For GEHRs, Lequeux et al. (1981; LMDK81) used values of $E_{\text{B-V}}^{\text{gal}}$, N_{HI} column densities and observed $\text{H}\alpha$, $\text{H}\beta$ and S_{v} fluxes for 8 GEHRs to estimate the different contributions to the total extinction at $\text{H}\beta$. By comparing $\tau_{\beta}^{\text{rad}}$ (derived from radio measurements) with $\tau_{\beta}^{\text{Bal}}$ (derived from the Balmer decrement) these authors found the need of including an additional “gray” contribution, arising presumably from dark regions covering an important fraction of the HII regions. From their reported contributions, we found that $c(\text{H}\beta)^{\text{int}}/c(\text{H}\beta)^{\text{tot}}$ varies in the range 0.10 – 0.84, with an average of 0.34. Considering the gray component as part of the internal extinction, the above ratio is in the range 0.28 – 0.91, with an average of 0.76. In another study, CKS94 used extinction maps of the Galaxy to derive the internal color excess $E_{\text{B-V}}^{\text{int}}$ for a sample of 39 Starburst galaxies, for which we obtain an average $E_{\text{B-V}}^{\text{int}}/E_{\text{B-V}}^{\text{tot}} \approx 0.78$ with an standard deviation of 0.31.

Given the above results, we would expect that the scattered continuum fraction χ^d will correlate with $c(\text{H}\beta)^{\text{int}}$ (being both proportional to $n_d \kappa_d^{\text{ext}}$). From the *int* / *tot* reddening proportions mentioned above, let us consider as a first approach that $c(\text{H}\beta)^{\text{int}}$ is the main contribution to $c(\text{H}\beta)^{\text{tot}}$. In Fig. 10 we show the relation $c(\text{H}\beta)^{\text{tot}}$ vs. χ^d for our nebula (including our 4 RCW objects) as well as observations for Orion, M16 and M17 adapted from the literature. With the exception of M17 (which shows a very high $c(\text{H}\beta)$ and is partly obscured by a molecular cloud, LMDK81), we see that there is a marginal trend, with $c(\text{H}\beta)^{\text{tot}}$ being larger for those nebula with higher χ^d values. We show below a very simple model and arguments to show that $c(\text{H}\beta)^{\text{int}}$ should correlate with χ^d .

Considering that the extinction is due only to dust within the HII region, the reddening constant is given by:

$$c(\text{H}\beta)^{\text{int}} = 0.434 n_d \kappa_d^{\text{ext}}(\text{H}\beta) R_{\text{HII}} f, \quad (7)$$

where n_d is the number density of dust particles within the nebula (cm^{-3}), $\kappa_d^{\text{ext}}(\text{H}\beta) = w\lambda \kappa_d^{\text{scat}}(\text{H}\beta)$ (cm^2) is the dust average effective extinction cross-section at $\text{H}\beta$ ($\kappa_d^{\text{ext}} = \kappa_d^{\text{abs}} + \kappa_d^{\text{scat}}$), $w\lambda$ is the dust albedo, R_{HII} (cm) is the length of the nebula along the line of sight, and f is the volume filling factor.

At the other hand, the emission coefficient of scattered light at a point r within the nebula j_λ^d , can be approximated as (Mathis, 1972):

$$j_\lambda^d \approx n_d g_\lambda w_\lambda \kappa_d^{\text{ext}}(\lambda) \left(\frac{\pi F_\lambda^*}{4\pi} \right) \quad (8)$$

where g_λ is the Henyey-Greenstein *phase parameter*, defined as the average cosine of the angle between incident and scattered radiation, $w_\lambda = \kappa_d^{\text{scat}}/\kappa_d^{\text{ext}}$ is the *albedo*, and πF_λ^* is the astrophysical flux from the star at point r . Eliminating $n_d \kappa_d^{\text{ext}}(\text{H}\beta)$ from Eqs. (7) and (8) and writing our χ^d parameter at $\text{H}\beta$ as $\chi^d = i^d / (i^a + i^d) = j^d / (j^a + j^d)$, we can write:

$$c(\text{H}\beta)^{\text{int}} = 0.434 \left(\frac{4\pi}{\pi F_\beta^*} \right) \left(\frac{j_\beta^a R_{\text{HII}} f}{g_\beta w_\beta} \right) \left(\frac{\chi^d}{1 - \chi^d} \right) \quad (9)$$

The ‘‘constant’’ multiplying the $\chi^d/(1 - \chi^d)$ term varies from object to object and we leave its accurate evaluation for each particular object as future work. However, as we can see from the above equation, $c(\text{H}\beta)^{\text{int}}$ correlates with χ^d and we show this relation in Fig. 10, arbitrarily normalized at $\chi^d = 0.88$. This bare correlation is consistent with the idea that an important fraction of the observed extinction takes place within the nebula.

6.8 Relation of gas-to-dust ratio and the fraction of scattered light

In Table 6 we have summarized the gas-to-dust ratios at $H\beta$ found in the literature for well-studied HII regions, including ours (adapted from Osterbrock & Ferland 2006), along with the derived fraction of scattered light for each nebula.

The gas-to-dust ratios given in Table 6 were all adapted from the literature, except for Carina, for which we could find none. For Carina, we used the following broad approach: as stated before, the total reddening constant can be written as the contribution from internal dust within the HII region and the contribution from foreground dust, $c(H\beta)^{\text{tot}} = c(H\beta)^{\text{int}} + c(H\beta)^{\text{for}}$. The internal contribution can be approximated using Eq. (7). From this expression we can write:

$$\frac{n_g}{n_d \kappa_d^{\text{ext}}(H\beta)} = \frac{0.434 n_g f L}{c(H\beta)^{\text{int}}} \quad (10)$$

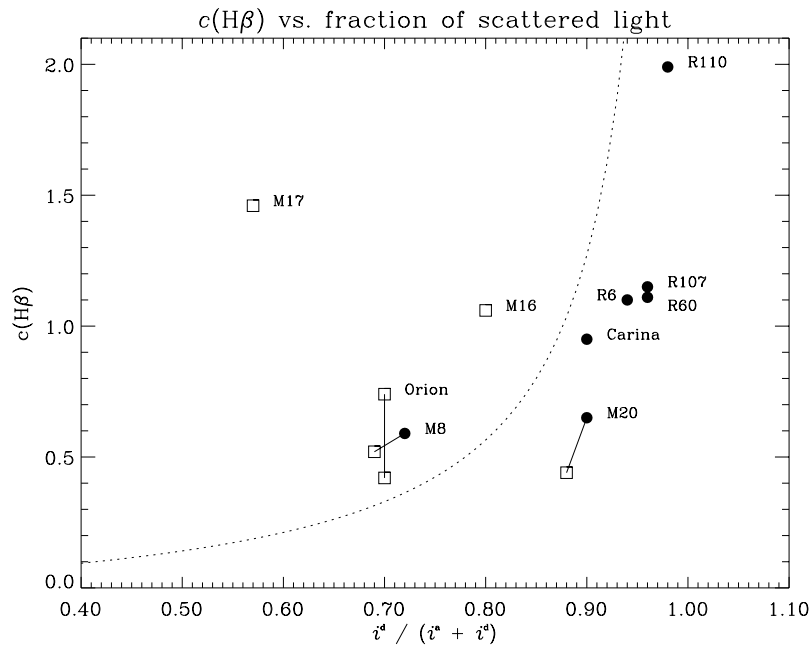


Fig. 10. Observed reddening constant $c(H\beta)$ vs. the fraction of scattered light $\chi^d = i^d / (i^* + i^d)$ at $H\beta$ for all our nebula and some Galactic H II regions adapted from the literature. The dotted line gives the derived analytical relation given by Eq. (13) arbitrarily normalized at $\chi^d = 0.88$.

We used our best choice for nebular parameters of Carina, based on the results found in Chapter IV and Appendix III: $n_g = 100 \pm 50 \text{ cm}^{-3}$; $f = 0.20 \pm 0.10$; $L_{\text{min}} = 20 \pm 10 \text{ pc}$ and $c(H\beta)^{\text{int}} = 0.80 \pm 0.10$. However, note the large uncertainty present in the above ratio (at least 50%), specially from uncertainties in the assigned length of the nebula L , and the adopted internal reddening constant $c(H\beta)^{\text{int}}$.

We ordered the nebulae in Table 6 according to the fraction of scattered light, and we found that the regions with smaller gas-to-dust ratio tend to present the larger fraction of scattering light, indicating that the fraction of scattered light is due to dust within the HII region and giving support to the idea that an important fraction of the extinction occur within the nebula as compared to the foreground extinction.

Table 6. Gas-to-dust ratio at H β for several HII regions and fraction of scattered light

Nebula	$n_g/n_d w\lambda\kappa\lambda$ ($\times 10^{21} \text{ cm}^{-2}$)	χ^d
M17	...	0.57
Orion (inner)	14	0.70
M8	2	0.72 ± 0.10
M16	2	0.80
Orion (outer)	0.5	...
Carina	$0.7^{+0.5}_{-0.3}$	0.90 ± 0.10
M20	0.4	0.90 ± 0.10
ISM Field	2	–

6.9 Conclusions

Our program spectra indicate the presence of a strong, and some times dominating, component of additional continuum. We interpret this continuum as dust-scattered starlight and show that it is correlated with the stellar continuum. We provide a plot (Fig. 2c) to estimate the predicted “pure atomic” equivalent width from H α to H δ W_λ^a , as function of temperature, for a hypothetical nebula free of dust in the low-density limit. By comparing the observed Balmer equivalent width W_λ^{obs} , with the theoretical prediction W_λ^a , we found that $\sim 70\%$ of the observed continua at these wavelengths is due to scattered light in Carina and M20, while in M8 this contribution amounts to $\sim 50\%$. Our derivations agree with those found in the literature for M8 and M20, and we report for the first time the fraction of scattered light in the Carina region.

We found that, taking off the reddening effects, the bluing of the *.neb* continuum is due to the bluing of the scattered continuum. The scattered continuum is bluer than the *.neb* continuum indicating that the albedo times the average extinction cross section ($w\lambda\kappa^{\text{ext}}$) of the scattering particles increases at shorter wavelengths in agreement with theoretical estimations (eg. Mathis, 1983). We also found that the H α to H δ *color* of the scattered continuum in Carina is bluer than the stellar continuum, with $\log(F_\alpha/F_\delta)^d = -0.68 \pm 0.07$ and $\log(F_\alpha/F_\delta)^* = -0.61 \pm 0.07$. However, for M8 and M20 we found an opposite trend, with $\log(F_\alpha/F_\delta)^*$ bluer than $\log(F_\alpha/F_\delta)^d$ by ~ 0.24 dex. This result is consistent with the

“flatter” anomalous extinction law ($R \approx 5$) found for Carina (Chapter IV), in the sense that the scattered component tends to *bluish* the final spectra.

We present and compile evidence showing that the internal extinction is on average 60% of the total extinction in Galactic and extragalactic HII regions, indicating the presence of large amounts of dust within the emitting region. We found a marginal correlation between the derived reddening constant $c(\text{H}\beta)$ and the estimated fraction of scattered light $\chi^{\text{d}} = i^{\text{d}} / (i^{\text{a}} + i^{\text{d}})$.

Given that scattering effects are larger toward bluer wavelengths, we found that the scattering-corrected reddening constant $c(\text{H}\beta)_{\text{corr}}$, is larger by 0.10 – 0.15 than the *observed* one $c(\text{H}\beta)_{\text{obs}}$, derived ignoring scattering effects. This yields in turn scattering-corrected electron temperatures $T_e(\text{corr})$ 120 – 150 K *larger* than those derived ignoring scattering effects. Propagating these effects to the ionic and total abundances, we found that O/H and Ne/H remain the same, because the larger reddening correction applied to the extreme blue lines is compensated by the larger scattering-corrected electron temperature. However, the scattering-corrected abundances $(\text{X}/\text{H})_{\text{corr}}$ for N/H, S/H and Ar/H are ~ 0.06 dex *smaller* than the observed ones.

If the scattering effects are also applied to the *observed* spectra (before the reddening correction is applied), then the effect of increasing the reddening due to scattering effects is compensated by the effect of decreasing (eg.) $\lambda 4363$ with respect to $\lambda 5007$ due to scattering effects, yielding basically the same scattering-corrected electron temperatures as those derived ignoring scattering effects. In this case, scattering-corrected total abundances are also basically the same as those derived ignoring scattering effects, except for S/H, which gives a scattering-corrected abundance 0.06 dex larger than the observed one. However, this estimation requires a more detailed treatment of scattering effects around the red sulfur line [SIII] $\lambda 9532$. Simón-Díaz et al. (2011) report similar differences for the low excitation HII region M43. These authors proved the existence of extended emission over the face of the nebula and found that the scattering-corrected $T_e(\text{OII})$ temperature is smaller by ~ 410 K than the non-corrected one, yielding corrected O/H abundances up to 0.09 dex larger than the non-corrected ones.

Finally, we found a positive correlation between the derived dust-to-gas ratio for bright nebulae (found in the literature) and the fraction of scattered light χ^{d} , evidencing thus the dusty nature of the observed extra continuum, and suggesting that an important fraction (more than 50%) of the observed extinction is due to internal extinction within the nebular plasma.

General conclusions

In this last section we summarize the main results and conclusions obtained along the present work.

a) In this thesis we have presented mid-resolution spectroscopy from 3600 – 10200 Å of 7 Galactic HII regions: Carina, M8, M20, RCW6, RCW60, RCW107 and RCW110, obtained with the 1.5-m telescope at CTIO. We aligned the slit N–S and *drifted* the telescope over the central part of each nebula during a given integration time. Working with the 2-D CCD frames, we were able to reduce the data so to obtain a *.all* and a *.neb* spectra. The *.all* spectra correspond to the emission arising both from the nebular gas *and* the stars that crossed the slit during the scans, while the *.neb* spectra correspond to the emission when the bright stars have been “removed” from the CCD before collapsing the 1D spectra. The *.all* spectra would be somehow comparable to low-spatial resolution observations of giant extragalactic HII regions where the bright stars cannot be disentangled from the pure nebular emission.

b) The effects produced by the spectra of the embedded exciting stars on the integrated spectra depend upon the spectral types and luminosities of these stars. For typical early O stars, the underlying stellar absorption decreases the Balmer lines by as much as 10% at H δ . At the other hand, if the emitting volume contains peculiar LBVs or WR stars (as it is the case for our CarSE and CarSW subregions), then the underlying stellar *emission* may increase the Balmer lines by as much as 15% at H δ . The stellar effects are larger for weaker lines of the Balmer series. We found that the helium lines are not affected within the errors. However, for the CarSE region (which contains η Car), and the further integrated Car Reg spectra, the brightest HeI λ 6678 and HeI λ 5876 are overestimated by as much as 20% if the stars are not removed from the integrated spectra. The forbidden lines are not affected by the underlying stellar spectra, as expected, except for the CarSE and Car Reg spectra, in which the [NII] λ 6584 and [NII] λ 5755 line fluxes appear overestimated by 20% in the *.all* spectra with respect to the *.neb* spectra.

c) We derived simultaneously the logarithmic reddening correction constant $c(\text{H}\beta)$, and the underlying stellar absorption equivalent width W_{abs} from our *.neb* and *.all* spectra. The regions that include early O stars, such as CarNW, M8 and M20, suggest an underlying equivalent width in absorption of $W_{\text{abs}} = 1 - 2 \pm 1.0$ Å. However, for CarSE and CarSW (which includes the star HD93162, WN6ha), our *.all* spectra suggest a *negative* underlying equivalent width of $W_{\text{abs}} = -2.0 \pm 1.0$ Å, indicating that it appears in emission. The $c(\text{H}\beta)$ values derived simultaneously with W_{abs} are about 0.20 dex *smaller* than the $c(\text{H}\beta)$ values derived ignoring W_{abs} .

d) Considering all our target objects: Carina, M8, M20 and the four RCW objects, we found that $c(\text{H}\beta)_{\text{.all}}$ derived only from the Balmer lines is on average 0.07 dex *larger* than $c(\text{H}\beta)_{\text{.neb}}$. Our $7' \times 7'$

average scans indicate in general low density nebulae, with $n_e(\text{SII}) \approx 100 - 400 \text{ cm}^{-3}$, and in general we found that $n_e(\text{SII}).all \approx n_e(\text{SII}).neb$ within the uncertainties.

e) Comparing the *.all* and *.neb* electron temperatures derived in Carina, M8 and M20, we found that on average, $T_e(\text{OIII}).all$ is 200 – 500 K *larger* than $T_e(\text{OIII}).neb$, although the assigned error for $T_e(\text{OIII})$ is about ± 600 K. This increment in electron temperature yields *.all* abundances about 0.05 dex *smaller* than the *.neb* abundances. For the low-ionization zone temperature, we found that $T_e(\text{NII}).all \approx T_e(\text{NII}).neb$ within the errors.

f) Except for the CarSE region, we found that $(\text{O}/\text{H}).all \approx (\text{O}/\text{H}).neb$, and $(\text{S}/\text{H}).all \approx (\text{S}/\text{H}).neb$, although both $(\text{N}/\text{H}).all$ and $(\text{Ar}/\text{H}).all$ appear 0.05 dex *smaller* on average than the corresponding $(\text{N}/\text{H}).neb$ and $(\text{Ar}/\text{H}).neb$ values. On the other hand, we found that $(\text{Ne}/\text{H}).all$ is 0.07 dex *larger* on average than $(\text{Ne}/\text{H}).neb$. However, we could not derive total abundances with a precision better than 0.10 – 0.15 dex, so we cannot establish a definitive trend among the *.all* and *.neb* total abundances.

g) Comparing our scan-integrated wide-angle spectra with spectra obtained from fixed narrow slit observations, it appears that our spectra favors the emission of high-ionization ions such as O^{++} and Ne^{++} , while decreasing the emission of low-ionization ions such as O^+ , N^+ and S^+ . As a consequence, our integrated spectra suggest a nebula of higher excitation (O^{++}/O), with a smaller N/H, smaller S/H and larger Ne/H abundances as compared with fixed slit observations.

h) We found that the use of the recent ICFs presented by Delgado-Inglada et al. (2014) yields the same total abundances for O/H and S/H as those derived using the classical ICFs compiled by Kingsburgh & Barlow (1994). However, we found that the “updated” N/H is decreased by about -0.10 dex, Ar/H is decreased by about -0.08 dex, but Ne/H is largely increased, by about $+0.25$ dex. Comparing the Ne/O ratio derived for our objects with similar studies found in the literature (García-Rojas, et al. 2006; 2007), with B stars in the Orion star-forming region (Nieva & Simón-Díaz, 2011) and with the Sun (Asplund et al. 2009), it appears that the use of the new ICFs proposed by Delgado-Inglada et al. (2014) may be overestimating the Ne/H abundance by 0.10 – 0.15 dex, except in nebula of low excitation ($\text{O}^{++}/\text{O} < 0.20$) as is the case for M20.

i) We derived an extinction law toward the Carina nebula fitting the observed Balmer and Paschen line decrements, and we confirm that it is anomalous, with $\langle R_V \rangle = 4.4 \pm 0.4$, in agreement with previous determinations.

j) We used the Balmer jump in emission for our Carina regions and we found that the temperature fluctuation parameter defined by Peimbert (1967) is $t^2 = 0.038 - 0.052$, with typical errors of ± 0.024 . Considering temperature fluctuations increases O/H by 0.20 – 0.30 dex. Our spectra confirm that Carina

is a relatively low metallicity HII region (by about 0.1 – 0.2 dex in O/H) as compared with other HII regions at the same galactocentric distance. The CarSE region (containing η Car) shows higher N/O and S/O ratios than the CarNW and CarSW regions, evidencing the strong contamination of the η Car ejecta in its surroundings. We consider that high-resolution and high S/N spectroscopic observations are needed for the extended Carina nebula in order to obtain accurate measurements of the faint auroral [OIII] and [NII] lines used to derive electron temperatures.

k) Our program spectra indicate the presence of a very strong component of additional continuum, interpreted as dust-scattered starlight and we show that it is correlated with the stellar continuum. By comparing the observed Balmer equivalent width W_{λ}^{obs} , with the theoretical prediction W_{λ}^{a} , we found that $\sim 70\%$ of the observed continua at these wavelengths is due to scattered light in Carina and M20, while in M8 this contribution amounts to $\sim 50\%$. Our derivations agree with those found in the literature for M8 and M20, and we report for the first time the fraction of scattered light in the Carina region.

l) We found that the scattered continuum is *bluer* than the *neb* continuum, indicating that the albedo times the average extinction cross section of the scattering particles increases at shorter wavelengths, in agreement with theoretical estimations (Mathis, 1983).

m) We present and compile evidence showing that the internal extinction can reach 50 – 70% of the total extinction in Galactic HII regions and GEHRs, indicating the presence of large amounts of dust within the emitting region. We found a marginal correlation between the derived reddening constant $c(\text{H}\beta)$ and the estimated fraction of scattered light $\chi^{\text{d}} = i^{\text{d}} / (i^{\text{a}} + i^{\text{d}})$.

n) Given that scattering effects are larger toward bluer wavelengths, we found that the scattering-corrected reddening constant, $c(\text{H}\beta)_{\text{corr}}$, is larger by 0.10 – 0.15 dex than the *observed* one, $c(\text{H}\beta)_{\text{obs}}$, derived ignoring scattering effects. This yields in turn scattering-corrected electron temperatures $T_e(\text{corr})$ about 120 – 150 K *larger* than those derived ignoring scattering effects. Propagating these effects to the ionic and total abundances, we found that the O/H and Ne/H abundances remain the same, but the scattering-corrected abundances for N/H, S/H and Ar/H are ~ 0.06 dex *smaller* than the non-corrected ones.

o) If the scattering effects are also applied to both the *observed spectra* and to the reddening constant, then the effect of increasing the reddening due to scattering effects is compensated by the effect of decreasing the blue lines with respect to the red ones due to scattering effects, in such a way that both effects cancel out, yielding pretty much the same electron temperatures and total abundances. These results do not agree with those reported by Simón-Díaz et al. (2011), whom showed the existence of an extended emission over the low-excitation nebula M43. They found that the scattering-corrected

$T_e(\text{OII})$ temperature is *smaller* by ~ 410 K than the non-corrected one, yielding corrected O/H abundances up to 0.09 dex larger than the non-corrected ones.

Appendix I. Additional information of our program nebulae and their exciting stars

Table 1. Additional information for M8 and M20 regions.

	M8	M20
$l(^{\circ}), b(^{\circ})$	5.95 ^d , -1.30 ^d	7.04 ^d , -0.26 ^d
V_{LSR} (km/s)	+12.0 ± 1.5 ^d	+19 ± 2.0 ^d
V (mag)	5.8 ^h	8.5 ^h
A_V (mag)	1.1 ^h	1.3 ^a , 1.0 ^h
d (kpc)	1.86 ^c , 1.6 ^e , 1.78 ^f , 1.80 ± 0.20 ^d	2.34 ^b , 1.95 ± 0.30 ^d
θ_{diam} ($'$)	25 ^h	15 ^h
R_G	8.6 ⁱ	8.5 ^{d,i}
$\langle E_{B-V} \rangle$ (mag)	0.36 (neb) ⁱ , 0.35 (star) ⁱ	0.45 (neb) ⁱ , 0.25 (star) ⁱ
N_e (cm ⁻³)	80 ^h	150 ^h
M_{tot} (M_{\odot})	1000 ^h	150 ^h
$S(\text{H}\alpha)$ (10 ⁻³ erg s ⁻¹ cm ⁻² ster ⁻¹)	7 ^h	6 ^h
$S(20 \text{ cm})$ (10 ⁻²² erg s ⁻¹ cm ⁻² Hz ⁻¹)	38 ^h	3 ^h

^a From Lynds & O'Neil (1985) and Lynds, Canzian & O'Neil (1985). ^b Derived using data from HD 164492 by O'Dell, Hubbard & Peimbert (1966; OHP66). ^c From McCall, Richer & Visvanathan (1990). ^d From Brand & Blitz (1993). ^e From OHP66. ^f From van Altena & Jones (1972). ^g From Lynds & O'Neil (1982; LO82). ^h Adapted from Allen (1976), and Cox (2000). ⁱ From Hawley (1978). $\langle E_{B-V} \rangle$ (neb) derived from $\text{H}\alpha/\text{H}\beta$, $\langle E_{B-V} \rangle$ (star) derived from cluster stars.

Table 2a. Identified stars in RCW6 field.^a

No.	Moff	ID	α (2000)	δ (2000)	B (mag)	$B - V$ (mag)	E_{B-V} (mag)	SpT	d_{star} (kpc)
1	-	HD 54977 SAO 152506 BD -18 1715	07 10 19.0	-18 23 46.9	8.5 ^f	-	-	G8 III/IV ^c	-
2	5	GCS 5968-03541	07 09 56.2	-18 25 45.4	11.7	0.17 ^g , 0.13 ⁱ	-	-	-
3	3	LSS 208 GSC 5968-02262	07 09 55.5	-18 26 09.0	11.6	0.18 ^g , 0.20 ⁱ	0.44 ^g , 0.50 ⁱ	B1 III ^g , B0.5 V ⁱ	7.6 ^d , 6.0 ⁱ
4	4	GCS 5968-03681	07 09 53.4	-18 26 20.1	12.0	0.42 ^{g,i}	-	-	-
5	-	GCS 5968-02613	07 09 42.2	-18 27 05.2	13.9	-	-	-	-
6	-	GCS 5968-03473	07 09 41.4	-18 27 42.4	13.6	-	-	-	-
7*	1	LSS 207 CGO 152 ^b	07 09 54.7	-18 29 59.4	10.9	0.44 ^g , 0.49 ⁱ 0.40 ^j	0.76 ^g , 0.81 ⁱ 0.71 ^j	O7 ^g , O6 V ^{h,i}	5.8 ^c , 5.0 ^d 6.0 ^h , 5.6 ⁱ 6.2 ^j , 6.6 ^k
8	-	GCS 5968-03386	07 09 48.9	-18 30 07.7	15.0	-	-	-	-
9	-	GCS 5968-0356	07 09 40.1	-18 29 47.7	13.9	-	-	-	-
10	-	-	07 09 56.6	-18 30 52.7	10.8	-	-	-	-
11	-	GCS 5968-02191	07 09 41.8	-18 30 43.8	14.2	-	-	-	-
12	-	GCS 5968-03768	07 09 58.8	-18 31 24.2	13.5	-	-	-	-

13	-	GCS 5968-02733	07 09 50.8	-18 31 30.7	12.3	-	-	-	-
14	-	GCS 5968-02619	07 10 02.0	-18 32 17.6	13.4	-	-	-	-
15*	-	GCS 5968-02659	07 10 02.4	-18 32 40.1	10.5	-	-	-	-
16	-	HD 54957	07 10 12.6	-18 32 46.0	7.9 ^f	-	-	G8/ K0 III ^c	-
		SAO 152499							
		GSC 5968-02617							
-	(2)* ^e				11.5 ^{f,g,i}	0.29 ^{g,i}	-	-	-
-	(6) ^e	LSS 212			12.1 ^{f,g,i}	0.21 ^g , 0.25 ⁱ	0.47 ^g , 0.52 ⁱ	B1 V ^{g,i}	5.2 ^d , 6.5 ⁱ
-	(7) ^e				12.7 ^{f,g,i}	0.33 ^{g,i}	-	-	-

^a Data extracted using *Simbad* Database querying for the following Catalogues: Bonner Durchmusterung Cat., Galactic O Stars Cat., Henry Draper and HD Extension Cat., Messier Nebulae Cat., Sharpless HII Regions Cat., NGC 2000 Cat., SAO Cat., and *HST* Guide Star Cat (1.1). The Galactic O Stars Cat. is from Gramany, Conti & Chiosi (1982), where most entries are from Cruz-González et al. (1974; CGO), and Humphreys (1978). ^b $M_{bol} = -9.14$ (Conti 1975). $M_V = -5.4$ (Vogt & Moffat 1975). CGO 152 = Goy 15, $z = -460$ pc, $V_{LSR} = +75$ km/s from CGO. ^c From *Simbad* Database. ^d Using $V - M_V$ from Moffat et al. (1979). ^e Moffat 6 is the bright star close to the NE corner of our scanned region, with declination between our stars No. 4 and No. 5; Moff 7 and Moff 2 are the 2 bright stars NE of our star No. 7, with Moff 7 south of Moff 2 (see Fig. 5a of Chapter II). ^f Gives V magnitude. ^g From Moffat et al. (1979). ^h From CGO. ⁱ From Lahulla (1987). ^j From Vogt & Moffat (1975). ^k From Georgelin et al. (1973). An asterisk means the star was removed from the 2-D CCD frame to obtain the *neb* spectra (Sec. 2.3 of Chapter II).

Table 2b. Identified stars in RCW60 field. ^a

No.	ID	α (2000)	δ (2000)	V (mag)	SpT
1	HD 99982	11 29 31.1	-62 31 03.5	9.1	B2/ B3 III ^b
2	GSC 8976-01902	11 28 37.1	-62 33 11.3	11.2	-
3	GSC 8976-01902	11 28 37.1	-62 33 11.3	11.2	-
4*	HD 100026	11 29 55.4	-62 36 04.0	9.0	B2/ B3 IV/ V ^b
5	GSC 8976-02976	11 28 17.7	-62 35 25.4	11.8	-
6*	GSC 8976-01654	11 28 38.4	-62 37 04.9	10.9	-
7	GSC 8976-05193	11 28 53.8	-62 38 08.2	11.9	-
8	GSC 8976-03129	11 29 26.9	-62 39 05.8	12.6	-
9	GSC 8976-04428	11 29 20.8	-62 38 35.0	11.7	-
10	GSC 8976-02967	11 29 08.2	-62 38 43.5	12.4	-
11*	HD 99897/ SAO 251420 ^c LSS 2355/ CGO 309	11 28 54.2	-62 39 08.7	8.23	O6 V ((f)), O6 V ^d
12	GSC 8976-04080	11 28 35.5	-62 38 17.0	12.0	-
13	GSC 8976-02943	11 28 17.0	-62 38 24.9	12.6	-
14*	GSC 8976-00069	11 28 58.4	-62 39 18.4	12.8	-
15	GSC 8976-05342	11 28 54.7	-62 39 26.5	12.7	-
16	GSC 8976-04967	11 28 49.4	-62 39 06.2	11.5	-
17	HD 99963/ SAO 251423 GSC 8976-04282	11 29 23.2	-62 41 27.6	9.1	B5 V ^b
18	GSC 8976-01470	11 28 35.7	-62 40 48.8	11.8	-
19	GSC 8976-03826	11 28 42.8	-62 41 29.0	10.6	-
20	HD 99771	11 27 59.0	-62 48 01.5	18.6	B7 Vn ^b

^a Searched Catalogues as in Table 2b. ^b SpT from HD Catalogue. ^c $M_{bol} = -8.94$, $M_V = -5.1$, $B - V = 0.18$, $d = 2.7$ kpc, $z = -59$ pc, $V_{LSR} = -8$ km/s and SpT from CGO. $E_{B-V} = 1.41$ from Georgelin et al. (1975). $d = 3.1$ kpc Georgelin et al. (1973). ^d From Feast et al. (1961). An asterisk means the star was removed from the 2-D CCD frame to obtain the *neb* spectra (Sec. 2.3 of Chapter II).

Table 2c. Identified stars in RCW107 field. ^a

No	ID	α (2000)	δ (2000)	V (mag)	SpT
1 *	HD 330913/GSC 8329 00075	16 33 50.4	-48 03 19.8	10.6	A0
2 *	GSC 8329 00059	16 33 41.0	-48 03 22.7	11.7	-
3	GSC 8329 03118	16 33 46.7	-48 03 41.9	13.7 ^c	-
4 *	HD 148988/GSC 8329 00001	16 34 06.9	-48 04 46.2	8.7	K1 III
5	GSC 8329 01264	16 33 52.2	-48 04 38.4	14.5 ^c	-
6	GSC 8329 00049	16 34 07.4	-48 06 02.3	13.9	-
7	CD -47 10855C/GSC 8329 03455	16 33 52.1	-48 06 04.9	13.8	-
8a*	HD 148937/SAO 226891 ^b LSS 3646/ CGO 380 CD -47 10855/GSC 8329 03343	16 33 52.2	-48 06 40.5	7.19	O6 I, O6 If
8b*	GSC 8329 01321	16 33 52.7	-48 06 37.6	5.4 ^c	-
9	GSC 8329 02306	16 33 31.4	-48 06 28.8	14.4 ^c	-
10	GSC 8329 02168	16 33 30.5	-48 06 59.6	14.25 ^c	-
11	GSC 8329 00625	16 33 27.4	-48 07 48.2	12.91	-
12	GSC 8329 00633	16 33 37.7	-48 09 34.8	13.17	-
13	GSC 8329 00483	16 34 08.9	-48 10 39.9	11.87	-

^a Searched catalogues as in Table 2b. RCW 107 = NGC 6164-65 is reported as type PL in the NGC 2000 Catalogue. ^b $M_{\text{bol}} = -9.68$, $M_V = -6$, $B - V = 0.34$, $d_{\text{star}} = 0.9$ kpc and SpT from CGO. Georgelin et al. (1996) give $U - B = -0.66$ and $A_V = 3.2 [(B - V) - (B - V)_0] = 2.08$ mag, with $(B - V)_0$ from Schmidt-Kaler (1982). HD and SAO Catalogues list it as class STAR B0 and give a V magnitude 0.3 mag brighter than GSC (listed). ^c Gives B magnitude. ^d CGO 380 = Goy 343, $z = -3$ pc, $V_{\text{LSR}} = -48$ km/s from CGO. ^e $d_{\text{star}} = 1.7$ kpc from Georgelin et al. (1996, based on the $M_V - \text{SpT}$ calibration of Humphreys & Mc. Elroy 1984.) An asterisk means the star was removed from the 2-D CCD frame to obtain the *neb* spectra (Sec. 2.3 of Chapter II).

Table 2d. Identified stars in RCW110 field. ^a

No.	IDs	α (2000)	δ (2000)	B (mag)	SpT
1	HD 329098/GSC 8327 00806	16 54 31.36	-45 08 31.6	11.31	B9
2	GCS 8327 01070	16 53 59.54	-45 09 19.6	11.82	-
3	GSC 8327 01096	16 53 55.41	-45 08 55.4	12.13	-
4	GCS 8327 01184	16 53 52.20	-45 08 46.2	13.69	-
5	HD 329099/GSC 8327 00832 CD -44 11243	16 54 08.10	-45 10 48.8	10.87	F0
6*	GSC 8327 00581	16 54 08.72	-45 11 02.7	14.55	-
7*	GSC 8327 01140	16 54 15.24	-45 11 22.3	13.30	-
8*	GSC 8327 01294	16 54 19.07	-45 12 05.8	13.05	-
9	HD 329103/GSC 8327 00988	16 53 50.16	-45 12 49.9	10.99	A0
10*	GSC 8327 00860	16 54 24.84	-45 13 25.1	14.84	-
11*	GSC 8327 00784	16 54 21.64	-45 13 45.3	12.87	-
12*	GSC 8327 01158	16 54 28.96	-45 14 14.8	14.20	-
13*	GSC 8327 01142	16 54 15.35	-45 14 18.4	13.04	-
14	HD 329100 A+B/CD -45 11051 ^c GSC 8327 01030/LSS 3815/CGO 420	16 54 42.13	-45 15 14.8	13.5/10.99 ^d	O8.5 V ^h
15*	GSC 8327 01154	16 54 10.31	-45 16 08.5	12.51	-
16	HD 329101/GSC 8327 01216	16 54 02.01	-45 16 18.9	11.76	F2
17	HD 329102/GSC 8327 01278 CD -45 11039	16 53 55.70	-45 16 36.7	10.33	F5
18	CD -45 11034/GSC 8327 00791 ^b LSS 3799/CGO 404	16 53 50.76	-45 18 19.5	11.08 ^d	O8.5, O8 III:n ⁱ

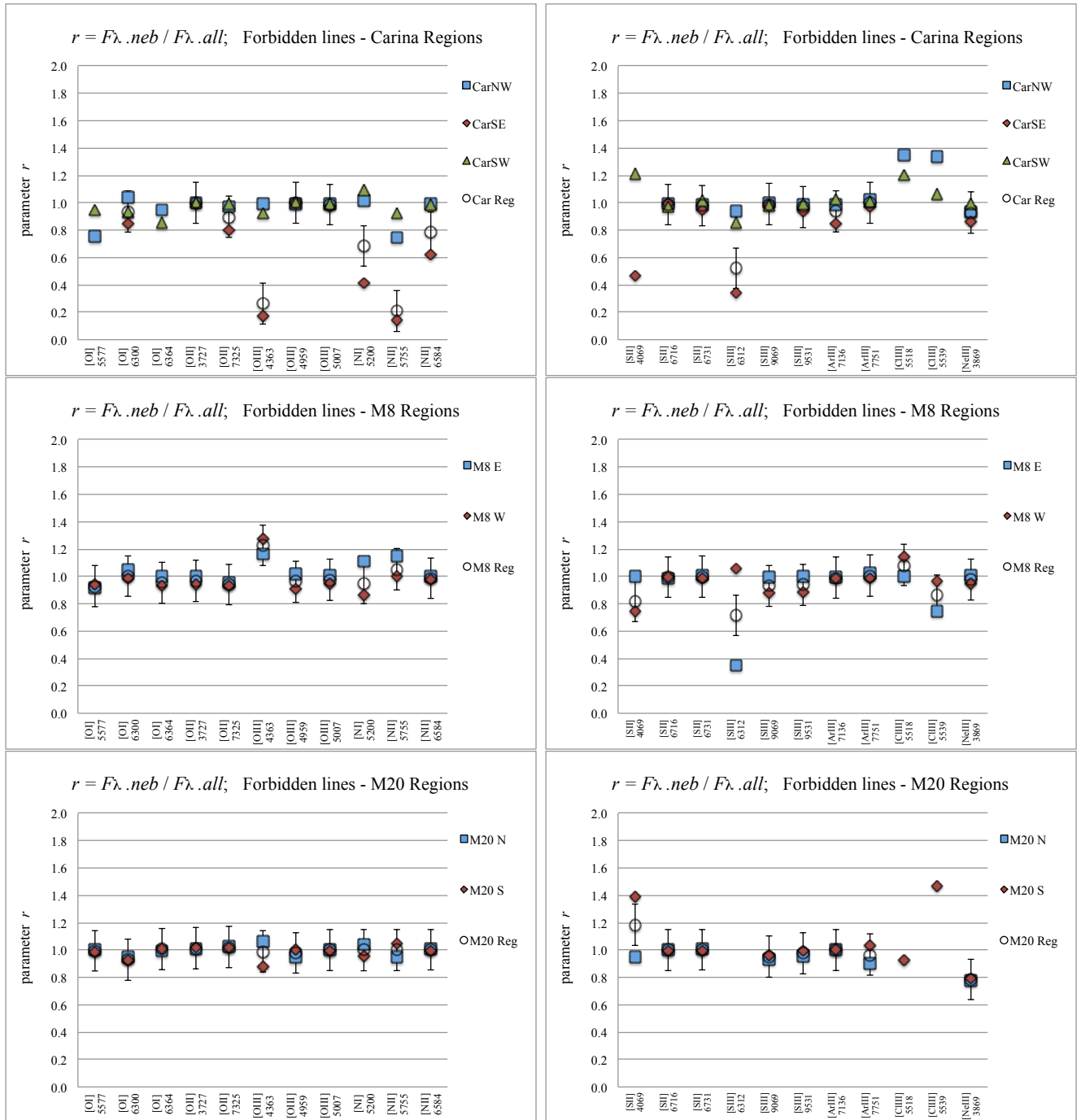
^a Searched catalogues as in Table 2*b*. Note that HD 152386 (LSS 3825, $V = 8.13$, O6f/ O5 Ia) is *not* the exciting star of RCW110 (as reported by Georgelin and Goergelin 1970*a*), since it lays 16' N – NE from it. Lynga (1987) reports a photometric distance of 2.30 kpc for star cluster Ly 14, to which RCW110 is probably related. ^b $M_{\text{bol}} = -7.73$, $M_V = -4.4$, $B - V = 0.89$ and SpT from CGO. $U - B = -0.24$, $A_V = 3.84$ from Georgelin et al. (1996). ^c $M_{\text{bol}} = -8.08$, $M_V = -4.75$. $B - V = 0.96$ and SpT from CGO. $B - V = 0.95$, $U - B = 0.11$, $A_V = 4.03$ from Georgelin et al. (1996). ^d Gives V magnitude. ^e CGO 420 = Goy 381, $z = -36$ pc, $V_{\text{LSR}} = -15$ km/s, $d_{\text{star}} = 2.0$ kpc from CGO. ^f CGO 404 = Goy 367, $z = -39$ pc, $V_{\text{LSR}} = -98$ km/s, $d_{\text{star}} = 2.4$ kpc from CGO. ^g $d_{\text{star}} = 1.7$ kpc (photometric) from Georgelin et al. (1973). ^h From Georgelin et al. (1975). ⁱ Georgelin et al. (1996) report $d_{\text{star}} = 3.0$ kpc for CGO 404 and $d_{\text{star}} = 2.0$ kpc for CGO 420. An asterisk means the star was removed from the 2-D CCD frame to obtain the *neb* spectra (Sec. 2.3 of Chapter II).

Table 3. Radio continuum, line temperatures, line velocities and distances of RCW nebulae. ^a

Nebula	l	b	T_c	θ	S_5^{cont}	T_L	ΔV_L	V_{LSR}	T_e^{rad}	R_G^1	d_{kin}
(1)	($^\circ$)	($^\circ$)	(K)	($'$)	(Jy)	(mK)	(km/s)	(km/s)	(kK)	(kpc)	(kpc)
(1)	(2)	(3)	(4)	(5)	(6)	(7)	(8)	(9)	(10)	(11)	
RCW6	231.351	-4.256	-	$\sim 9^p$	-	-	33.3 ± 0.2^n	$+54.3^k, +56.1^n$	$7.3-7.7^o$	12.3-12.9	3.8 ± 0.4^j
RCW6	231.481	-4.401	-	-	3.96^m	28 ± 2.4^d	25.5 ± 2.7^d	$+58.4 \pm 1.1^d$	-	-	-
BBW7A	231.51	-4.36	-	-	-	-	-	$+58.3 \pm 0.5^b$	-	-	4.22 ± 0.55^b
BBW6	231.57	-4.47	-	-	-	-	-	$+51.8 \pm 0.5^b$	-	-	1.50 ± 0.31^b
Sh 301	231.45	-4.41	-	-	-	-	-	$+53 \pm 0.5^c$	-	-	5.10 ± 1.20^c
RCW60	293.600	-1.280	0.75	~ 15	13.8	80	15	$-27, -23.8^k$	6.8	7.8-7.9	$4.0^f, 3.6 \pm 1.4$
RCW60	293.64	-1.41	-	-	-	-	-	-24^c	-	-	$2.5 \pm 0.60^c, 2.4^l$
BBW362C	294.04	-1.75	-	-	-	-	-	-17.9 ± 0.5^g	-	-	2.25 ± 0.13^g
RCW107 ^e	336.404	+0.234	3.5	5	10.9	310	36	$-93, -50.5^k$	3.7	7.2-7.7	$6.9, 11.4^f, 4.2^k$
RCW110 ^h	340.777	-1.008	6.11	5×3	14.3	380	35	$-25, -25.4^k$	5.1	6.3-6.6	$2.5^f, 2.2 \pm 0.4^g$
	340.88	-0.80						-28^c			2.30 ± 0.30^c

^a Columns give: (1) Nebula ID; (2) 1950 Galactic coordinates; (3) Continuum temperature at 5 GHz; (4) Optical angular size; (5) Continuum flux at 5 GHz; (6) Peak antenna line temperature (from H109 α and H110 α); (7) Line FWHM; (8) Line velocity; (9) Radio-derived electron temperature; (10) Galactocentric radius and (11) Distance. Adapted from Caswell & Haynes (1987; CH87). ^b From Brand & Blitz (1993). ^c From Avedisova & Palous (1989, AP89). ^d From LPH96, T_L recombination line temperature at 9 cm (from H126 α and H127 α). ^e Considerable superposition of features along this line of sight. ^f Near and far solutions assuming $R_\odot = 10.0$ kpc; ^g From BBW. ^h RCW110 from AP89 could be RCW111 within the estimated l and b errors. ⁱ Re-computed distance from $R^2 = R_\odot^2 + d^2 - 2R_\odot d \cos(l)$, using $R_\odot = 8.5$ kpc and $d^* = 5.0-5.8; 2.4-2.7; 0.9-1.4$; and $2.0-2.4$ kpc for RCW6; RCW60; RCW107 and RCW110, respectively. ^j From Georgelin et al. (1973). ^k From Georgelin & Georgelin (1970*b*). V_{LSR} from H α (corrected for solar motion, with U = -7.5, V = +13, W = +7 km/s). ^l From Georgelin & Georgelin (1976). ^m Total radio continuum flux at 3.17 GHz from Fich & Silkey (1991). ⁿ From H α Fabry-Perot by Fich et al. (1990). ^o From total radio continuum flux by S83 and FS91. ^p From a POSS red picture.

Appendix II. Comparison of *.all* vs. *.neb* for forbidden lines



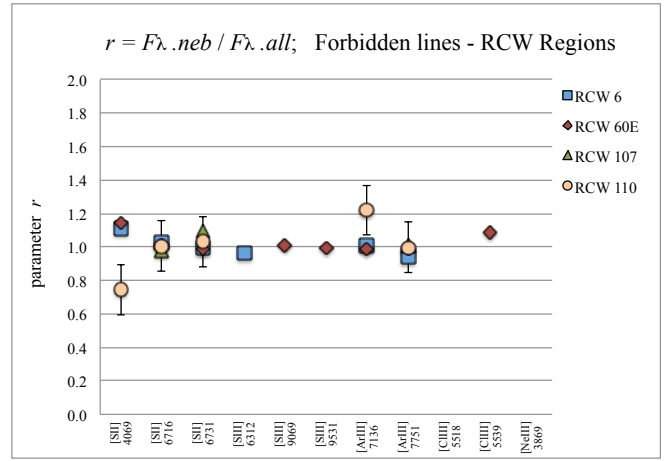
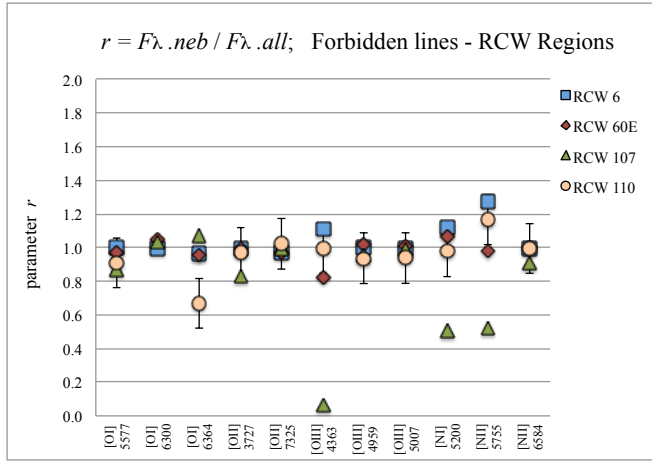


Fig. 1. Observed parameter $r = F\lambda_{.neb} / F\lambda_{.all}$ for a larger set of forbidden lines for our sample objects: a) Carina regions, b) M8 regions, c) M20 regions and d) RCW objects. Error bars of $\pm 15\%$ are show for all lines in the integrated spectra.

Appendix III. Carina root mean square density and filling factor

In this Appendix, we estimate the root mean square N_{rms} , and volume-filling factor f , of the Carina nebula through two different methods. In the first one, we use the observed integrated radio continuum flux of our regions adapted from the literature and in the second one, we use the observed $H\beta$ flux. Both methods allow us to derive the root mean square density for the emitting plasma N_{rms} , which traces the volume occupied by the H^+ ions. Knowing N_{rms} , we can compare it with the electron density derived from forbidden lines, eg. N_{SII} , to derive the filling factor of the nebula (Mallik & Peimbert 1988),

$$f = \left(\frac{N_{\text{rms}}}{N_{\text{SII}}} \right)^2. \quad (1)$$

III.1 Radio method

In this section, we present different derivations of the emission measure, root mean square density and filling factor of our Carina regions using different radio fluxes reported in the literature. For an optically thin homogeneous spherical volume of radius R , the emission measure can be approximated by $EM = \int N_e^2 dl \approx N_{\text{rms}}^2 L$, where $L = 2R$ at the center of the nebula. It can be shown that the relation between the radio continuum flux as function of frequency S_ν ($\text{erg s}^{-1} \text{cm}^{-2} \text{Hz}^{-1}$), electron temperature T_e (K), emission measure EM , ($\text{cm}^{-6} \text{pc}$) and source solid angle Ω_s (rad^2), in the optically thin case is:

$$S_\nu = 2.01 \times 10^{-19} \left[\frac{\nu}{\text{Hz}} \right]^{-0.1} \left[\frac{T_e}{\text{K}} \right]^{-0.35} \left[\frac{EM}{\text{cm}^{-6} \text{pc}} \right] \left[\frac{\Omega_s}{\text{rad}^2} \right]. \quad (2)$$

There have been many attempts to derive the distance to the Carina Nebula through different techniques, obtaining distances ranging from $d_{\text{Car}} = 2.2$ to 3.4 kpc, for $R_V = 4.0$ to 3.0 (Faulkner 1963; Thé & Vleeming 1971; Feinstein et al. 1973; Walborn 1973a; Herbst 1976; Thé, Bakker, & Antalova 1980; Levato & Malaroda 1982; Tapia et al. 2003). In what follows, we will adopt $d_{\text{Car}} = 2.6 \pm 0.2$ kpc.

The solid angle of our slit projected on the sky is $\Omega_{\text{slit}} = 6.5' \times 5'' = 4.58 \times 10^{-8} \text{rad}^2$, corresponding to an area $A_{\text{slit}} = 4.92 \text{pc} \times 0.063 \text{pc} = 0.310 \text{pc}^2$. On the other hand, our spectra represent an average *integrated* spectra over a $7.5'$ length in RA (5.67pc), so the solid angle covered by our scans is $\Omega_{\text{scan}} = 6.5' \times 7.5' = 4.12 \times 10^{-6} \text{rad}^2$, corresponding to an area $A_{\text{scan}} = 27.9 \text{pc}^2$. To get a rough estimate of L , we considered a wide-field optical picture of the Carina Nebula ($\sim 3 \times 3 \text{deg}^2$). We estimate that the whole nebula extends at least over 60pc , so we will consider $L \approx 60 \text{pc}$ as a lower

limit. We also get an estimated $L \approx 60$ pc from the 5 GHz radio map presented by Gardner et al. (1970), by considering the outer continuum contours at $T_B = 1.1$ K.

There were several radio studies of the Carina Nebula in the mid 60's and early 70's. Komesaroff (1966) made a low-resolution (50') survey at 86, 408, and 1440 MHz. Beard & Kerr (1966) surveyed the nebula at 1410 and 2650 MHz and found evidence for an optically thin spectrum. Gardner et al. (1970; G70) compared their 5 GHz maps (4' beam), with the 408 MHz map of Shaver & Goss (1970), and concluded that the spectrum is thermal everywhere and optically thin at 408 MHz.

Komesaroff (1966) observations encompass our 3 regions and could be used along with Eq. (2) to estimate an upper limit for N_{rms} . We show the results in Table 1, where we considered $\Omega_{\text{source}} = (\pi/4)(50')^2$, and we assumed an average temperature for the radio-emitting zone, $T_{\text{rad}} = 8300$ K, adapted from radio line and continuum measurements (G70 and references therein). If we use our average $T_{\text{OIII}} = 9600$ K, instead of T_{rad} , then N_{rms} increases by 3%, so T_e is not an important source of error. Note that T_e derived from radio continuum and radio recombination lines (G70) tends to be smaller than optical determinations from forbidden lines ($\sim 1.0 - 1.5$ kK).

Gardner & Morimoto (1968) observed the Carina Nebula at 5 GHz continuum with a beam-width of 4.2' and found two components, referred hereafter as **Car I** and **Car II** (G70). Car I is within our CarNW region, close to its southern edge, while Car II is located within our CarSE region, 2' NW from η Car (Figs. 1a – 1b). We used Eq. (2) with their reported fluxes and source sizes $\Omega_{\text{source}} = \theta_a^{\text{obs}} \times \theta_b^{\text{obs}}$, to obtain the EM , N_{rms} and filling factors given in Table 1 for Car I and Car II. We used a higher $N_{\text{SII}} = 200 \text{ cm}^{-3}$ in CarSE (Car II) than $N_{\text{SII}} = 100 \text{ cm}^{-3}$ in CarNW and CarSW (Car I), therefore our derived filling factor is a factor of 4 smaller for Car II than for Car I. Gardner & Morimoto (1968) report lower limits for the peak $EM = 3.4$ and $3.6 \times 10^5 \text{ cm}^{-6} \text{ pc}$ for Car I and Car II, respectively, in good agreement with our derived values.

Wilson et al. (1970) also report 5 GHz fluxes at two positions in the Carina Nebula within given source diameters. We used these fluxes and source diameters along with Eq. (2) to estimate the EM , N_{rms} and f values given in Table 1.

G70 made a detailed radio study of the Carina Nebula at 5 GHz with a beam of 4' resolution. These authors do not report an integrated radio flux for the whole nebula, instead they present calibrated continuum T_B -isocontours maps and recombination line temperatures at different positions over the nebula. To estimate the approximate radio fluxes arising from our observed regions, we plotted our rectangular scans over the T_B -contours, which range from $T_B = 1.1$ K to $T_B^{\text{peak}} = 29.9$ K for Car I and $T_B^{\text{peak}} = 27.7$ K for Car II. Most of the emission above $T_B = 11$ K from Car I is covered by our CarNW and CarSW scans, while that for Car II is encompassed by our CarSE scan (see Figs. 1a – 1b).

We estimated the flux arising from CarSE by taking the product of the peak temperature T_B^{peak} , times the elliptical angular area A_θ of the isocontour with $T_B = 17.6$ K (this choice motivated from Fig. 1b), with $A_\theta = (\pi/4) (6.96' \times 5.22')$, to obtain $T_B^{\text{peak}} \times A_\theta = 6.69 \times 10^{-5}$ K rad². In the optically thin regime, the 5 GHz flux can be approximated by

$$S(5 \text{ GHz}) = \frac{2k}{c^2} \nu^2 \Omega_s T_e \tau_\nu \approx \frac{2k}{c^2} \nu^2 A_\theta T_B^{\text{peak}}, \quad (3)$$

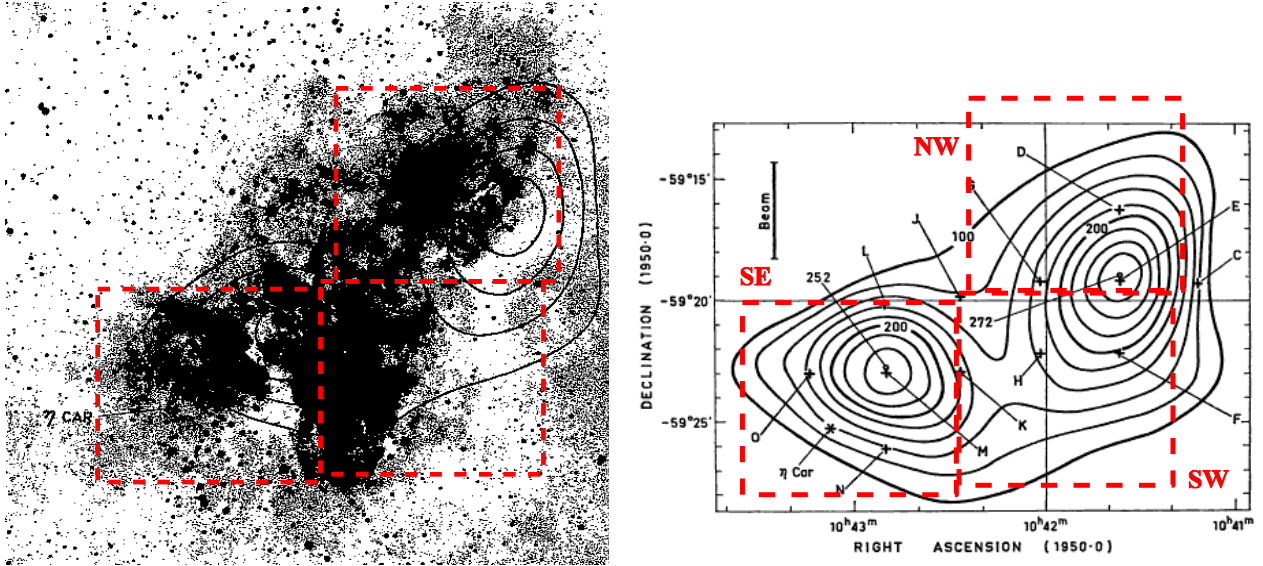
Table 1. Emission measure, N_{rms} density and filling factor for Carina. ^a

ν	S_ν			EM			N_{rms}			f			Ref
(1)	(2)	(3)	(4)	(5)	(6)	(7)	(8)	(9)	(10)	(11)	(12)	(13)	(14)
0.086	242			0.106			13			0.02			A
0.408	610			0.313			23			0.05			A
1.440	650			0.378			25			0.06			A
	Car I	Car II		Car I	Car II		Car I	Car II		Car I	Car II		
5.0	125	103		3.27	3.02		74	71		0.54	0.13		B
5.0	114.5	86.0		4.98	4.68		92	88		0.83	0.20		C
	NW+SW	SE		NW+SW	SE		NW+SW	SE		NW+SW	SE		
5.0	82.7	51.3		1.10	1.36		43	48		0.18	0.06		D
	NW+SW+SE			NW+SW+SE			NW+SW+SE			NW+SW+SE			
5.0	208			1.84			55			0.18			D
	NW	SE	SW	NW	SE	SW	NW	SE	SW	NW	SE	SW	
H β	2.40	2.82	1.79	1.88	2.61	1.01	56	66	41	0.31	0.11	0.17	E

^a Columns: (1) Observation frequency in GHz; (2) – (4) Observed flux in 10^{-23} erg s⁻¹ cm⁻² Hz⁻¹; (5) – (7) Emission measure (10^5 cm⁻⁶ pc); (8) – (10) Root mean square density (cm⁻³) from Eq. (2); (11) – (13) Volume filling factor. Column (14) References: (A) Komesaroff (1966); (B) Gardner & Morimoto (1968); (C) Wilson et al. (1970). Fluxes from sources G-287.4-0.6 (Car I) and G-287.5-0.6 (Car II); (D) Gardner et al. (1970). (E) This work. Columns (2) – (4) give the de-reddened H β flux emerging from our slit, $F(\text{H}\beta)_0$ in 10^{-10} erg s⁻¹ cm⁻² (Tables 2a – 2c of Chapter III). N_{rms} values from an emitting volume, $V_{\text{em}} = 4.92 \times 0.063 \times 60$ pc³

Substituting values, we get for our CarSE region, $S(5 \text{ GHz})_{\text{SE}} = 51.3$ Jy as a lower limit, and from Eq. (2) we get the results presented in Table 1, where we have used $\Omega_s = \Omega_{\text{scan}}$. The corresponding flux for CarNW and CarSW was estimated in the same manner. We chose the same T_B -contour ($T_B = 17.6$ K), to compute the elliptical angular area $A_\theta = (\pi/4) (8.91' \times 6.09')$, so that $T_B^{\text{peak}} \times A_\theta = 10.8 \times 10^{-5}$ K rad², and $S(5 \text{ GHz})_{\text{NW+SW}} = 82.7$ Jy. The corresponding EM , N_{rms} and filling factor f , with $\Omega_s = 2 \Omega_{\text{scan}}$ are shown in Table 1.

To get an idea of the uncertainties involved, we estimated the flux arising from our 3 regions, considering this time the elliptical areas defined by the isocontours with $T_B = 0.5 T_B^{\text{peak}} = 14.0$ K. For Car I we find $A_\theta = (\pi/4) (10.4' \times 7.17')$; $T_B^{\text{peak}} \times A_\theta = 14.9 \times 10^{-5}$ K rad², and $S(5 \text{ GHz})_{\text{NW+SW}} = 114$ Jy. For Car II we find $A_\theta = (\pi/4) (9.57' \times 6.74')$; $T_B^{\text{peak}} \times A_\theta = 12.2 \times 10^{-5}$ K rad², and $S(5 \text{ GHz})_{\text{SE}} = 93.9$ Jy. Finally, the total 5 GHz flux from our 3 regions amounts to $S(5 \text{ GHz})_{\text{NW+SW+SE}} = 208$ Jy, with the corresponding EM , N_{rms} and f values given in Table 1. In this case, we took $\Omega_s = 3 \Omega_{\text{scan}}$ and $\langle N_{\text{SII}} \rangle = 130 \text{ cm}^{-3}$ in Eq. (2). Note that although the integrated $S_{5\text{GHz}}$ flux depends on the T_B -isocontour adopted, the derived N_{rms} and f do not depend strongly of this parameter.



Figs. 1a (left) and 1b (right). Our scanned regions are superposed upon Gardner et al.'s (1970) 5 GHz continuum contour map. On the contour scale given in Fig. 1b, 100 units corresponds to $T_B = 11$ K. Car I is the right peak close to our CarNW and CarSW boundary, and Car II is the left peak in CarSE.

There is a considerable spread in the radio-derived EM , depending on the values of the adopted fluxes, and especially, on the adopted solid angle Ω_s for the emitting source. However, since $N_{\text{rms}} \propto (EM)^{1/2}$, the N_{rms} and f values have a much lower spread. From Table 1 we see that there is reasonable agreement for the different radio-derived N_{rms} and f values for our Carina regions, with $N_{\text{rms}} = 43 - 55 \text{ cm}^{-3}$ and $f = 0.06 - 0.18$.

III.2 Optical method

An alternative approach to derive N_{rms} and f is to estimate N_{rms} from optical recombination lines such as $H\beta$. In the simplest model, the de-reddened $H\beta$ flux $F(H\beta)_0$, from an optically thin pure-H Strömngren sphere with volume $V_S = (4\pi/3) r^3$ and root mean square density N_{rms} , situated at a distance d is,

$$F(\text{H}\beta)_0 = \frac{1}{4\pi d^2} V_S N_{\text{rms}}^2 \alpha_{\text{H}\beta}^{\text{eff}} h\nu_{\text{H}\beta} . \quad (4)$$

From Eq. (20) of Chapter III, $\alpha_{\text{H}\beta}^{\text{eff}} \approx 3.01 \times 10^{-14} \text{ cm}^3 \text{ s}^{-1}$ at $T_e = 10^4 \text{ K}$. Including helium, with $\text{He}^+/\text{H}^+ = 0.09$ (Table 6 of Chapter III), we have

$$N_{\text{rms}}^2 = \frac{4\pi d^2}{\alpha_{\text{H}\beta}^{\text{eff}} h\nu_{\text{H}\beta}} \times \frac{1.09 F(\text{H}\beta)_0}{V_S} . \quad (5)$$

Given the depth of the nebula assumed earlier, $L \geq 60 \text{ pc}$, we approximated the observed emitting volume by a rectangular slice of dimensions, $V_{\text{em}} = 4.92 \times 0.063 \times 60 \text{ pc}^3 = 18.6 \text{ pc}^3$, which implies $N_{\text{rms}} = 40 - 70 \text{ cm}^{-3}$ and $f = 0.11 - 0.31$, as given in Table 1, which are in good agreement with the values derived from radio fluxes. Considering the uncertainties involved in the radio and optical methods, we give a larger weight to the values derived using G70 radio maps (reference D in Table 1) and we adopt $EM = 1.8 \pm 0.4 \times 10^5 \text{ cm}^{-6} \text{ pc}$, $N_{\text{rms}} = 50 \pm 10 \text{ cm}^{-3}$, and $f = 0.2 \pm 0.1$ as representative values for our Carina regions. The knowledge of the filling factor is important when one attempts to build a photoionization model of the nebula.

Appendix IV. Dust extinction efficiency factors from scattered continuum

In this appendix we relate the observed scattered continuum colors with know dust parameters in order to constrain the type of dust particles present in our program nebulae.

The emergent $H\alpha/H\beta$ Balmer flux decrement, for pure internal extinction with no scattering, is given by:

$$\frac{F_\alpha}{F_\beta} = \frac{j_\alpha}{j_\beta} \frac{\tau_\beta (1 - e^{-\tau_\alpha})}{\tau_\alpha (1 - e^{-\tau_\beta})}, \quad (1)$$

where j_λ is the recombination coefficient at wavelength λ ($\text{erg s}^{-1} \text{cm}^{-3}$) and $\tau_\lambda \approx n_d \kappa_\lambda^{\text{ext}} L$, is the optical depth at wavelength λ ; n_d is the number density of dust particles (cm^{-3}), $\kappa_\lambda^{\text{ext}} = \pi a^2 Q_\lambda^{\text{ext}}$, is extinction cross section of dust particles (cm^2), πa^2 is the average geometrical cross section of dust particles (cm^2), Q_λ^{ext} is a function of λ called the dust extinction efficiency factor, and L is the length (cm) of the emitting region. From this equation, we see that for large internal optical depths, the observed Balmer decrement tends to the limit:

$$\left(\frac{F_\alpha}{F_\beta} \right)_{\text{lim}} = 2.86 \left(\frac{\tau_\beta}{\tau_\alpha} \right) = 2.86 \left(\frac{\kappa_\beta^{\text{ext}}}{\kappa_\alpha^{\text{ext}}} \right) = 2.86 \left(\frac{Q_\beta^{\text{ext}}}{Q_\alpha^{\text{ext}}} \right) \quad (2)$$

The second equality is valid since we are dealing with the ratio of optical depths, no matter if the origin of the extinction and reddening is internal or interstellar. If it is internal, the $Q_\beta^{\text{ext}}/Q_\alpha^{\text{ext}}$ ratio gives us information on the properties of the dust inside the HII region, and if it is external, it bears information of the ISM dust.

In Table 1 we present the ratios of the extinction efficiency factors ($Q_\beta^{\text{ext}}/Q_\alpha^{\text{ext}}$), ($Q_\gamma^{\text{ext}}/Q_\beta^{\text{ext}}$) and ($Q_\delta^{\text{ext}}/Q_\beta^{\text{ext}}$) derived for Carina and compare them with the corresponding ratios for Orion and for different fits of the general ISM extinction laws, using $A_\lambda/A_\beta = Q_\lambda^{\text{ext}}/Q_\beta^{\text{ext}}$. The estimated errors are ± 0.06 for ($Q_\beta^{\text{ext}}/Q_\alpha^{\text{ext}}$), and ± 0.07 for ($Q_\gamma^{\text{ext}}/Q_\beta^{\text{ext}}$) and ($Q_\delta^{\text{ext}}/Q_\beta^{\text{ext}}$). We see that the ratio of extinction factors for Carina and Orion are very similar and less steep (by ~ 0.09) than those of the general ISM, in agreement with their higher $R_V \approx 5$ extinction laws (Chapter IV, and CP70, respectively). The agreement between the different ISM extinction laws is very good within the assigned errors.

Table 1. Ratios of extinction efficiency factors derived from different extinction laws. ^a

	----- Carina Region -----			----- Orion -----		----- Standard -----		
	This work			CP70	MP71	SM79	CCM89	F99
	Car NW	Car SE	Car SW	$R = 5$	$R = 5$	$R = 3.1$	$R = 3.1$	$R = 3.1$
$Q_{\beta}^{\text{ext}}/Q_{\alpha}^{\text{ext}}$	1.40	1.40	1.41	1.41	1.36	1.48	1.47	1.53
$Q_{\gamma}^{\text{ext}}/Q_{\beta}^{\text{ext}}$	1.11	1.11	1.08	1.08	1.08	1.13	1.12	1.13
$Q_{\delta}^{\text{ext}}/Q_{\beta}^{\text{ext}}$	1.14	1.18	1.15	1.13	–	1.18	1.18	1.20

^a Cols. (1) – (3) adapted from Chapter IV. Adapted from Costero & Peimbert (1970; CP70); Munch & Persson (1971; MP71); Savage & Mathis (1979; SM79); Cardelli, Clayton & Mathis (1989; CCM89); and Fitzpatrick (1999; F99).

We will consider as representative the “standard” ratios from SM79: $Q_{\beta}^{\text{ext}}/Q_{\alpha}^{\text{ext}} = 1.48$, $Q_{\gamma}^{\text{ext}}/Q_{\beta}^{\text{ext}} = 1.13$ and $Q_{\delta}^{\text{ext}}/Q_{\beta}^{\text{ext}} = 1.18$. For this $Q_{\beta}^{\text{ext}}/Q_{\alpha}^{\text{ext}}$ ratio, the highest observed $(F_{\alpha}/F_{\beta})_{\text{lim}}$ ratio due to internal extinction would be 4.23, and the corresponding highest color excess would be $E_{\beta-\alpha} \approx 0.44$. In the case of interstellar extinction, there is no upper limit to the observed Balmer decrement, and observed ratios higher than 4.23 would indicate that, besides the internal reddening, there is a component due to external extinction, either from a dusty slab or from the general ISM, or both.

In Table 2a of Chapter VI, we gave the de-reddened scattered continuum surface brightness, $s_{(\lambda)}^d$ from H α to H δ for our integrated spectra Car Reg, M8 Reg and M20 Reg, which can be used to estimate the ratio of extinction efficiency factors. Using Eq. (8) of Chapter VI, we can write:

$$\frac{s(\text{H}\beta)_0^d}{s(\text{H}\alpha)_0^d} = \frac{j_{\beta}^d}{j_{\alpha}^d} = \frac{g_{\beta} w_{\beta} Q_{\beta}^{\text{ext}}}{g_{\alpha} w_{\alpha} Q_{\alpha}^{\text{ext}}}, \quad (3)$$

with similar expressions for the H γ /H β and H δ /H β ratios.

In Table 2 below we present the ratios of the scattered continuum surface brightness at $\lambda 4861/\lambda 6563$ (H β /H α), $\lambda 4340/\lambda 4861$ (H γ /H β) and $\lambda 4102/\lambda 4861$ (H δ /H β) for Car Reg, M8 Reg and M20 Reg from Chapter VI. We also present the $g_{\lambda 1} w_{\lambda 1} / g_{\lambda 2} w_{\lambda 2}$ (phase function and albedo) ratios given by Mathis (1983; M83), adapted from the theoretical model of Mathis, Rumpl & Nordsieck, (1977; MRN77) for a mixture of uncoated graphite and silicates. We illustrate these phase function and albedo parameters in Fig. 1 below. We also show in the same figure w_{λ} for iron grains as function of grain radius a , adapted from Spitzer (1978; S78). Finally, in the upper part of Table 2 we present the *scattering efficiency factor* ratios for Car Reg, M8 Reg and M20 Reg ($Q_{\lambda 1}^{\text{scatt}}/Q_{\lambda 2}^{\text{scatt}}$) derived from Eq. (3), with estimated errors of ± 0.06 for the (H β /H α) ratio and ± 0.07 for the (H γ /H β) and (H δ /H β) ratios.

In the lower part of Table 2 we present interpolations of the *scattering* efficiency factor ratios $Q_{\lambda 1}^{\text{scat}}/Q_{\lambda 2}^{\text{scat}}$ and *extinction* efficiency factor ratios $Q_{\lambda 1}^{\text{ext}}/Q_{\lambda 2}^{\text{ext}}$ for different compositions of spherical grains: ice, dirty-ice and iron particles for a range of representative grain sizes, from $a = 0.05 \mu\text{m}$ to $0.50 \mu\text{m}$, adapted from S78. For grains larger than $a = 0.10 \mu\text{m}$, the efficiency factor *ratios* tend to 1. We also include results for amorphous carbon, graphite and silicate adapted from Draine (1985), Cox (1999) and Draine (2003). In the graphite column we also include results for amorphous carbon adapted from Brussoletti et al. (1987) and Maron (1990). Note that $Q_{\lambda}^{\text{ext}} = Q_{\lambda}^{\text{abs}} + Q_{\lambda}^{\text{scat}}$; $w_{\lambda} = Q_{\lambda}^{\text{scat}}/Q_{\lambda}^{\text{ext}}$, and $w_{\lambda} = 1$ for ice particles, since $Q_{\lambda}^{\text{abs}} = 0$. In Fig. 2 we present the $Q_{\beta}^{\text{ext}}/Q_{\alpha}^{\text{ext}}$ and $Q_{\gamma}^{\text{ext}}/Q_{\beta}^{\text{ext}}$ ratios as function of grain radius a , adapted from S78.

From Table 2, we see that the dust in Carina has “bluer” (steeper) $Q_{\lambda 1}^{\text{scat}}/Q_{\lambda 2}^{\text{scat}}$ ratios than those found in M8 and M20. For Carina, its $Q_{\beta}^{\text{scat}}/Q_{\alpha}^{\text{scat}}$ ratio is consistent with dust composed by small graphite grains with $a = 0.01 \mu\text{m}$ and/or larger dirty-ice grains with $a = 0.10 \mu\text{m}$. At the other hand, its $Q_{\gamma}^{\text{scat}}/Q_{\beta}^{\text{scat}}$ and $Q_{\delta}^{\text{scat}}/Q_{\beta}^{\text{scat}}$ ratios are consistent with small ($a = 0.05 \mu\text{m}$) dirty-ice and iron grains. However, we do not expect large amounts of ices to survive in ionized nebulae. The observed $Q_{\lambda 1}^{\text{scat}}/Q_{\lambda 2}^{\text{scat}}$ ratios are incompatible with large ($a > 0.10 \mu\text{m}$) silicate grains. Besides, the broad near-IR peaks associated with η Carinae’s 5.5 yr variability are due to thermal emission from hot dust. With the high grain temperatures and η Car’s C-poor abundances, the grains are probably composed of corundum or similar species that condense at high temperatures, rather than silicates or graphite (Smith 2010).

For M8 and M20, we found that their $Q_{\beta}^{\text{scat}}/Q_{\alpha}^{\text{scat}}$ ratios are consistent with small ($a = 0.01 \mu\text{m}$) graphite and silicate grains and medium ($a = 0.10 \mu\text{m}$) iron grains. At the other hand, their $Q_{\gamma}^{\text{scat}}/Q_{\beta}^{\text{scat}}$ and $Q_{\delta}^{\text{scat}}/Q_{\beta}^{\text{scat}}$ ratios are consistent with relatively small ($a = 0.05 \mu\text{m}$) dirty-ice and iron grains. As with Carina, none of the M8 and M20 efficiency ratios are consistent with large $a > 0.05 \mu\text{m}$ grains, except for ice grains, which could reach $a = 0.10 \mu\text{m}$. However, comparing our average $Q_{\gamma}^{\text{scat}}/Q_{\beta}^{\text{scat}}$ and $Q_{\delta}^{\text{scat}}/Q_{\beta}^{\text{scat}}$ ratios with regular values (Table 2), suggest that we may be overestimating the steepness of these ratios in the blue, indicating probably contamination of $s_{\lambda}^{\text{scat}}$ with s_{λ}^* in our *neb* spectra. Part of this discrepancy may be due to the approximate g_{λ} w_{λ} values that we are considering (MRN77). We conclude that a more detailed treatment of these parameters is needed in order to further constrain the size and types of grains present in our nebula.

Conclusions

We found that the dust particles in the Carina region present *bluer* scattering efficiency factor ratios than those in M8 and M20. The observed scattered continua colors in Carina are consistent with small ($a = 0.01 \mu\text{m}$) graphite and iron grains and with larger ($a = 0.10 \mu\text{m}$) dirty-ice grains. The derived ratio

of scattering efficiency factors in Carina is not consistent with grains composed by silicates, unless they are very small ($a = 0.01 \mu\text{m}$). For M8 and M20, we found that their $Q_{\lambda 1}^{\text{scatt}}/Q_{\lambda 2}^{\text{scatt}}$ ratios are consistent with very small ($a = 0.01 \mu\text{m}$) graphite and silicate grains and with medium-sizes ($a = 0.05 \mu\text{m}$) iron grains. In general, our observed $Q_{\lambda 1}^{\text{scatt}}/Q_{\lambda 2}^{\text{scatt}}$ ratios are incompatible with large ($a > 0.10 \mu\text{m}$) silicate grains

Table 2. Comparison of scatter and extinction efficiency factors for Car Reg, M8 Reg and M20 Reg and for different spherical grains as function of radius ^a

	$s(\lambda_1)_0^d/s(\lambda_2)_0^d$			$g\lambda_1w\lambda_1/g\lambda_2w\lambda_2$ (MRN77)	$Q_{\lambda 1}^{\text{scatt}}/Q_{\lambda 2}^{\text{scatt}}$			
	Car Reg	M8 Reg	M20 Reg		Car Reg	M8 Reg	M20 Reg	
$\lambda 4861/\lambda 6563 \text{ H}\beta/\text{H}\alpha$	2.13	1.82	1.95	1.420	1.50	1.28	1.37	
$\lambda 4340/\lambda 4861 \text{ H}\gamma/\text{H}\beta$	1.58	1.51	1.62	1.028	1.54	1.47	1.58	
$\lambda 4102/\lambda 4861 \text{ H}\delta/\text{H}\beta$	2.34	1.90	2.04	1.053	2.22	1.80	1.94	
	$Q_{\lambda 1}/Q_{\lambda 2}$ Ice		$Q_{\lambda 1}/Q_{\lambda 2}$ Dirty-Ice		$Q_{\lambda 1}/Q_{\lambda 2}$ Iron		$Q_{\lambda 1}/Q_{\lambda 2}$ Graphite	$Q_{\lambda 1}/Q_{\lambda 2}$ Silicate
	<i>scatt</i>	<i>ext</i>	<i>scatt</i>	<i>ext</i>	<i>scatt</i>	<i>ext</i>	<i>ext</i>	<i>ext</i>
$a (\mu\text{m}) = 0.05$							<i>0.01</i>	<i>0.01</i>
$\lambda 4861/\lambda 6563 \text{ H}\beta/\text{H}\alpha$	6.00	6.00	2.50	1.23	(2.74)	1.35	1.60 (152)	1.35
$\lambda 4340/\lambda 4861 \text{ H}\gamma/\text{H}\beta$	1.50	1.50	1.60	1.18	1.55	1.15	1.24 (1.16)	1.12
$\lambda 4102/\lambda 4861 \text{ H}\delta/\text{H}\beta$	1.67	1.67	2.0	1.30	2.00	1.20	1.39 (1.24)	1.18
$a (\mu\text{m}) = 0.10$								
$\lambda 4861/\lambda 6563 \text{ H}\beta/\text{H}\alpha$	2.12	2.12	1.67	1.50	1.30	1.06	1.26	1.33
$\lambda 4340/\lambda 4861 \text{ H}\gamma/\text{H}\beta$	1.23	1.23	1.03	1.17	1.14	0.997	0.976	1.40
$\lambda 4102/\lambda 4861 \text{ H}\delta/\text{H}\beta$	1.47	1.47	1.27	1.30	1.20	1.00	0.958	1.65
$a (\mu\text{m}) = 0.50$								
$\lambda 4861/\lambda 6563 \text{ H}\beta/\text{H}\alpha$	1.13	1.13	1.00	1.02	0.987	0.954		
$\lambda 4340/\lambda 4861 \text{ H}\gamma/\text{H}\beta$	0.949	0.949	0.938	0.979	0.960	0.976		
$\lambda 4102/\lambda 4861 \text{ H}\delta/\text{H}\beta$	0.911	0.911	0.906	0.958	0.960	0.968		

^a Adapted from Spitzer (1978), for ice, dirty-ice and iron, and from Draine (1985, 2003) for graphite and silicate. We include also data for amorphous carbon adapted from Brussetti et al. (1987) and Maron (1990). πa^2 is the geometrical cross section of the grain.

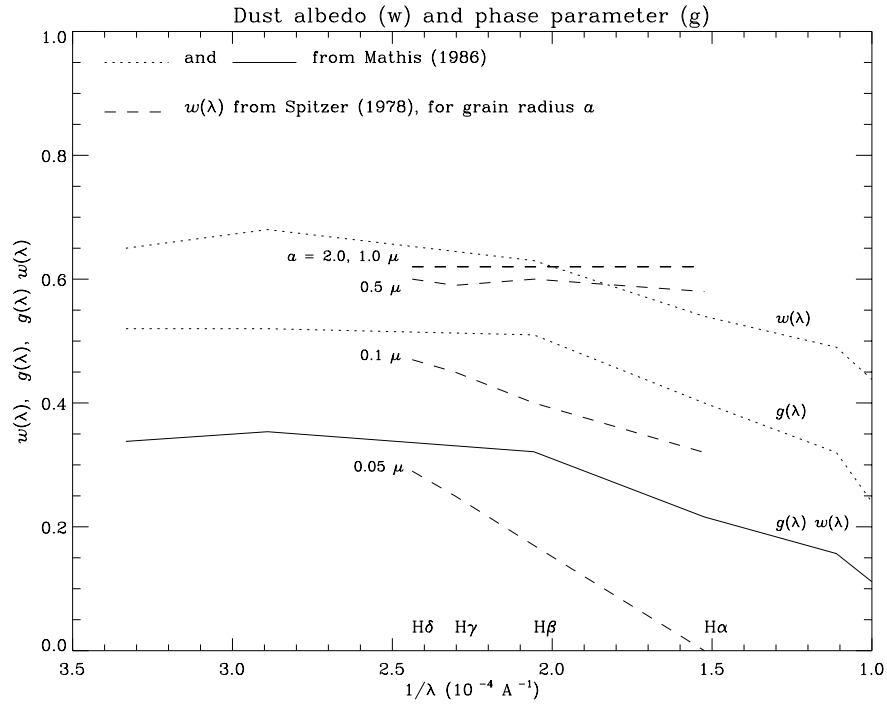


Fig. 1. Predicted albedo w_λ and phase parameter g_λ for the MNR77 mixture of uncoated graphite and silicate particles from M83 (solid and dotted lines), and w_λ for iron grains from S78 (dashed lines).

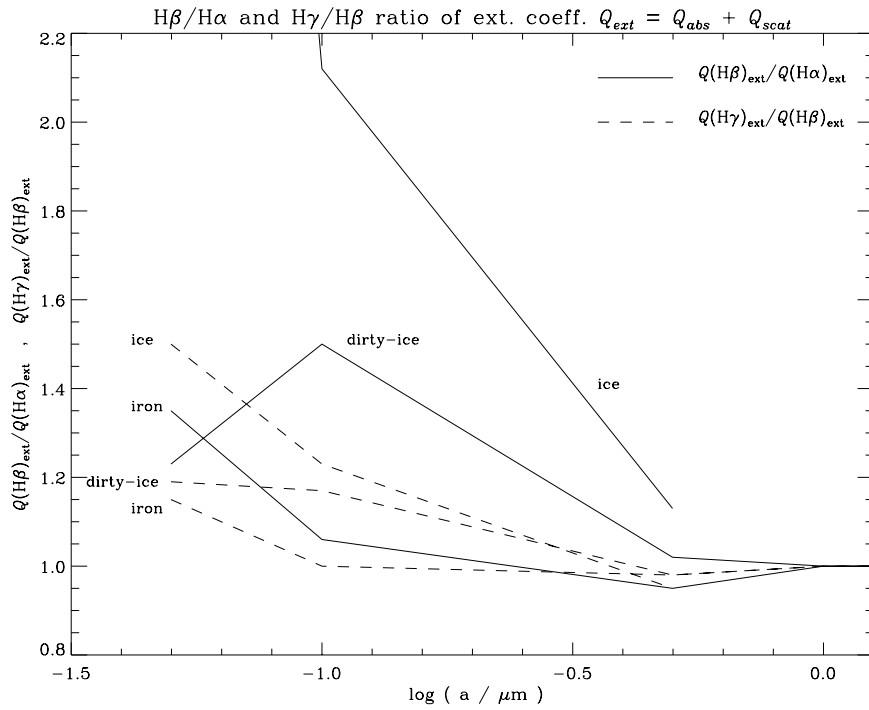


Fig. 2. Predicted $Q_\beta^{ext}/Q_\alpha^{ext}$ and $Q_\gamma^{ext}/Q_\beta^{ext}$ extinction efficiency factors ratios for ice, dirty-ice and iron particles, adapted from S78.

Appendix V. Review of models of dusty nebulae and implications for giant extragalactic HII regions

V.1 Introduction

As we saw in Chapter VI, there are several observational evidences of the presence of dust within galactic HII regions, which must be taken into account in order to elaborate a correct model of these nebulae. In this Appendix we review some models of dusty HII regions presented in the literature and compare these results with galactic and extragalactic HII regions. In Sec. V.2 we review simple dusty models of the nebula to better understand the relation between internal extinction and reddening. In Sec. V.3 we present evidence of scattered light present in the spectra of giant extragalactic HII regions (GEHRs) and HII galaxies (HIIGs) and comment on the effects that this scattered light may have on the derivation of some physical parameters. In Section V.3 we summarize our main conclusions.

V.2 Review of models of dusty nebulae: internal extinction and reddening

V.2.1 Signatures of dust within HII regions

The accurate knowledge of the total extinction affecting the UV and optical luminosities of GEHRs and HIIGs is needed in order to derive their intrinsic physical parameters such as the slope of the UV and optical continuum, initial mass function (IMF), total luminosity, total cluster stellar mass, star formation rate (SFR) and the age of the star formation burst. As mentioned in Chapter VI, the presence of dust in galactic HII regions modifies the stellar spectra seen by the gas, especially in the far UV, altering thus the ionization structure and thermal equilibrium of the nebula (eg. Simón-Díaz & Stasińska 2011).

In Sec. 6.3 of Chapter VI, we showed that there is an important fraction of scattered light present in our integrated spectra. Tables 2a and 2b of that chapter showed that the scattered continuum between H α and H δ is about 0.04 mag *bluer* than the *.neb* continuum, meaning that the scattering cross section of the dust increases at shorter wavelengths, which is in agreement with current dust models (eg. Draine, 2003). We showed also that this scattered-light component has noticeable effects on the derived Balmer reddening, producing an underestimated reddening if scattering effects are ignored.

The actual relation between the scattered light and the derived reddening is not a trivial issue. At one side, increasing the amount of internal dust increases the *radio*-derived extinction A_{β}^{rad} , and this increases the derived *Balmer*-reddening A_{β}^{Bal} . However, this increment of dust also increases the effects of the scattered light on the Balmer lines, enhancing the flux in H β as compared to the flux in H α ,

yielding thus a more neutral reddening. Witt, Thronson & Capuano (1992) found from detailed transfer calculations in the context of galaxies, that the *bluing* due to scattering is partially compensated by the increased reddening due to the increased extinction, and in fact, for some plausible geometries, these authors found that the maximum reddening occurs for intermediate optical depths, while both, very small and very large amounts of dust produce almost neutral broad-band colors.

For GEHRs, Caplan & Deharveng (1985) obtained $H\alpha$ and $H\beta$ absolute photometry with a large aperture of $5'$ for a number of HII regions in the Large Magellanic Cloud (LMC) and compared their observed F_α/F_β ratios with previous slit observations of Peimbert & Torres-Peimbert (1974) and Dufour (1975), usually placed on the brightest spots. They report that 12 out of 14 HII regions show F_α/F_β ratios equal or larger than the slit ratios. Similarly, Matthews' (1981) F_α/F_β observed ratios, obtained through $5'$ wide aperture filter photometry of a sample of 10 Galactic HII regions, are a factor of 2 larger, on average, when compared with the corresponding line ratios from slit observations of the same nebulae reported by Chopinet & Lortet-Zuckermann (1976). We interpret this as evidence of dust mixed with the gas and stars within the HII regions: for the small angular beam (slit observations), the scattering contribution is larger, suggesting a milder reddening and therefore lower F_α/F_β ratios, as compared with the wider beam aperture, where the scattering would tend to cancel out. For an isolated HII region observed at low resolution with a large enough aperture covering the whole nebula, we consider that the scattering contribution would cancel out, since for each photon scattered into the line of sight, there should be another one being scattered away from it, even if we have a quite forward-throwing phase parameter $g (\leq 1)$, as suggested by Mathis (1972). Part of this effect, however, may be due to an observational bias, since slit observations select the brightest and least attenuated parts of each nebula, sampling preferentially zones of lower reddening, with relatively low F_α/F_β ratios.

At the other hand, the fact that $A_\beta^{\text{Bal}} < A_\beta^{\text{rad}}$ for most GEHRs (eg. Melnick 1979), is usually attributed to either internal dust within the nebula or to opaque foreground dust clouds which obscure a sizable fraction of the nebula in $H\alpha$ and $H\beta$ [eg. Mathis, 1983; M83; Natta & Panagia 1984, Caplan and Deharveng, 1986; CD86, Calzetti, 2001]. M83 studied the effects of scattering by internal dust and found that modest differences in the albedo as function of wavelength w_λ , have important differences on the emergent fluxes, while the effects of the phase parameter g_λ , have a minor effect. White (1979) used Mathis, Rimpl & Nordsieck (1977; MRN77) theoretical model for the ISM of uncoated graphite and silicate particles, and found that $w_\beta \approx 0.63$ while $w_\alpha \approx 0.54$, in agreement with our results presented in Chapter VI. That is, more light is reflected at $H\beta$ than at $H\alpha$, what means that $H\alpha$ is absorbed more per optical depth of extinction than $H\beta$, although $H\beta$ is absorbed more totally because it has a larger optical depth (M83). Therefore, ignoring the albedo difference would yield an under-estimated A_β^{Bal} . The fact that $w_\beta > w_\alpha$ is expected, since a given grain of radius a appears smaller to an $H\alpha$ photon than to an $H\beta$ photon, being the grain more efficient in scattering $H\beta$ than $H\alpha$. Actually, as we show below,

the fact that $A_{\beta}^{\text{Bal}} < A_{\beta}^{\text{rad}}$, arises naturally by considering that extinction and reddening are due to internal dust (or due to a foreground slab), even in the case that scattering effects are ignored ($w_{\alpha} = w_{\beta} = 0$). Considering the scattering, increases even further the difference $A_{\beta}^{\text{Bal}} < A_{\beta}^{\text{rad}}$.

V.2.2 Internal extinction and reddening

In this section we discuss briefly the effects of internal extinction with and without scattering in dusty plasma. Let us assume that all extinction is internal to the HII region and that the dust and gas are well mixed within the emitting volume. The radiative transfer equation for the intensity $I_{\lambda}(r)$, in a plane parallel geometry, ignoring the scattering contribution to the beam, can be written as (Múnch & Persson 1971; MP71; and Melnick 1979; M79):

$$\frac{dI_{\lambda}}{dr} = \varepsilon_{\lambda} n_e^2 - n_d \kappa_{\lambda}^{\text{ext}} I_{\lambda}, \quad (1)$$

where ε_{λ} represents the gas emissivity ($\text{erg cm}^3 \text{ s}^{-1}$) in the case of continuum emission or a recombination coefficient in the case of a Balmer line, n_e is the electron number density (cm^{-3}), n_d is the number density of dust particles (cm^{-3}), and $\kappa_{\lambda}^{\text{ext}}$ is the *extinction cross section* of dust particles (cm^2), assumed to be given by $\kappa_{\lambda}^{\text{ext}} = \pi a^2 Q_{\lambda}^{\text{ext}}$, where πa^2 is the average geometrical cross section of dust grains and Q_{λ}^{ext} is a function of λ called the *extinction efficiency factor*, which takes into account the extinction properties of dust. Writing the optical depth as $d\tau_{\lambda} = n_d \kappa_{\lambda}^{\text{ext}} dr$ (increasing outwards), we can approximate the *net optical depth within the nebula* as $\tau_{\lambda} \approx n_d \kappa_{\lambda}^{\text{ext}} R_{\text{HII}}$, where R_{HII} is the radius of the emitting region. The above equation can then be written as:

$$\frac{dI_{\lambda}}{d\tau_{\lambda}} + I_{\lambda} = \frac{\varepsilon_{\lambda} n_e^2}{n_d \kappa_{\lambda}^{\text{ext}}}. \quad (2)$$

Assuming the dust to gas ratio to be independent of distance within the nebula (as found by MP71 in the Orion nebula), the emergent flux from the nebula is:

$$I_{\lambda} = \varepsilon_{\lambda} n_e^2 R_{\text{HII}} (1 - e^{-\tau_{\lambda}}) / \tau_{\lambda}, \quad (3)$$

and the relation between the observed (emergent) flux and the un-attenuated flux (for $\tau_{\lambda} = 0$), $I_{\lambda}^0 = \varepsilon_{\lambda} n_e^2 R_{\text{HII}}$, is therefore given by:

$$I_{\lambda} = I_{\lambda}^0 (1 - e^{-\tau_{\lambda}}) / \tau_{\lambda}. \quad (4)$$

This formalism can be used to estimate the net optical depth at H β due to dust embedded *within* the nebula τ_β , by means of observations of radio continuum density flux at frequency ν :

$$\frac{S_\nu}{F_\beta} = \frac{j_\nu}{j_\beta} \frac{\tau_\beta}{(1 - e^{-\tau_\beta})}. \quad (5)$$

At $\nu = 5$ GHz (6 cm), $T_e = 10^4$ K and $\text{He}^+/\text{H}^+ = 0.10$, we have $j_5/j_\beta = 3.11 \times 10^{-14} \text{ Hz}^{-1}$ (according to the expression for j_β/j_ν given by CD86). For convenience, we define the function

$$\log K_\beta = \log \left(\frac{\tau_\beta}{1 - e^{-\tau_\beta}} \right) = \log \left(\frac{S_\nu}{F_\beta} \right) - \log \left(\frac{j_\nu}{j_\beta} \right) = \frac{1}{2.5} A_\beta \quad , \quad (6)$$

We see that under this assumptions, the extinction at H β , is no longer linear with the optical depth, but instead $A_\beta^{\text{rad}} = 2.5 \log K_\beta = 2.5 \log \tau_\beta / [1 - \exp(-\tau_\beta)]$. This A_β^{rad} can be used to define an *apparent* radio optical depth at H β : $\tau(\text{H}\beta)_{\text{rad}}^{\text{app}} = 0.921 A_\beta^{\text{rad}} = 2.30 \log K_\beta$. That is,

$$\tau(\text{H}\beta)_{\text{rad}}^{\text{app}} = 2.30 \log \frac{\tau_\beta}{(1 - e^{-\tau_\beta})} \quad . \quad (7)$$

In Fig. 1 we present the relation K_β vs. τ_β , which can be used along with S_ν and F_β , to estimate the *radio-derived* net optical depth at H β within the nebula τ_β^{rad} .

At the other hand, the emergent H α /H β Balmer decrement, for pure internal extinction with no scattering, is given by:

$$\frac{F_\alpha}{F_\beta} = \frac{j_\alpha}{j_\beta} \frac{\tau_\beta (1 - e^{-\tau_\alpha})}{\tau_\alpha (1 - e^{-\tau_\beta})}. \quad (8)$$

We also define the function

$$\log K_{\alpha,\beta} = \log k \frac{(1 - e^{-\tau_\beta/k})}{(1 - e^{-\tau_\beta})} = \log \left(\frac{F_\alpha}{F_\beta} \right) - \log \left(\frac{j_\alpha}{j_\beta} \right) = \frac{1}{2.5} E_{\beta-\alpha} \quad , \quad (9)$$

where we set for convenience, $k = \tau_\beta/\tau_\alpha$. We see that the observed H α to H β color excess is no longer linear with τ_β but instead, $E_{\beta-\alpha} = 2.5 \log K_{\alpha,\beta} = 2.5 \log k [1 - \exp(-\tau_\beta/k)] / [1 - \exp(-\tau_\beta)]$. As with A_β^{rad} , this function allows us to estimate an *apparent* Balmer “extinction” $A(\text{H}\beta)_{\text{Bal}}^{\text{app}} = -2.5 \log K_{\alpha,\beta} / f(\text{H}\alpha)$, and the corresponding *apparent* Balmer optical depth at H β : $\tau(\text{H}\beta)_{\text{Bal}}^{\text{app}} = 0.921 A(\text{H}\beta)_{\text{Bal}}^{\text{app}} = 7.13 \log$

$K_{\alpha,\beta}$, where we have evaluated $f(H\alpha) = -0.323$ from Savage & Mathis (1979; SM79) extinction law. That is,

$$\tau(H\beta)_{Bal}^{app} = 7.13 \log k \frac{(1 - e^{-\tau_\beta/k})}{(1 - e^{-\tau_\beta})} . \quad (10)$$

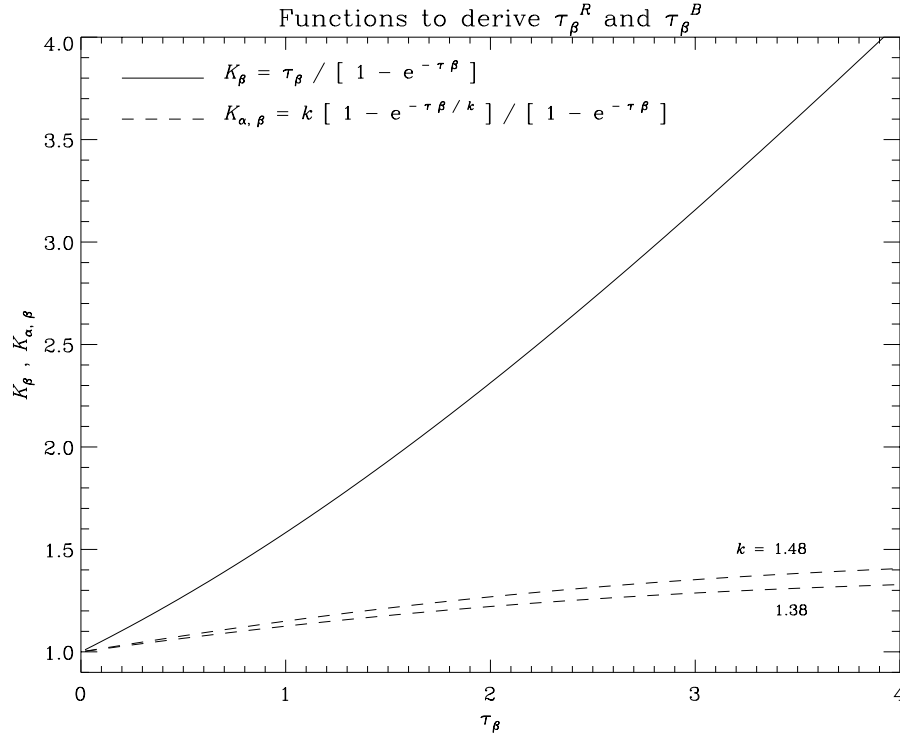


Fig. 1. Functions K_β (solid line; Eq. 6) and $K_{\alpha,\beta}$ (dashed lines; Eq. 9) vs. τ_β (the net optical depth at H β of the dust embedded in the nebula). We show $K_{\alpha,\beta}$ for 2 different values of $k = (\tau_\beta/\tau_\alpha)$ (see text for details).

We have over plotted in Fig. 1 the function $K_{\alpha,\beta}$ vs. τ_β for $k = 1.48$, with $R_V = 3.1$ from SM79, and $k = 1.38$, with $R_V = 5.0$ for Orion, from Costero & Peimbert (1970; CP70). This plot can be used along with F_α and F_β , to estimate the net *Balmer*-derived optical depth within the nebula τ_β^{Bal} .

If the scattering contribution is included in the radiative transfer equation, we must add a right-hand term to Eq. (1) of the form (Bruzual et al. 1988; Calzetti, Kinney & Storchi-Bergmann, 1994; CKS94): $n_d \kappa_d^{ext}(\lambda) w_\lambda \int I_\lambda \Phi(\cos\Theta) d\Omega / 4\pi$, where $\Phi(\cos\Theta)$ is the *phase function* of the dust grains, $d\Omega = \cos\theta d\theta d\varphi$ is an element of solid angle as seen from a dust grain, and Θ is the angle between the incident and scattered photon. The albedo w_λ , represents the probability of a photon to be scattered, and the phase function $\Phi(\cos\Theta)$, is the probability of a photon to be scattered in a certain direction. Natta & Panagia (1984) considered a uniform scattering slab for two extreme cases: *i*) isotropic scattering and *ii*) forward-only scattering. In the isotropic case, they found an approximate solution of the form, $I_\lambda = I_\lambda^0 \exp(-\tau_\lambda^{scat})$, with a diminished optical depth, $\tau_\lambda^{scat} \approx (1 - w_\lambda)^{1/2} \tau_\lambda$, being τ_λ the optical depth for the

zero scattering configuration. In the forward-only case, CKS94 found that, $\tau_\lambda^{\text{scat}} \approx (1 - w_\lambda) \tau_\lambda$, and the solution for the internal dust model is still given by Eq. (4), with τ_λ replaced by $\tau_\lambda^{\text{scat}}$.

We adopted the albedo w_α and w_β values from M83 and computed the functions K_β^{scat} and $K_{\alpha,\beta}^{\text{scat}}$ for the internal dust model including scattering for these two extreme regimes: isotropic and forward-only scattering. Our results are shown in Fig. 2a in the plane $\tau(\text{H}\beta)_{\text{rad}}^{\text{app}}$ vs. $\tau(\text{H}\beta)_{\text{Bal}}^{\text{app}}$. Each black dot corresponds to increasing values of the net *internal optical depth* τ_β , as indicated for the track with no scattering. We show our solutions for *a*) zero scattering ($w_\alpha = w_\beta = 0$); *b*) isotropic scattering (with $w_\alpha = 0.54$, $w_\beta = 0.63$, $g_\alpha = g_\beta = 0$), and *c*) forward-only scattering (using CKS94 approximation). For comparison, we show the curves for anisotropic scattering obtained by M83 (using numerical simulations) and by CKS94 (using an analytical fit to the phase function).

The configuration of interstellar extinction, uniform over the face of the nebula, with no scattering, yields $\tau(\text{H}\beta)_{\text{rad}}^{\text{app}} = \tau(\text{H}\beta)_{\text{Bal}}^{\text{app}}$. A uniform scattering slab or a clumpy slab with constant optical depth per clump, in front of the emitting region, would also yield straight lines but with a slope > 1 [M83, Natta & Panagia (1984), CD86], while clumps with variable optical depth will produce curved tracks very similar to those of internal extinction, what makes it very difficult to disentangle the different possible scenarios (uniform or clumpy front slab vs. internal dust) from these two observables only (M83 and CD86).

The tracks of Fig. 2a can also be plotted in terms of the pure observational quantities A_β^{rad} and $E_{\beta-\alpha}$, without the need of assuming exponential extinction and regardless of any assumed extinction law (i.e. $A_\beta^{\text{rad}} = 2.5 \log K_\beta$ and $E_{\beta-\alpha} = 2.5 \log K_{\alpha,\beta}$). In Fig. 2b we compare the positions of Galactic and extragalactic HII regions in the Magellanic Clouds in the A_β^{rad} vs. $E_{\beta-\alpha}$ plane, using Eqs. (6) and (9). For the Galactic nebulae, we include 11 objects from Gebel (1968), 8 from Matthews (1981), 1 from Cox, Deharveng & Caplan (1987) and our 7 nebulae. For the extragalactic nebulae we include 23 SMC objects from Caplan et al. (1996) and 49 LMC objects from Ye (1998). We have also over plotted the two limiting tracks from Fig. 2a. The error bars for the Galactic nebulae are quite large due to several uncertainties, including: *a*) mismatch of the optical and radio centers, *b*) differences in the area covered by the optical and radio observations, and *c*) errors in the adopted electron temperature. In this sense, the SMC and LMC data are of better confidence. For Car Reg we used the radio flux density given in Chapter IV and the F_β and F_α/F_β ratio from Table 1a of Chapter III. For M8 Reg and M20 Reg we used the radio flux density at 6 cm given by Reifenstein et al. (1970) and Wilson et al. (1970), and the F_β and F_α/F_β ratios from Table 1b of Chapter III. For the RCW nebulae we used the radio and optical fluxes given in Appendix I and Chapter II. We considered in each case the errors on T_e inferred from the optical lines and radio continuum to estimate the error bars of A_β^{rad} . For the error bars in $E_{\beta-\alpha}$, we

assigned a 5% uncertainty in the $H\alpha$ and $H\beta$ fluxes of Car Reg, M8 Reg and M20 Reg, and a 10% uncertainty in the fluxes of RCW6, RCW60, RCW107 and RCW110.

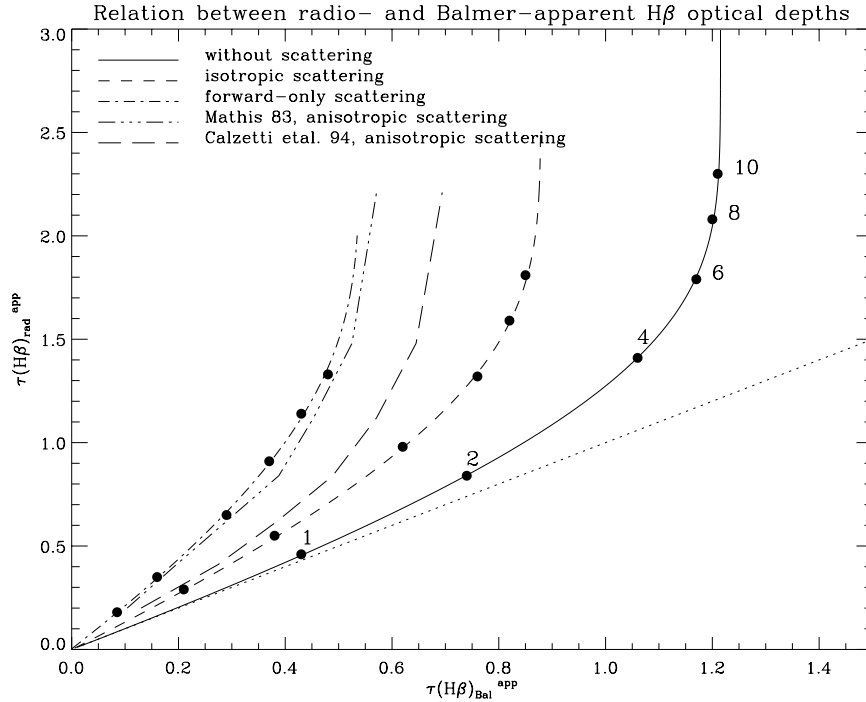


Fig. 2a. Relation between *radio*-derived apparent optical depth (Eq. 7) and *Balmer*-derived apparent optical depth (Eq. 10) at $H\beta$ for a dusty nebula with different scattering conditions. Increasing values of the net *internal optical depth* at $H\beta$ τ_β , are indicated along selected tracks (see text for details).

To compute F_β in Eq. (6) for each nebula, we consider the ratio of our scanned length to that of the slit width ($\Omega_{\text{scan}}/\Omega_{\text{slit}} = 90$) as an approximation to the total $H\beta$ flux, corresponding to the larger radio aperture. Note however, that even these area-corrected $H\beta$ fluxes are lower limits to the total $H\beta$ fluxes, especially for Car Reg, M8 Reg and M20 Reg. This under-estimation may yield A_β^{rad} plotted values about 0.2 – 0.4 mag larger than the real ones.

Two remarks can be drawn from this plot: *a)* for GEHRs, $E_{\beta-\alpha} < 0.5$, while the Galactic sample have $E_{\beta-\alpha}$ values in the 0.4 – 1.7 range, and *b)* for GEHRs, A_β^{rad} is usually larger than $3.1 \times E_{\beta-\alpha}$, that is $\tau(H\beta)_{\text{rad}}^{\text{app}} > \tau(H\beta)_{\text{Bal}}^{\text{app}}$, while several Galactic HII regions present the opposite trend! As with Fig. 2a, uniform interstellar extinction with the standard extinction law follows the dotted track, $A_\beta^{\text{rad}} = (3.1 \times E_{\beta-\alpha})$. From the high fractions of scattered continuum suggested by our observations, we had expected our nebulae to deviate much more from the “interstellar” line, however some of them follow this track, what tell us about the uncertainties inherent in these calculations. Note however that Car Reg, M8 Reg, RCW107 and RCW110 are well above the interstellar line. Cox, Deharveng & Caplan (1987) also noted this dichotomy between Galactic and extragalactic HII regions and proposed an alternative solution arguing that most Galactic HII regions are usually in front of their associated molecular clouds

and that large quantities of dust just behind the ionized gas could enhance the effects of backscattering. In Table 1 we summarize the average differences $\langle A_{\beta}^{\text{rad}} - 3.1 \times E_{\beta-\alpha} \rangle$ and the average parameter $\langle R_{\text{H}} \rangle = \langle A_{\beta}^{\text{rad}} / E_{\beta-\alpha} \rangle$ for different groups of nebulae.

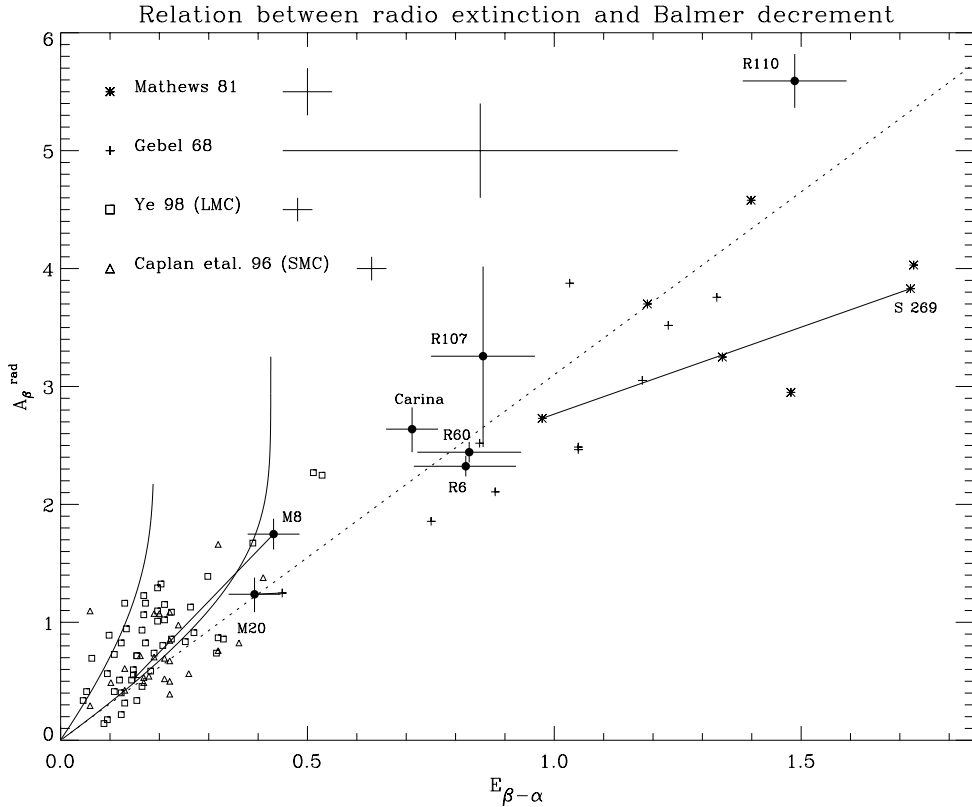


Fig. 2b. Relation between radio-derived extinction and Balmer color excess for Galactic and extragalactic H II regions (see text for details).

Table 1. Average extinction and reddening for several group of nebulae. ^a

	Gebel 68 Gal	Mathews 81 Gal	This work Gal	$\langle \text{Galactic} \rangle$	Caplan et al $\langle \text{SMC} \rangle$	Ye (98) $\langle \text{LMC} \rangle$	$\langle \text{SMC} + \text{LMC} \rangle$
(1)	(2)	(3)	(4)	(5)	(6)	(7)	(8)
n	11	9	7	27	23	49	72
$\langle A_{\beta}^{\text{rad}} - 3.1 \times E_{\beta-\alpha} \rangle$	-0.31 ± 0.43	-1.21 ± 1.15	$+0.30 \pm 0.43$	-0.45 ± 0.67	$+0.12 \pm 0.30$	$+0.27 \pm 0.28$	$+0.22 \pm 0.29$
$\langle A_{\beta}^{\text{rad}} / E_{\beta-\alpha} \rangle$	2.81 ± 0.47	2.45 ± 0.51	3.47 ± 0.48	2.86 ± 0.49	4.22 ± 3.16	4.82 ± 2.05	4.63 ± 2.40

^a n is the number of regions in each group. A_{β}^{rad} and $E_{\beta-\alpha}$ are observational quantities defined in Eqs. (6) and (9). Columns (5) give the average for all the Galactic nebulae, and column (8) give the average for the SMC and LMC nebulae.

Overall, the Galactic nebulae present different extinction and reddening properties than the nebulae in the Magellanic Clouds. For the galactic nebula, we obtain $\langle R_{\text{H}} \rangle = 2.86 \pm 0.49$, in fair agreement with $R_{\text{H}} = 3.12$ from CCM89 or $R_{\text{H}} = 2.90$ from Fitzpatrick (1999) extinction laws [note that

$R_H = -1/f(H\alpha)$]. For the LMC we found a higher value, with $\langle R_H \rangle = 4.82 \pm 2.05$, while Howard (1983) extinction law for the LMC yields $R_H = 3.42$. For the SMC, with a shallower extinction law than the LMC, we found some discrepancy. From Caplan et al. (1996) data we obtain $\langle R_H \rangle = 4.22 \pm 3.16$, while we derive $R_H = 2.70$ from Gordon et al. (2003) extinction law for the SMC. However, note the large variations found in R_H for the SMC nebulae.

As commented in Fig. 2a above, in the case of extinction due to internal dust or due to a close-by foreground scattering slab, the behavior of the A_β^{rad} vs. $E_{\beta-\alpha}$ track is very sensitive to the choice of grain albedo and phase parameters, w_λ and g_λ : the greater the difference $(w_\beta - w_\alpha) > 0$, the more the track is shifted to the left of the $w_\beta = w_\alpha$ curve. To explain that $A_\beta^{\text{rad}} < (3.1 \times E_{\beta-\alpha})$ would require a scattering slab with $w_\alpha > w_\beta$, what seems unlikely. Our results presented in Chapter VI, are consistent with the theoretical dust model of MRN77, where $w_\beta > w_\alpha$ and $g_\beta > g_\alpha$; however w_λ and g_λ affect the Balmer decrement in opposite directions (M83). The phase parameter g_λ for the diffuse ISM's grains may be different from that of grains located at the boundary between the molecular cloud and the ionized gas. Witt (1977) showed that dust behind an illuminating source enhances the role of the phase parameter, and this mechanism may account for the unexpected behavior of some Galactic HII regions in the A_β^{rad} vs. $E_{\beta-\alpha}$ plane. This problem deserves further investigation, in particular through coordinated accurate radio and optical observations of evolved Galactic HII regions.

V.3 Scattered light in GEHRs and HIIGs

In this section we present evidence of dust in GEHRs and HIIGs and discuss some of its implications. In the context of emission line galaxies (or HIIGs), CKS94 combined UV and optical data to derive an “effective” extinction law from a “template starburst” parameterized as function of $E_{\beta-\alpha}$, considering the combined effects of clumpiness and anisotropic scattering. They found that this effective extinction law is substantially *grayer* than that for the Milky Way and the LMC, reproducing well the diminishing or absence of the 2175 Å bump in most of these galaxies. They also found that the difference in optical depth between H α and H β emission lines is a factor of 2 larger than the difference in the optical depth between the continua underlying these two lines. Their interpretation is that the hot ionizing stars are associated with dustier regions as compared with the cold stellar population. Latter, Calzetti, Kinney, & Storchi-Bergmann (1996) stressed the importance of the geometrical distribution of the dust associated with the massive stars in HII galaxies, and favored the presence of foreground dust, either homogeneous or clumpy, to explain the observed reddening.

In Fig. 3 we present the observed continuum at 4861 Å vs. the H β flux for a compilation of GEHRs and HIIGs. We include: *i*) 36 HIIGs from Campbell, Terlevich & Melnick (1986); *ii*) 15 HIIGs in the Bootes void from Peimbert & Torres-Peimbert (1992); *iii*) 4 Dwarf Irregular Galaxies from

Skillman, Terlevich & Melnick (1990); *iv*) 346 HIIGs from Terlevich et al. (1991); *v*) 17 GEHRs in M33, M101, M51 and NGC 4214 from Searle (1971); and *vi*) 29 GEHRs in the SMC from Copetti & Dottori (1989). For comparison, we also include *vii*) 27 Galactic HII regions from Copetti (2000), and *viii*) our 7 galactic HII regions. The interpretation of this plot is more complicated since there are objects of different nature, observed with different slits/apertures and uncorrected for reddening. As expected, the Galactic nebulae occupy the bright end of the plot, the GEHRs present middle range fluxes and the HIIGs populate the faint end. For the extragalactic objects, the vertical shift above the atomic continua straight lines represent the contribution to the $H\beta$ continuum from old (and young) stellar populations embedded in the observed knots, as well as the scattered light contribution in the case of spatially resolved observations of nearby GEHRs.

An important problem in extragalactic studies is the determination of the relative contributions to the observed continuum from the embedded stellar populations and the scattered continuum. The group of Dottori (1981), Dottori & Bica (1981), Copetti, Pastoriza & Dottori (1985, 1986) and Cerviño & Mas-Hesse (1994, and references therein), have proposed to use the equivalent width at $H\beta$ in emission W_β , as an age indicator in GEHRs and HIIGs. Other possible age-indicators are the so-called “WR-bump” and effective temperature T_{eff} -sensitive UV line ratios. At one hand, F_β is proportional to the UV radiation field, which depends on the number of massive stars present in the burst, and at the other hand, i_{4861} is dominated by intermediate mass stars. Since massive stars evolve much faster than intermediate mass stars, it turns out that W_β is a strong decreasing function of time. During the first 5 Myr, W_β evolves from an initial theoretical value of around 400 Å to much lower values, below ~ 30 Å, depending on the metallicity Z , the adopted IMF and SFR regime of the starburst (Cerviño & Mas-Hesse 1994).

The observed equivalent widths W_β^{obs} , are however affected by several factors which may introduce serious errors when comparing with predictions from synthesis model equivalent widths W_β^{syn} , and may explain in part the discrepancies in W_β^{obs} often found for a given object as reported by different authors. These factors include: *i*) if the emitting region is density-bounded, instead of radiation-bounded, then W_β^{obs} gives only an upper limit to the age; *ii*) W_β^{obs} has to be measured in such a way as to include all the line-emitting and continuum-emitting regions simultaneously, avoiding contamination from background or foreground stars contributing to the continuum, but not to the line emission; *iii*) the presence of an old stellar population will increase the optical continuum, and therefore decrease W_β^{obs} , yielding only an upper limit to the real age; *iv*) for extended (spatially resolved) objects, there could be differential extinction between the continuum and line emission regions if the dust is not homogeneously distributed over the integrated area as in NGC 4214 (Maíz-Apellániz et al. 1998) and I Zw 18 (Vílchez & Iglesias-Páramo 1998). In this later case, W_β^{obs} will depend on the aperture’s diameter or slit’s width employed, as long as it does not encompass the whole

emitting region; v) if the diaphragm or slit does not cover the whole nebula, there could be an additional contribution from dust scattered starlight from stars close to the observed position but *outside* the aperture; vi) stars with SpT in the range F2 to O6 present Balmer lines in absorption, being this absorption stronger at A0, so that W_{β}^{obs} has to be corrected for stellar underlying absorption; vii) although less important, the atomic nebular continuum contribution ($\sim 0.1\% F_{\beta} \text{ \AA}^{-1}$) should also be considered, specially when comparing model predictions with evolved HII regions that have relatively small W_{β}^{obs} ; and finally, viii) the formal error in measuring W_{β}^{obs} has also to be taken into account, which could be as high as 20 – 30% in the case of faint objects with a weak continuum.

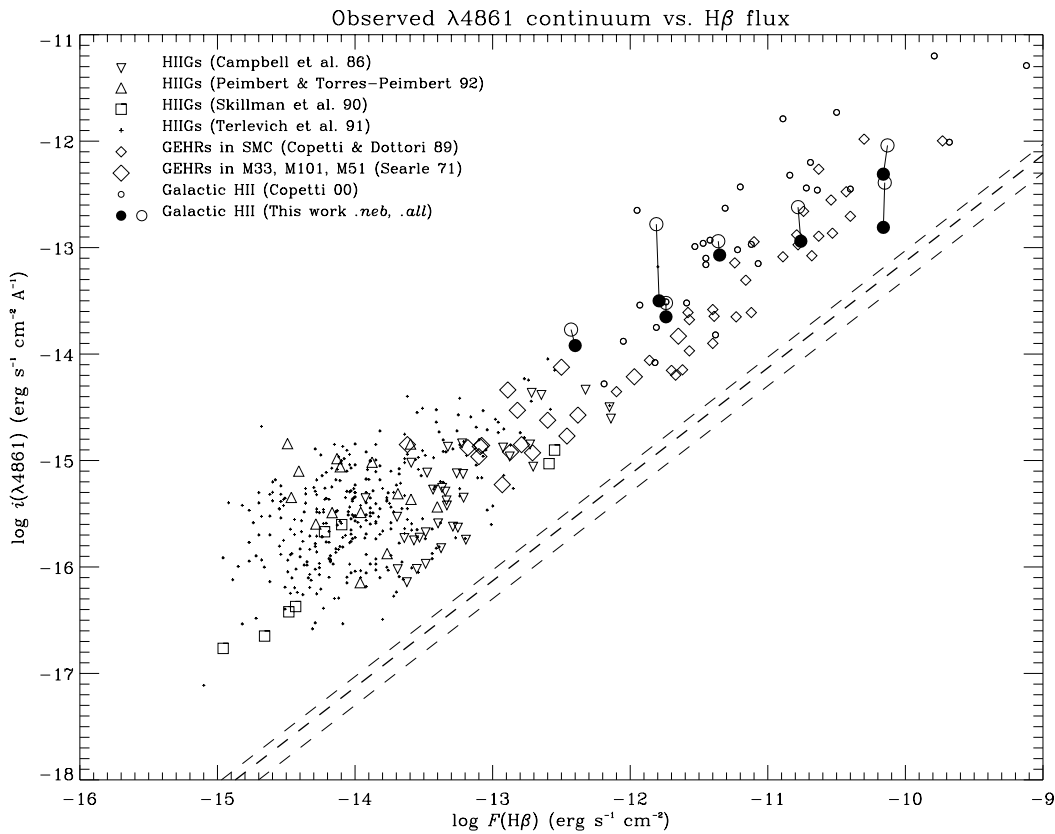


Fig. 3. Observed $\lambda 4861 \text{ \AA}$ continuum vs. $H\beta$ flux for several HIIGs, GEHRs and Galactic HII regions as indicated. Straight lines give the atomic continuum at 6, 10 and 14 kK (see Fig. 1a of Chapter VI).

Dottori's group method to estimate the edge of the stellar burst is useful for HII regions younger than $\sim 8 - 9$ Myr old (or $5 - 7$ Myr according to Cerviño & Mas-Hesse, 1994), because for regions at these ages or older, W_{β}^{obs} becomes very small ($\leq 10 \text{ \AA}$) and comparable to common measurements' errors. Dottori (1981) used population synthesis methods and an underlying stellar absorption contribution $W_{\beta}^{* \text{ abs}} \approx 1 - 2 \text{ \AA}$, much lower than the observed $W_{\beta}^{\text{obs}} \approx 30 - 270 \text{ \AA}$ measured in GEHRs of the Magellanic Clouds (Dottori and Bica 1981).

Maíz-Apellániz et al. (1998; MA98) built evolutionary synthesis models of the nearby galaxy NGC 4214. They corrected W_{β}^{obs} both for the differential reddening observed over the galaxy and the

underlying old stellar population. Comparing the $(H\alpha/H\beta)$ color of the old and young stellar populations, they found that the young stars contribute from 25 – 70% of the total continuum, depending on the radii of the synthesized aperture employed. Taking off the old stellar continua, the corrected W_{β}^{obs} increase from 60 to 150 Å, reducing the age of a nearly instantaneous burst from ~ 4.4 to 3.2 Myr. MA98 also found indications of a non-uniform extinction distribution, accompanied with a decoupling between the spatial distribution of the line emission zones with respect to the continuum emission zones, with shifts up to $2''$ (~ 40 pc) between the brightest $H\alpha$ and $H\alpha$ -continuum maxima. Such spatial decoupling has also been observed in the dwarf HIIG I Zw 18 by Vilchez & Iglesias-Páramo 1998, where the $H\alpha$ emission distribution is much more extended than that of the optical continua. The usual interpretation of this spatial decoupling is that these objects have experienced a star formation episode in the recent past such that the surrounding ISM has been disrupted by the action of massive stars through photo-ionization, winds and SN explosions.

As with the Orion Extended Nebula observations reported by O’Dell & Harris (2010), or the M43 observations presented by Simón-Díaz et al (2012), MA98 found that some regions within NGC 4214 show F_{α}/F_{β} observed ratios clearly *below* the minimum expected value of 2.86, suggesting *bluing* scattering effects on the Balmer lines. These effects are stronger in smaller aperture observations of non-resolved objects. Similarly, Hidalgo-Gómez et al. (2012) report 5 spiral galaxies with F_{α}/F_{β} observed Balmer decrements *smaller* than the theoretical ratio, and they attribute this effect to scattered light within the observed regions.

Guseva et al. (2009) present observations of 38 GEHRs in 28 low-metallicity emission line galaxies observed with the ESO 3.6-m telescope. They report that 27 objects (71%) of the sample present reddening constants $c(H\beta) \leq 0$, which is a strong indicator of scattering effects in the Balmer lines. As suggested below (see. Fig. 4), these low $c(H\beta)$ values may also be affected by relatively high values of the underlying stellar absorption equivalent width W_{abs}^* . However, from these 27 objects, 9 present $W_{\text{abs}}^* = 0$, what *cannot* explain the $c(H\beta) \leq 0$ derived values. That is, 24% of the GEHRs in the Guseva (2009) sample are definitively affected by scattering effects.

In a later paper, Guseva et al. (2011) present observations of 79 GEHRs and GHIs in a sample of 31 low-metallicity emission line galaxies. As in Guseva et al. (2009), they estimated simultaneously $c(H\beta)$ and W_{abs}^* so to best fit the observed Balmer line decrement, using the formalism outlined in Chapter III. We present their results in Fig. 4, which shows a mild correlation, in the sense that the HII regions with larger W_{abs}^* tend to present smaller values of $c(H\beta)$, indicating that the assigned value of $c(H\beta)$ is still affected by W_{abs}^* ! From their data set, we found that 17 objects (that is 22%) show $c(H\beta) < 0.10$, which we consider indicative of scattering effects. We performed a visual examination of their images, and found that 76% of the objects with $c(H\beta) < 0.10$ present *extended* morphologies, giving

support to the idea that scattering effects are increasingly important in extended (resolved) observations. We include in Fig. 4 also data for 69 GEHRs in 5 nearby spiral galaxies observed by Bresolin et al. (2005), which yields a steeper relation between $c(\text{H}\beta)$ and W_{abs}^* . In this sample, only 12% of the objects present $c(\text{H}\beta) < 0.10$, and all of them are non-resolved objects. The uncertainty in W_{β} for a given object is about 20% and in W_{abs}^* can easily reach up to 70%.

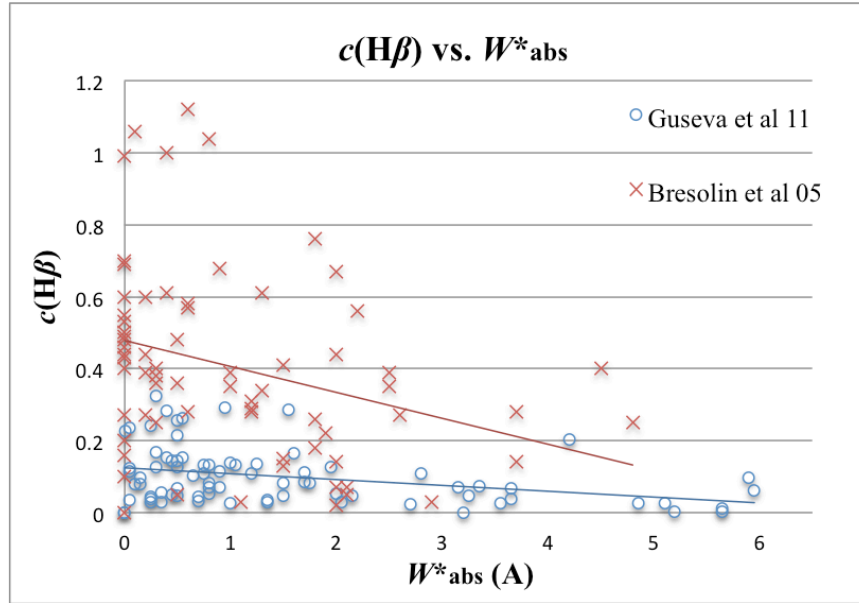


Fig. 4. Relation between the derived $c(\text{H}\beta)$ vs. the underlying stellar absorption equivalent width W_{abs}^* (in Å) from a sample of 79 GEHRs from Guseva et al. (2011) and 69 GEHRs from Bresolin et al. (2005). A linear fit to the data is shown in each case.

We stress out that in works such as Bresolin et al. (2009) or Pilyugin, Vílchez & Thuan (2010), although they estimate the contribution due to underlying stellar absorption in the observed spectra, they *do not* take into account the effects of scattered light in the derivation of the reddening, nor in the subsequent analyses of the plasma diagnostics. The justification may be that most of their observations are *not* spatially resolved. In the work of Sánchez et al. (2012), although they estimate the physical conditions of thousands of GEHRs in nearby spiral galaxies using sophisticated Integral Field Spectroscopy (IFS) techniques, along with up-to-date population synthesis to decouple the underlying continuum from the emission lines, they *do not* consider the effects of scattering, even though their high spatial resolution allow them to resolve most of their targets. However, the fact that these authors are able to obtain very good fits to the observed continuum spectra using their population synthesis, seems to indicate that scattering effects are not very important after all in many cases.

Given the results presented in this work, we consider that the line- and continuum-spatial decoupling observed in nearby GEHRs and HIIGs must include an accurate estimation of the scattering continuum contribution, which can reach values as high as 20 – 50% of the total observed continuum.

This scattered continuum contribution is increased in small-aperture observations of spatially resolved objects and it should be taken into account in order to use the *corrected–young continuum* emission equivalent width at $H\beta$ W_β , as a starburst age-indicator. This line and continuum scattering contribution must be considered to derive accurate extinction and reddening estimations, along with their derived physical conditions, abundances and physical parameters of GEHRs or emission line galaxies.

V.4 Conclusions

In this Appendix we present evidence indicating that scattering effects are more pronounced in narrow slit observations of Galactic HII regions that do not cover the whole emitting nebulae, as compared to wide-aperture observations of the same nebula encompassing most of the unresolved HII region.

Galactic HII regions (including nebulae) appear to have larger color excess $E_{\beta-\alpha}$ than HII regions in the Large and Small Magellanic Clouds. Radio and optical observations indicate different extinction and reddening properties of the dust in this two groups of nebula, with $\langle A_\beta/E_{\alpha-\beta} \rangle = 2.9 \pm 0.5$ for Galactic nebulae, and $\langle A_\beta/E_{\alpha-\beta} \rangle = 4.6 \pm 2.4$ for the MC nebulae. However, note the large assigned errors

Given the presented evidence of scattered light in the spectra of resolved GEHRs and HIIGs, we conclude that the use of their emission equivalent widths at $H\beta$ W_β as age-indicators, must be corrected not only for underlying stellar absorption (or emission!) as most researches do, but also for the *bluing* of the observed spectra which will alter the derived reddening and extinction, affecting thus to the derivation of physical conditions and parameters for these objects. This is a hard task however that has to be done individually for each object since the accurate evaluation of the scattering effects is hampered by uncertainties in the amount of foreground and internal extinction, as well as the geometric distribution of the gas, dust and the stellar populations within the emitting volume.

Bibliography

- Abt, H.A. 1983, Lowell Observatory Bol., 167, 118
- Asplund, M., Grevesse, N., Sauval, A.J. & Scott, P. 2009, ARA&A, 47, 481
- Avedisova, V.S. & Palouš, J. 1989, BAICze, 40, 42
- Baldwin, J.A., Ferland, G.J., Martin, P.G., Corbin, M., Cota, S., Peterson, B.M. & Slettebak, A. 1991, ApJ, 374, 580
- Baldwin, J.A. & Stone, R.P.S. 1984, MNRAS, 206, 241
- Beard, M. & Kerr, F.J. 1966, Aust. J. Phys., 19, 875
- Blaauw, A. 1963, *Basic Astronomical Data*, Ed. K. Aa. Strand (Chicago University Press)
- Brand, J. & Blitz, L. 1993, AA, 275, 67
- Brand, J., Blitz, L. & Wouterloot, J.G.A. 1986, AAS, 65, 537
- Bresolin, F., Schaerer, D., González-Delgado, R.M. & Stasińska, G. 2005, AA, 441, 981
- Bresolin, F., Gieren, W., Kudritzki, R., Pietrzynski, G., Urbaneja, M.A., Carraro, G. 2009, ApJ, 700, 309
- Brown, R.L. & Mathews, W.G. 1970, ApJ, 160, 939
- Brussoletti, E. et al. 1987, AAS, 70, 257
- Bruzual, A., Magris, G.C. & Calvet, N. 1988, ApJ, 333, 673
- Calzetti, D. 1997, AJ, 113, 162
- Calzetti, D. 2001, PASP, 113, 1449
- Calzetti, D., Kinney, A.L. & Storchi-Bergmann, T. 1994, ApJ, 429, 582
- Calzetti, D., Kinney, A.L. & Storchi-Bergmann, T. 1996, ApJ, 458, 132
- Campbell, A., Terlevich, R. & Melnick, J. 1986, MNRAS, 223, 811
- Cardelli, J.A., Clayton, G.C. & Mathis, J.S. 1989, ApJ, 345, 245
- Caplan, J. & Deharveng, L. 1985, AAS, 62, 63
- Caplan, J. & Deharveng, L. 1986, AA, 155, 297
- Caplan, J., Ye, T., Deharveng, L., Turtle, A.J. & Kennicutt, R.C. 1996, AA, 307, 403
- Caswell, J.L. & Haynes, R.F. 1987, AA, 171, 261
- Cerviño, M. & Mas-Hesse, J.M. 1994, AA, 284, 789
- Chopinet, M. & Lortet-Zuckermann, M.C. 1976, AAS, 25, 179
- Conti, P.S. 1975, in *H II regions and related topics*. Notes in Physics, Vol. 42. Eds. T. L. Wilson and D. Downes (Springer-Verlag: Berlin), p. 207
- Conti, P.S., 1991, ApJ, 377, 115
- Conti, P.S., 2000, PASP, 112, 1413
- Conti, P.S. & Walborn, N.R. 1976, ApJ, 207, 502
- Copetti, M.V.F. 2000, AAS, 147, 93

- Copetti, M.V.F. & Dottori, H.A. 1989, AAS, 77, 327
- Copetti, M.V.F., Pastoriza, M.G. & Dottori, H.A. 1985, AA, 152, 427
- Copetti, M.V.F., Pastoriza, M.G. & Dottori, H.A. 1986, AA, 156, 111
- Costero, R. & Peimbert, M. 1970, Boll. Obs. Tonan. Tac., 5, 229
- Cox, A.N. 1999 (Ed.) *Allen's Astrophysical Quantities*, 4th edition, Springer-Verlag, New York
- Cox, A.N. (ed.) 2000, *Allen's Astrophysical Quantities*, AIP Press
- Cox, O., Deharveng, L. & Caplan, J. 1987, AA, 171, 277
- Crowther, P.A. 1997, in *Fundamental Stellar Parameters: The interaction between Observation and Theory*, IAU Symp. 189, p. 137
- Crowther, P.A. & Dessart, L. 1998, MNRAS 296, 622
- Cruz-González, C., Recillas-Cruz, E., Costero, R., Peimbert, M. & Torres-Peimbert, S. 1974, RMexAA, 1, 211
- Cudworth K.M., Martin S.C., DeGioia-Eastwood K., 1993, AJ, 105, 1822
- Damineli, A., Stahl, O., Kaufer, A., Wolf, B., Quast, G. & Lopes, D.F. 1998, AAS, 133, 299
- Davidson, K. 1971, MNRAS, 154, 415
- Davidson, K., Dufour, R.J., Walborn, N.R. & Gull, T.R. 1986, ApJ, 305, 867
- Davidson, K., Ebbets, D., Johansson, S., Morse, J.A., Hamann, F.W., Balick, B., Humphreys, R.M., Weigelt, G. & Frank, A. 1997, AJ, 113, 335
- Deharveng, L., Peña, M., Caplan, J. & Costero, R. 2000, MNRAS, 311, 329
- Delgado-Inglada, G., Morisset, C. & Stasińska, G. 2014, MNRAS, 440, 536
- Dennefeld, M. & Stasińska, G. 1983, AA, 118, 234
- Dottori, H.A. 1981, Ap. Sp. Sci. 80, 267
- Dottori, H.A. & Bica, E.L.D. 1981, AA, 102, 245
- Draine, B.L. 1985, ApJS, 57, 587
- Draine, B.T. 2003, ARAA, 41, 241
- Dufour, R.J. 1975, ApJ, 195, 315
- Dufour, R.J., Glover, T.W., Hester, J.J., Currie, D.G., van Orsow, D. & Walter, D.K. 1997, in *Luminous Blue Variables: Massive Stars in Transition*, ASPCS, 120, 255
- Esteban, C., Peimbert, M., Torres-Peimbert, S. & Escalante, V. 1998, MNRAS, 295, 401
- Esteban, C., Peimbert, M., Torres-Peimbert, S., García-Rojas, J. & Rodríguez, M. 1999, ApJS, 120, 113
- Esteban, C., Peimbert, M., García-Rojas, J., Ruiz, M. T., Peimbert, A. & Rodríguez, M. 2004, MNRAS, 355, 229
- Faulkner, D.J. 1963, PASP, 75, 269
- Faulkner & Aller 1965, MNRAS, 130, 393
- Feast, M.W., Stoy, R.H., Thackeray, A.D. & Wesselink, A.J. 1961, MNRAS, 122, 240

Feinstein, A., Marraco, H.G. & Muzzio, J.C. 1973, AAS, 12, 331

Fich, M. & Silkey, M. 1991, ApJ, 366, 107

Fich, M., Treffers, R.R. & Dahl, G.P. 1990, AJ, 99, 622

Fitzpatrick, E.L. 1999, PASP, 111, 63

Forte, J.C. 1978, AJ, 83, 1199

Gagné, M., Fehon, G., Savoy, R.S., et al. 2011, ApJS, 194; 5

García-Rojas, J., Esteban, C., Peimbert, A., Peimbert, M., Rodríguez, M. & Ruiz, M. T. 2005, MNRAS, 362, 301

García-Rojas, J., Esteban, C., Peimbert, M., Costado, M.T., Rodríguez, M., Peimbert, A. & Ruiz, M.T. 2006, MNRAS, 368, 253

García-Rojas, J. & Esteban, C. 2007, ApJ, 670, 457

García-Rojas, J., Esteban, C., Peimbert, A., Rodríguez, M., Peimbert, M. & Ruiz, M.T. 2007, RMexAA, 43, 3

Gardner, F.F., Milne, D.K., Mezger, P.G. & Wilson, T.L. 1970, AA, 7, 349

Gardner, F.F. & Morimoto, M. 1968, Aust. J. Phys., 21, 881

Garmany, C.D., Conti, P.S. & Chiosi, C. 1982, ApJ, 263, 777

Garnett, D.R. 1992, AJ, 103, 1330

Gebel, W.L. 1968, ApJ, 153, 743

Georgelin, Y.M. 1975, PhD. Thesis, Univ. de Provence

Georgelin, Y.P. & Georgelin, Y.M. 1970a, AA, 6, 349

Georgelin, Y.P. & Georgelin, Y.M. 1970b, AAS, 3, 1

Georgelin, Y.M. & Georgelin, Y.P. 1976, AA, 49, 57

Georgelin, Y.M., Georgelin, Y.P. & Roux, S. 1973 AA, 25, 337

Georgelin, Y.M., Lortet-Zuckermann, M.C. & Monnet, G. 1975, AA, 42, 273

Georgelin, Y.M., Russeil, D., Marcelin, M., Amram, P., Georgelin, Y.P., Goldès, G., le Coarer, E. & Morandini, M. 1996 AAS, 120, 41

Glover, T.M., Dufour, R.J., Hester, J.J., Currie, D.G., van Orsow, D. & Walter, D.K. 1998, RMexAA-SC, 7, 158

González-Delgado, R.M., Pérez, E., Díaz, A.I., García-Vargas, M.L., Terlevich, E. & Vílchez, J.M. 1995, ApJ, 439, 604

González-Delgado, R.M., Pérez, E., Tenorio-Tagle, G., Vílchez, J.M., Terlevich, E., Terlevich, R., Telles, E., Rodríguez-Espinoza, J.M., Mas-Hesse, M, García-Vargas, M.L. & Díaz, A.I. 1994, ApJ, 437, 239

Gordon, K.D., Clayton, G.C., Misselt, K.A., Landolt, K.U. & Wolff, M.J. 2003, ApJ, 594, 279

Gum, C.S. 1955, MemRAS, 67, 155 (G)

Guseva, N.G., Papaderos, P., Meyer, H.T., Izotov, Y.I. & Fricke, K.J, 2009, AA, 505, 63

- Guseva, N.G., Izotov, Y.I., Stasińska, G., Fricke, K.J., Henkel, C. & Papaderos, P. 2011, AA, 529, A149
- Hamuy, M. & Wells, L. 1992. *CSCCD Reduction with IRAF Cookbook*. Personal communication
- Hawley, S.A. 1978, ApJ, 224, 417
- Henney, W.J. 1994, ApJ, 427, 288
- Henney, W.J. 1998, ApJ, 503, 760
- Herbst, W. 1976, ApJ, 208, 923
- Hester, J.J., Light, R.M., Westphal, J.A., Currie, D.G., Groth, E.J., Holtzman, J.A., Lauer, T.R. & O'Neil, Jr., E.J. 1991, AJ, 102, 654
- Hidalgo-Gómez, A.M, Moranchel-Basurto, A. & González-Fajardo, A.F. 2012, RMexAA, 48, 183
- Hipparcos and Tycho Catalogues*, 1997, ESA, SP-1200
- Hoffleit, D. & Jascheck, C. 1982, *The Bright Star Catalogue, Fourth Revised Ed.* New Haven: Yale University Observatory
- Howard, I.D., 1983, MNRAS, 203, 301
- Hummer, D.G. & Storey, P.J. 1987, MNRAS, 224, 801
- Humphreys, R. M. 1978, ApJS, 39, 389
- Humphreys, R.M. & Davidson, K. 1994, PASP, 106, 1025
- Humphreys, R.M. & Mc. Elroy D.B. 1984, ApJ, 284, 565
- Israel, F.P. & Kennicutt, R.C. 1980, Astrophys. Lett. 21, 1
- Izotov, Y.I., Thuan, T.X. & Lipovetsky, V.A. 1994, ApJ, 435, 647
- Izotov, Y.I, Stasińska, G., Meynet, G., Guseva, N.G. & Thuan, T.X. 2006, AA, 448, 955
- Kehrig, C., Telles, E. & Cuisinier, F. 2004, AJ, 128, 1141
- Kennicutt, R.C., 1992, ApJ, 388, 310
- Kennicutt, R.C., Bresolin, F. & Garnett, D.R. 2003, ApJ, 591, 801
- Kingsburgh, R.L. & Barlow, M.J. 1994, MNRAS, 271, 257
- Kobulnicky, H.A., Kennicutt, R.C.Jr. & Pizagno, J.L. 1999, ApJ, 514, 544
- Komesaroff, M.M. 1966, Aust. J. Phys., 19, 75
- Krishna Swamy, K.S. & O'Dell, R.C. 1966, ApJ, 147, 529
- Kudritzki, R.P. & Hummer, D.G. 1990, ARAA, 28, 303
- Kurucz, R.L., 1979, ApJS, 40, 1
- Lahulla, J.F 1987, AJ, 94, 1062
- Lang, K.R. 1991, *Astrophysical Data: Planets and Stars* (Springer-Verlag, Berlin; QB461.L35,1991)
- Leitherer, C. & Chavarría-K., C. 1987, AA, 175, 208
- Lequeux, J., Maucherat-Joubert, M., Deharveng, J.M. & Kunth, D. 1981, AA, 103, 305
- Levato, H & Malaroda, S. 1982, PASP, 94, 807
- Liu, X.W., Barlow, M.J., Danziger, I.J. & Storey, P.J. 1995, ApJ, 450, 59L

- Liu, X.W. & Danziger, J. 1993, MNRAS, 263, 256
- Liu, X.W., Storey, P.J., Barlow, M.J., Danziger, I.J., Cohen, M. & Bryce, M. 2000, MNRAS, 312, 585
- Lockman, F.J., Pisano, D.J. & Howard, G.J. 1996, ApJ, 472, 173
- Lynds, B.T., Canzian, B.J. & O'Neil, E.J.Jr. 1985, ApJ, 288, 164
- Lynds, B.T. & O'Neil, E.J.Jr. 1982, ApJ, 263, 130
- Lynds, B.T. & O'Neil, E.J.Jr. 1985, ApJ, 294, 578
- Lynds, B.T. & O'Neil, E.J.Jr. 1986, AJ, 92, 1125
- Lynga, G. 1987, Catalogue of Open Star Clusters Data (CDS Strasbourg)
- Mallik, D.C.V. & Peimbert, M. 1988, RMexAA, 16, 111
- Maron, M. 1990, Ap. Sp. Sci., 172, 21
- Massey, P. & Johnson, J. 1993, AJ, 105, 3
- Matthews, C.L. 1981, ApJ, 245, 560
- Mathis, J.S. 1970, ApJ, 159, 263
- Mathis, J.S. 1971, ApJ, 167, 261
- Mathis, J.S. 1972, ApJ, 176, 651
- Mathis, J.S. 1983, ApJ, 267, 119
- Mathis, J.S., Rumpl, W. & Nordsieck, K.H. 1977, ApJ, 217, 425
- Maíz-Apellániz, J.M., Mas-Hess, J.M., Muñoz-Tuñón, C., Vilchez, J.M. & Castañeda, H.O. 1998, AA, 329, 409
- Maron, M. 1990, ApS&S, 172, 21
- Mármol-Queraltó, E., Sánchez, S.F., Marino, R.A., Mast, D., Viironen, K., Gil de Paz, A., Iglesias-Páramo, J., Rosales-Ortega, F.F. & Vilchez, J.M. 2011, AA 534, A8
- Martin, P.G. 1978, *Cosmic Dust, Its impact on Astronomy*, Oxford University Press
- Martins, F. Shaerer, D. & Hillier, D.J. 2005, AA, 436, 1049
- Melnick, J. 1979, ApJ, 228, 112
- Mesa-Delgado, A. & Esteban, C. 2010, MNRAS, 405, 2651
- McCall, M.L., Rybski, P.M. & Shields, G.A. 1985, ApJS, 57, 1
- McCall, M.L., Richer, M. & Visvanathan, N. 1990, ApJ, 357, 502
- McGlynn, T., Scollick, K. & White, N. 1996, *SkyView: The Multi-Wavelength Sky on the Internet*, <http://skyview.gsfc.nasa.gov>
- McLean, B.J. et al. 1996, in *New Horizons from Multi-Wavelength Sky Surveys*, IAU Symposium No. 179 (Kluwer Academic Publishers), p. 465
- Moffat, A.F.J., FitzGerald, M.P. & Jackson, P.D. 1979, AAS, 38, 197
- Moustakas, J. & Kennicutt, R.C.Jr. 2006, ApJS, 164, 81
- Münch, G. & Persson, S.E. 1971, ApJ, 165, 241
- Natta, A. & Panagia, N. 1984, ApJ, 287, 228

- Nelan, E.P., Walborn, N.R., Wallace, D.J., Moffat, A.F.J., Makidon, R.B., Gies, D.R. & Panagia, N. 2004, AJ, 128, 323
- Nieva, M.F. & Simón-Díaz, S. 2011, AA, 532, A2
- O'Dell, C.R., Ferland, G.J., Henney, W.J. & Peimbert, M. 2013, AJ, 145, 93
- O'Dell, C.R. & Goss, W.M. 2009, AJ, 138, 1235
- O'Dell, C.R. & Harris, J.A. 2010, AJ, 140, 985
- O'Dell, C.R. & Hubbard, W.B. 1965, ApJ, 142, 591
- O'Dell, C.R., Hubbard, W.B. & Peimbert, M. 1966, ApJ, 143, 743
- O'Dell, C.R., Walter, D.K. & Dufour, R.J. 1992, ApJ, 399, L67
- Olive, K.A. & Skillman, E.D. 2001, New Ast., 6, 119
- Olofsson, K. 1995, AAS, 111, 57
- Osterbrock, D.E. 1989, *Astrophysics of Gaseous Nebula and Active Galactic Nuclei*, University Science Press
- Osterbrock, D.E. & Ferland, G.F. 2006, *Astrophysics of gaseous nebulae and Active Galactic Nuclei*, 2nd ed. University Science Books
- Pagel, B.E.J. 1969, Nature, 221, 325
- Panagia, N. 1973, AJ, 78, 929
- Peimbert, A. & Peimbert, M. 2010, ApJ, 724, 791
- Peimbert, M. 1967, ApJ, 150, 825
- Peimbert, M. 1971, Bol. Obs. Tonan. Tac., 36, 29
- Peimbert, M. & Costero, R. 1969, Bol. Obs. Tonan. Tac., 5, 3
- Peimbert, M. & Goldsmith, D.W. 1972, AA, 19, 398
- Peimbert, M. & Peimbert, A. 2011, RMexAA-SC, 39, 1
- Peimbert, M., Storey, P.J. & Torres-Peimbert, S. 1993, ApJ, 414, 626
- Peimbert, M. & Torres-Peimbert, S. 1971, Bol. Obs. Tonan. Tac., 6, 21
- Peimbert, M. & Torres-Peimbert, S. 1974, ApJ, 193, 327
- Peimbert, M. & Torres-Peimbert, S. 1977, MNRAS, 179, 217
- Peimbert, M. & Torres-Peimbert, S. 1992, AA, 253, 349
- Peimbert, M., Torres-Peimbert, S. & Dufour, R.J. 1993, ApJ, 418, 760
- Peimbert, M., Torres-Peimbert, S. & Rayo, J.F. 1978, ApJ, 220, 516
- Peimbert, M., Torres-Peimbert, S. & Ruiz, M.T. 1992, RMexAA, 24, 155
- Péquignot, D., Petitjean, P. & Boisson, C. 1991, AA, 251, 680
- Pilyugin, L.S., Vílchez, J.M. & Thuan, T.X. 2010, ApJ, 720, 1738
- Pilyugin, L.S., Grebel, E.K., Mattsson, L. 2012, MNRAS, 424, 2316
- Pişmiş, P. 1974, RMexAA, 1, 45

- Pradhan, A.K. & Peng, J. 1995, in *The Analysis of Emission Lines*, STSci Symp. Ser. 8, Eds. R.E. Williams and M. Livio (Cambridge University Press), p. 8
- Preibisch, T., Ratzka, T., Kuderna, B., Ohlendorf, H., King, R.R., Hodgkin, S., Irwin, M., Lewis, J.R., McCaughrean, M.J., and Zinnecker, H. AA 530, A34
- Povich, M.S., Townsley, L.K., Broos, P.S., et al. 2011, ApJS, 194, 6
- Reifenstein, E.C. III, Wilson, T.L., Burke, B.F., Mezger, P.G. & Altenhoff, W.J. 1970, AA, 4, 357
- Robledo-Rella, V. 2000, RMexAA-SC, 9, 181
- Robledo-Rella, V. 2002, RMexAA-SC, 12, 31
- Robledo-Rella, V. & Conti, P.S. 1994, RMexAA, 29, 79
- Robledo-Rella, V. & Firmani, C. 1990, RMexAA, 21, 236
- Robledo-Rella, V. & Peña, M. 1999, in *Wolf-Rayet Phenomena in Massive Stars and Starburst Galaxies*, Eds. K.A. van der Hucht, G. Koenigsberger & P.R.J. Eenens. Proc. IAU Symp. No. 193, (1999) (San Francisco: ASP), p. 493.
- Rodgers, A.W., Campbell, C.T. & Whiteoak, J.B. 1960, MNRAS, 121, 103
- Rodríguez, M. 1999, AA, 351, 1075
- Rosales-Ortega, F.F., Kennicutt, R.C., Sánchez, S.F., Díaz, A.I., Pasquali, A., Johnson, B.D. & Hao, C.N. 2010, MNRAS 405, 735
- Sánchez, L.J. 1990, Bach. Thesis, Instituto de Astronomía, UNAM, México
- Sánchez, L.J. & Peimbert, M. 1991, RMexAA, 22, 285
- Sánchez, S.F., Rosales-Ortega, F.F., Kennicutt, R.C., Johnson, B.D., Díaz, A.I., Pasquali, A. & Hao, C.N. 2011, MNRAS, 410, 313
- Sánchez, S.F., Rosales-Ortega, F.F., Marino, et al. 2012, AA, 546, A2
- Savage, B.D. & Mathis, J.S. 1979, ARAA, 17, 73
- Schaerer, D. & de Koter, A. 1997, AA, 322, 598
- Schmidt-Kaler, T.H. 1982 *Physical parameters of the stars*. Landolt-Börnstein New Series, Group VI, Vol. 2b, Astronomy and Astrophysics - stars and star clusters, Eds. K. Schaifers, H.H. Voigt (New York: Springer-Verlag)
- Searle, L. 1971, ApJ, 168, 327
- Seaton, M.J. 1960, Repts. Prog. Phys. 23, 313
- Seaton, M.J. 1979, MNRAS, 187, 785
- Sharpless, S. 1959, ApJS, 4, 257
- Shaver, P.A. & Goss, W.M. 1970, Aust. J. Phys. Ap. Sup., 13, 133
- Shaver, P.A., McGee, R.X., Newton, L.M., Danks, A.C. & Pottasch, S.R. 1983, MNRAS 204, 53
- Shaw, R.A. & Dufour, R. 1995, PASP, 107, 896
- Simbad* Data Base of the Centre de Données Stellaires de Strasbourg: <http://simbad.harvard.edu>
- Simon, K.P., Jonas, G., Kudritzki, R.P. & Rahe, J. 1983, AA, 125, 34

- Simón-Díaz, S. 2010, AA, 510, A22
- Simón-Díaz, S & Stasińska, G. 2011, AA, 526, A48
- Simón-Díaz, S., García-Rojas, J., Esteban, C., Stasińska, G., López-Sánchez, A.R., Morisset, C. 2011, AA, 530, A57
- Skillman, E.D., Terlevich, R. & Melnick, J. 1990, MNRAS, 240, 563
- Smith, N. & Morse, J.A. 2004, ApJ, 605, 854
- Smith, N. 2006, MNRAS, 367, 763.
- Smith, N. 2010, MNRAS, 402, 145
- Smith, R.G. 1987, MNRAS, 227, 943
- Spitzer, L. Jr. 1978, *Physical Processes in the Interstellar Medium*, Wiley-Interscience Publication (John Wiley & Sons, Inc.)
- Stasińska, G. 1978, AAS, 32, 429
- Stasińska, G. 1980, AA, 84, 320
- Stasińska, G. 1982, AAS, 48, 299
- Stasińska, G. & Leitherer, C. 1996, ApJS, 107, 661
- Stevenson, C.C. 1994, MNRAS, 267, 904
- Storey, P.J. & Hummer, D.G. 1995, MNRAS, 272, 41
- Tapia, M., Roth, M., Marraco, H. & Ruiz, M.T. 1988, MNRAS, 32, 661
- Tapia, M., Roth, M., Vázquez, R.A. & Feinstein, A. 2003, MNRAS, 339, 44
- Terlevich, R., Melnick, J., Masegosa, J., Moles, M. & Copetti, V.F. 1991, AAS, 91, 285
- Thé, P.S., Bakker, R. & Antalova, A. 1980, AAS, 41, 107
- Thé, P.S., Bakker, R. & Tjin A Djie, H.R.E. 1980, AA, 89, 209
- Thé, P.S. & Graafland, F. 1995, RMexAA-SC, 2, 75
- Thé, P.S. & Vleeming, G. 1971, AA, 14, 120
- Torres-Peimbert, S. & Peimbert, M. 1977, RMexAA, 2, 181
- Torres-Peimbert, S., Peimbert, M. & Daltabuit, E. (1980), ApJ, 238, 133
- Tsamis, Y.G., Barlow, M.J., Liu, W.-W., Danziger, I.J. & Storey, P.J. 2003, MNRAS, 338, 667
- Vacca, W.D., Garmany, C.D. & Shull, J.M. 1996, ApJ, 460, 914
- van Altena, W.F. & Jones, B.F., 1972, AA, 20, 425
- Vázquez, R.A., Baume, G., Feinstein, A. & Prado P. 1996, A&AS, 116, 75
- Vílchez, J.M. & Esteban, C. 1996, MNRAS, 280, 720
- Vílchez, J.M. & Iglesias-Páramo, J. 1998, ApJ, 508, 248
- Vogt, N. & Moffat, A.F.J. 1975, AA, 45, 405
- Walborn, N.R. 1973a, ApJ, 179, 517
- Walborn, N.R. 1973b, AJ, 78, 1067
- Walborn, N.R. 1995, RMexAA-SC, 2, 51

Walborn, N.R., Danks, A.C., Sembach, K.R., Bohlin, R.C., Jenkins, E.B., Gull, T.R., Lindler, D.J., Fegans, J.K., Hulbert, S.J., Linsky, J., Hutchings, J.B. & Joseph, C.L. 1998, ApJ, 492, L169

Walter, D.K. & Dufour, R.J. 1994, ApJ, 434, 29L

White, R.L. 1979, ApJ, 229, 954

Whiteoak, J.B. 1963, MNRAS, 125, 105

Whitford, A.E. 1958, AJ, 63, 201

Wilson, T.L., Mezger, P.G., Gardner, F.F. & Milne, D.K. 1970, AA, 6, 364

Witt, A.N. 1977, ApJS, 35, 1

Witt, A.N., Thronson, H.A. & Capuano, J.M. 1992, ApJ, 393, 611

Wolf, N.J. 1961, PASP, 73, 206

Wynn-Williams, C.G., Becklin, E.E. & Neugebauer, G., 1972, MNRAS, 160, 1

Ye, T. 1998, MNRAS, 294, 422

Zaritsky, D., Kennicutt, R.C.Jr. & Huchra, J.P. 1994, ApJ, 420, 87